NAVAL POSTGRADUATE SCHOOL
Monterey, California

THESIS

EFFECTS OF AN EMBEDDED VORTEX ON A SINGLE FILM-COOLING JET IN A TURBULENT BOUNDARY LAYER

by

Warren W. Williams

June 1988

Thesis Advisor: P. M. Ligrani

UNCLASSIFIED
SECURITY CLASSIFICATION OF THIS PAGE

REPORT DOCUMENTATION PAGE

1a. REPORT SECURITY CLASSIFICATION UNCLASSIFIED	1b RESTRICTIVE MARKINGS
2a. SECURITY CLASSIFICATION AUTHORITY	3 DISTRIBUTION / AVAILABILITY OF REPORT Approved for public release; distribution is unlimited
2b. DECLASSIFICATION / DOWNGRADING SCHEDULE	
4. PERFORMING ORGANIZATION REPORT NUMBER(S)	5 MONITORING ORGANIZATION REPORT NUMBER(S)
6a NAME OF PERFORMING ORGANIZATION Naval Postgraduate School 6b OFFICE SYMBOL (If applicable) Code 69	7a NAME OF MONITORING ORGANIZATION
6c. ADDRESS (City, State, and ZIP Code) Monterey, California 93943-50000	7b ADDRESS (City, State, and ZIP Code)
8a. NAME OF FUNDING / SPONSORING ORGANIZATION 8b OFFICE SYMBOL (If applicable)	9 PROCUREMENT INSTRUMENT IDENTIFICATION NUMBER
8c. ADDRESS (City, State, and ZIP Code)	10 SOURCE OF FUNDING NUMBERS PROGRAM ELEMENT NO / PROJECT NO / TASK NO / WORK UNIT ACCESSION NO

11 TITLE (Include Security Classification)

Effects of an Embedded Vortex on a Single Film-Cooling Jet in a Turbulent Boundary Layer

12. PERSONAL AUTHOR(S)

Williams, Warren W.

13a. TYPE OF REPORT	13b TIME COVERED	14 DATE OF REPORT (Year, Month, Day)	15 PAGE COUNT
Master's Thesis	FROM _____ TO _____	1988, June	224

16. SUPPLEMENTARY NOTATION

The views expressed in this thesis are those of the author and do not reflect the official policy or position of the Department of Defense or the U. S. Government.

17 COSATI CODES			18 SUBJECT TERMS (Continue on reverse if necessary and identify by block number)
FIELD	GROUP	SUB-GROUP	Embedded Vortex, Film-Cooling Single Jet, Heat Transfer, Endwall Secondary Flows. (JES)

19. ABSTRACT (Continue on reverse if necessary and identify by block number)

Effects of embedded longitudinal vortices on heat transfer in a turbulent boundary layer film cooled from a single injection hole are discussed. Film coolant was injected at blowing ratios 0.50 to 1.50 at a freestream velocity of 10 m/s. A single longitudinal vortex was induced upstream of the film-cooling holes. Heat transfer measurements were made downstream of injection. Flow visualization tests were conducted after the injectant was contaminated with smoke. Surveys of mean velocity and mean temperature were also made in different spanwise normal planes. For all blowing ratios examined, the embedded vortices cause significant alterations to wall heat transfer and to film-cooling distributions.

Measurement of mean temperature and mean velocities in spanwise planes show that injectant is pushed to the upwash side of the vortex when the injection hole is located beneath the vortex core or vortex downwash. Evidence of injection is seen only for $x/d \geq 7.4$. For other injection locations with respect to the vortex core, evidence of injectant appears for x/d up to 96, and the injectant is not swept into the vortex upwash by secondary flows.

20 DISTRIBUTION / AVAILABILITY OF ABSTRACT	21 ABSTRACT SECURITY CLASSIFICATION
☒ UNCLASSIFIED/UNLIMITED ☐ SAME AS RPT ☐ DTIC USERS	UNCLASSIFIED
22a NAME OF RESPONSIBLE INDIVIDUAL Phillip M. Ligrani	22b TELEPHONE (Include Area Code) (408)646-3382 / 22c OFFICE SYMBOL 69Li

DD FORM 1473, 84 MAR 83 APR edition may be used until exhausted
All other editions are obsolete

SECURITY CLASSIFICATION OF THIS PAGE

U.S. Government Printing Office 1986—606-243

UNCLASSIFIED

#19 (Con't)
Also measured are secondary heat transfer peaks which appear for blowing ratios of 1.0 and 1.5.

Approved for public release; distribution is unlimited.

Effects of an Embedded Vortex on a Single Film-Cooling Jet in a Turbulent Boundary Layer

by

Warren W. Williams
Lieutenant Commander, United States Navy
B.A., The Citadel, 1976

Submitted in partial fulfillment of the
requirements for the degree of

MASTER OF SCIENCE IN MECHANICAL ENGINEERING

from the

NAVAL POSTGRADUATE SCHOOL
June 1988

Author: 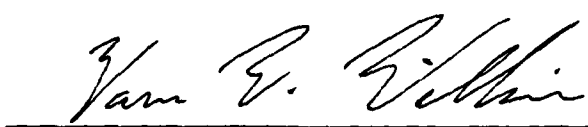
Warren W. Williams

Approved by: 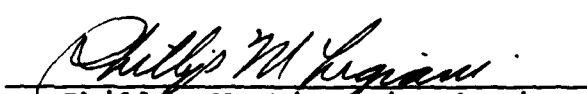
Phillip M. Ligrani, Thesis Advisor

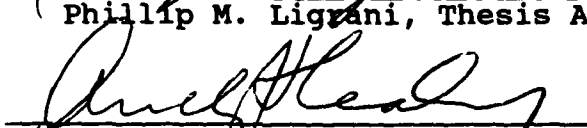
Anthony J. Healey, Chairman,
Department of Mechanical Engineering

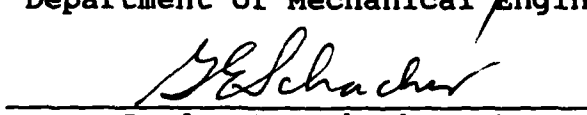
Gordon E. Schacher, Dean of
Science and Engineering

ABSTRACT

Effects of embedded longitudinal vortices on heat transfer in a turbulent boundary layer film cooled from a single injection hole are discussed. Film coolant was injected at blowing ratios 0.50 to 1.50 at a freestream velocity of 10 m/s. A single longitudinal vortex was induced upstream of the film-cooling holes. Heat transfer measurements were made downstream of injection. Flow visualization tests were conducted after the injectant was contaminated with smoke. Surveys of mean velocity and mean temperature were also made in different spanwise normal planes. For all blowing ratios examined, the embedded vortices cause significant alterations to wall heat transfer and to film-cooling distributions.

Measurement of mean temperature and mean velocities in spanwise planes show that injectant is pusned to the upwash side of the vortex when the injection hole is located beneath the vortex core or vortex downwash. Evidence of injection is seen only for $x/d \leq 7.4$. For other injection locations with respect to the vortex core, evidence of injectant appears for x/d up to 96, and the injectant is not swept into the vortex upwash by secondary flows.

Also measured are secondary heat transfer peaks which appear for blowing ratios of 1.0 and 1.5.

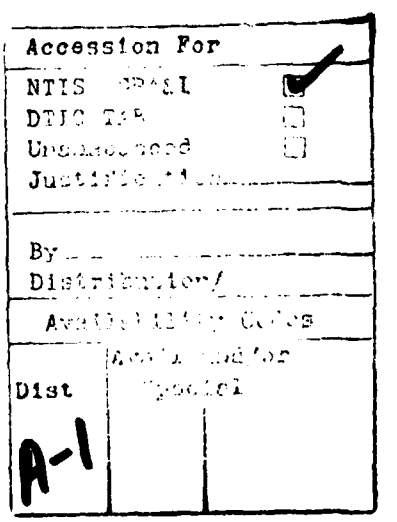

TABLE OF CONTENTS

LIST OF FIGURES

TABLE OF SYMBOLS

A - area of injection holes

C_D - discharge coefficient

C_p - specific heat at constant pressure

d - injection hole diameter

h - heat transfer coefficient

$q'' / (T_{r\infty} - T_w)$

m - blowing ratio, $\rho_c U_c / \rho_\infty U_\infty$

P - static pressure

R - gas constant

St - Stanton number

St - baseline Stanton number, no film-cooling, no vortex

St - Stanton number with film-cooling only

T - static temperature

U - mean velocity

V - volumetric flowrate

x - downstream distance as measured from the leading edge of the boundary layer trip or from the downstream edges of injection holes when used as x/d

y - vertical distance from the test surfacce upward

z - spanwise distance from the test section center line

ξ - unheated starting length

ρ - density

θ - non-dimensional coolant temperature,

$(T_{rc} - T_{r\infty}) / (T_w - T_{r\infty})$

δ_1 - boundary layer displacement thickness

SUBSCRIPTS

c - coolant at exit of injection holes

i - isentriopic

o - stagnation condition

p - injection plenum chamber

r - recovery condition

w - wall

∞ - freestream

ACKNOWLEDGEMENTS

This work was supported by Wright Aeronautical Laboratories, Wright-Patterson Air Force Base. Dr. Dick Rivir was program monitor.

The composition of this work was greatly influenced by P. M. Ligrani along with the work of S. L. Joseph, A. Ortiz and D. L. Evans.

Technical contributions were made by Dr. Bart Singer, for his work on computor software and G. E. Schwartz for his work on uncertanity analysis.

I wish to express my thanks to Professor Phil Ligrani for his understanding, persistence and good humor.

I. INTRODUCTION

Current turbine inlet temperatures are approaching 2000 K. Because of the substantial thermal load resulting on blades and endwalls, an understanding of the heat distributions in turbine passages is needed. This is because both high temperatures and large temperature gradients can lead to increased thermal stresses and reduced component life. Consequently, local hot spots must be avoided by providing adequate protection of turbine surfaces. One method of protection is film cooling. However, as injectant from film-cooling holes spreads over blade and endwall surfaces, it may be distorted by the secondary flows. This can lead to local hot spots just downstream of injection sites at exact locations where film-cooling would ordinarily be expected to provide adequate protection, and where protection is most needed.

One type of secondary flow expected to cause disturbances to film-cooling is the embedded vortex. Near the walls of turbine blade passages, such vortices result from at least two different mechanisms. First, they initially develop from the pressure gradient formed at the intersection of the blade leading edge and endwall.

Second, a centrifugal instability results in spanwise varying regions of high and low speed flow which form into Taylor-Gortler vortices.

Some of the earliest evidence that embedded vortices cause alterations to film-cooling was reported by Blair (1). He measured large variations of heat transfer and film-cooling effectivenesss on an endwell. These variations were attributed to a large vortex located in the corner between the endwall and the suction surface of their cascade. Goldstein and Chen (2,3) performed experimental studies on the influence of the endwall on film-cooling from blades using one and two rows of injection holes. The authors concluded that a triangular region exists on the convex side of the blade where coolant is swept away from the surface by the passage vortex. Sato, Aoki, Takeishi and Matsuura (4) studied distributions of heat transfer and film-cooling effectiveness on the endwall and airfoil within an annular low aspect ratio cascade.

Of work near concave surfaces with injection, Kobayashi (5) examined how homogeneous suction from a permeable wall affected the onset of longitudinal vortices in laminar boundary layers. In a later study,

Kobayashi (6) examined the effects of both blowing and suction. Results showed that suction increases the stability of laminar boundary layers to centrifugal instabilities, whereas blowing had little influence on the instability. In a study of similar phenomena, El-Hady and Verma (7) reached slightly different conclusions. They showed that the overall effect of suction or cooling was to stabilize boundary layers by reducing the amplitude ratio of the vortices. The layers were found to be less stable at higher Mach numbers and at higher cooling injection rates.

Recent studies conducted at the Naval Postgraduate School show that the protection provided by film-cooling can be altered significantly by embedded vorticies such as the ones existing in turbine blade passages. Without understanding the interaction of such secondary flows with film-cooling, it will not be possible to design schemes for efficient and uniform protection near turbine passage surfaces. Joseph (8) shows that heat transfer coefficients in boundary layers with film-cooling can be altered by as much as 30 percent by the presence of embedded vortices. These were obtained using a constant heat flux surface, instrumented with thermocouples

to measure surface temperature. Spanwise-average Stanton numbers show excellent agreement with the expected turbulent heat transfer correlation for a flow without film-cooling and without an embedded vortex. Evans (9) used a five-hole pressure probe to document the mean flow field characteristics of a boundary layer with film-cooling and embedded vortices. Heat transfer is generally higher on the downwash side of the vortex due to local boundary layer thinning, and lower on the upwash side due to local thickening of the boundary layer. Some of Evan's streamwise velocity results, provide evidence of the dominating effect that vortices have on local flow behavior. Near the downwash side of the vortex high velocity fluid is brought near the wall, where it dominates flow field behavior by minimizing the effects of the film-cooling. Ortiz (10) repeated some of these results and provided additional data on the effects that vortices have on local flow.

In order to better understand phenonena described by Joseph (8), Evans (9) and Ortiz (10) the objective of the present work is to document the effects of an embedded longitudinal vortex on a single film-cooling jet in a turbulent boundary layer. Attention is focusssed on the downstream development of flow fields, effects of spanwise

vortex positions, and on how the interactions between vortices and film-cooling changes with blowing ratio.

In order to isolate an influence of the vortex only, tests were conducted on a flat plate in a zero pressure gradient. With earlier data (8,9,10) the present results will aid the gas turbine heat transfer analyst to obtain a detailed cooling scheme for both the turbine blades and endwalls which allow for maximum inlet temperature. Experimental data for such design are particularly valuable since the complicated three-dimensional character of the flow interactions makes prediction and modelling impractical at the present time.

The organization of this report is now discussed. In section 2 experimental apparatus and procedure are presented. This is followed by section 3 which gives experimental results. The results consist of flow visualization results, heat transfer data, surveys of mean velocity, mean pressure, and mean temperature. In Section 4 is a summary. This is followed by Appendix A, which contains photographs and figures. Appendix B presents the uncertainity analysis. A list of references follows along with a Distribution List.

II. EXPERIMENTAL APPARATUS AND PROCEDURES

A. WIND TUNNEL AND COORDINATE SYSTEM

The experiments were conducted in an open-circuit, subsonic wind tunnel located in the laboratories of the Department of Mechanical Engineering at the Naval Postgraduate School. A centrifugal blower was located at the upstream end of the tunnel. Air entered the inlet from the surrounding room through a coarse filter. The discharge from the fan passed to the inlet of the diffuser. A 1.6mm clearance between fan and diffuser isolated vibrations from the fan to the wind tunnel body. The diffuser contained a second fine filter to remove small particles from the air as well as four baffle vanes to reduce noise and minimize the likelihood of flow separations. The diffuser was then followed by a header containing a honeycomb and three screens to reduce spatial nonuniformities in the flow. Afterwards, a 16 to 1 contraction ratio nozzle lead to the test section. The test section was a rectangular duct 3.05 m long and 0.61 m wide. The height of the topwall was adjustable to permit changes in the streamwise pressure gradient. For the present study, a zero presure gradient was maintained without vortex or film-cooling to within .007 inches of

water differential pressure along the length of the test section. The air speed through the test section was adjustable from 1m/s to 40m/s.

At the exit plane of the nozzle, the variation of total pressure was less than 0.4% at 26m/s and 34m/s. Mean velocity varied less than 0.7% for the same speeds. Profile measurements of the mean velocity and longitudinal turbulence intensity in the turbulent boundary layer developing at 20 m/s indicated normal, spanwise uniform behavior. At x= 1.8m, measurements from hot-wire probes showed that boundary layer thickness, boundary layer displacement thickness, and boundary layer momentum thickness were 29.7mm, 5.09mm and 3.59mm, respectively. At a freestream velocity of 21.0m/s, the momentum thicknes Reynolds number was 4780 and the friction velocity was .8m/s. The freestream turbulence intensity was about .1 percent (based on freestream velocity) for freestream velocities from 20 m/s to 30 m/s. For this qualification test, and the present study, the boundary layer was tripped near the exit of the nozzle with a 1.5 mm high strip of tape.

The coordinate system is shown in figure 1. With the heat transfer surface at elevated temperature, an unheated starting length of 1.10 m existed. Freestream

air was maintained at ambient temperature, and thus, the direction of heat transfer was from the wall to the gas. Temperature differences were maintained less than about 30 °C to minimize the effects of variable properties. Referring again to Figure 1, the downstream edges of the injection nozzles were located 1.08m downstream of the boundary layer trip and 0.02m upstream of the test surface. The leading edge of the vortex generator was placed 0.48m downstream of the trip. Also labelled in Figure 1 are the locations of thermocouple rows along the test surface.

B. VORTEX GENERATORS

Each Vortex generator consisted of a half-delta wing attached to the wind tunnel floor at an angle of 18 ° with respect to the tunnel centerline. The generator design was similar to ones employed by Joseph (8) Evans (9), Ortiz (10), Westphal, et. al. (11,12) and Eibeck and Eaton (13). The heights of or vortex generators one, two, three, and four were 1.9, 3.3, 5.2, and 7.4 cm, respectively. The bases measured 4.5, 7.7, 12.4 and 17.4cm respectively. Vortex generator positions with respect to the wind tunnel centerline are given labelled a-k in Table I.

TABLE I. Vortex Generator Position in CM and Inches

TABLE I

VORTEX POSITION	CM	INCHES
a	-5.1	-2.0
b	-3.8	-1.5
c	-2.5	-1.0
d	-1.3	-0.5
e	0.0	0.0
f	1.3	0.5
g	2.5	1.0
h	3.8	1.5
i	5.1	2.0
j	6.3	2.5
k	7.6	3.0

C. INJECTION SYSTEM

In the present study coolant was ejected from circular injection holes into the boundary layer developing along the bottom wall of the test section. Diameters of the injection holes were .952 cm, scaled such that δ_1/d was approximately 0.38. The injection parameters m and Θ were also scaled to resemble parameters near gas turbine blades. Injection holes were inclined at angle of 30° with a three diameter spanwise spacing between center lines. The middle tube was located on the center line of the test surface. Three injection tubes were used during most heat transfer measurements.

The centerline injection tube was used in addition to two other tubes open on the ends of the injection row, one on each side. The flow was studied as the vortex affected the jet from the center injection hole. Injectant from the two peripheral holes did not touch the heat transfer surface or affect the heat transfer measurements. Injection from these two holes was required in order to maintain steady flow in the injection system at measurable flows rates. Blowing ratios (m) of 0.5, 1.0, and 1.5 were employed for measurements with film-cooling and a vortex.

Air for the injection system originated in a 10 HP two stage, 150 psig Ingersol-Rand air compressor. From the compressor, air flowed through an adjustable pressure regulator, a cut-off valve, flexible tubing, a moisture separator, a flow regulator, a Fisher and Porter rotometer, a diffuser, and finally into the injection heat exchanger and plenum chamber. The exchanger provided means to heat injectant above ambient temperature. The top surface of the plenum contained 13 plexiglass injection tubes, each 8 cm long with a length-to-diameter ratio of 8.4. When three holes were used, ten of the holes were plugged and covered with transparent tape on the wind tunnel bottom wall. Qualification tests of the injection system showed satisfactory uniformity of the

plenum chamber pressure over a range of blowing ratios. Discharge coefficients ranged between 0.5 and 0.77, and increased with Reynolds number in agreement with results given by Ligrani and Camci (14) and Joseph (8). In order to determine the discharge coefficient and other injection parameters, a number of quantities were measured, including P_∞, T_∞, V_c, P_{op}, T_{op}, and A. The coolant velocity and static density were then given by

$$U_c = \frac{V_c}{A} \quad \text{and} \quad \rho_c = \frac{P_\infty}{RT_c} \qquad (1,2)$$

where T_c is the static temperature at the exits of injection holes. The temperature drop between T_{op} and T_{oc} was measured and correlated as a function of T_{op} and Reynolds number. The coolant mass flux is then the product of U_c and ρ_c. To calculate the isentropic mass flux, ρ_{ci} and U_{ci} were found using

$$\rho_{ci} = \frac{P_\infty}{RT_{ci}} \qquad (3)$$

and

$$U_{ci} = \frac{2\,(P_{op} - P_\infty)^{\frac{1}{2}}}{\rho_{ci}} \qquad (4)$$

where $T_{ci} = T_{op} - U_c^2/2g_cC_p$. Discharge coefficients, C_d, were then given by

$$C_d = \frac{\rho_c U_c}{(\rho_c U_c)i} \qquad (5)$$

Results of qualification tests are presented in Figures 2a, 2b, and 2c for one hole, two holes and thirteen injection holes, respectively. The qualification tests were performed with the injected heated at three different levels, and without heating. Higher discharge coefficients are present when no heat is provided to the injectant. Data for a given number of injectant holes, no matter which heat level is employed, fall on the same curve. The lower C_D with heating are believed to be a result of expansion of the plenum chamber, causing some expansion of cracks in injection holes. This results in roughness on injection tube surfaces which impedes flow through the system.

D. HEAT TRANSFER MEASUREMENT

The heat transfer surface was designed and developed to provide a constant heat flux over its area. The plate was constructed so that its upward facing part was adjacent to the wind tunnel air stream, with minimal heat loss by conduction from the sides and beneath the test surface. It consisted of a thin stainless steel foil 1.3m x .467m x 20mm, painted flat black with seven layers of liquid crystals. Attached to the underside of the foil were 126 copper-constantan thermocouples in six rows. In

each of the six rows, 21 thermocouples were located 1.27 cm apart to provide adequate spanwise resolution of temperature distributions. Thermocouple lead wires were located in grooves cut into a triple sheet of 0.254mm thick double sided tape, manufactured by 3M Company. The grooves were then filled with RTV epoxy. A thin foil heater, 1.0mm x 1.118 m x 0.438 m, rated at 120V and 1500W and manufactured by Electrofilm Corp., was attached to the tape with Electrobond epoxy. Beneath the heater was a 12.7mm thick lexan sheet, followed by 25.4mm of foam insulation, 82.55mm thick styrofoam, three sheets of .254mm thick lexan and one sheet of 9.53mm thick balsa wood. This surface was developed and constructed by Ortiz (10), based on an earlier design by Joseph (8).

The vertical height of the surface was adjustable in order to account for thermal expansion. It was maintained level with the test surface by adjusting screws in the plexiglass frame supporting the heat transfer surface from below. During heat transfer tests, the top surface of the foil remained flat and smooth with minimal surface irregularities. The surface temperature was controlled by adjusting input voltage to the heater using a Standard Electrical Co. Variac, type 3000B.

To determine the heat loss by conduction from the heat transfer test surface, results from the energy balance of Ortiz (10) were used. Radiation losses from the top of the test plate were estimated analytically. For an average plate temperature of 40° C with a freestream at 10 m/s and 18° C, radiation losses were approximately 55 watts or about 8.5 percent of the total power into the test plate.

Tests to determine the thermal contact resistance between thermocouples and the foil top surface were conducted and compared to earlier tests. The first step in this procedure was to calibrate the liquid crystals used to measure the temperature of the foil surface. This involved coating several samples with liquid crystals and placing them in an isothermal bath whose temperature could be regulated. A platinum resistance thermometer was used to measure the bath temperature. These temperatures were then matched to colors appearing on the liquid crystals. Once the calibration of the liquid crystals was complete, they were then applied to the heat transfer surface. Heat was applied to the surface and a test case was run without injection and without a vortex generator. Temperatures of thermocouples attached to the foil immediately below the liquid crystals were obtained when the liquid crystals

clearly showed a color identifiable with a temperature from the earlier calibration. The temperature difference ΔT divided by the convection heat transfer q_{conv} is the contact resistance given by

$$C_R = \Delta T/q_{conv} \quad (6)$$

A value of 0.0154 was found for CR. Because this value was very close to 0.016, the CR determined by Joseph (8), CR=0.016, was used for all data reduction.

Experimental uncertainties of Stanton numbers and quantities used to deduce Stanton numbers are given in Appendix B. These uncertainties were estimated by Schwartz (15)

E. TEMPERATURE MEASUREMENTS

The copper-constantan thermocouples used with the heat transfer surface were calibrated by Ortiz (10). His calibration data was used for all but three thermocouples used in the present work. These three thermocouples were used to measure freestream temperature, plenum chamber temperature, and the temperature in surveys. From calibration results, a third order polynomial equation was used to represent temperature as a function of voltage in millvolts. For the freestream temperature on channel 147,

$$T=-2.6 + 32178E - 5483059E^2 + 12473940000E^3 \quad (7)$$

For the plenum chamber temperature on channel 148,

$$T=1.66 + 21973E + 248196E^2 - 7809850000E^3 \quad (8)$$

Finally, for the thermocouple attached to the tranverse apparatus on channel 152,

$$T=-0.776 + 27843E - 2196907E^2 + 4408860000E^3 \quad (9)$$

For all three equations E is read in millivolts. For the boundary layer/vortex temperature survey, 800 probe locations were used, covering an area of 12cm x 22cm. The probe was positioned by means of a motorized traversing device controlled by a Mitas controller. This, in turn was operated by the HP 9836S computer. Voltages from the thermocouples were received by an HP-3497A Data Acquisition/Control unit with an HP-3498A Extender. These units were also controlled by the Hewlett-Packard Series 300, Model 9836S computer, equipped with a MC68000, 8MHz 16/32-bit processor, dual 5-1/4 inch floppy disk drives, and 1M byte of memory.

F. MEAN VELOCITY MEASUREMENTS

The three mean velocity components were measured using a five-hole pressure probe manufactured by United Sensors and Control Corporation. The probe is a DC-250-24CD conical five-hole probe with a tip diameter of 6.35mm. During

measurements, the pressure from each of the five holes is directed to its own differential pressure transducer with one end open to the atmosphere. Celesco model LCVR variable reluctance transducers are used with the United sensors probe. These transducers have a full scale pressure range of 2cm of water. Transducer output signals were converted to DC signals by Celesco CD-10D carrier demodulators which then connected to the same data acquisition system as used for temperature measurement.

The probe was calibrated in the uniform freestream of an open circuit blower tunnel located in the laboratories of the Department of Mechanical Engineering. Calibration is performed by yawing the probe in 10 degree increments from -20 degrees to +20 degrees. At each yaw angle, the probe is pitched through a 40 degree range, also at 10 degree increments. A total of 25 combination angles are used.

At each angle, pressure coefficients are computed as follows:

$$C_{pyaw} = (P_2 - P_3) / (P_1 - \bar{P}) \quad (10)$$

$$C_{ppitch} = (P_4 - P_5) / (P_1 - \bar{P}) \quad (11)$$

$$C_{pt-s} = (P_0 - P_s) / (P_1 - \bar{P}) \quad (12)$$

and

$$C_{PTOTAL} = (P_0 - \bar{P}) / (P_1 - \bar{P}) \quad (13)$$

Here, P_o is the total pressure, P_s is the static pressure, $\bar{P}=(P_2+P_3+P_4+P_5)/4$, and pressure numbers correspond to ones at probe ports. Figures 3-6 show calibration curves for the United Sensor probe. The variations of the coefficients follow expected behavior for this type of probe.

G. FLOW VISUALIZATION

Injectant was visualized by providing white smoke to the injection plenum, produced by a Rosco Electric Fog/Smoke Machine, Model 1500. The Fog/Smoke machine has ten smoke settings, and utilizes liquid smoke fluid. Flexible 10.3cm diameter tubing carried the smoke from the smoke generator to the plenum chamber. For these tests, plenum pressure was maintained entirely by the Fog/Smoke machine. Freestream wind tunnel conditions were then set to achieve desired blowing ratios.

III. EXPERIMENTAL RESULTS

A. FLOW VISUALIZATION

Flow visualization photographs are presented in Figures 7-25. These are presented in three parts. In the first part, injection is provided through seven injection holes where the vortex affects injectant only from one central hole. Injection from the remaining six holes is needed to maintain steady injection plenum conditions at measurable flow rates. In the second part, flow is studied as the vortex affects injectant from two holes, with peripheral injection from five other holes. In the third part, all thirteen injection holes are used. For all three cases, smoke is provided to the injection plenum and thus, coolant jets are visualized as they are contaminated by smoke.

The effects of an embedded vortex on injection from a single injection hole is evident from results in Figures 7-11. In these Figures, flow is moving from the top of the photograph to the bottom of the photograph as viewed looking down on the test surface. Figure 7 shows the behavior of the smoke from injection holes with no vortex in the flow. The smoke moves in the downstream

direction without spanwise motion. Figure 8 shows the smoke when the vortex is at position e. Here skewing of the smoke is evident when using vortex generator #2. For spanwise vortex positions f. g. and h in Figures 9, 10 and 11, less smoke is present, but with more disorder as the smoke proceeds downstream. The photographs shown in Figures 8 -11 show the effects upon the smoke of spanwise vortex position. Farther downstream for vortex positions f, g, and h, some waviness of the smoke is evident as a result of vortex motion.

The effects of an embedded vortex on injection from two injection holes is evident from results in Figures 12-15. The injection flow is shown in Figure 12 without a vortex in the flow. With generator #4 at position h, the upstream viewed pattern in Figure 13 shows how the injectant is distorted and lifted off the wall. Figure 14 shows how the swirl from the vortex lifts the injectant and swirls it in the flow field. Figure 15 shows a downward view of smoke from jets which is greatly skewed. For Figures 13 and 14, vortex generator #4 was used at position h. For Figure 15, vortex generator #4 was used at position i.

The effects of an embedded vortex on injection from thirteen holes is evident from results in Figures 16-25.

The injectant is shown in Figure 16 without a vortex in the flow. Figures 17-20 show the effects on the smoke as vortex generator #2 is moved spanwise from positions e-h. The largest amount of distortion to smoke from the vortex generator is shown in Figure 19. Such distortion results in a high heat transfer region where the injectant is spread away from the wall.

Figures 21-23 show how the smoke pattern changes as the size of the vortex generator is changed. Figures 24 and 25 show injectant from thirteen holes as distorted by vortex generator #2 at positions e and g, respectively. Distortion to the injectant is greatest in Figure 25.

B. MEAN VELOCITY AND MEAN TOTAL PRESSURE SURVEYS

Distributions of mean velocity and mean total pressure are presented in Figures 26-37. These surveys were obtained using the five-hole pressure probe. For each survey, the probe was positioned at 800 different locations in spanwise planes at chosen downstream locations. Four different sets of data are presented. Downstream locations are given as x/d, nondimensional distance from the downstream edge of injection holes. All results were obtained with a blowing ratio of 0.5 and vortex generator #2.

Figures 26-28 show the effects of the vortex generator positioned at spanwise location e. The pressure probe is

positioned at x/d=5.2. Figures 29-37 show the effects of the vortex generator positioned at three different spanwise locations for x/d=41.9.

Results in Figures 26-28 were obtained to locate the vortex position with respect to the film-cooling holes. Figure 26 shows the velocity vector field. Figure 27 shows streamwise velocity distribution. Figure 28 shows the total pressure field. Strong secondary spanwise velocities are observed close to the wall in Figure 26. Very high streamwise velocities are evident near the wall at the downwash side of the vortex in Figure 27. Here, the boundary layer is quite thin. Within the upwash region, low-pressure fluid is convected away from the wall, as shown in Figure 28.

Results in Figures 29-37 were obtained to document effects of different spanwise vortex positions e, h, and k. Figures 29-31 show measurements for the vortex generator positioned at spanwise location e. Figures 32-34 show data for spanwise location h and Figures 35-39 are for spanwise location k. For results in Figures 29-37 the probe streamwise position is held constant at x/d=41.9. Figures 29, 32 and 35 show the vortex at different spanwise locations with respect to the wind tunnel centerline. A qualitative comparison of these Figures indicates no significant

changes in local vortex structure. For each case, a region of low streamwise velocity and low pressure exists near the upwash side of the vortex. A region of high streamwise velocity and high pressure is present near the downwash side of each vortex.

C. MEAN TEMPERATURE SURVEY

Utilizing vortex generator #2 and a constant blowing ratio of 0.5, surveys of mean temperature were made over spanwise planes. The survey was performed at four different streamwise locations for x/d=5.2, 41.9, 82.9 and 109.2. The film-cooling injectant was heated to 51 C without providing any heat to the test plate. Thus, the temperature field shows how fluid from the film-cooling holes is convected and distorted by the vortex, where higher temperatures indicate greater amounts of coolant.

The temperature survey is presented in two parts. First, the downstream development effects are discussed, followed by effects of spanwise vortex position.

The results in Figures 38-41 show the downstream development of the film coolant. As the flow moves downstream, most coolant is convected into the upwash side of the vortex. Near the downwash side, a very thin boundary layer is present and there is little coolant.

As downstream distance increases, coolant is convected farther from the wall and spread over a larger area.

The results in Figures 39, 42, and 43 show coolant distributions at x/d=4.19 for vortex positions h, k, and e, respectively. Figures 39 and 43 show the injectant being lifted away from the wall and convected into the upwash of the vortex. For vortex position k, coolant is less spread out and not pushed to the vortex upwash side. These changes result due to different locations of the vortex as it passes near film-cooling injection locations.

D. HEAT TRANSFER RESULTS

Heat transfer results are presented in five parts. These five parts are: (1) baseline heat transfer without vortex and without film-cooling. (2) boundary layer with film-cooling from a row of thirteen injection holes, (3) boundary layer film-cooling from a single injection hole, (4) boundary layer with embedded vortex, and (5) boundary layer with embedded vortex and film-cooling from a single injection hole. A step by step procedure was used in order to verify and check facilities and measurement techniques.

1. Baseline Heat Transfer Without Vortex and Without Film-Cooling

Figure 44 shows spanwise - averaged Stanton numbers plotted with respect to Reynolds number for a free stream velocity of 10 m/s. Results are given for six streamwise locations. These data lie approximately 5-6 percent below the correlations for constant heat flux and unheated starting length given by Kays and Crawford (1980).

$$St_x Pr^{0.04} = 0.03\, Re_x^{-0.2} \left[1-\left(\frac{\xi}{x}\right)^{0.9}\right]^{-0.111} \qquad (14)$$

$$St_x Pr^{0.04} = 0.03\, Re_x^{-0.2} \left[\frac{b_1\left(\frac{\xi}{\delta}, \frac{1.0}{\delta}\right)}{B_{u1}\left(\frac{1}{\delta}, \frac{1.0}{\delta}\right)}\right] \qquad (15)$$

Here, $u_1 = 1-(\xi/x)^{0.9}$

Figure 45 shows the heat transfer coefficient plotted as a function of spanwise location. Results for 10 m/s show good spanwise uniformity with exception of some variations in the first row.

2. Boundary Layer With Film-Cooling from a Row of Thirteen Injection Holes

To check the heat transfer surface and film-cooling system, measurements of St/St_o were made with film-cooling and no embedded vortex. Figures 46a and 46b show spanwise - averaged ratios for freestream speeds for 10 m/s and 15 m/s at different blowing ratios. St/St_o increases with Reynolds number for each set of data. The lowest St/St_o are observed

for blowing ratios between 0.38 and 0.64. This behavior is consistant with the results of Joseph (8) and Ortiz (10).

Local St/St_o for a blowing ratio of 1.1 at 10 m/s, and for a blowing ratio of 0.5 at 15 m/s are shown in Figures 48 and 47, respectively. These data show good spanwise uniformity with the exception of the first row.

3. Boundary Layer With Film-Cooling from a Single Injection Hole

Figures 49-51 show local St/St_o distributions from the boundary layer with film-cooling injection from a single hole. These data were collected at a free stream velocity of 10 m/s with blowing ratios of 0.5, 1.0, and 1.5. No vortex was present. The value for θ was maintained at approximately 1.5 for these tests.

Results show low St/St_o at locations where injectant is present in the flow. This is most evident for a blowing ratio of 0.5. With streamwise development the effects of heat transfer diminish for all three blowing ratios.

4. Boundary layer With Embedded Vortex

Measurements of St/St_o were made with an embedded vortex and no film-cooling. For the tests, the injection system was turned off and the cooling holes were sealed and taped. The free stream velocity was maintained at

10 m/s. Local distributions of St/St_o showed good agreement with the measurements of Ortiz (10) and Joseph (8), as expected.

5. Boundary Layer With Embedded Vortex and Film-Cooling From a Single Injection Hole

These data are presented according to the blowing ratio used in the tests. Data for a blowing ratio of 0.5 are given in Figures 52-100. Data for a blowing ratio of 1.0 are given in Figures 101-133. Data for a blowing ratio of 1.5 are given in Figures 134-166. In each Figure, spanwise distributions of St_f/St_o and St/St_o are given. Three-dimensional plots of results documenting streamwise development are given in Figures 52-55 for a blowing ratio m of 0.5, in Figures 101-133 for m=1.0, and in Figures 134-136 for m=1.5. The other Figures provide additional information on streamwise development as well as information on the effects of spanwise vortex position. All St_f/St_o and St/St_o data were measured at a free steam velocity of 10 m/s and θ approximately equal to 1.5.

The effect of the vortex on the film-cooled boundary layer is evident from the Figures by comparing St/St_o distributions to St_f/St_o distributions. When the boundary layer is not affected by the film-cooling or the vortex, the values of St/St_o and St_f/St_o are close to 1.0.

In general terms, the vortex upwash and downwash regions result in local regions of low St/St_o and high St/St_o respectively, compared to St_f/St_o distributions.

A. RESULTS FOR THE BLOWING RATIO m=0.5

Tables II and III give experimental conditions corresponding to Figures 52-100.

TABLE II. m=0.5 Data

Figure	m	Vortex Position	x(m)	x/d
52	.52	b	1.15-2.00	7.4-96.6
53	.53	e	1.15-2.00	7.4-96.6
54	.51	h	1.15-2.00	7.4-96.6
55	.51	k	1.15-2.00	7.4-96.6
56	.51	a	1.15	7.4
57	.52	b	1.15	7.4
58	.51	c	1.15	7.4
59	.51	d	1.15	7.4
60	.53	e	1.15	7.4
61	.51	f	1.15	7.4
62	.50	g	1.15	7.4
63	.51	h	1.15	7.4
64	.49	i	1.15	7.4
65	.46	j	1.15	7.4
66	.51	k	1.15	7.4
67	.51	a	1.25	17.5
68	.52	b	1.25	17.5
69	.51	c	1.25	17.5
70	.51	d	1.25	17.5
71	.53	e	1.25	17.5
72	.51	f	1.25	17.5
73	.50	g	1.25	17.5
74	.51	h	1.25	17.5
75	.49	i	1.25	17.5
76	.46	j	1.25	17.5
77	.51	k	1.25	17.5
78	.51	a	1.4	33.6
79	.52	b	1.4	33.6
80	.51	c	1.4	33.6
81	.51	d	1.4	33.6

TABLE III. m=0.5 Data

Figure	m	Vortex Position	x(m)	x/d
82	.53	e	1.4	33.6
83	.51	f	1.4	33.6
84	.50	g	1.4	33.6
85	.51	h	1.4	33.6
86	.49	i	1.4	33.6
87	.46	j	1.4	33.6
88	.51	K	1.4	33.6
89	.52	b	1.6	54.6
90	.53	e	1.6	54.6
91	.51	h	1.6	54.6
92	.51	k	1.6	54.6
93	.52	b	1.8	75.6
94	.53	e	1.8	75.6
95	.51	h	1.8	75.6
96	.51	k	1.8	75.6
97	.52	b	2.0	96.6
98	.53	e	2.0	96.6
99	.51	h	2.0	96.6
100	.51	k	2.0	96.6

Figures 52-55 show three-dimensional presentations of experimental data illustrating the effects of streamwise development for vortex positions b, e, h, and k. A comparison of these Figures shows how St/St_o distributions change as the spanwise position of the vortex is changed. For position b the film injectant is initially located to the right of the vortex downwash and the effects of film-cooling are seen for x/d up to 54.6. For positions e and h the coolant is ejected just beneath the downwash and the St/St_o signature of the film injectant disappears for $x/d \geq 17.5$. Thus, for these situations, local St/St_o

variations are a result of the vortex rather than film-cooling injection. For vortex position k the injectant is initially located beneath the vortex upwash. Here, the film coolant seems to affect local St/St_o distributions for x/d up to 33.6. Of the four vortex positions. St/St_o peaks are largest for position k.

Additional information on the influence of spanwise vortex position may be found in Figures 56-66 for x/d=7.41, in Figures 67-77 for x/d=17.5, in Figures 78-88 for x/d=33.6, in Figures 89-92 for x/d=54.6, in Figures 93-96 for x/d=75.6, and in Figures 97-100 for x/d=96.6.

B. RESULTS FOR BLOWING RATIO m=1.0

Table IV gives experimental conditions corresponding to Figures 101-133.

TABLE IV. m=1.0 Data

Figure	m	Vortex Position	x(m)	x/d
101	0.99	b	1.15-2.00	7.4-96.6
102	0.99	e	1.15-2.00	7.4-96.6
103	1.0	h	1.15-2.00	7.4-96.6
104	.99	b	1.15	7.4
105	.99	c	1.15	7.4
106	.99	d	1.15	7.4
107	.99	e	1.15	7.4
108	1.1	f	1.15	7.4
109	1.1	g	1.15	7.4
110	1.0	h	1.15	7.4
111	.99	b	1.25	17.5
112	.99	c	1.25	17.5
113	.99	d	1.25	17.5
114	.99	e	1.25	17.5
115	1.1	f	1.25	17.5
116	1.1	g	1.25	17.5
117	1.0	h	1.25	17.5
118	.99	b	1.4	33.6
119	.99	c	1.4	33.6
120	.99	d	1.4	33.6
121	.99	e	1.4	33.6
122	1.1	f	1.4	33.6
123	1.1	g	1.4	33.6
124	1.0	h	1.4	33.6
125	.99	b	1.6	54.6
126	.99	e	1.6	54.6
127	1.0	h	1.6	54.6
128	.99	b	1.8	75.6
129	.99	e	1.8	75.6
130	1.0	h	1.8	75.6
131	.99	b	2.0	96.6
132	.99	e	2.0	96.6
133	1.0	h	2.0	96.6

Figures 101-103 show three-dimensional presentations of experimental data illustrating the effects of streamwise development for vortex positions b, e, and h. As for the m=0.5 data, these results show st/st_o distribution changes as the spanwise position of the vortex is changed.

For position b the effects of the injection are seen for $7.41<x/d<96.6$. For positions e and h, the effects of injection on St/St_o are evident only for $x/d=7.41$. This is because the injectant is issued beneath the downwash of the vortex where the vortex dominates local boundary layer behavior. Of the three vortex positions, the highest St/St_o are observed for vortex position h. Also of particular interest is a double peak of St/St_o evident for vortex position e at $x/d=7.41$.

Additional information on the influence of spanwise vortex position may be found in Figures 104-110 for $x/d=7.41$, in Figures 111-117 for $x/d=17.5$, and in Figures 118-124 for $x/d=33.6$, in Figures 125-127 for $x/d=54.6$, in Figures 128-130 for $x/d=75.6$, and in Figures 131-133 for $x/d=96.6$.

C. RESULTS FOR BLOWING RATIO m=1.5 data

Table V gives experimental conditions corresponding to Figures 134-166.

TABLE V. m=1.5 Data

Figure	m	Vortex Position	x(m)	x/d
134	1.3	b	1.15-2.00	7.4-96.6
135	1.51	e	1.15-2.00	7.4-96.6
136	1.5	h	1.15-2.00	7.4-96.6
137	1.3	b	1.15	7.4
138	1.6	c	1.15	7.4
139	1.6	d	1.15	7.4
140	1.5	e	1.15	7.4
141	1.6	f	1.15	7.4
142	1.6	g	1.15	7.4
143	1.5	h	1.15	7.4
144	1.3	b	1.25	17.5
145	1.6	c	1.25	17.5
146	1.6	d	1.25	17.5
147	1.5	e	1.25	17.5
148	1.6	f	1.25	17.5
149	1.6	g	1.25	17.5
150	1.5	h	1.25	17.5
151	1.3	b	1.4	33.6
152	1.6	c	1.4	33.6
153	1.6	d	1.4	33.6
154	1.5	e	1.4	33.6
155	1.6	f	1.4	33.6
156	1.6	g	1.4	33.6
157	1.5	h	1.4	33.6
158	1.3	b	1.6	54.6
159	1.5	e	1.6	54.6
160	1.5	h	1.6	54.6
161	1.3	b	1.8	75.6
162	1.5	e	1.8	75.6
163	1.5	h	1.8	75.6
164	1.3	b	2.0	96.6
165	1.5	e	2.0	96.6
166	1.5	h	2.0	96.6

Figures 134-136 show three-dimensional presentations of experimental data illustrating the effects of streamwise development for vortex positions b, e, and h. As for m=0.5

and m=1.0 data for positions e and h, the vortex downwash rather than the injectant is most responsible for the local distributions seen. For these two sets of data with vortex, evidence of injection is apparent only for x/d=7.41 for vortex position e. For vortex position b data in Figure 134, the injectant seems to affect local St/St_o variations for x/d up to 96.6. For this situation, injectant is issued at larger z than locations of the vortex downwash.

Additional information on the influence of spanwise vortex position may be found in Figures 137-143 for x/d=741, in Figures 144-150 for x/d=17.5, and in Figures 151-157 for x/d=33.6, in Figures 158-160 for x/d=54.6, in Figures 161-163 for x/d=75.6, and in Figures 164-166 for x/d=96.6.

IV. SUMMARY AND CONCLUSIONS

Local Stanton number distributions are significantly changed by longitudinal vortices in film-cooled turbulent boundary layers. For all experimental conditions investigated, the vortices caused significant disturbances to the film coolant. Film coolant was ejected from a single hole at blowing ratios of 0.5, 1.0, and 1.5. Freestream velocity was maintained at 10 m/s. Non-dimensional coolant temperature θ was maintained at about 1.5.

Measurement of mean temperature and mean velocities in spanwise planes show that injectant is pushed to the upwash side of the vortex when the injection hole is located beneath the vortex core or vortex downwash. For these situations regardless of blowing ratio, local heat transfer distributions are altered significantly by the vortex. Evidence of injection is seen only for $x/d \leq 7.4$, where x is downstream distance from injection holes and d is injection hole diameter. For other injection locations with respect to the vortex core, evidence of injectant appears for x/d up to 96, and the injectant is not swept into the vortex upwash by secondary flows.

Also measured are secondary heat transfer peaks which appear for blowing ratios of 1.0 and 1.5 and result from a shear layer interaction between injectant and vortices.

APPENDIX A

FIGURES

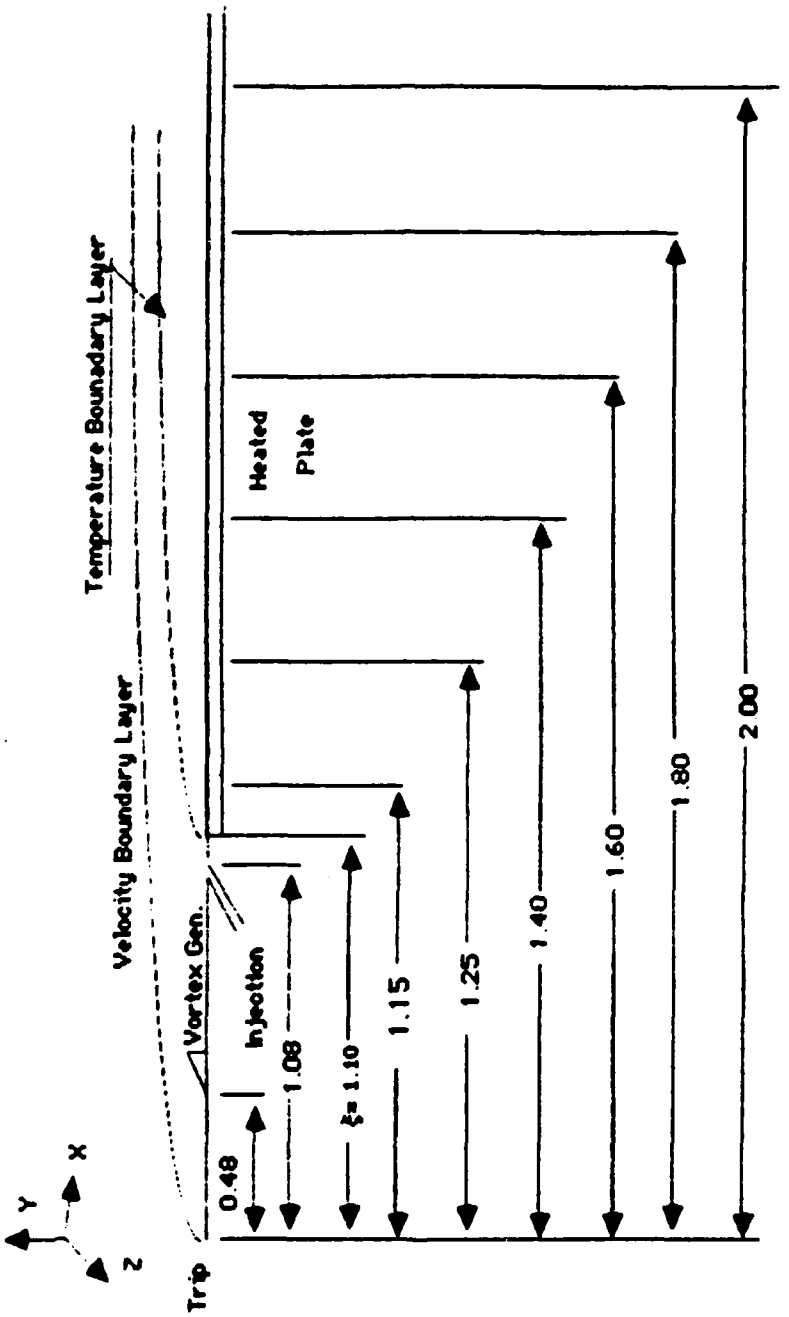

ALL DIMENSIONS IN METERS

Figure 1. Coordinate System of the Test Section

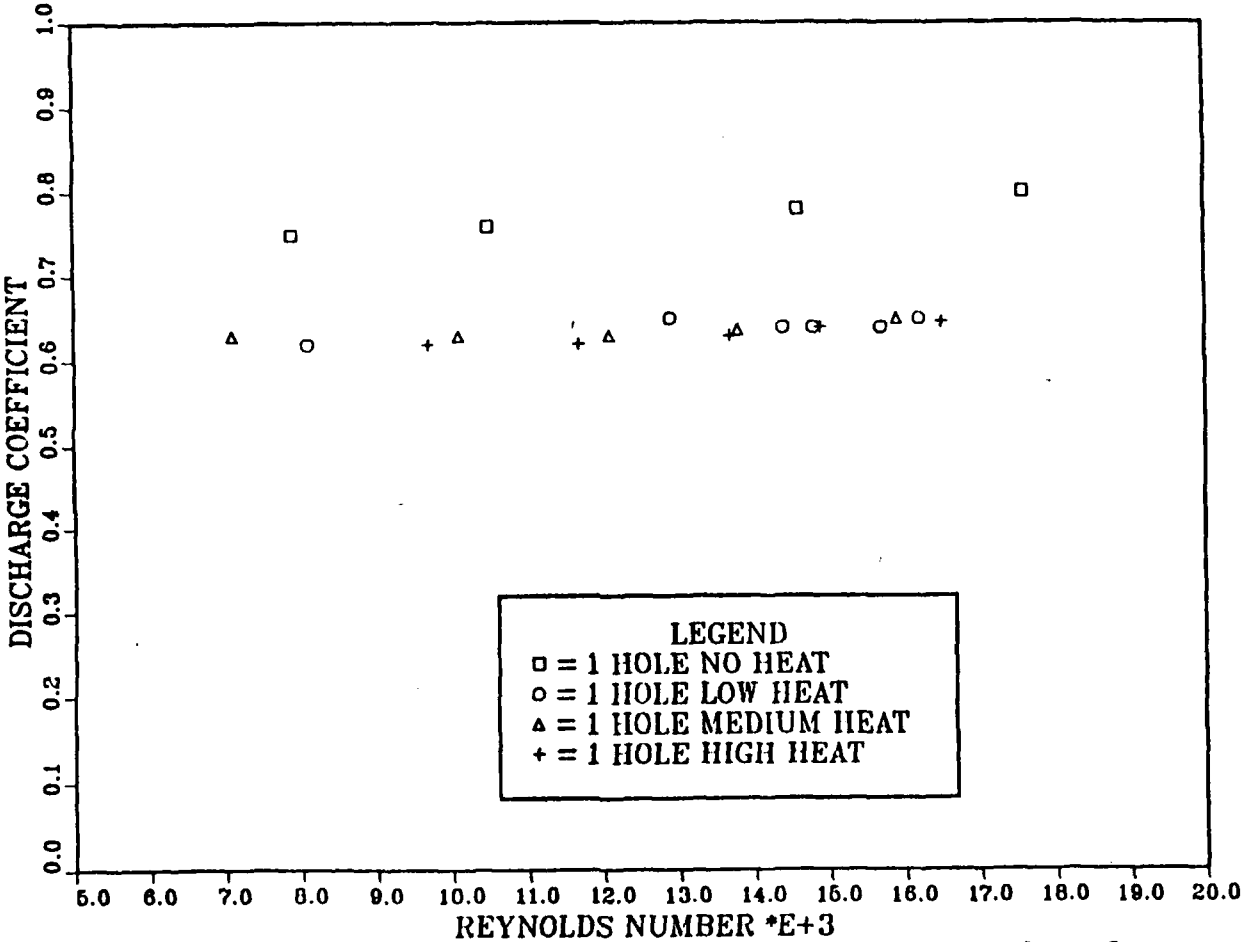

Figure 2a. **Discharge Coefficient vs. Reynolds Number for One Injection Hole**

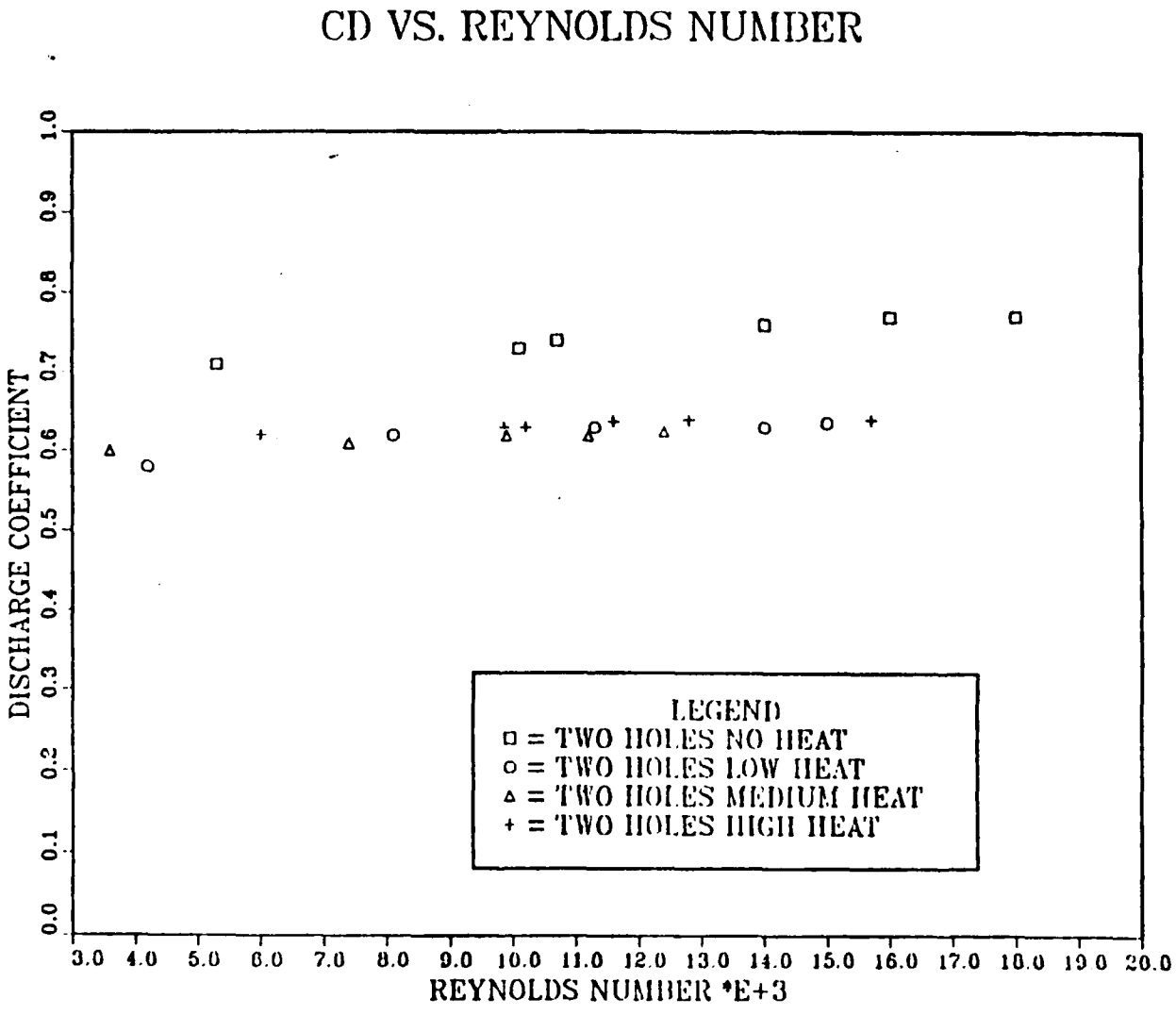

Figure 2b. **Discharge Coefficient vs Reynolds Number for Two Injection Holes**

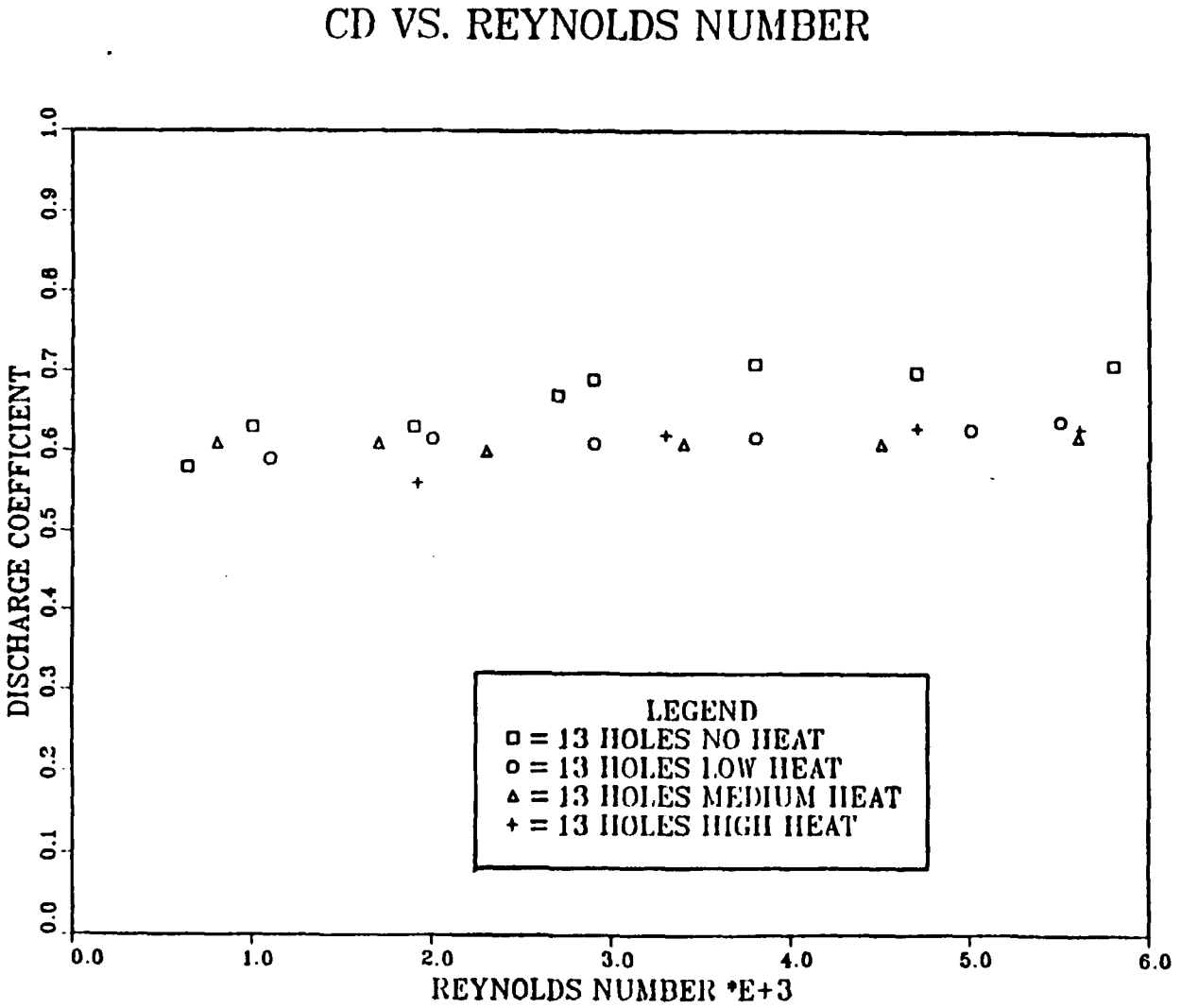

Figure 2c. Discharge Coefficient vs Reynolds Number for Thirteen Injection Holes

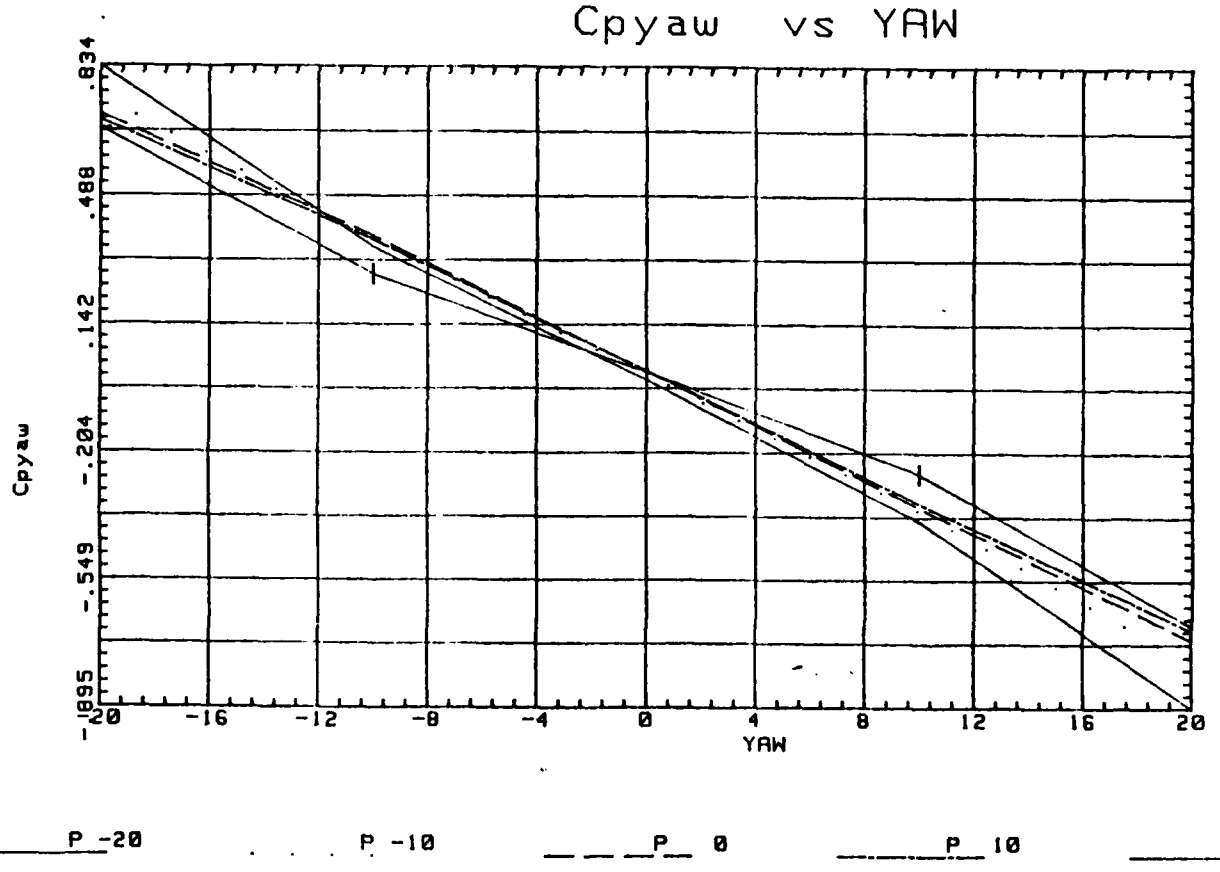

Figure 3. **Five Hole Probe Calibration Cpyaw vs. Yaw**

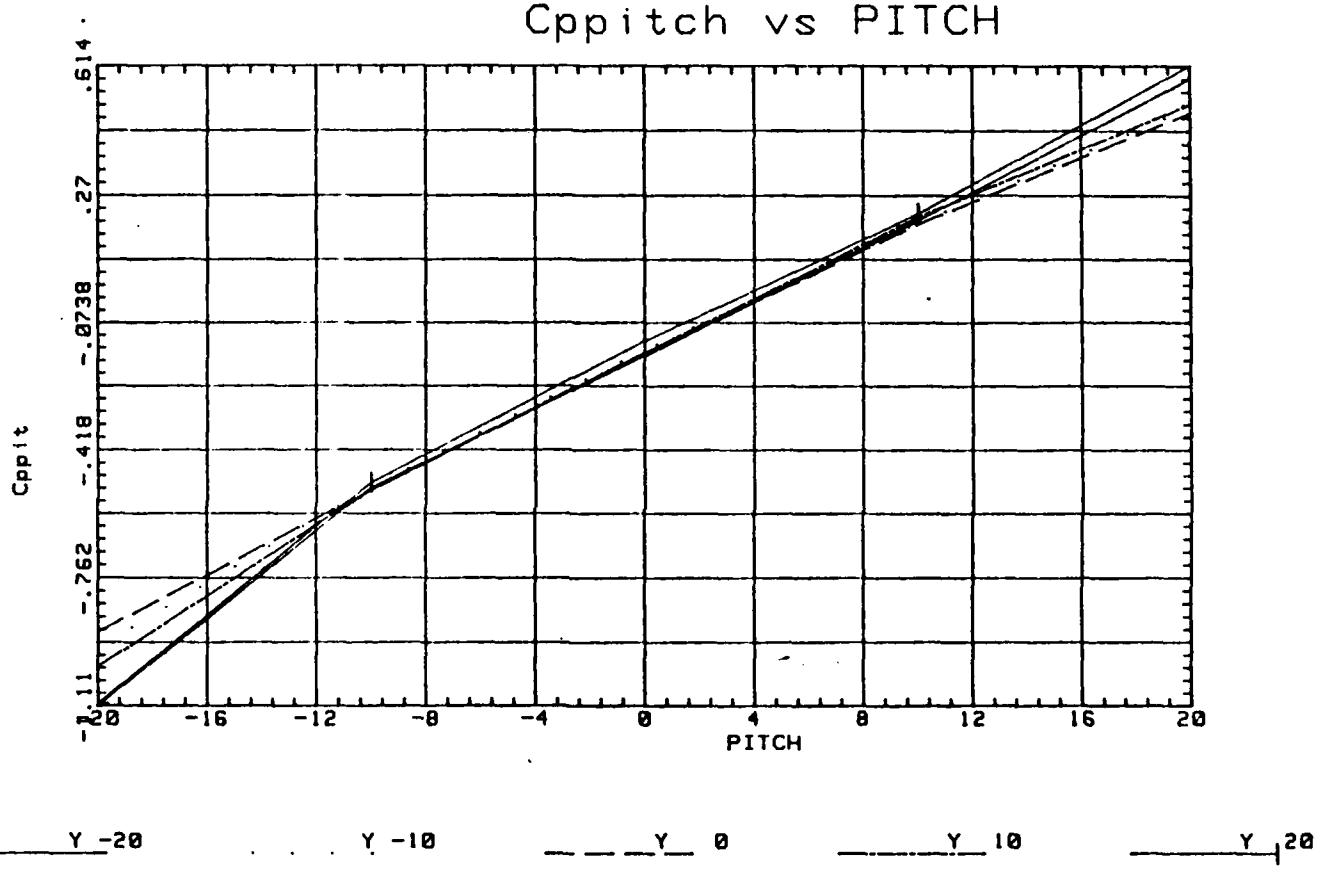

Figure 4. **Five Hole Probe Calibration CpPitch vs Pitch**

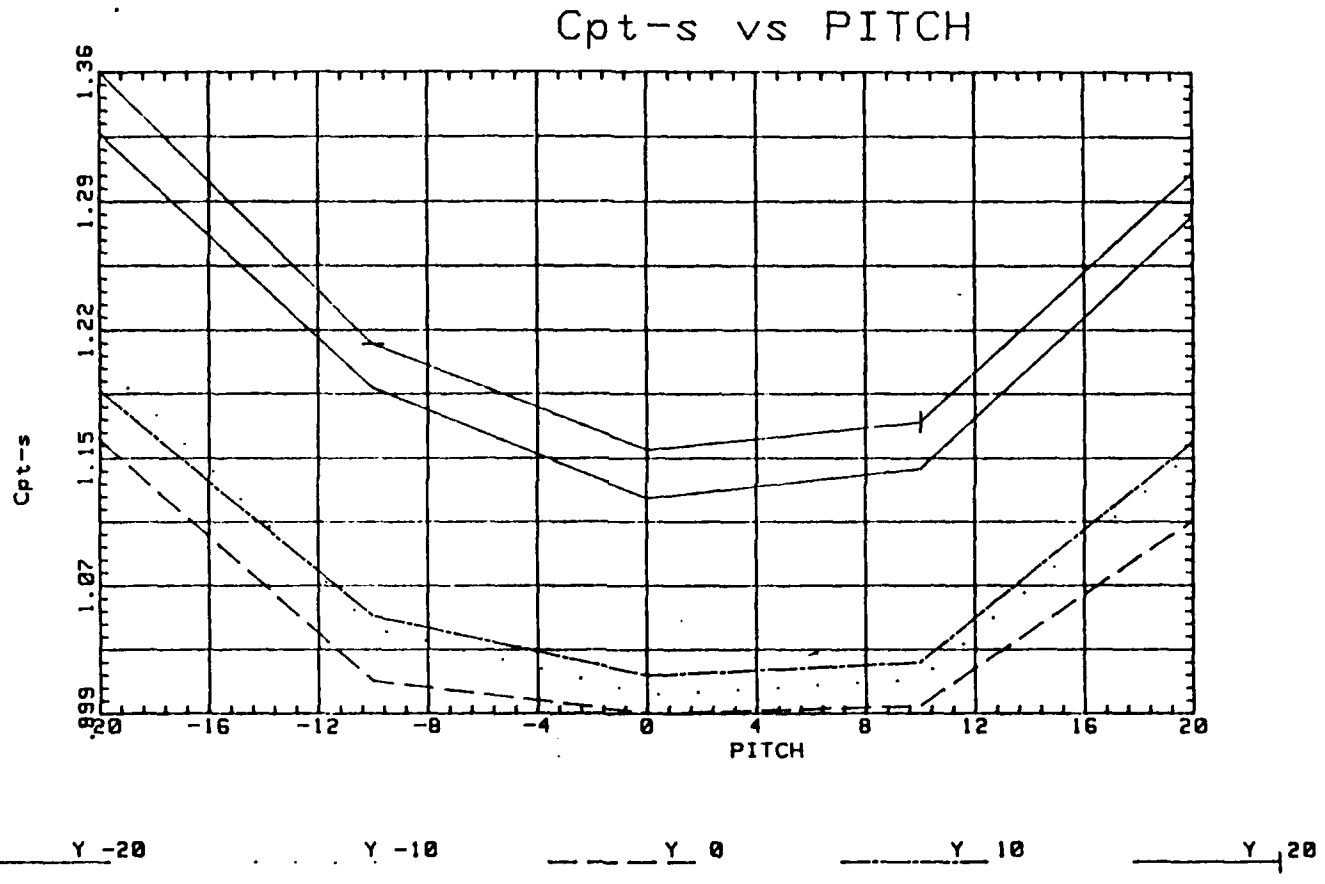

Figure 5. **Five Hole Probe Calibration Cpt-S vs Pitch**

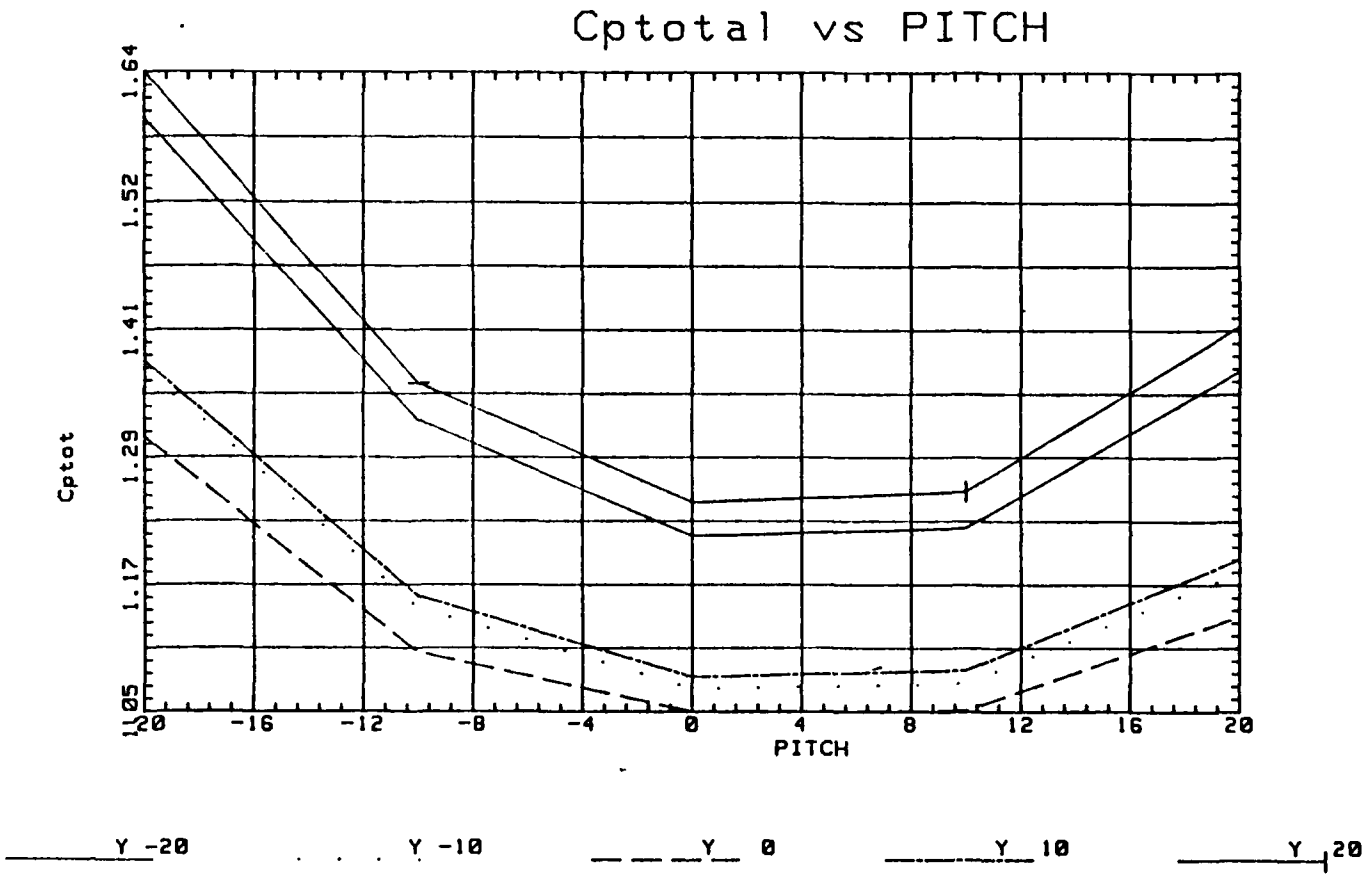

Figure 6. **Five Hole Probe Calibration Cptotal vs Pitch**

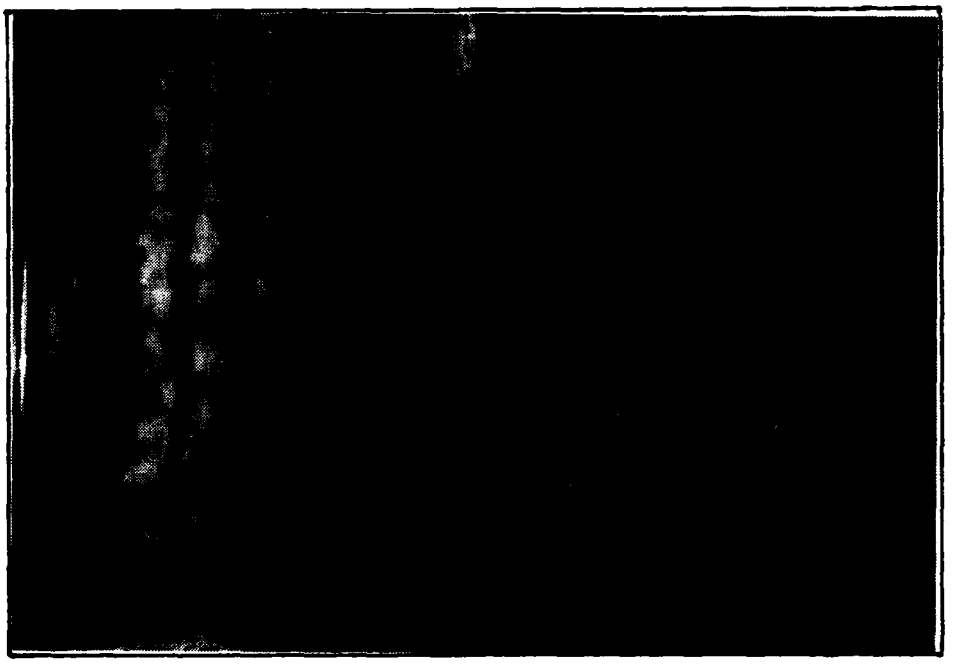

Figure 7. 7/1 Injection Holes, m=0.5 No Vortex Generator

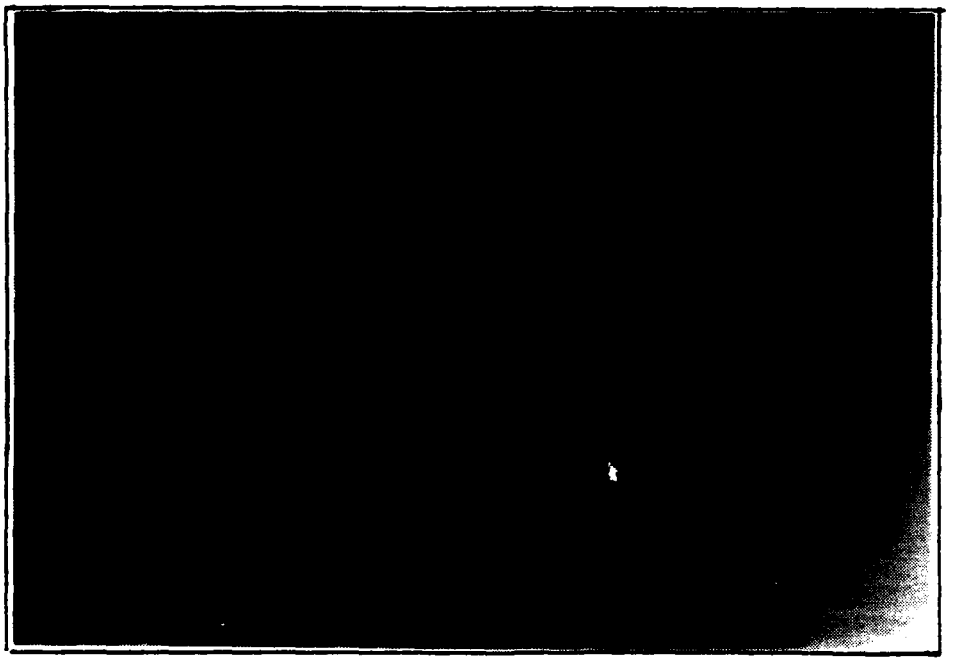

Figure 8. 7/1 Injection Holes, m=0.5 Vortex Generator #2, Position e

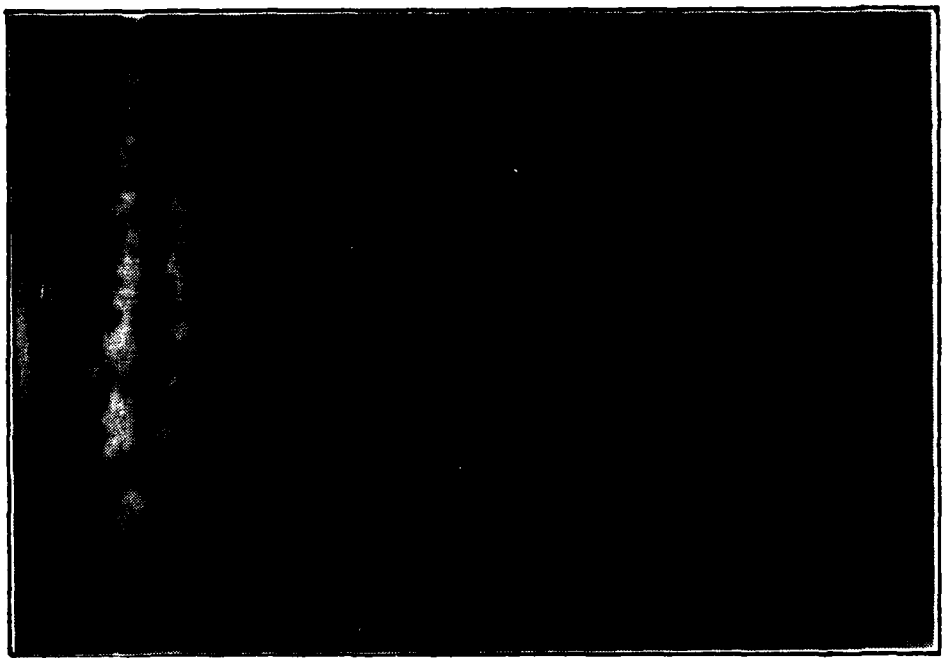

Figure 9. 7/1 Injection Holes, m=0.5 Vortex Generator #2 Position f

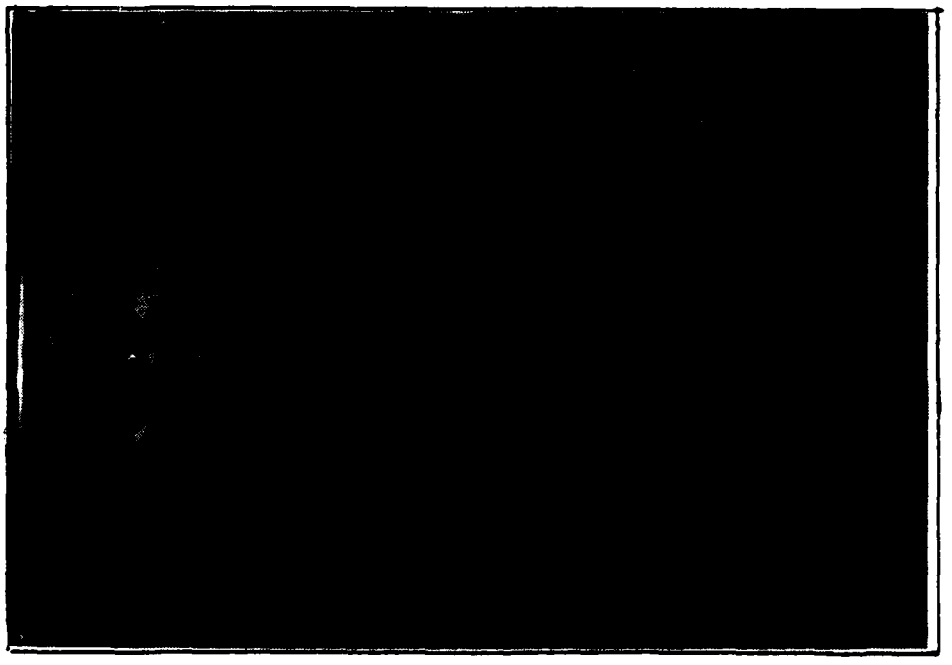

Figure 10. 7/1 Injection Holes, m=0.5 Vortex Generator #2 Position g

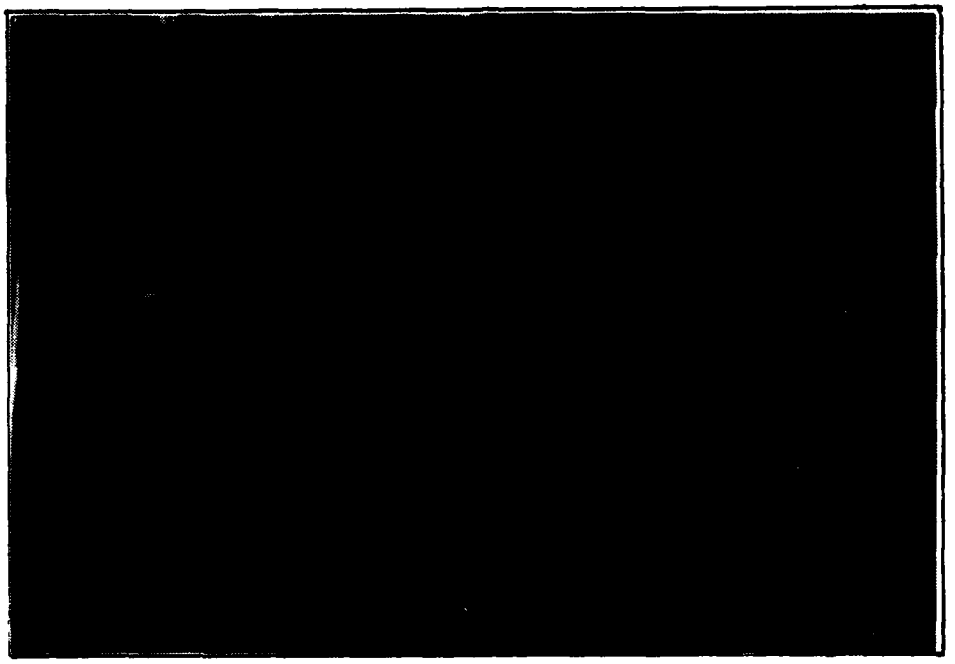

Figure 11. 7/1 Injection Holes, m=0.5 Vortex Generator #2 Position h

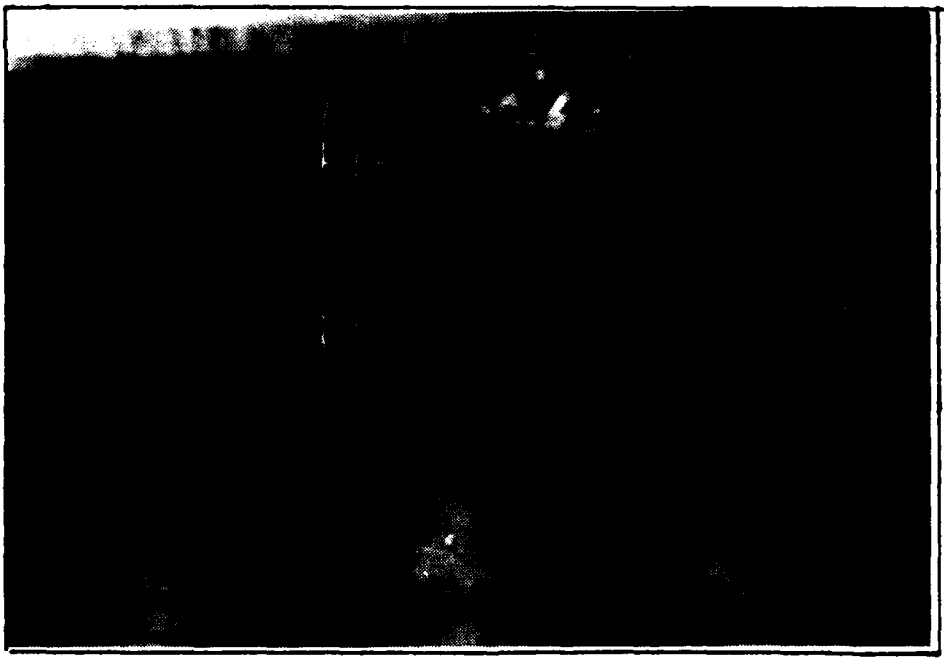

Figure 12. 7/2 Injection Holes, m=0.5 No Vortex Generator

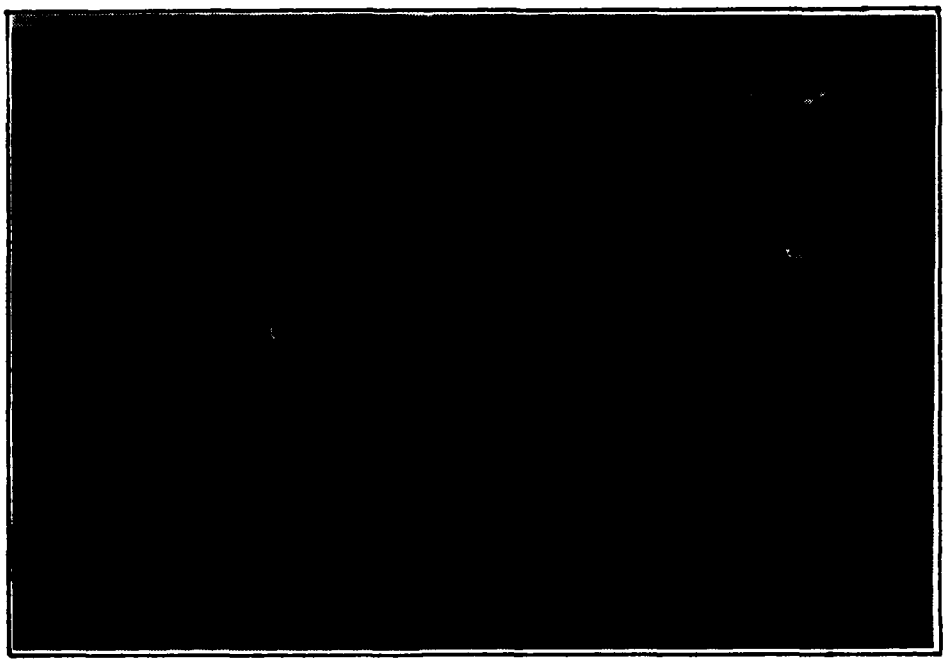

Figure 13. 7/2 Injection Holes, m=0.5 Vortex Generator #4 Position h

Figure 14. 7/1 Injection Holes, m=0.5 Vortex Generator #4 Position h

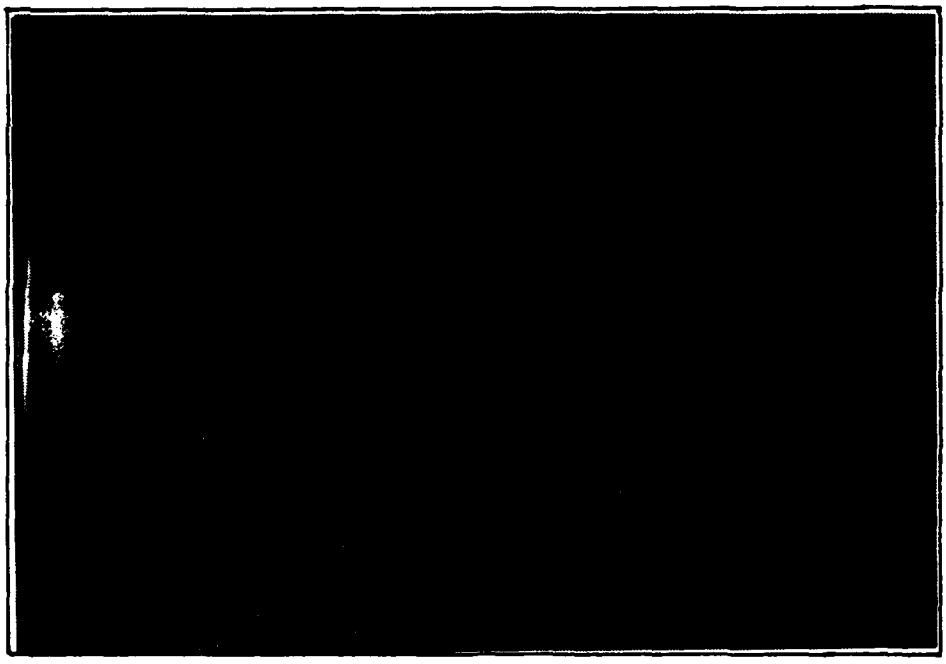

Figure 15. 7/2 Injection Holes, m=0.5 Vortex Generator #4 Position i

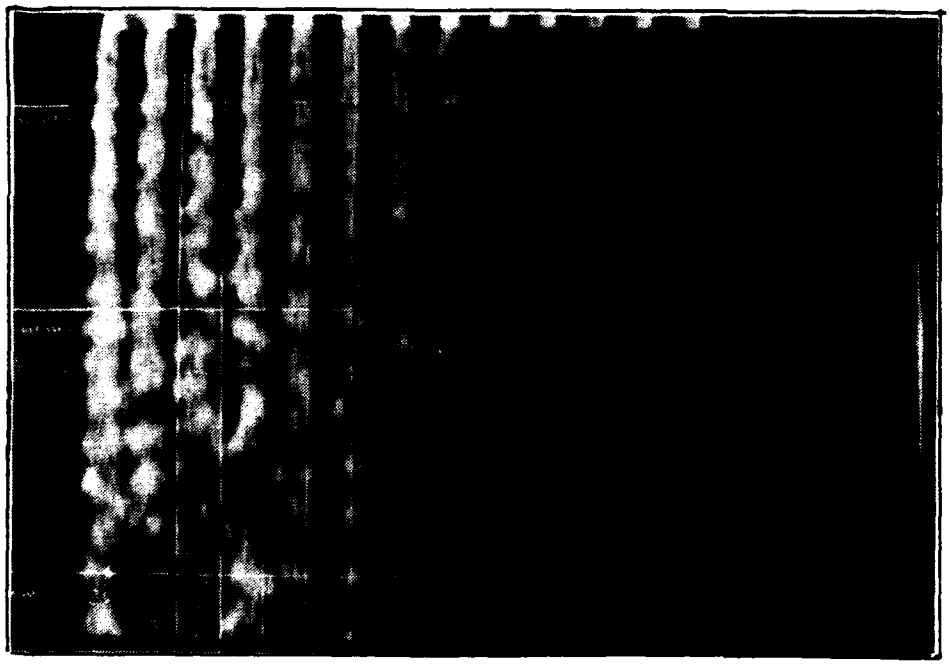

Figure 16. 13 Injection Holes, m=1.0 No Vortex Generator

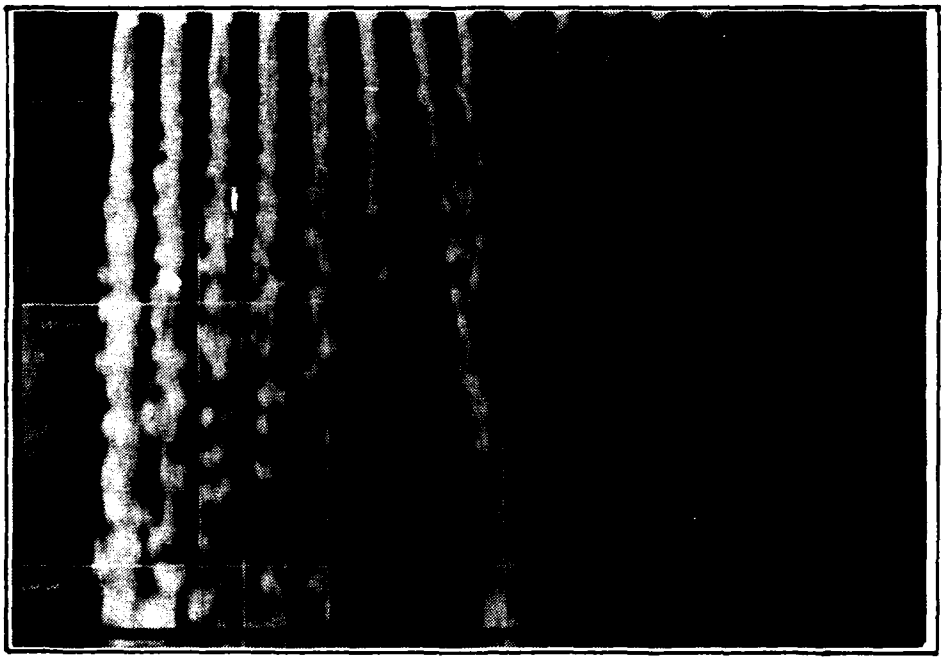

Figure 17. 13 Injection Holes, m=1.0 Vortex Generator #2 Position e

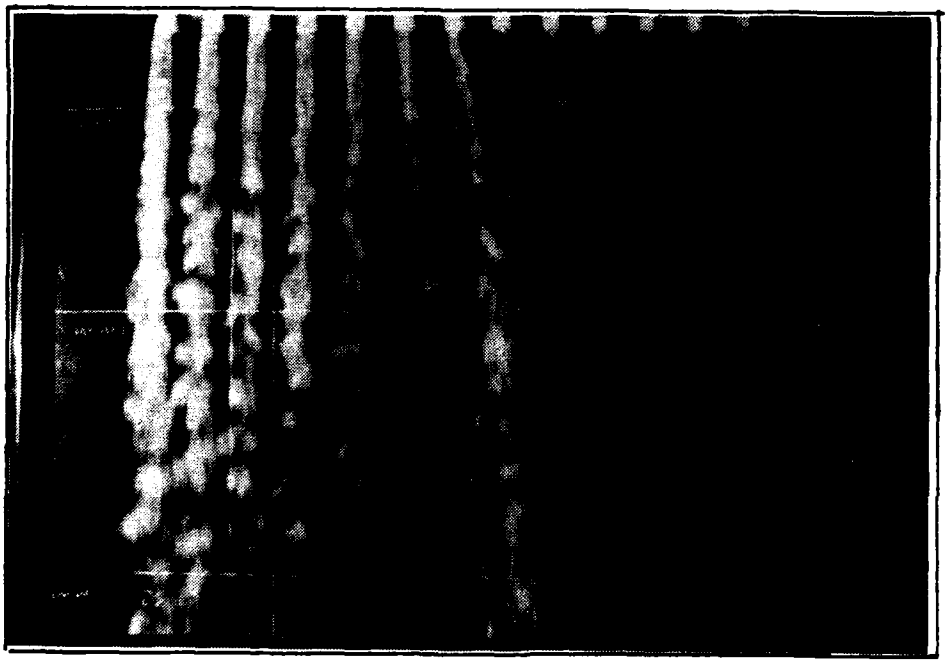

Figure 18. 13 Injection Holes, m=1.0 Vortex Generator #2 Position f

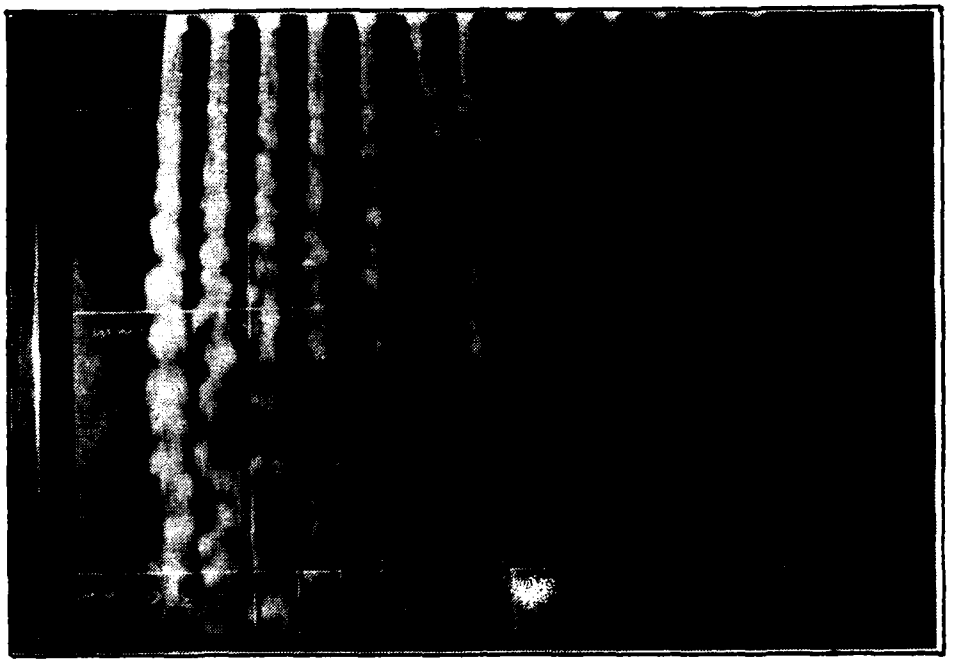

Figure 19. 13 Injection Holes, m=1.0 Vortex Generator #2 Position g

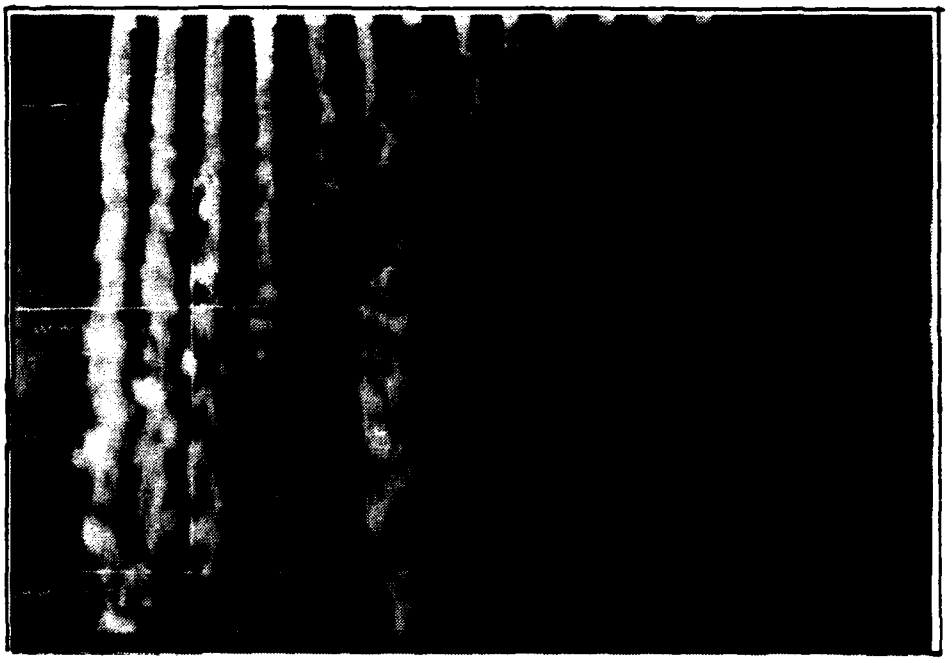

Figure 20. 13 Injection Holes, m=1.0 Vortex Gererator #2 Position h

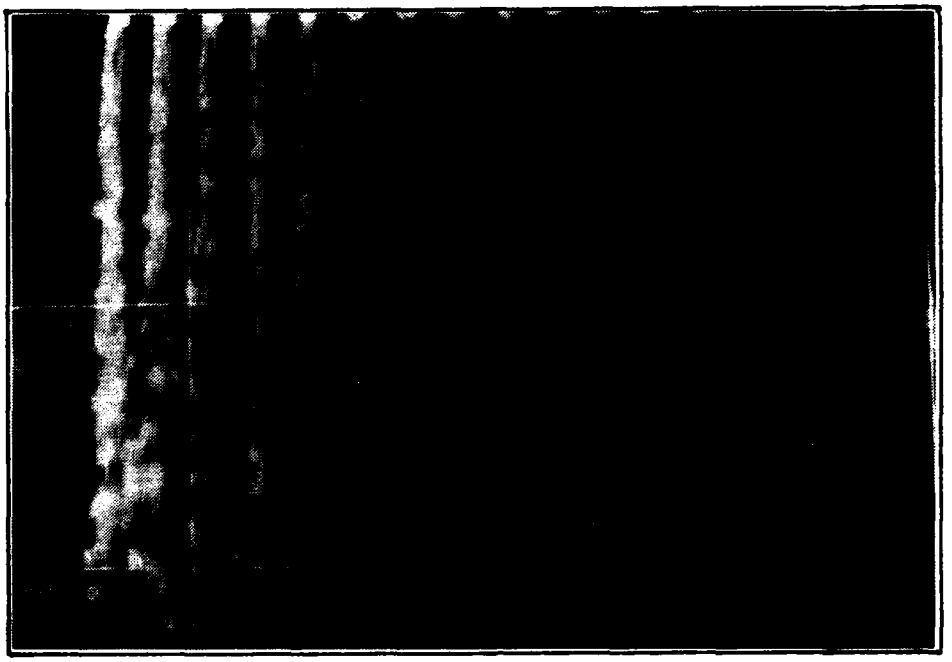

Figure 21. 13 Injection Holes, m=1.0 Vortex Generator #1 Position e

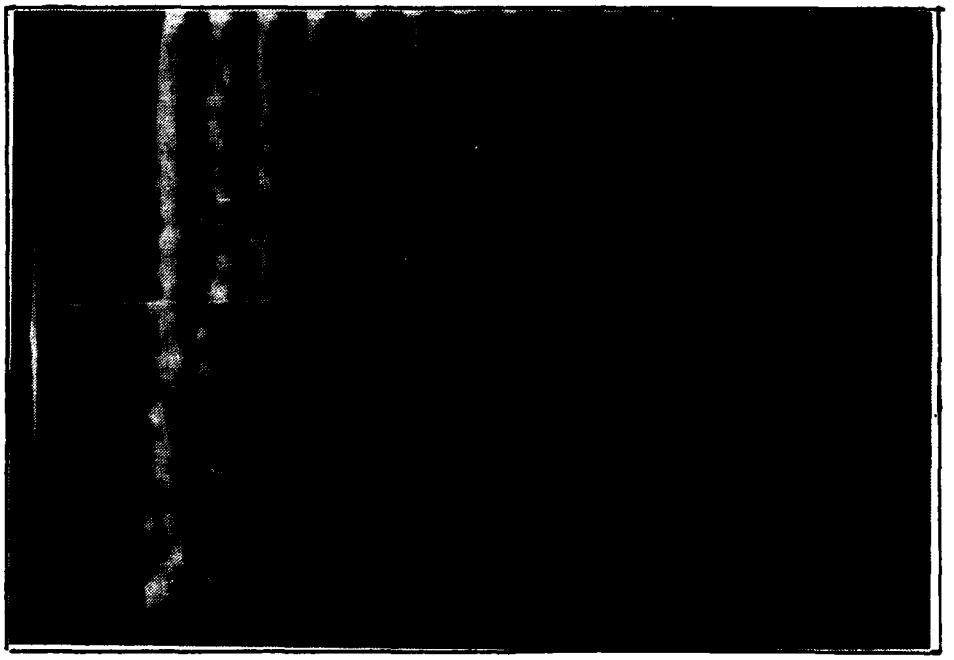

Figure 22. 13 Injection Holes, m=1.0 Vortex Generator #3 Position e

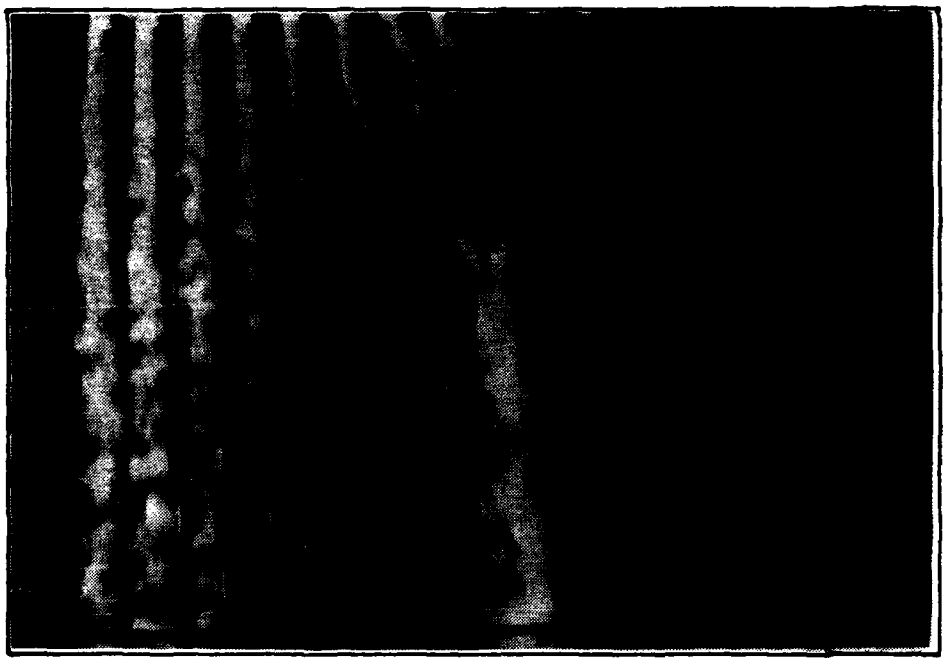

Figure 23. 13 Injection Holes, m=1.4 Vortex Generator #4 Position e

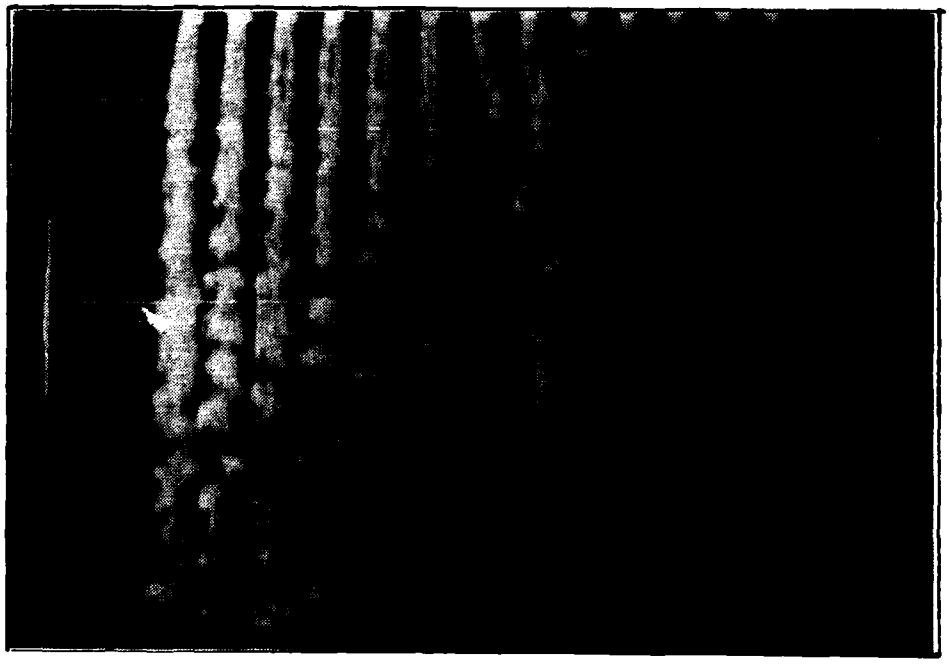

Figure 24. 13 Injection Holes, m=1.4 Vortex Generator #2 Position e

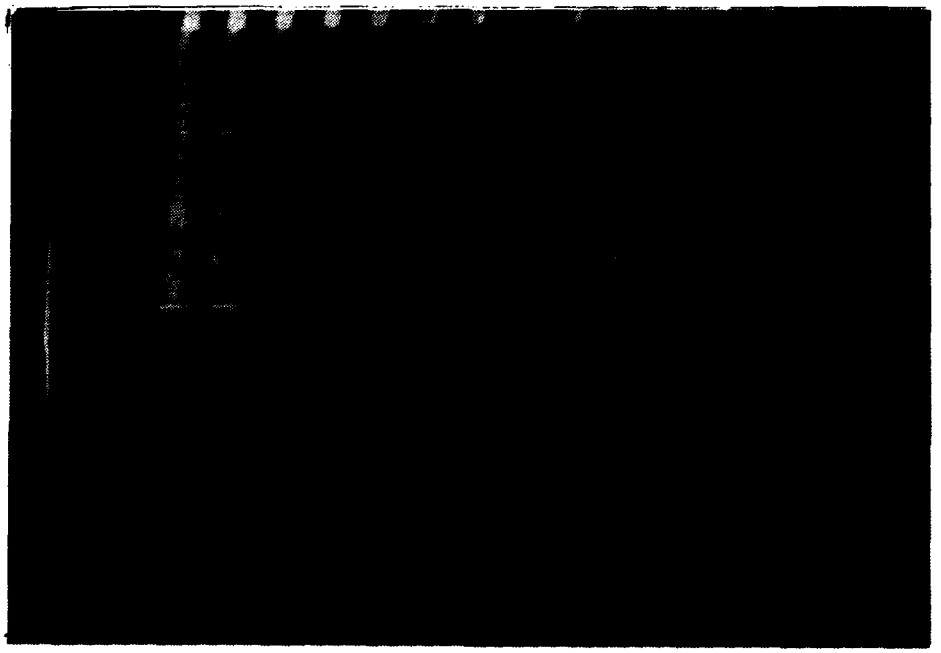

Figure 25. 13 Injection Holes, m=1.4 Vortex Generator #2 Position g

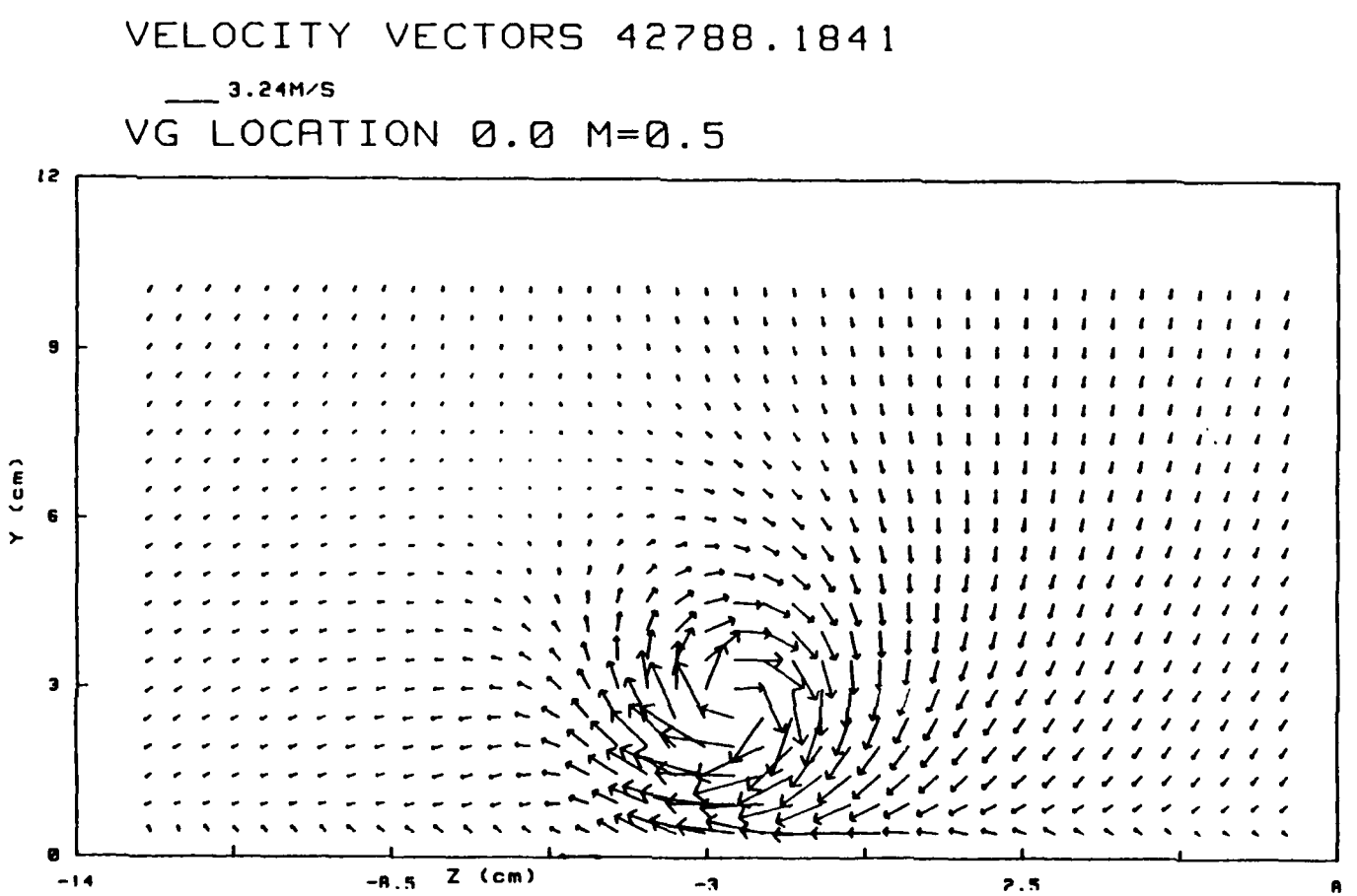

Figure 26. Secondary Flow Vectors, m=0.5 Vortex Generator #2, Position e, Probe Position x/d=5.2

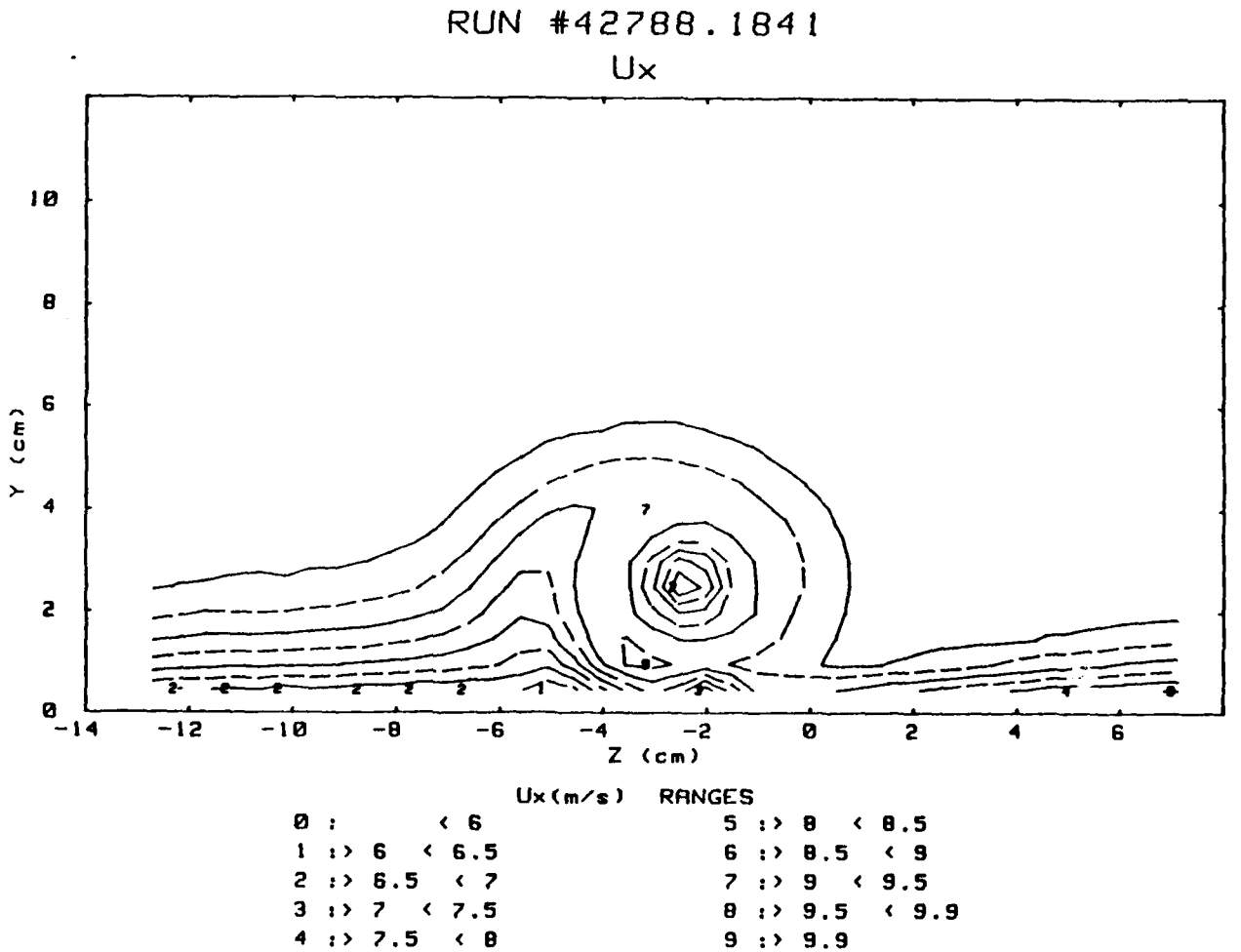

Figure 27. **Streamwise Velocity Field, m=0.5 Vortex Generator #2 Position e, Probe Position x/d=5.2**

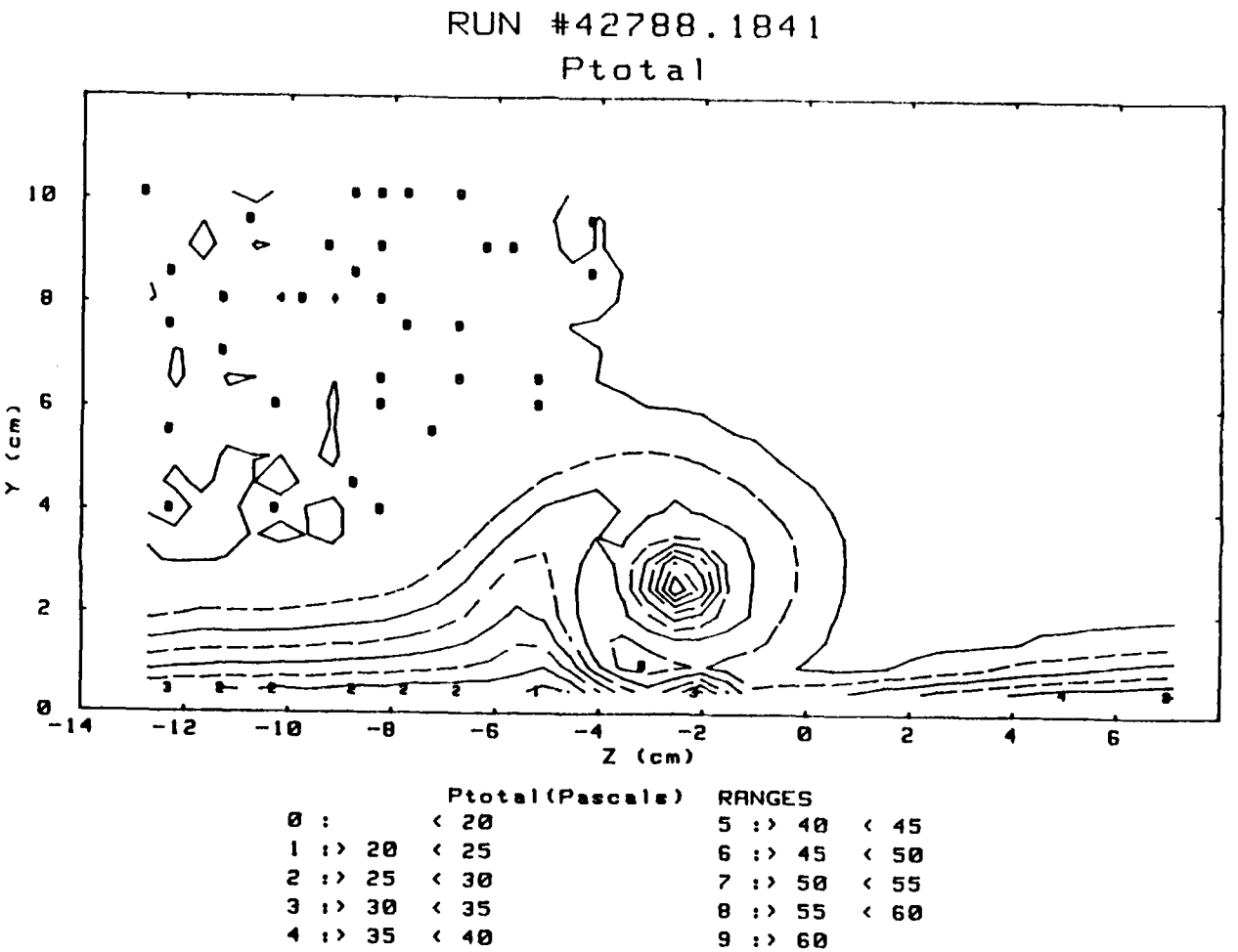

Figure 28. Total Pressure Field, m=0.5 Vortex Generator #2, Position e, Probe Position x/d=5.2

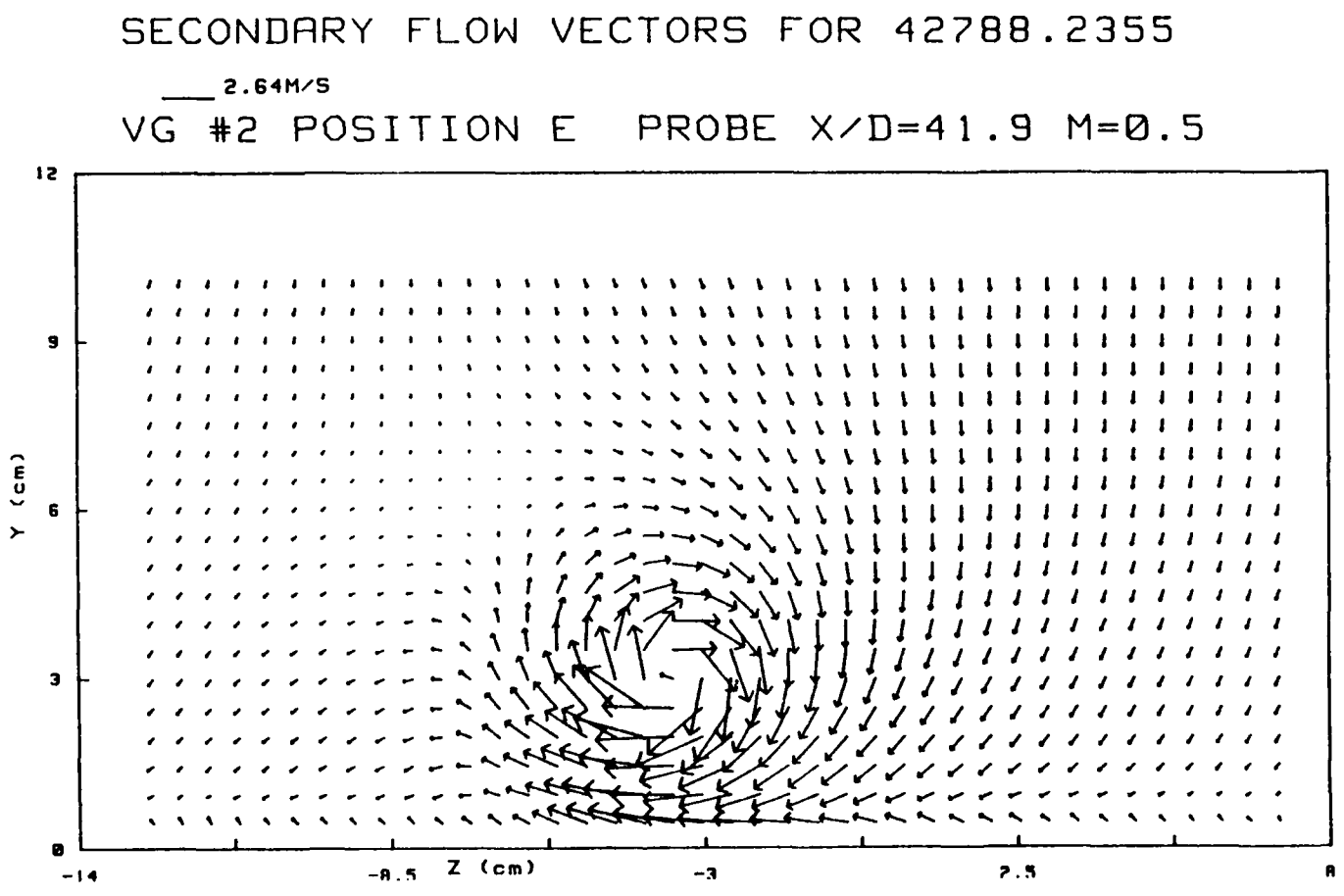

Figure 29. Secondary Flow Vectors, m=0.5 Vortex Generator #2, Position e, Probe Position x/d=41.9

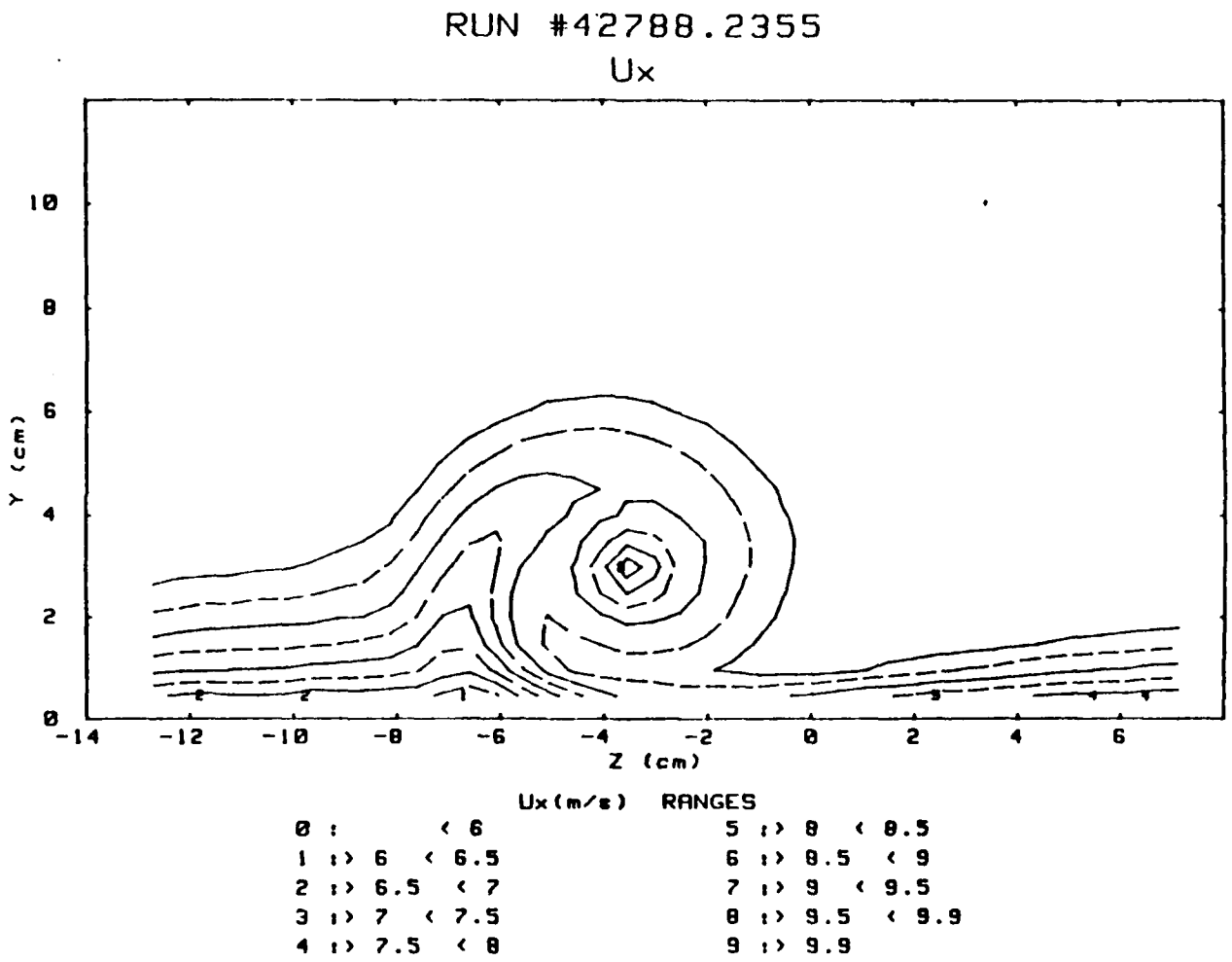

Figure 30. Streamwise Velocity Field m=0.5 Vortex Generator #2, Position e, Probe Position x/d=41.9

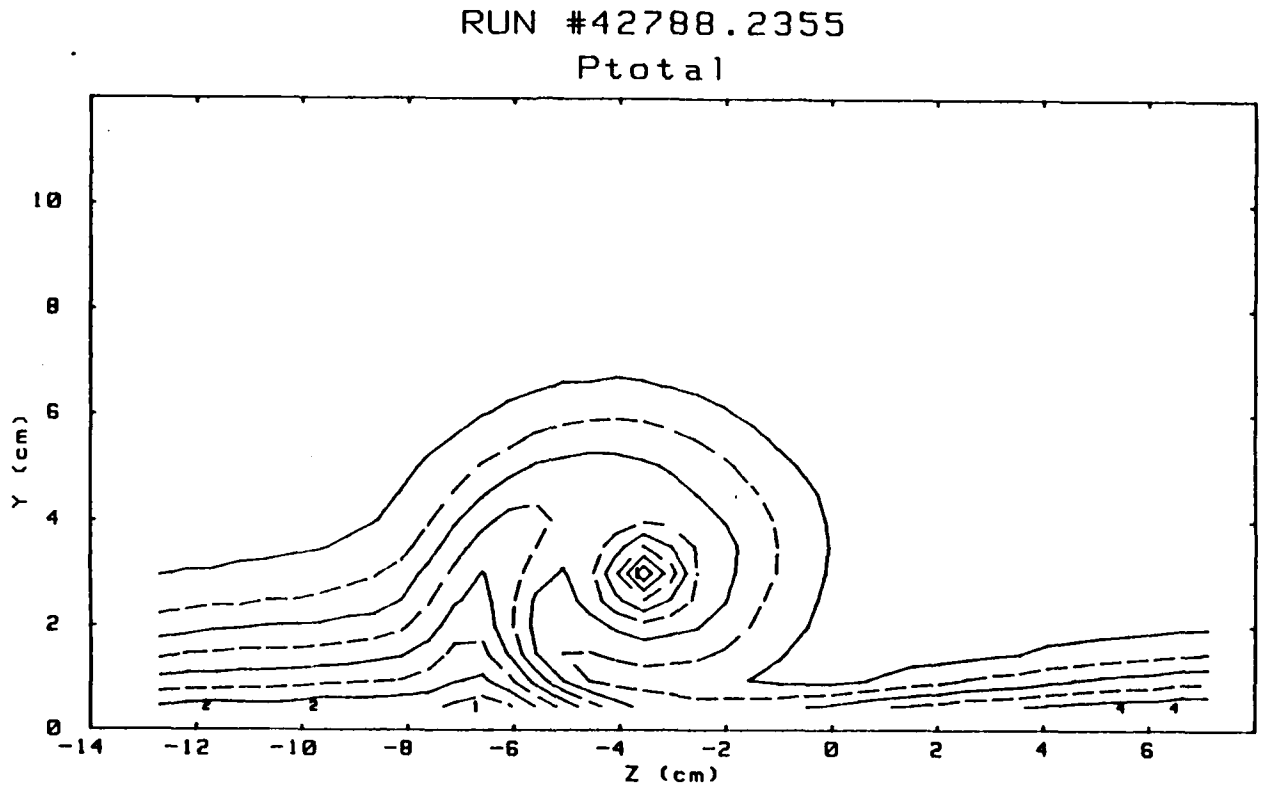

Figure 31. Total Pressure Field, m=0.5 Vortex Generator #2, Position e,Probe Position x/d=41.9

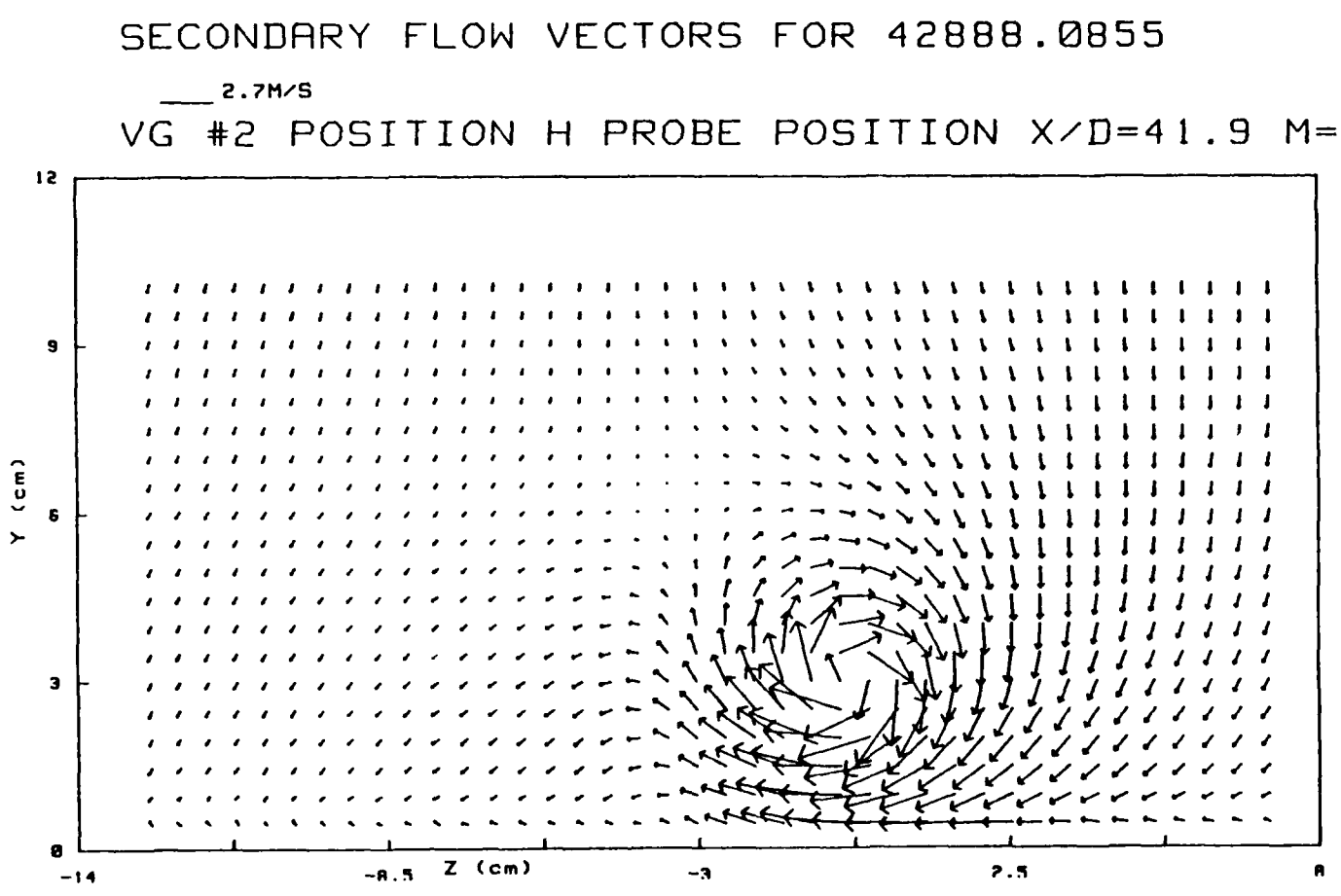

Figures 32. **Secondary Flow Vectors, m=0.5 Vortex Generator #2, Position h_1 Probe Position x/d=41.9**

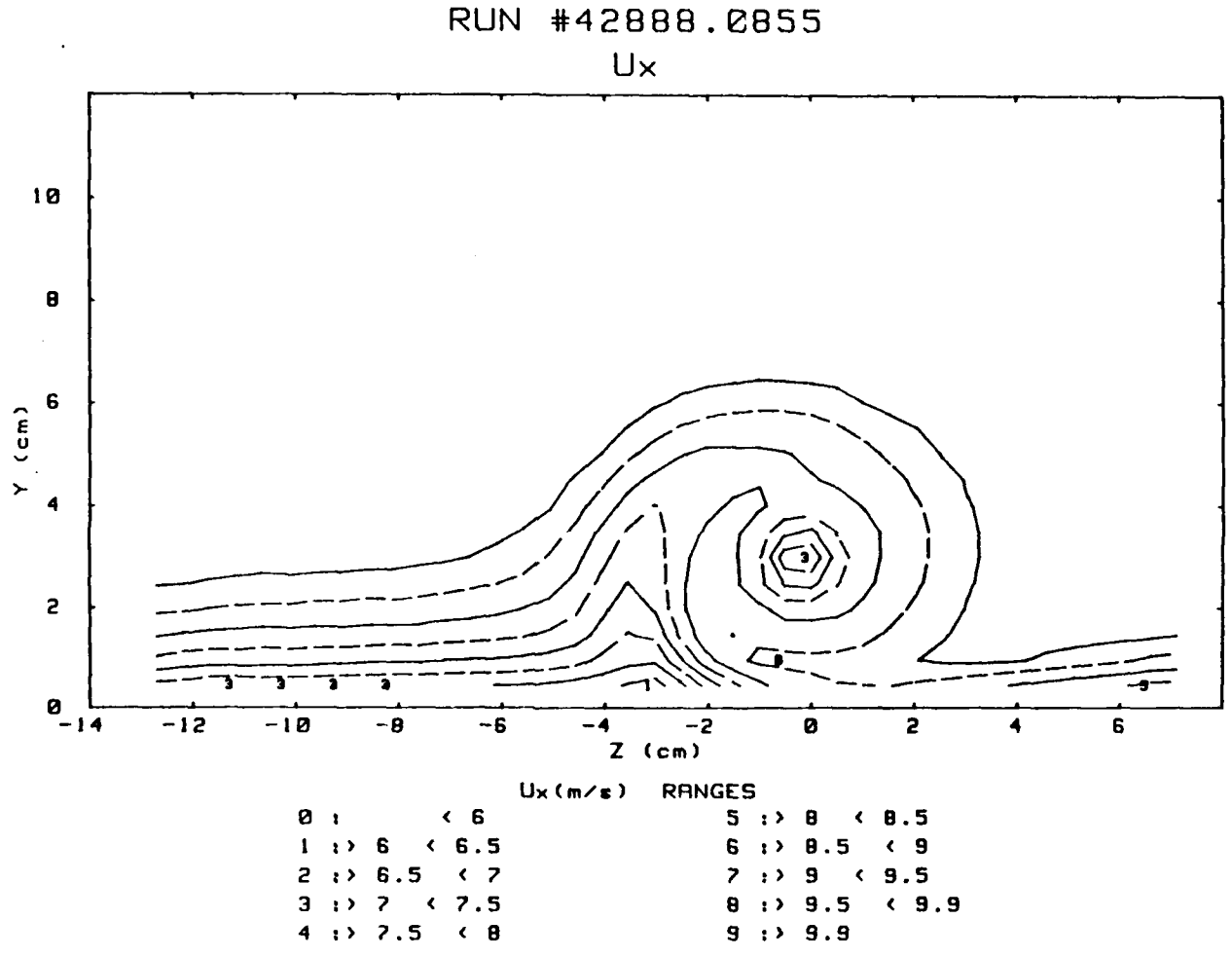

Figures 33. **Streamwise Velocity Field, m=0.5 Vortex Generator #2, Position h, Probe Position x/d=41.9**

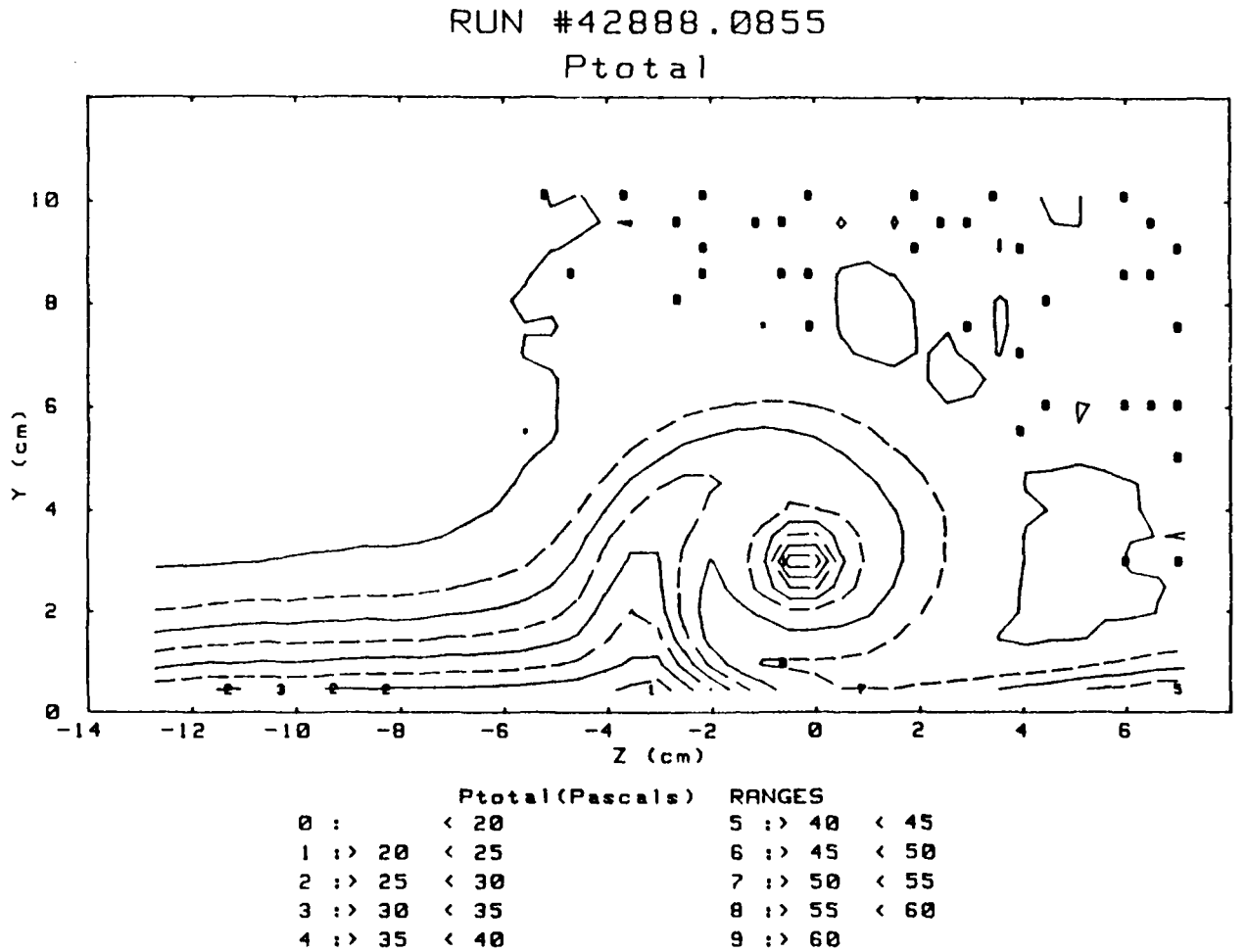

Figures 34. **Total Pressure Field, m=0.5 Vortex Generator #2, Position h,Probe Position x/d=41.9**

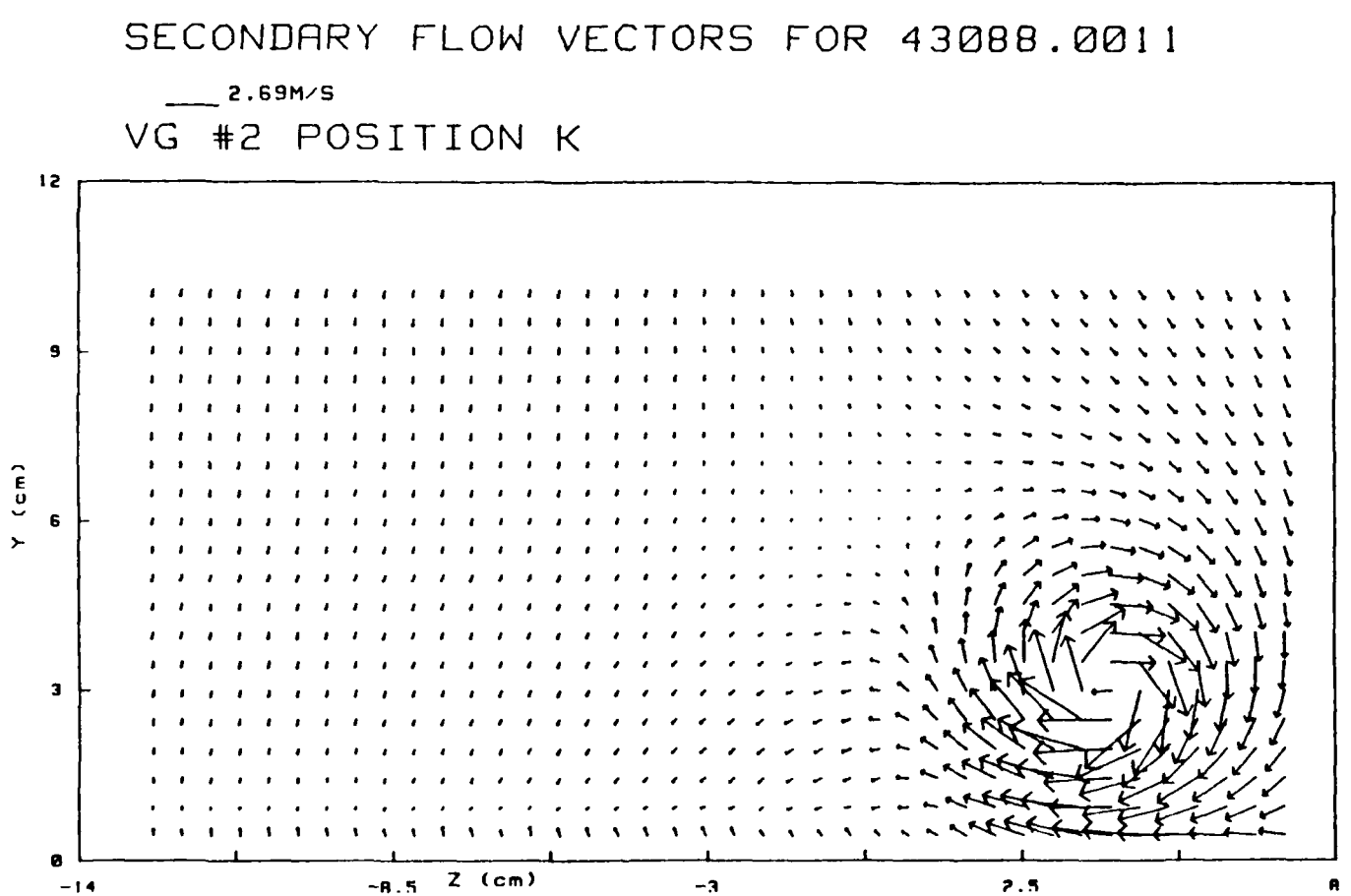

Figures 35. Secondary Flow Vectors, m=0.5 Vortex Generator #2, Position k, Probe Position x/d=41.9

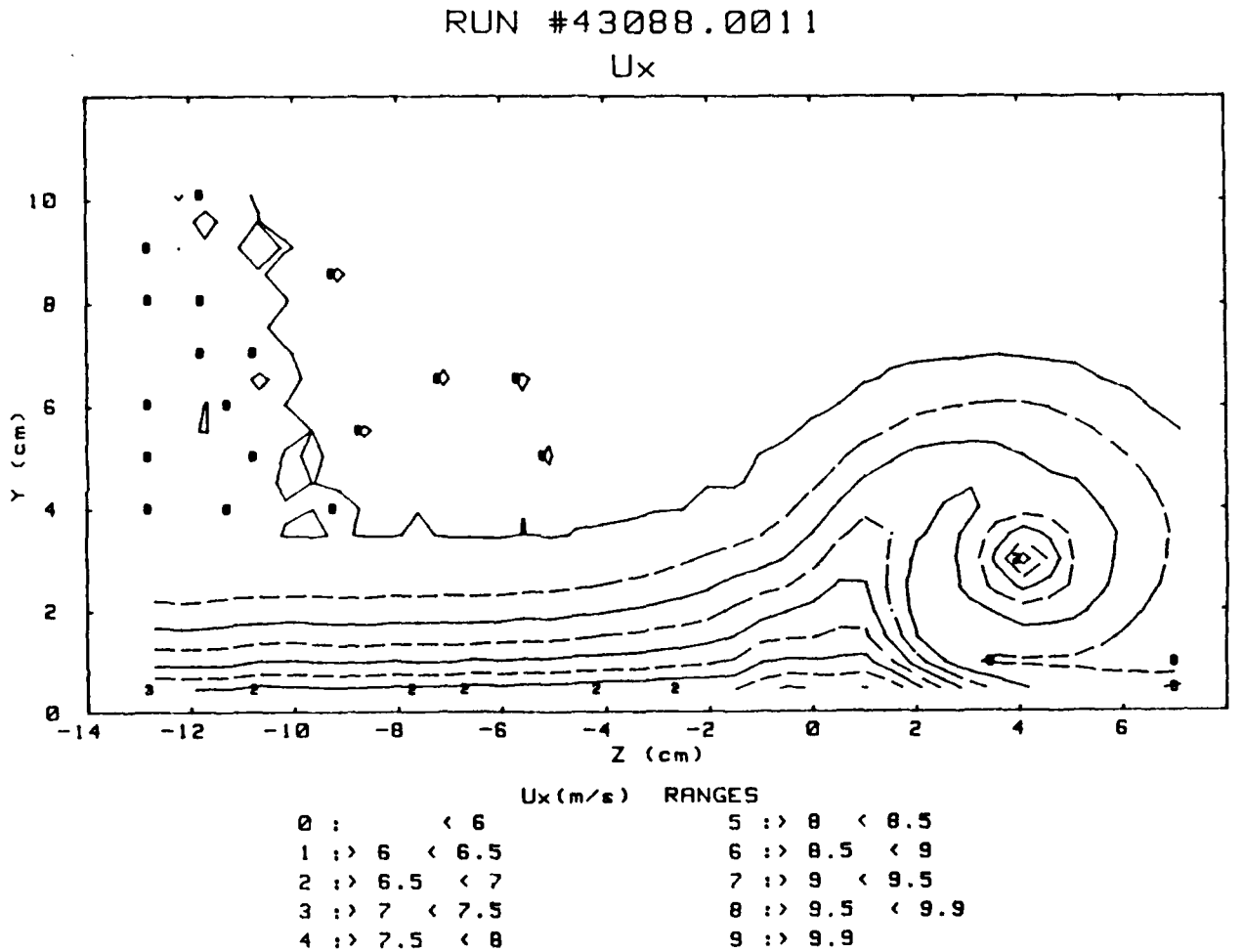

Figures 36. **Streamwise Velocity Field, m=0.5 Vortex Generator #2, Position k, Probe Position x/d=41.9**

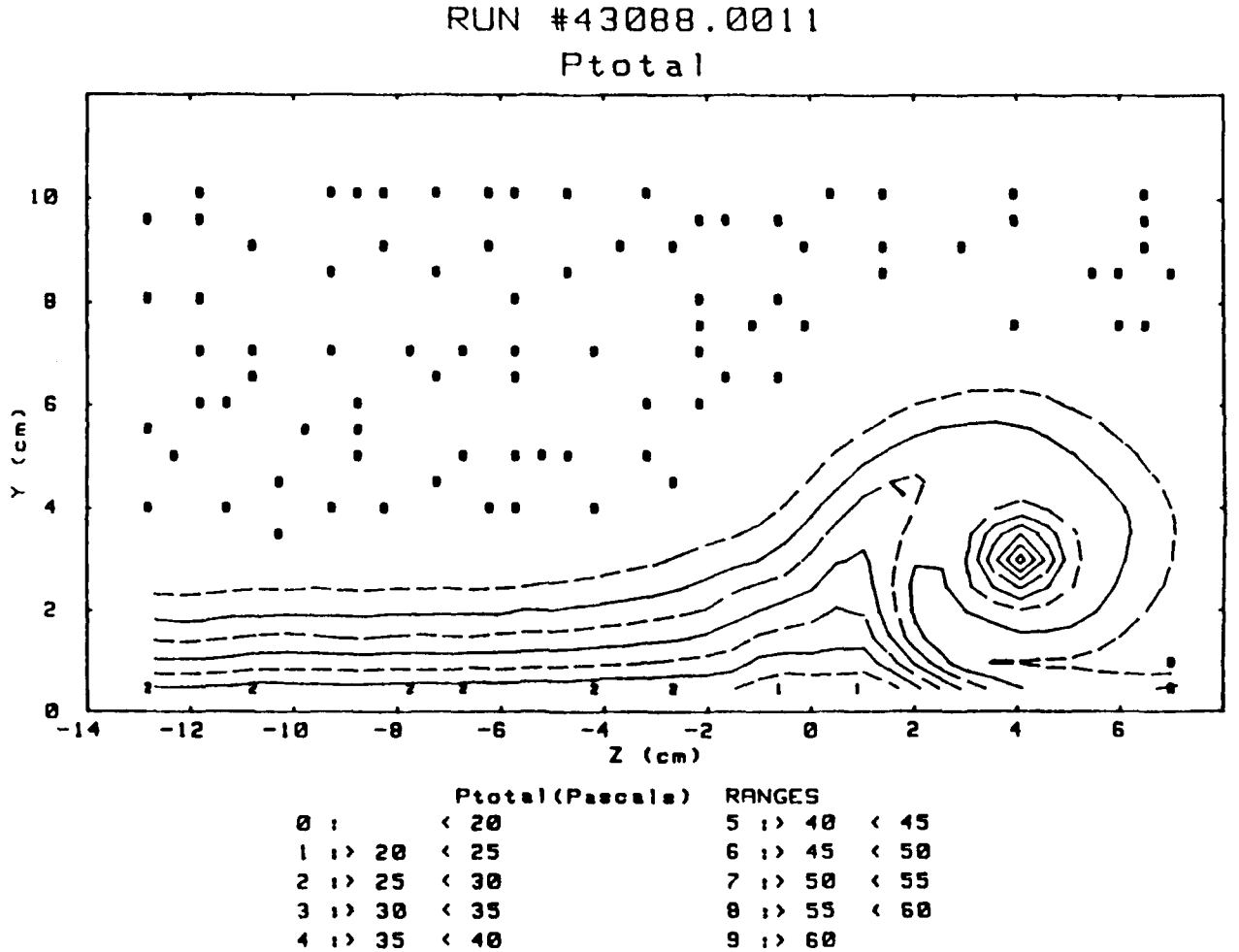

Figure 37. Total Pressure Field, m=0.5 Vortex Generator #2, Position k, Probe Position x/d=41.9

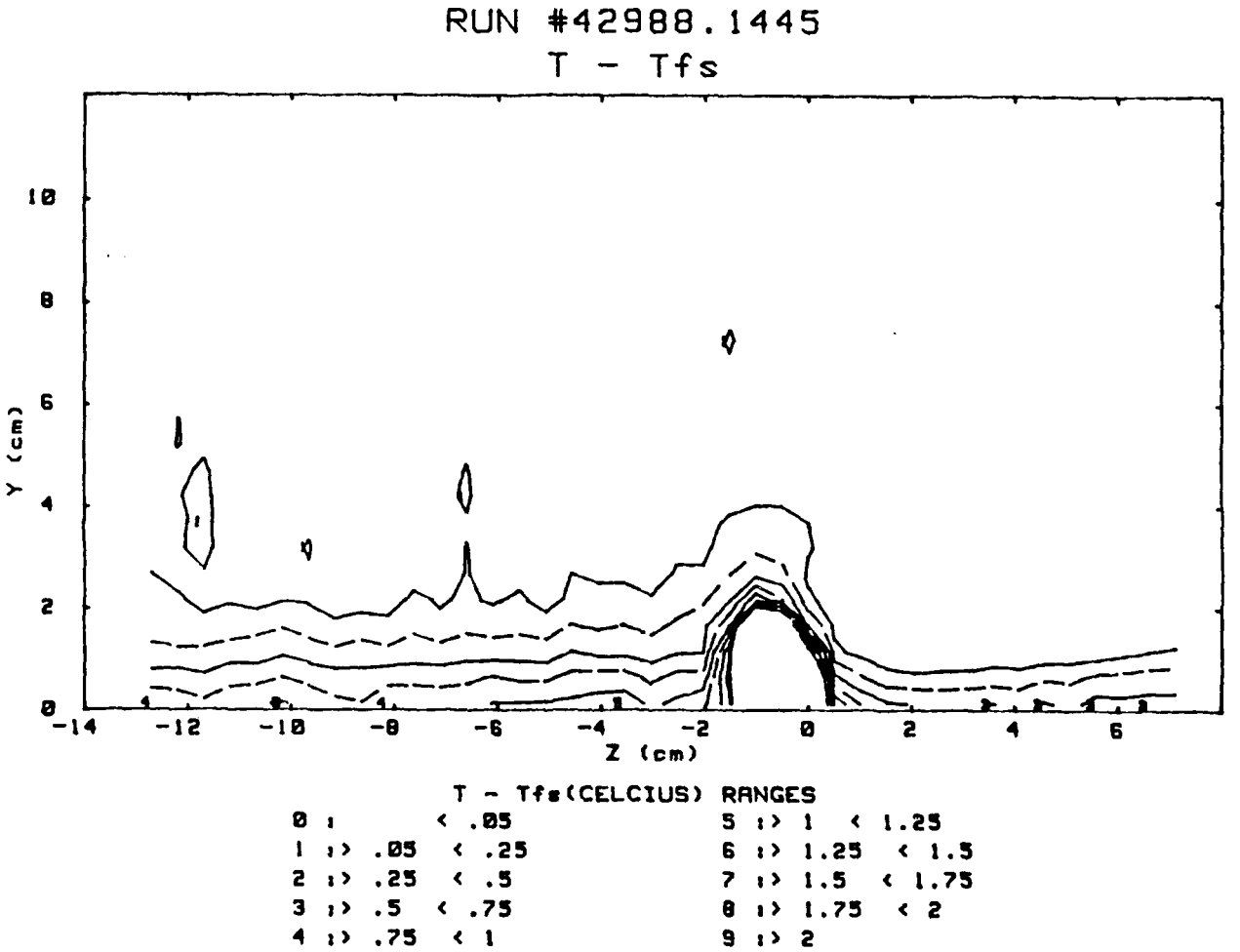

Figure 38. ***Local Temperature Minus Free Stream Temperature m=0.5 Vortex #2 Position h, Probe Position x/d=5.2***

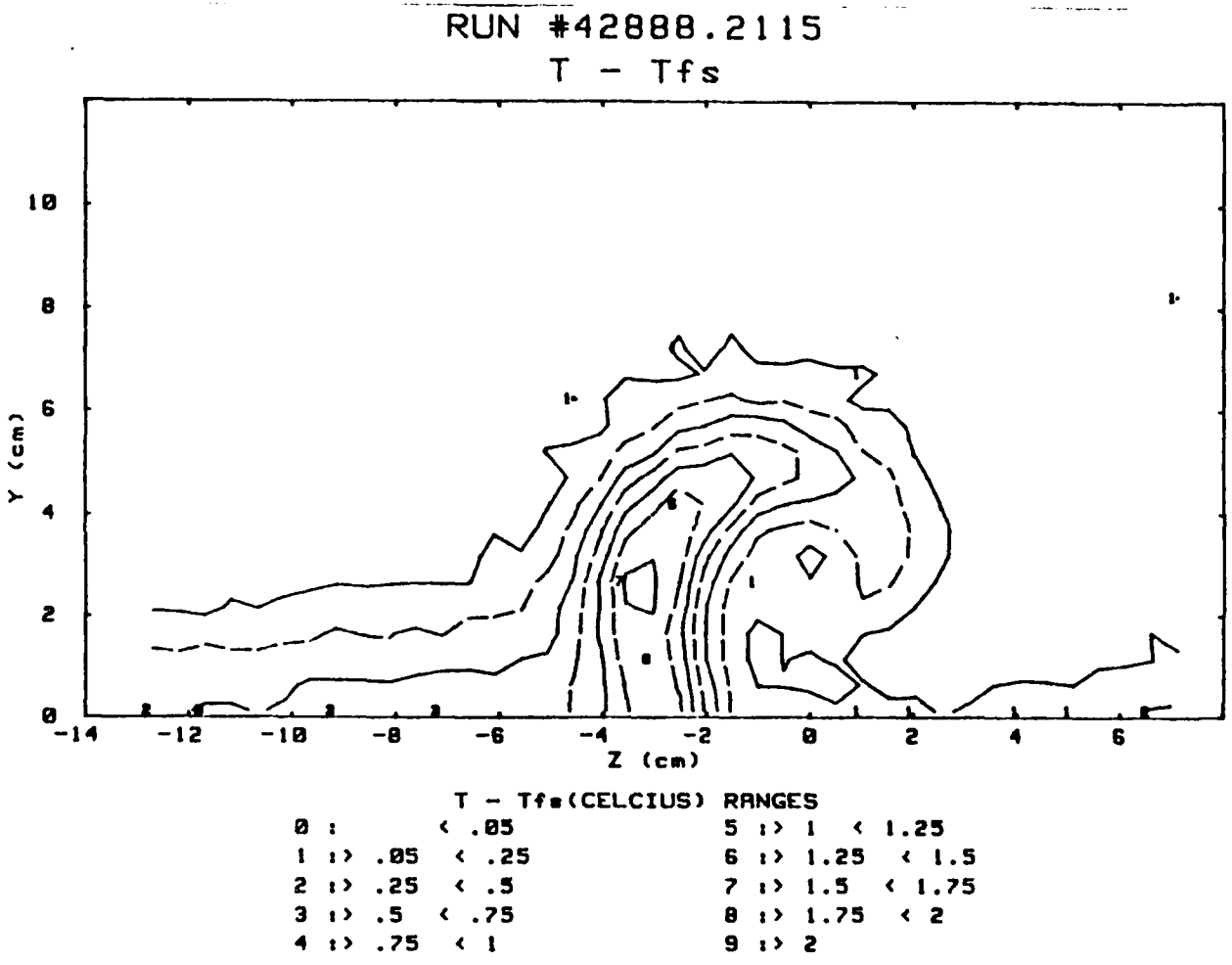

Figure 39. Local Temperature Minus Free Stream Temperature m=0.5 Vortex #2 Position h, Probe Position x/d=41.9

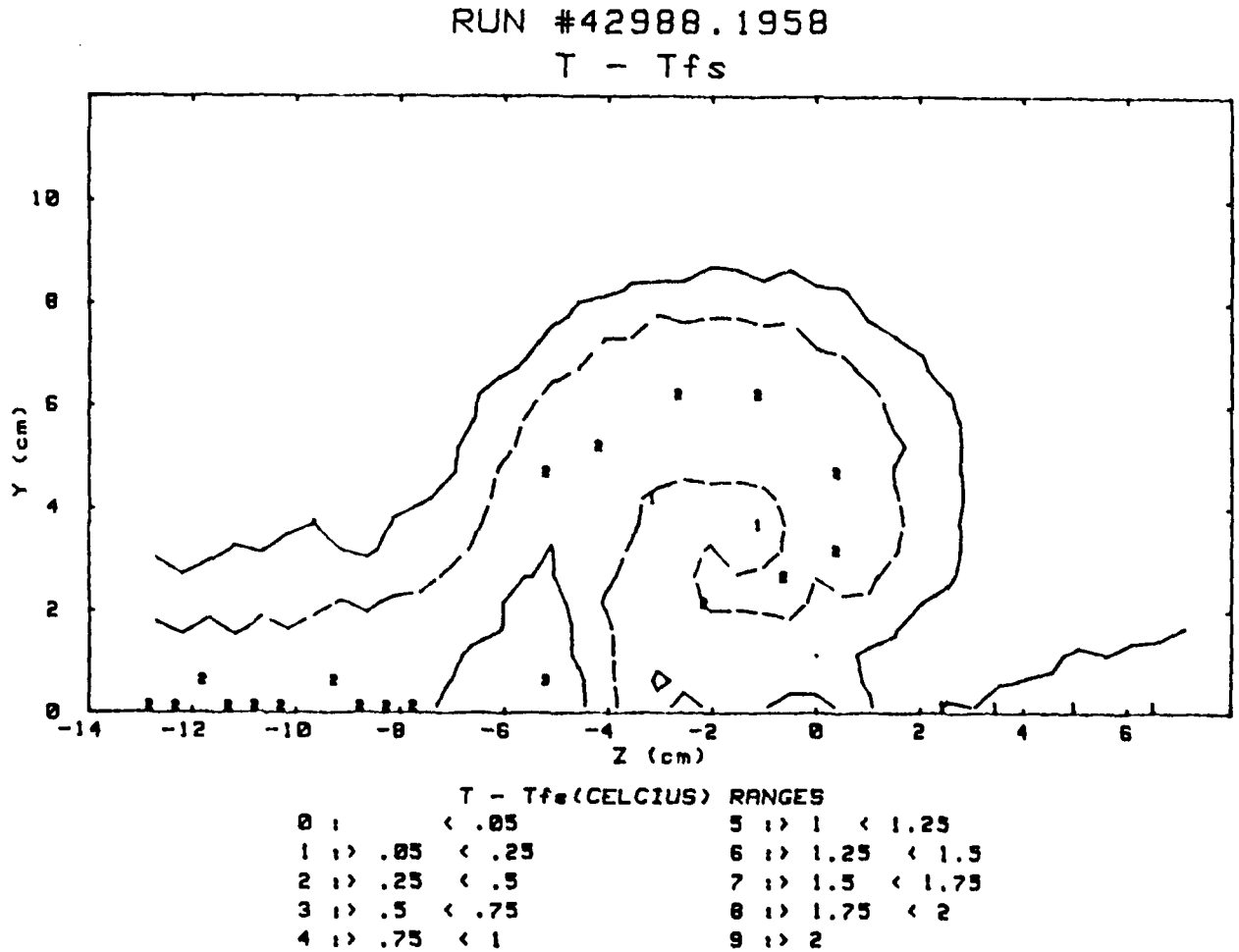

Figure 40. Local Temperature Minus Free Stream Temperature m=0.5 Vortex #2 Position h, Probe Position x/d=82.9

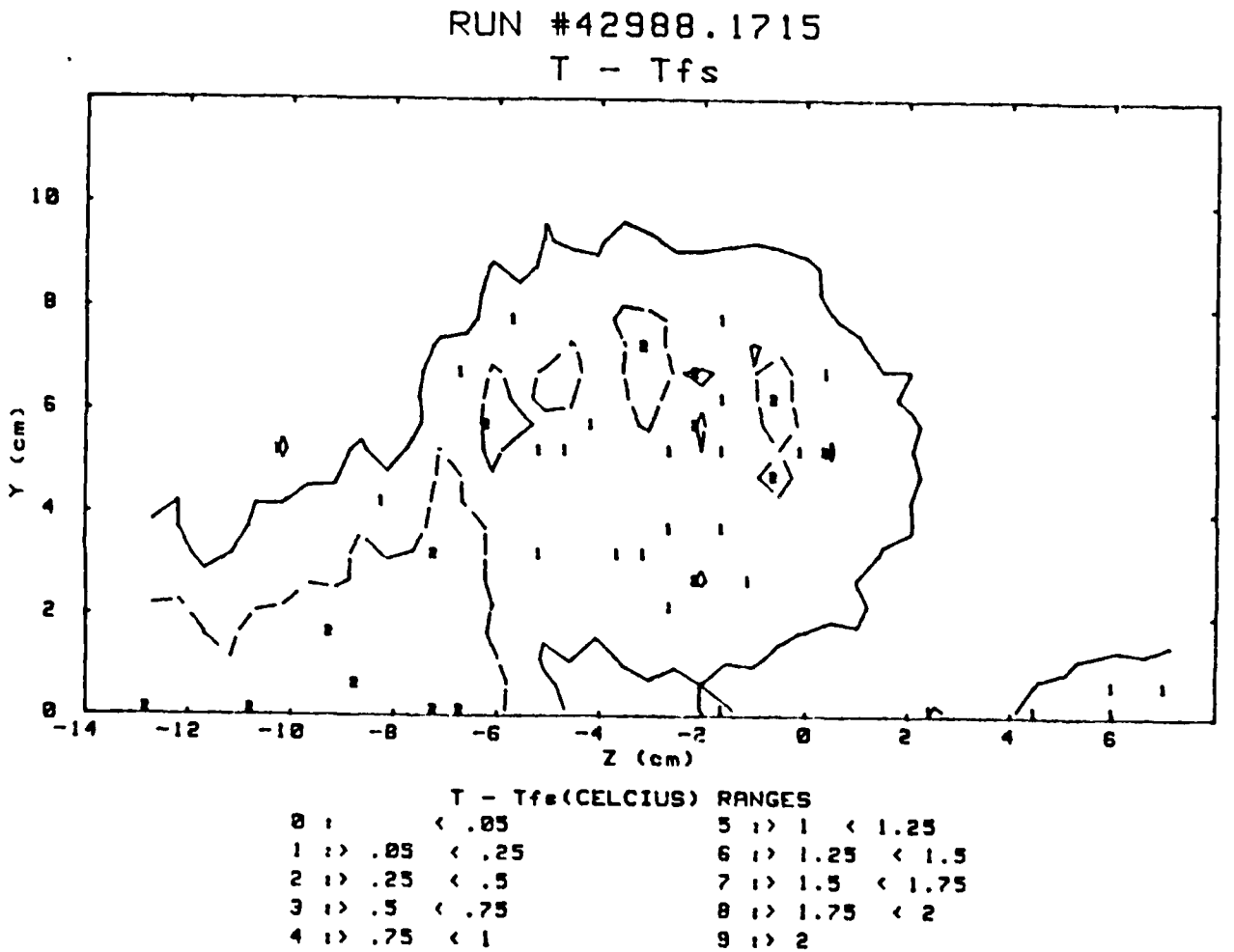

Figure 41. Local Temperature Minus Free Steam Temperature m=0.5 Vortex #2 Position h, Probe Position x/d=109.2

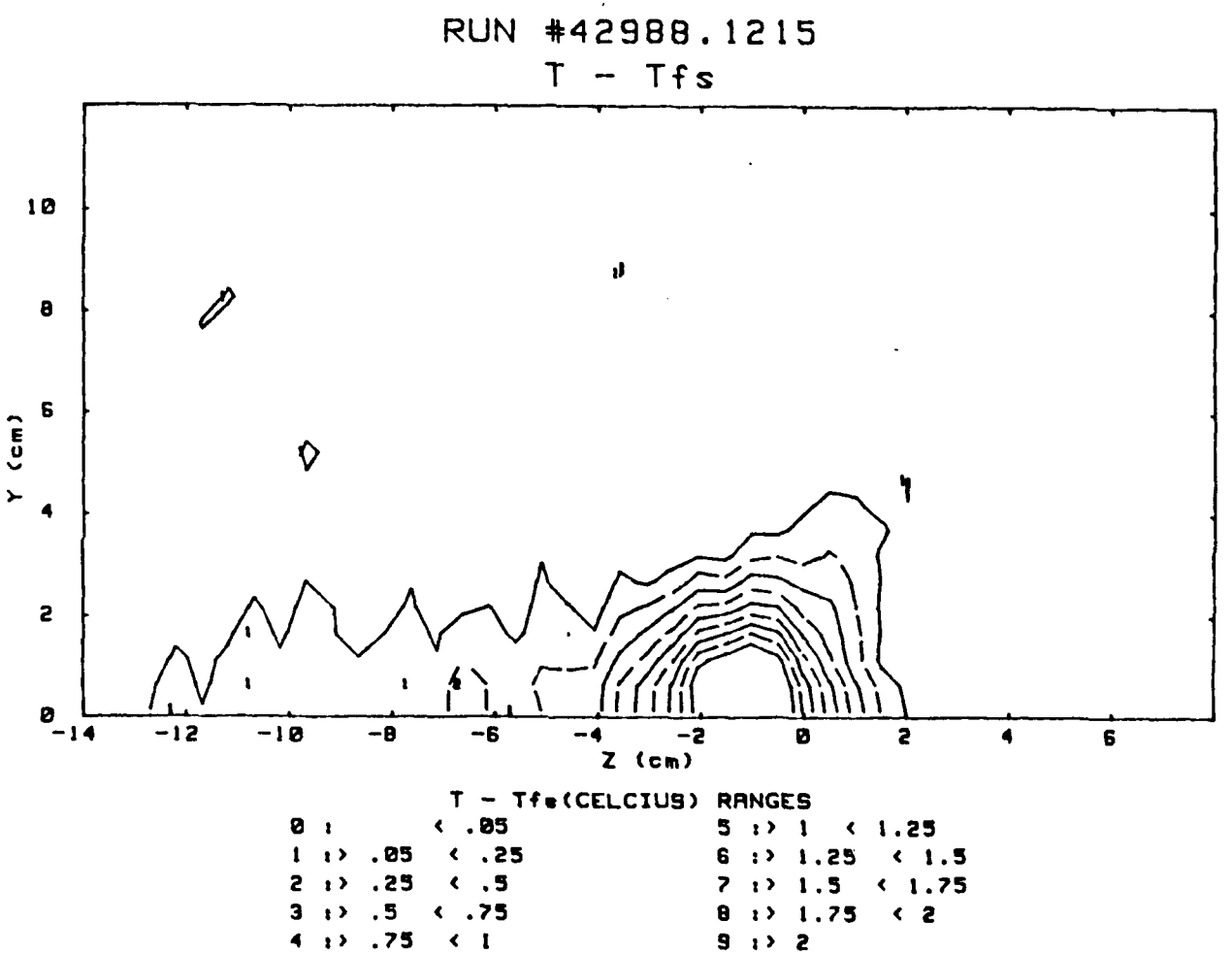

Figure 42. Local Temperature Minus Free Stream Temperature m=0.5 Vortex Generator Position k, Probe Position x/d=41.9

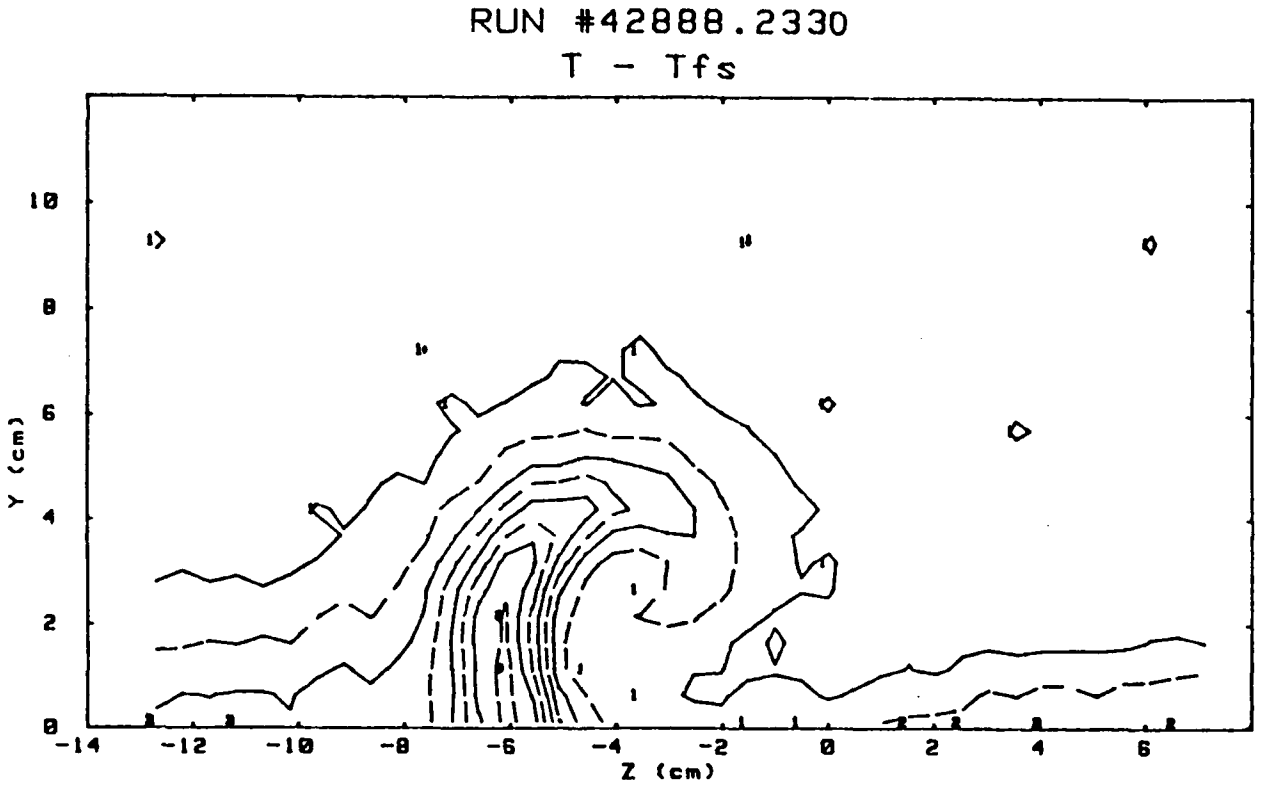

Figure 43. Local Temperature Minus Free Stream Temperature m=0.5 Vortex Generator Position e, Probe Position x/d=41.9

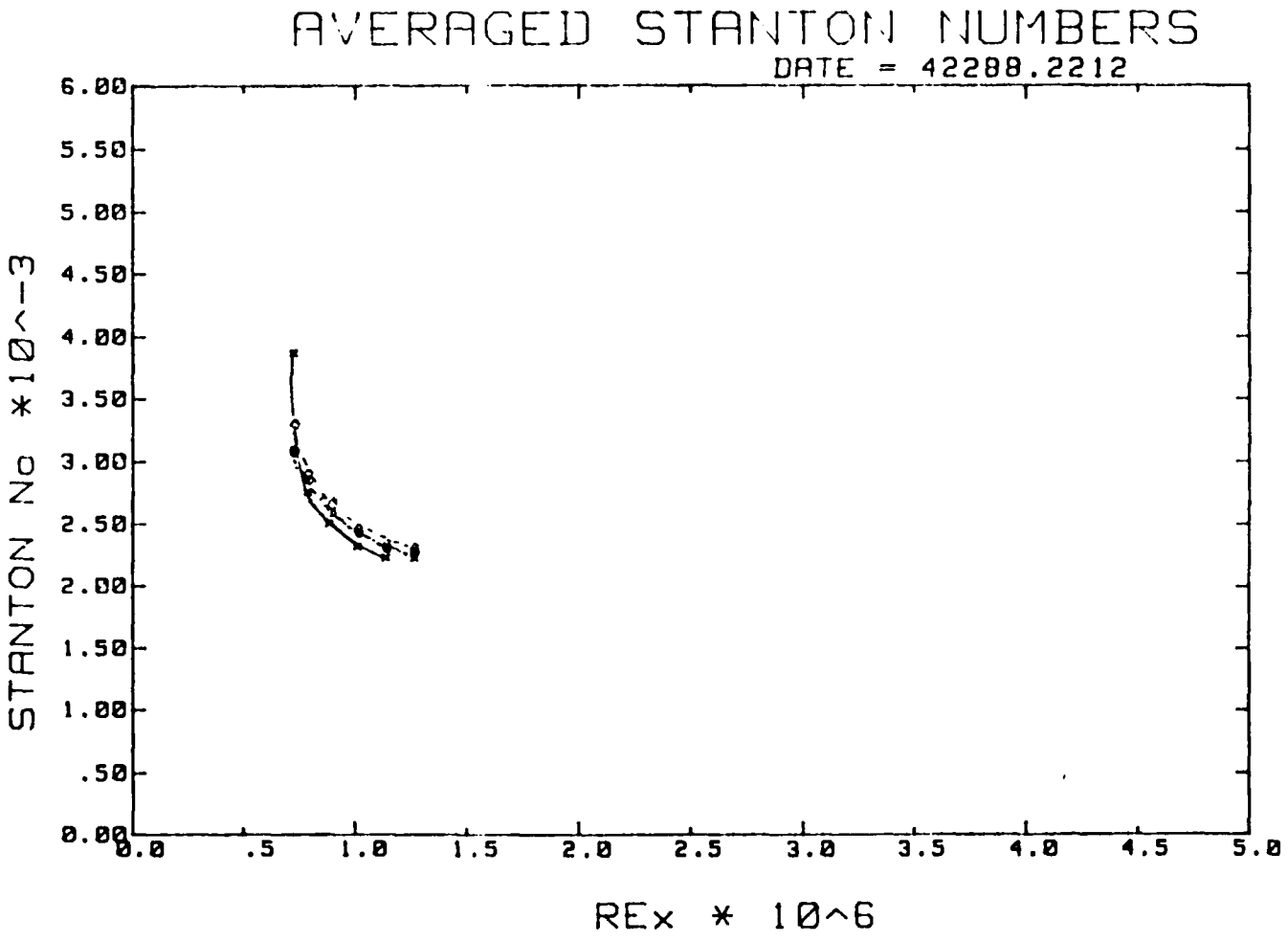

Figure 44. Spanwise Averaged Stanton Numbers at 10m/s Without Vortex and Without Film-Cooling

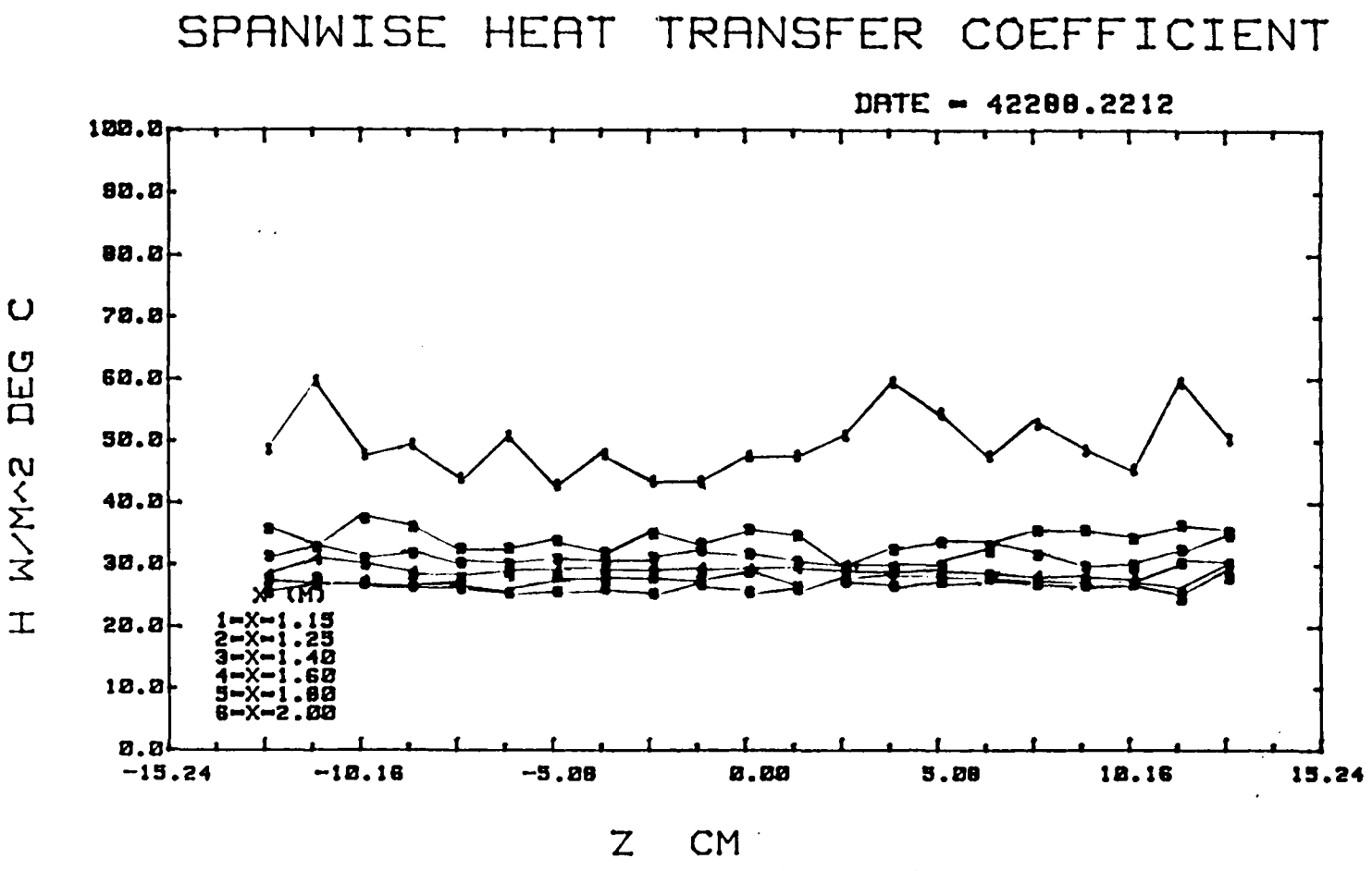

Figure 45. Local Heat Transfer Coefficient Distribution for Baseline Tests Without Vortex and Without Film-Cooling

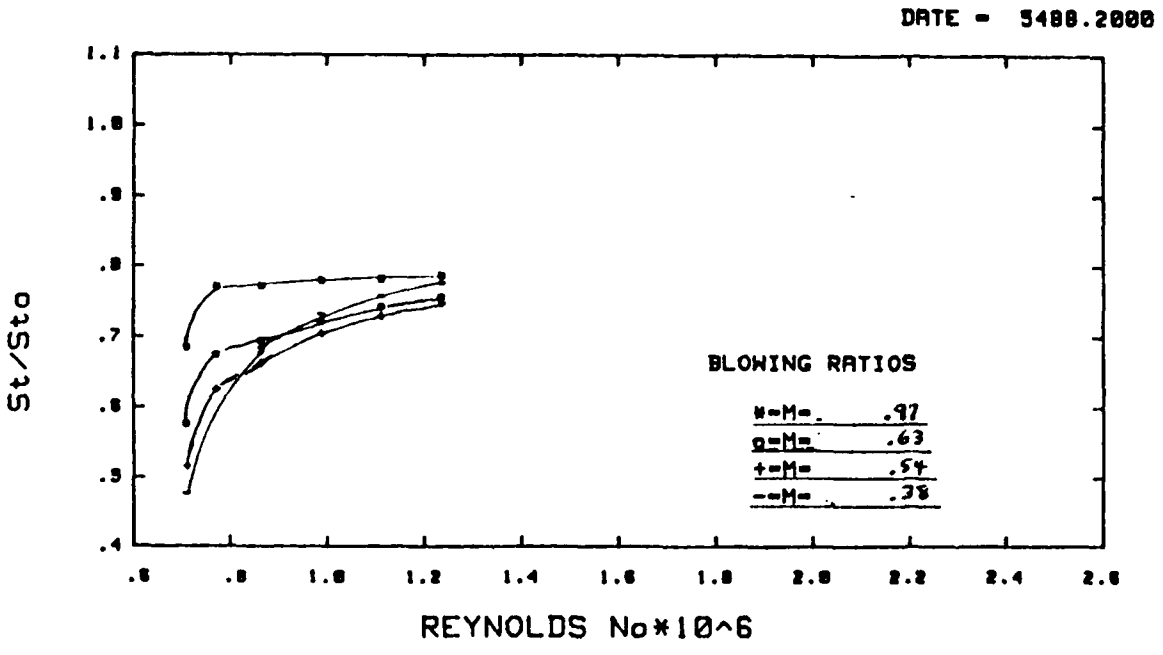

Figure 46a. Film-Cooling Data Without Vortex, Four Blowing Ratios, Free Stream Velocity 10m/s

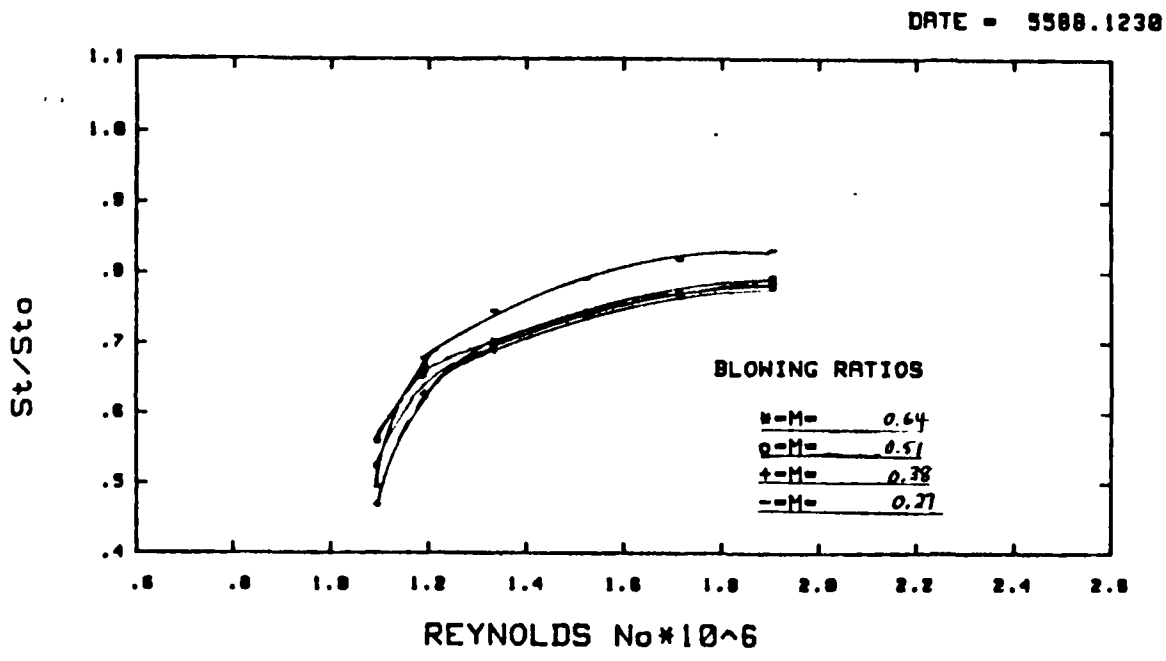

Figure 46b. Film-Cooling Data Without Vortex, Four Blowing Ratios, 15m/s Free Stream Velocity

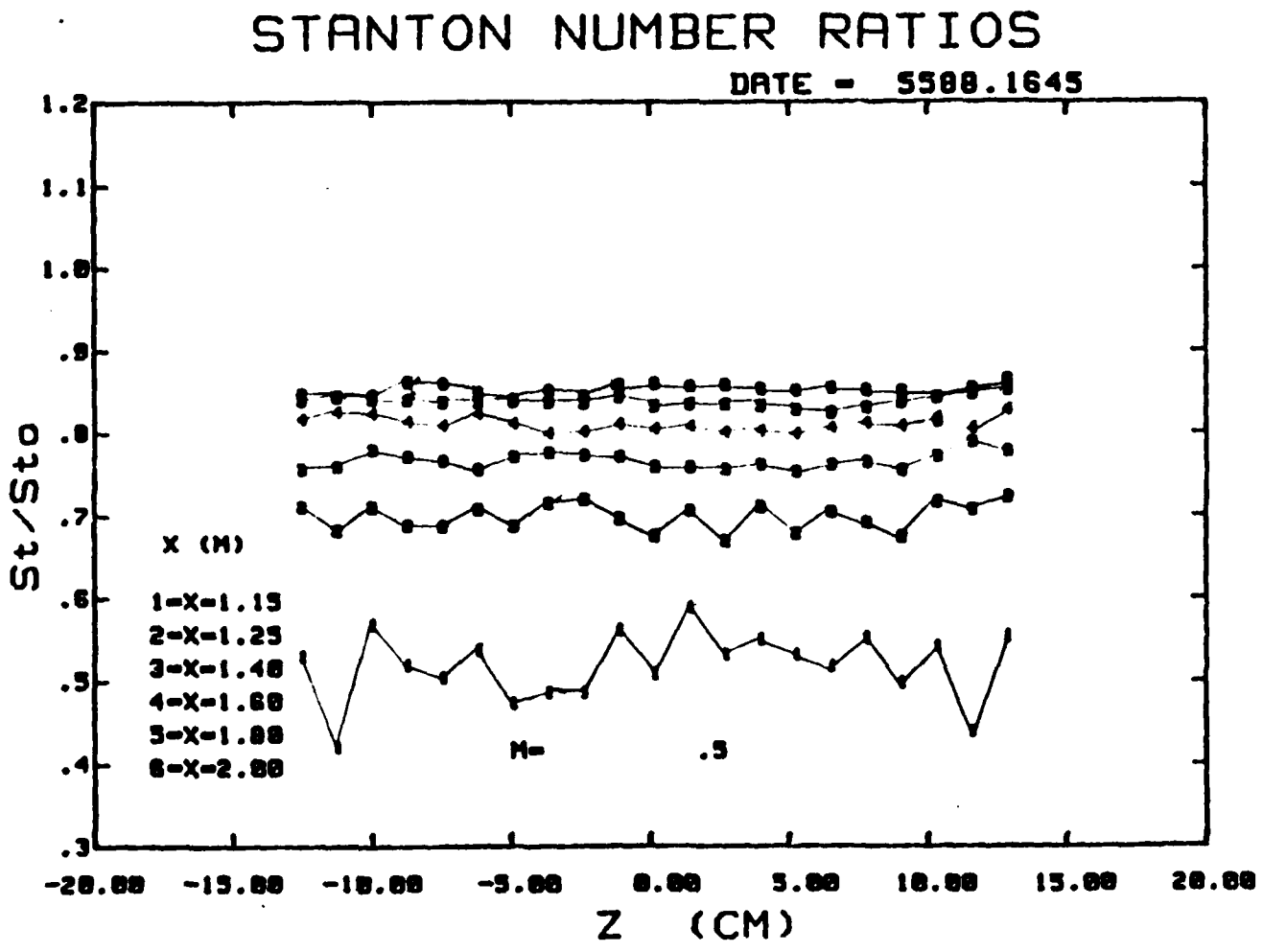

Figure 47. Local St/Sto for Film-Cooled Boundary Layer without Vortex, 15m/s Free Stream Velocity

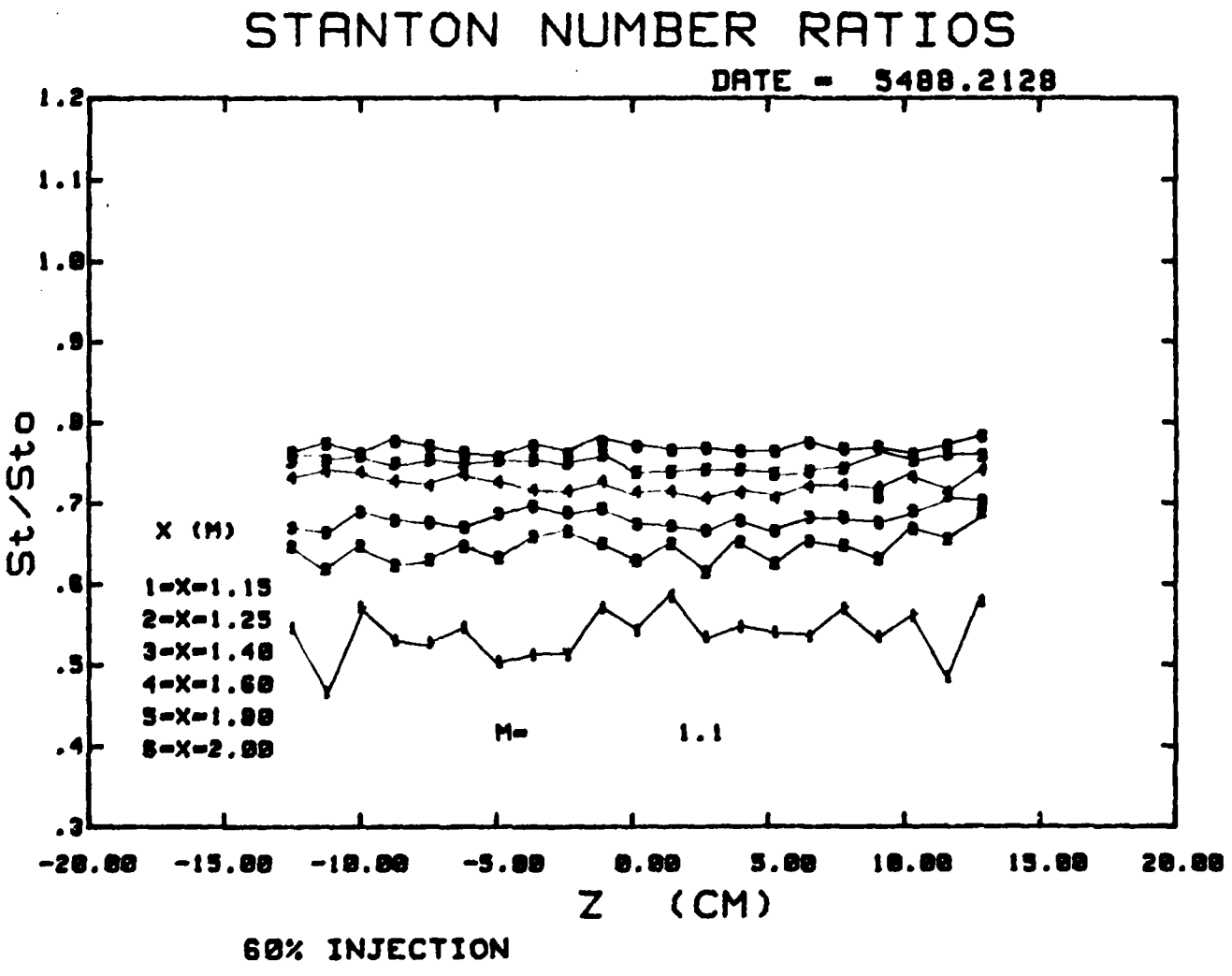

Figure 48. Local St/Sto for Film-Cooled Turbulent Boundary Layer Without Vortex, 10m/s Free Stream Velocity

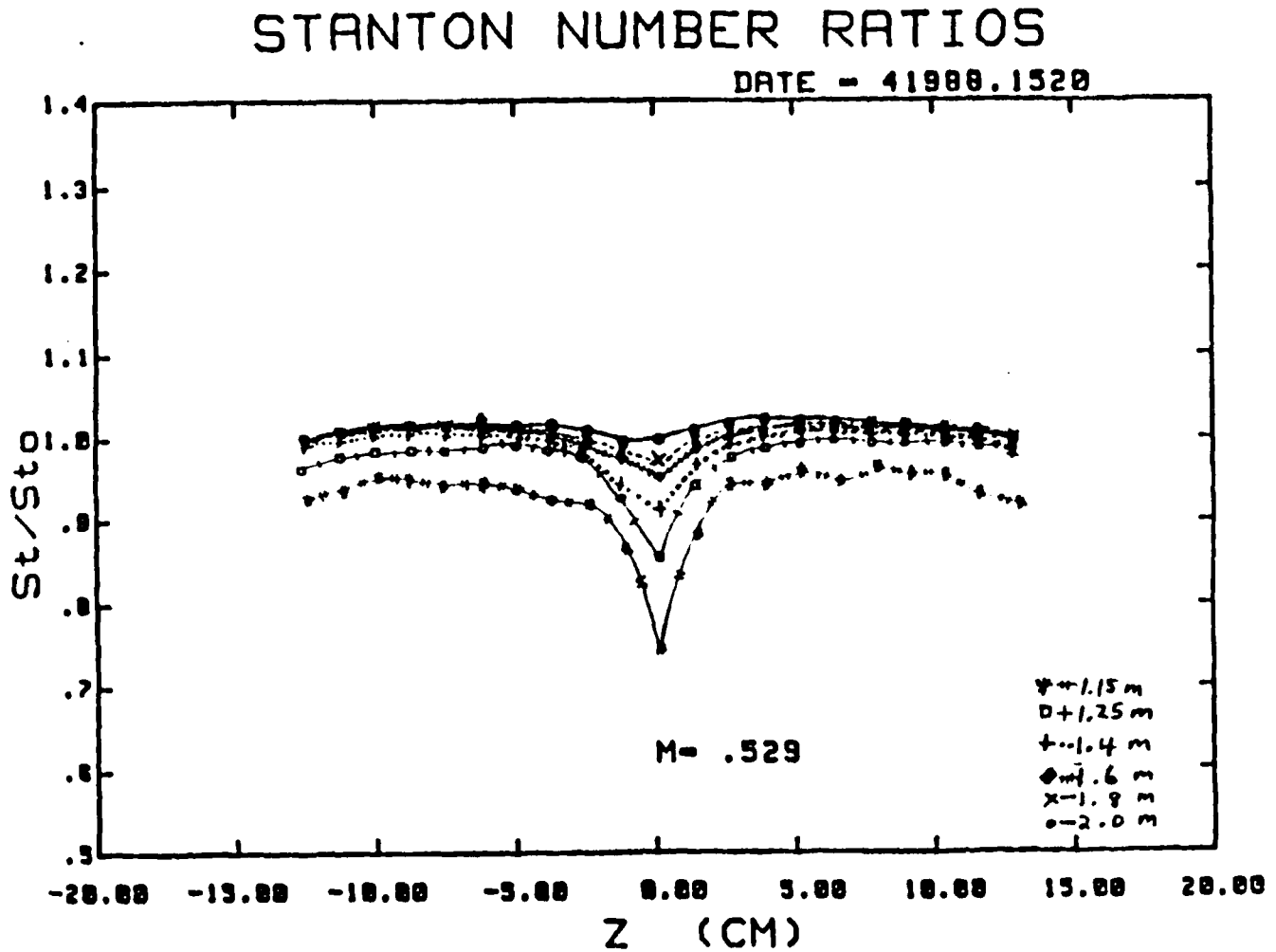

0 IN FROM THE C/L, 10M/S, 3 INJECTION HOLES

Figure 49. Local St/Sto with Film-Cooling from a Single Hole and No Vortex m=0.5

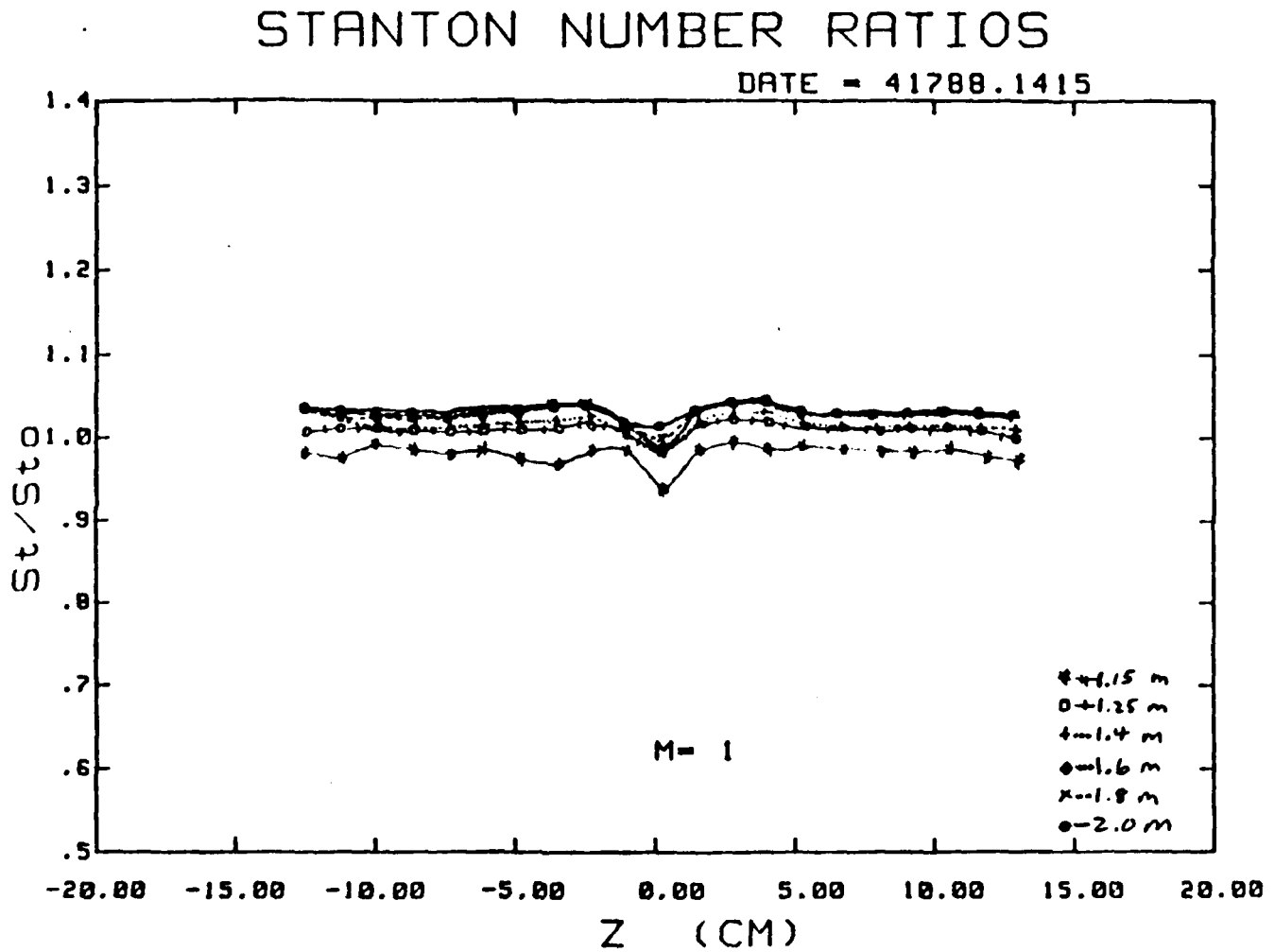

VG 1.5 INCHES FROM C/L, 10 M/S, 3 INJECTION HOLES

Figure 50. Local St/Sto with Film-Cooling from a Single Hole and No Vortex, m=1.0

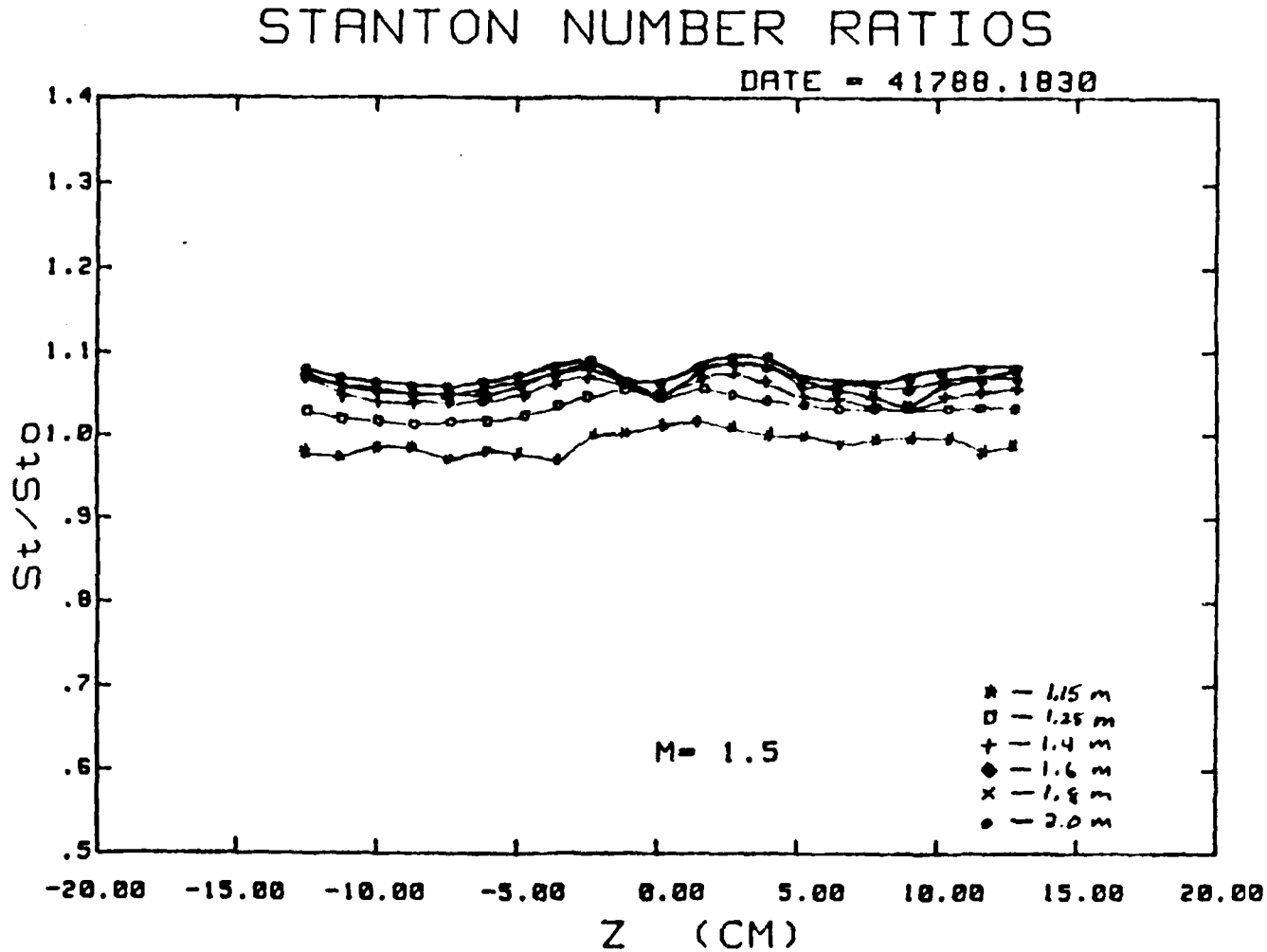

VG 1.5 INCHES FROM C/L, 10 M/S, 3 INJECTION HOLES

Figure 51. Local St/Sto with Film-Cooling from a Single Hole, and No Vortex, m=1.5

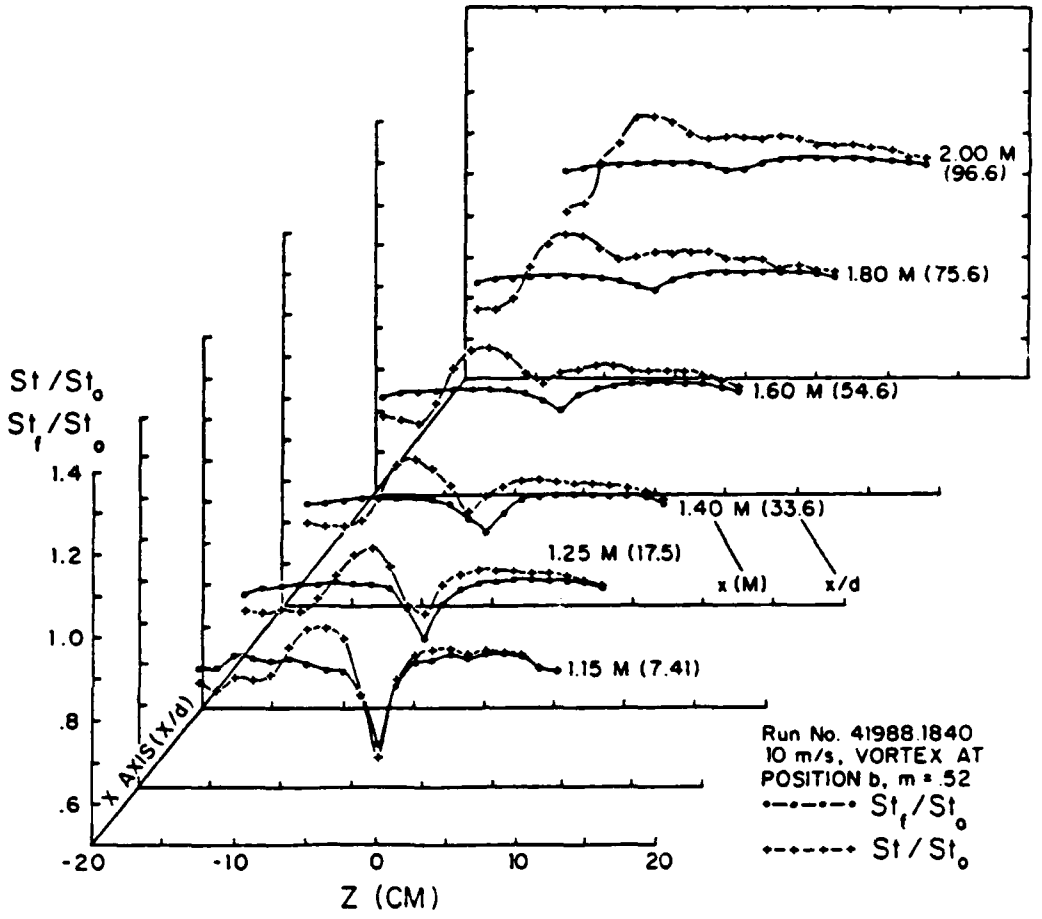

Figure 52. **Local Stanton Number Ratios in Boundary Layers with Film Cooling, with and without an Embedded Vortex**

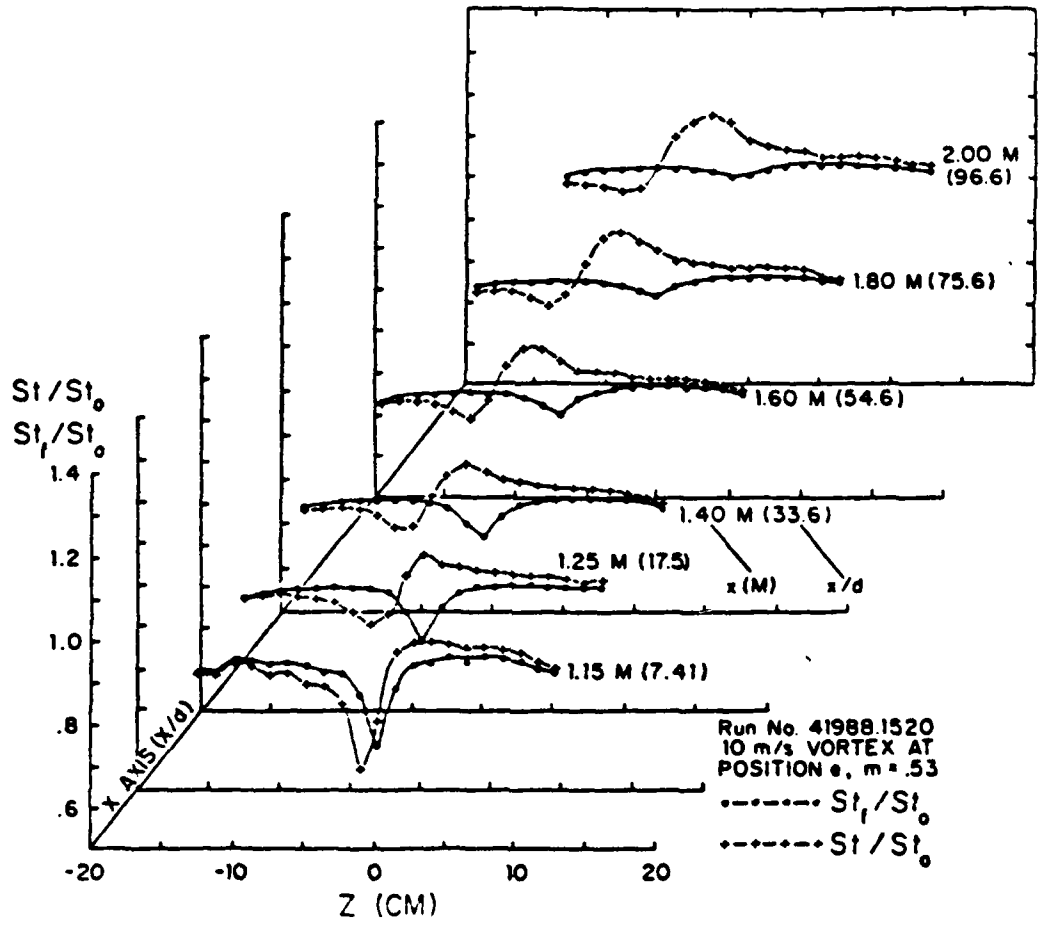

Figure 53. **Local Stanton Number Ratios in Boundary Layers with Film-Cooling, with and without an Embedded Vortex**

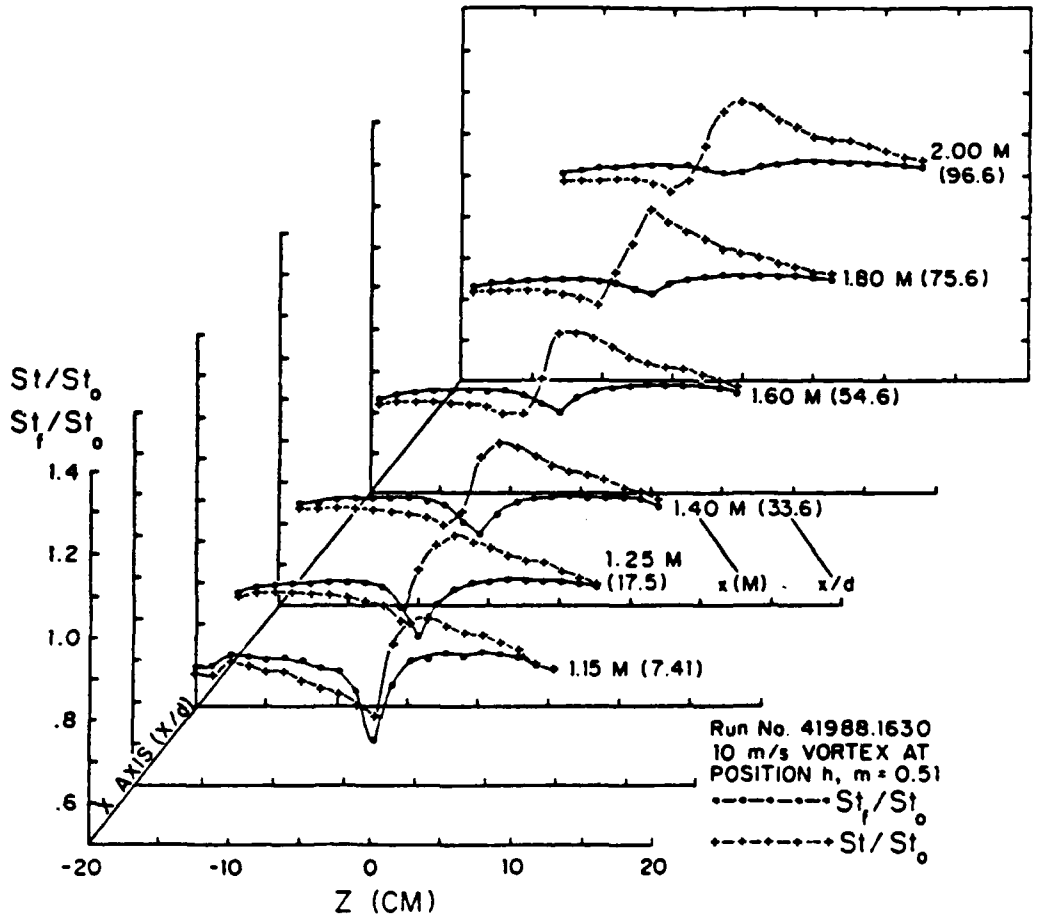

Figure 54. **Local Stanton Number Ratios in Boundary Layers with Film-Cooling, with and without an Embedded Vortex**

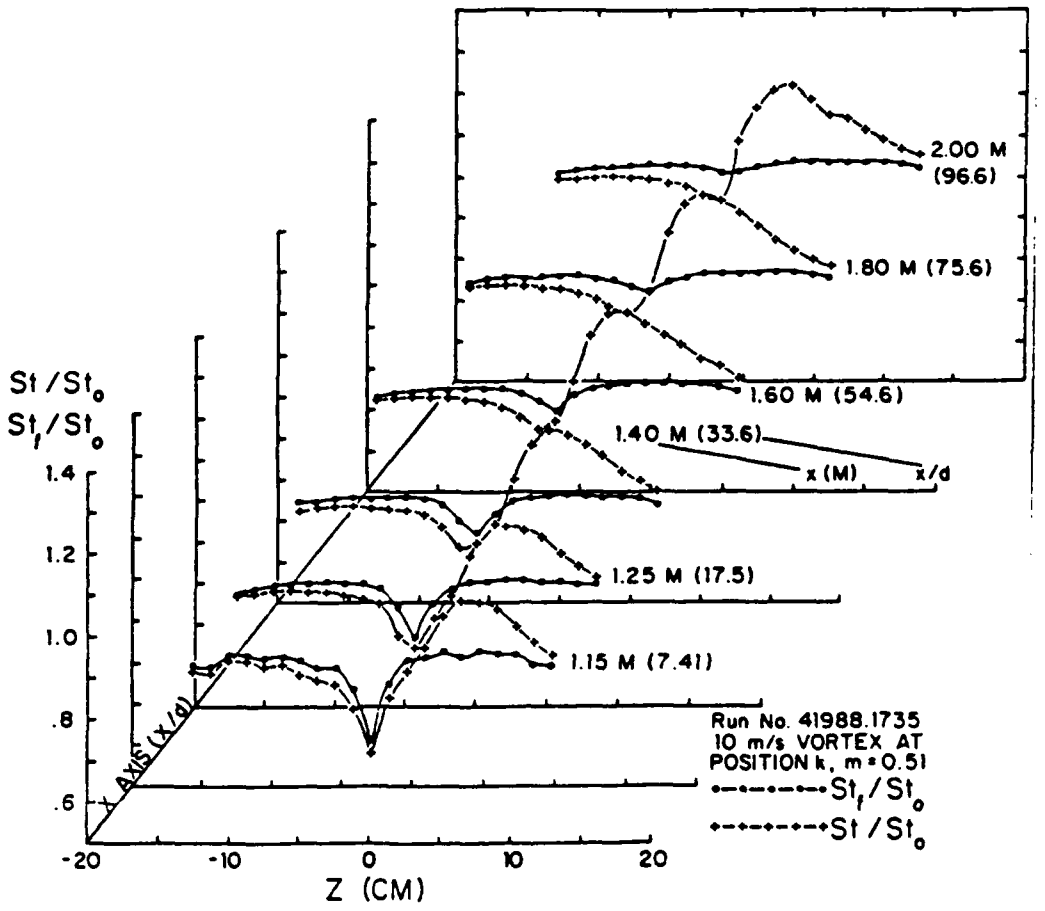

Figure 55. **Local Stanton Number Ratios in Boundary Layers with Film-Cooling, with and without an Embedded Vortex**

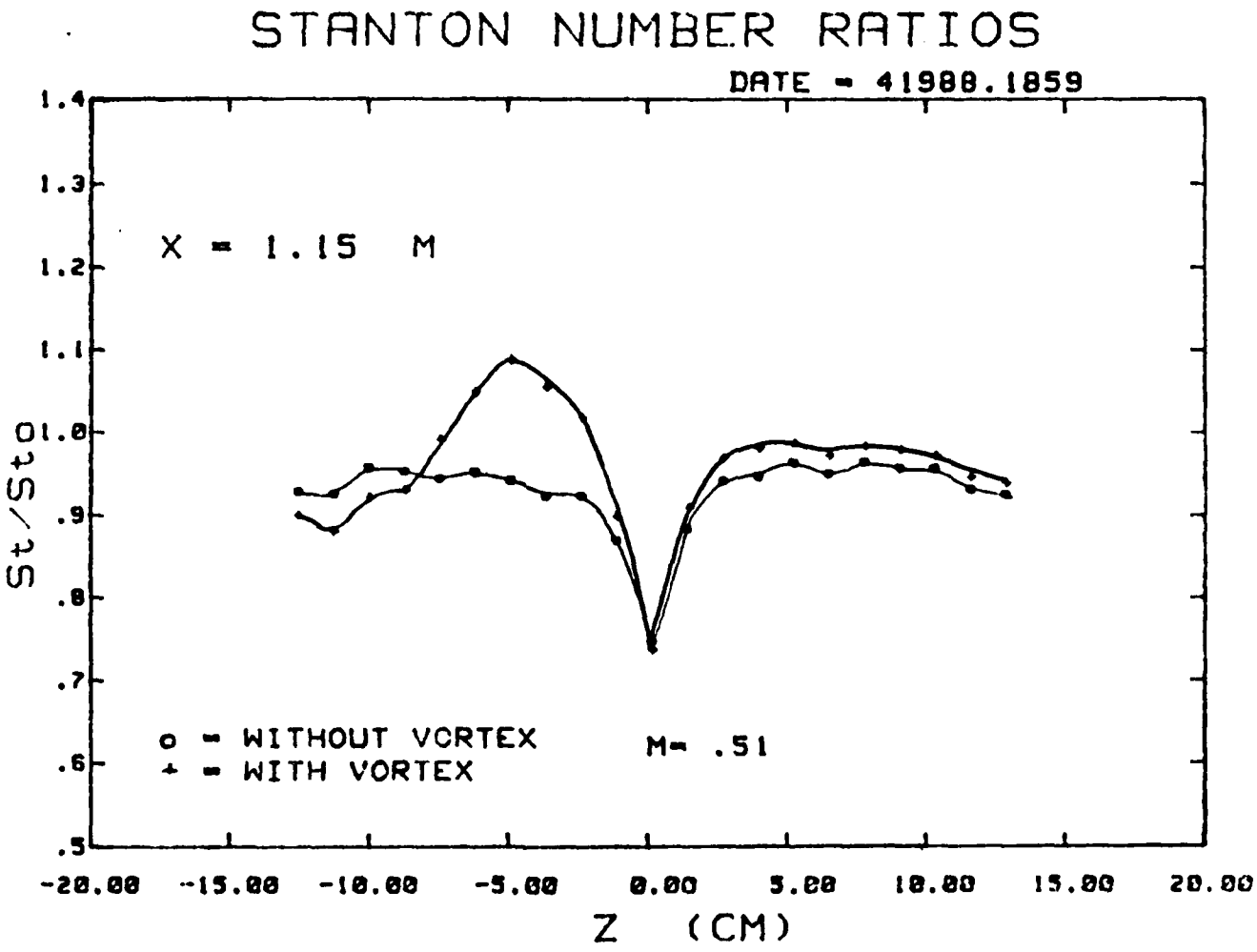

VG -2.0 INCHES FROM C/L, 10 M/S, 3 INJECTION HOLES

Figure 56. Spanwise Variation of Stanton Number Ratios Vortex #2 Position a

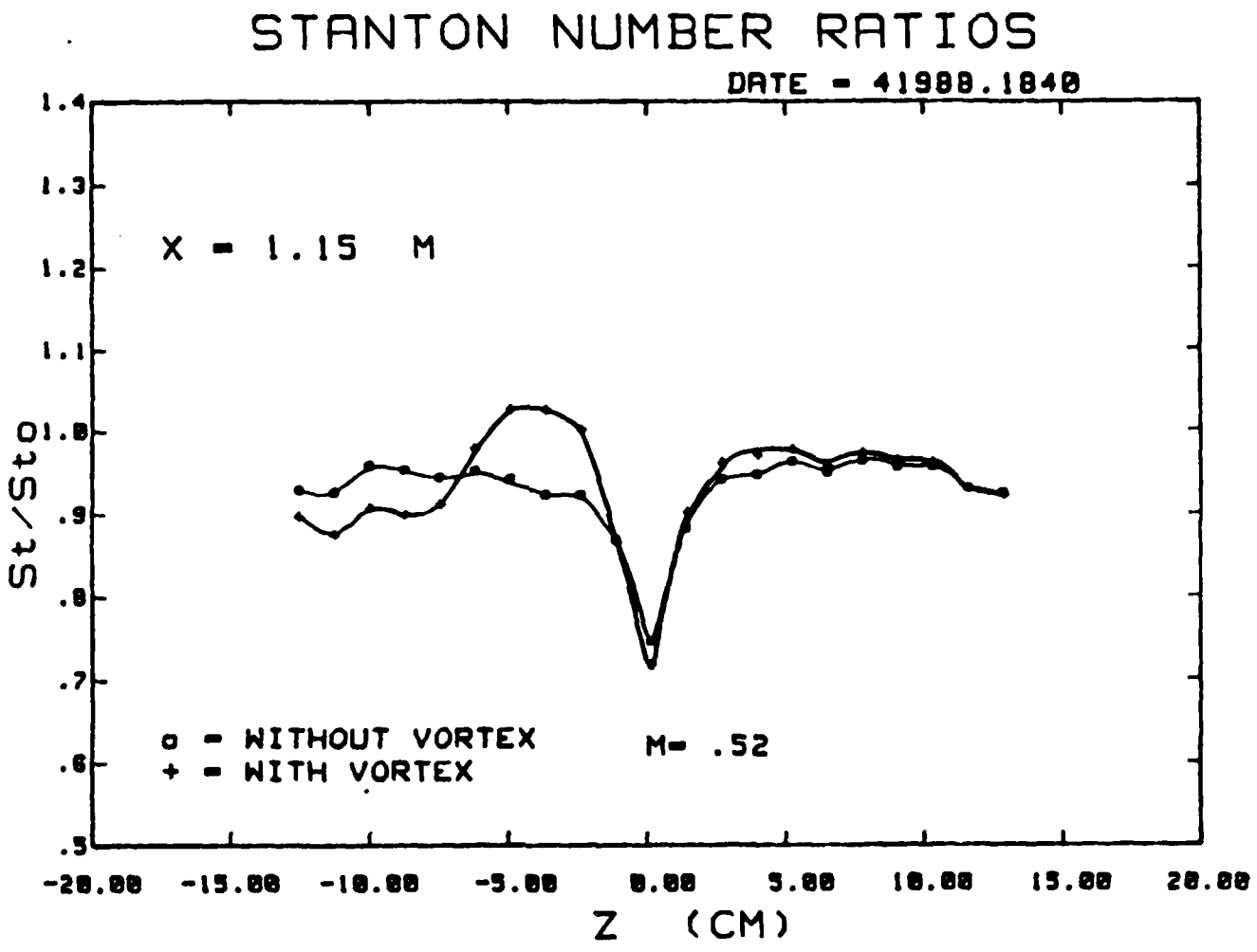

VG -1.5 INCHES FROM C/L, 10 M/S, 3 INJECTION HOLES

Figure 57. Spanwise Variation of Stanton Number Ratios Vortex #2 Position b

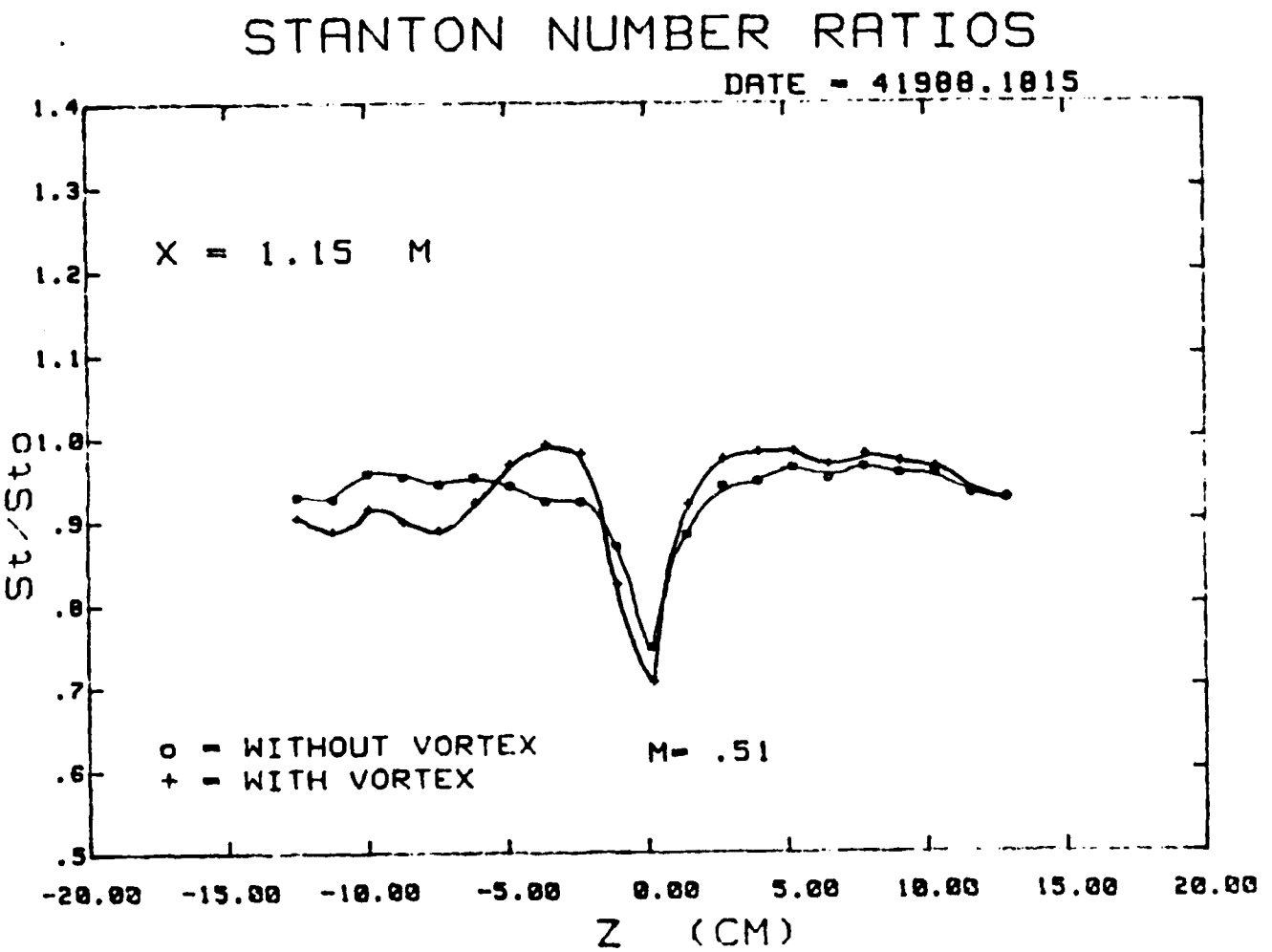

VG -1.0 INCHES FROM C/L, 10 M/S, 3 INJECTION HOLES

Figure 58. Spanwise Variation of Stanton Number Ratios Vortex #2 Position c

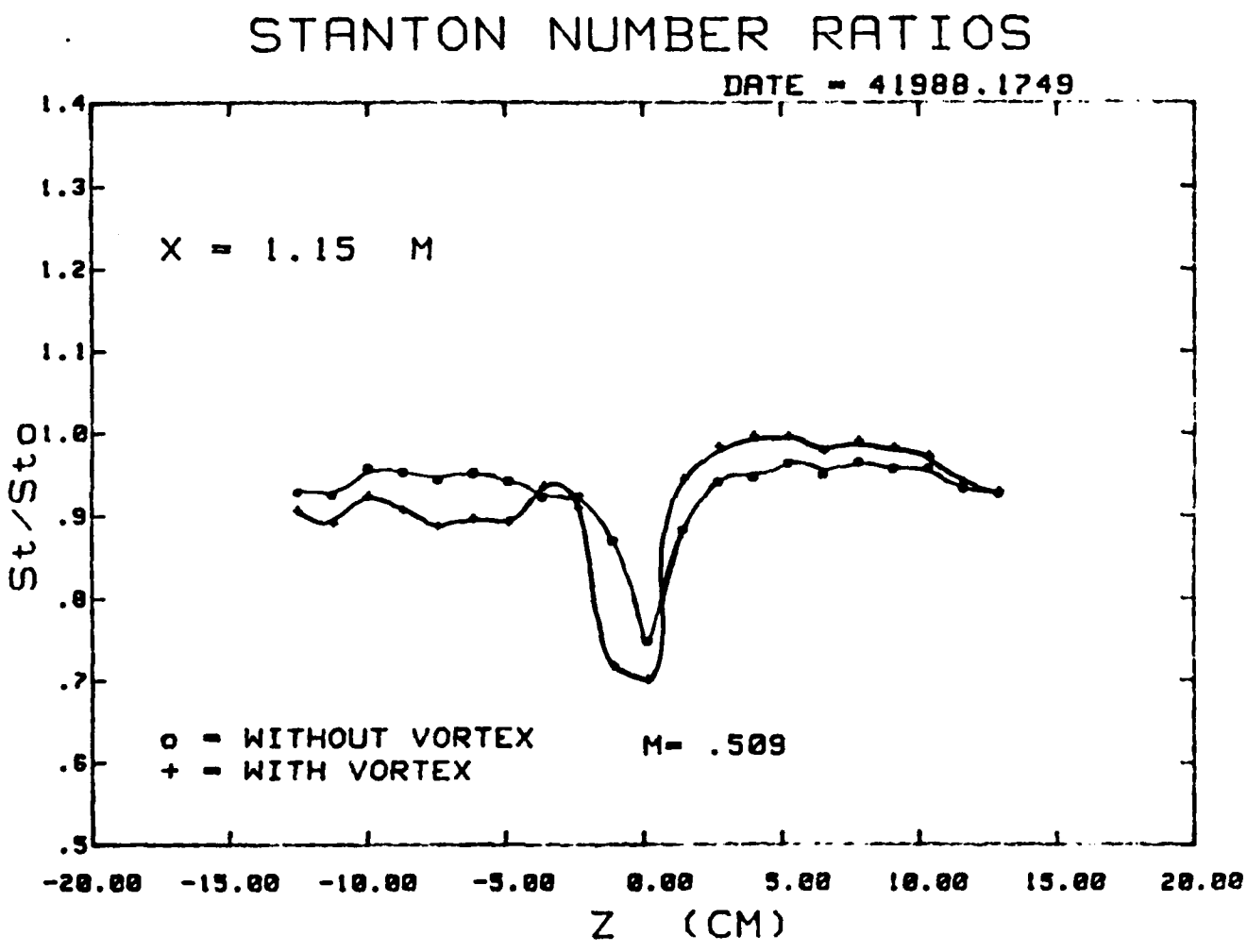

VG -0.5 INCHES FROM C/L, 10 M/S, 3 INJECTION HOLES

Figure 59. Spanwise Variation of Stanton Number Ratios Vortex #2 Position d

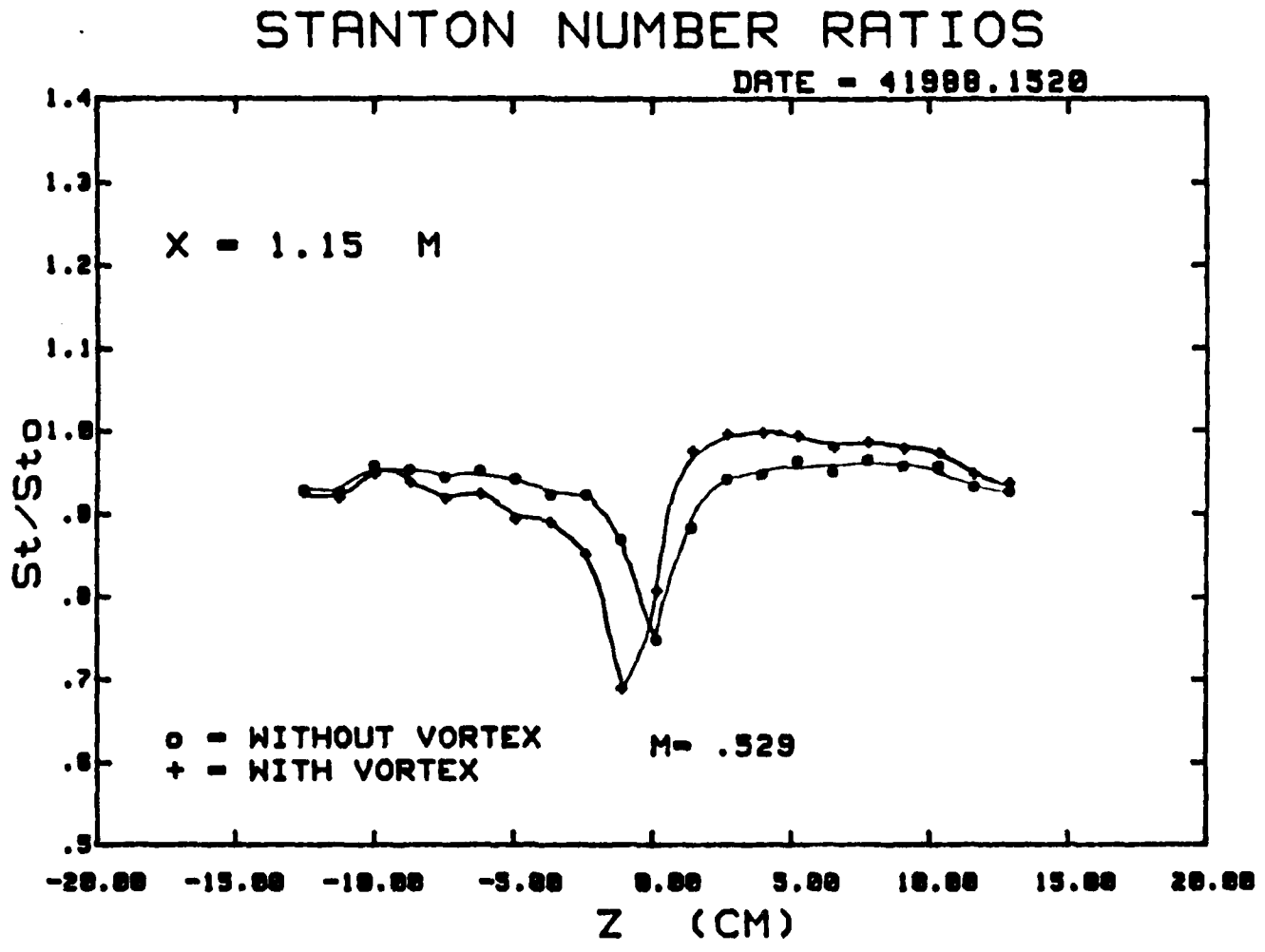

0 IN FROM C/L,10M/S,3 INJ HOLES

Figure 60. Spanwise Variation of Stanton Number Ratios Vortex #2 Position e

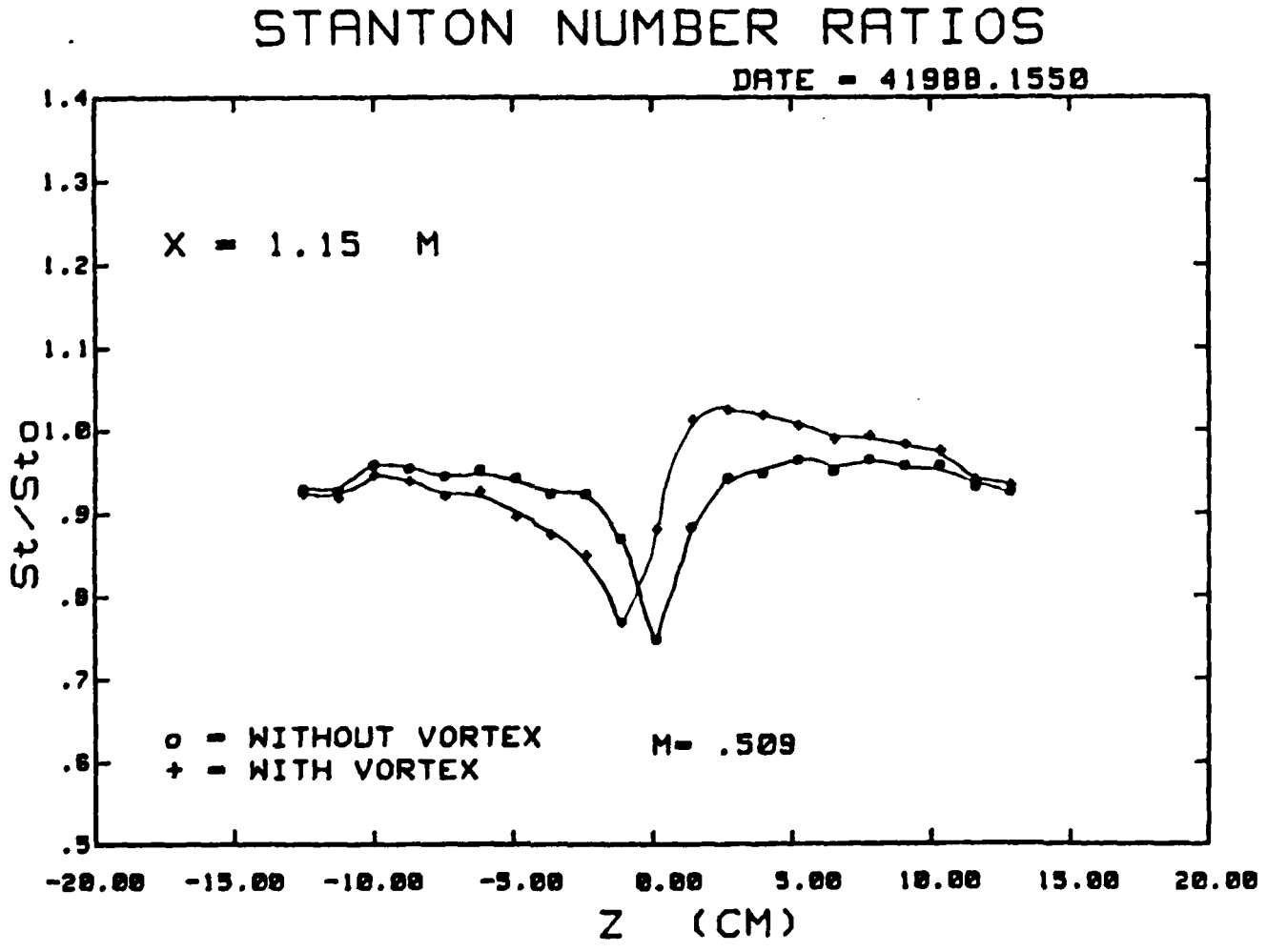

.5 IN FROM C/L, 10M/S, 3 INJECTION HOLES

Figure 61. Spanwise Variation of Stanton Number Ratios Vortex #2 Position f

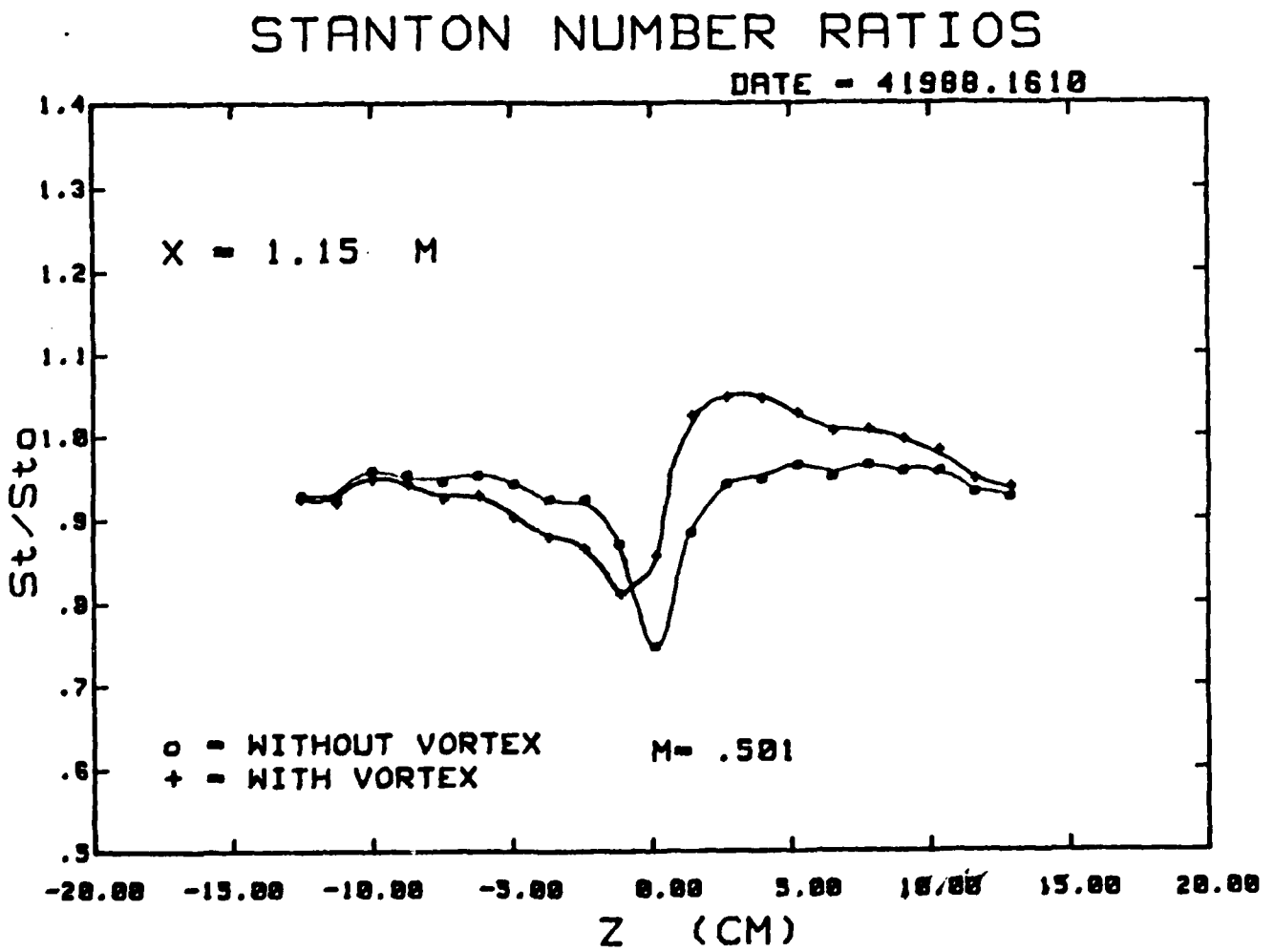

Figure 62. Spanwise Variation of Stanton Number Ratios Vortex #2 Position g

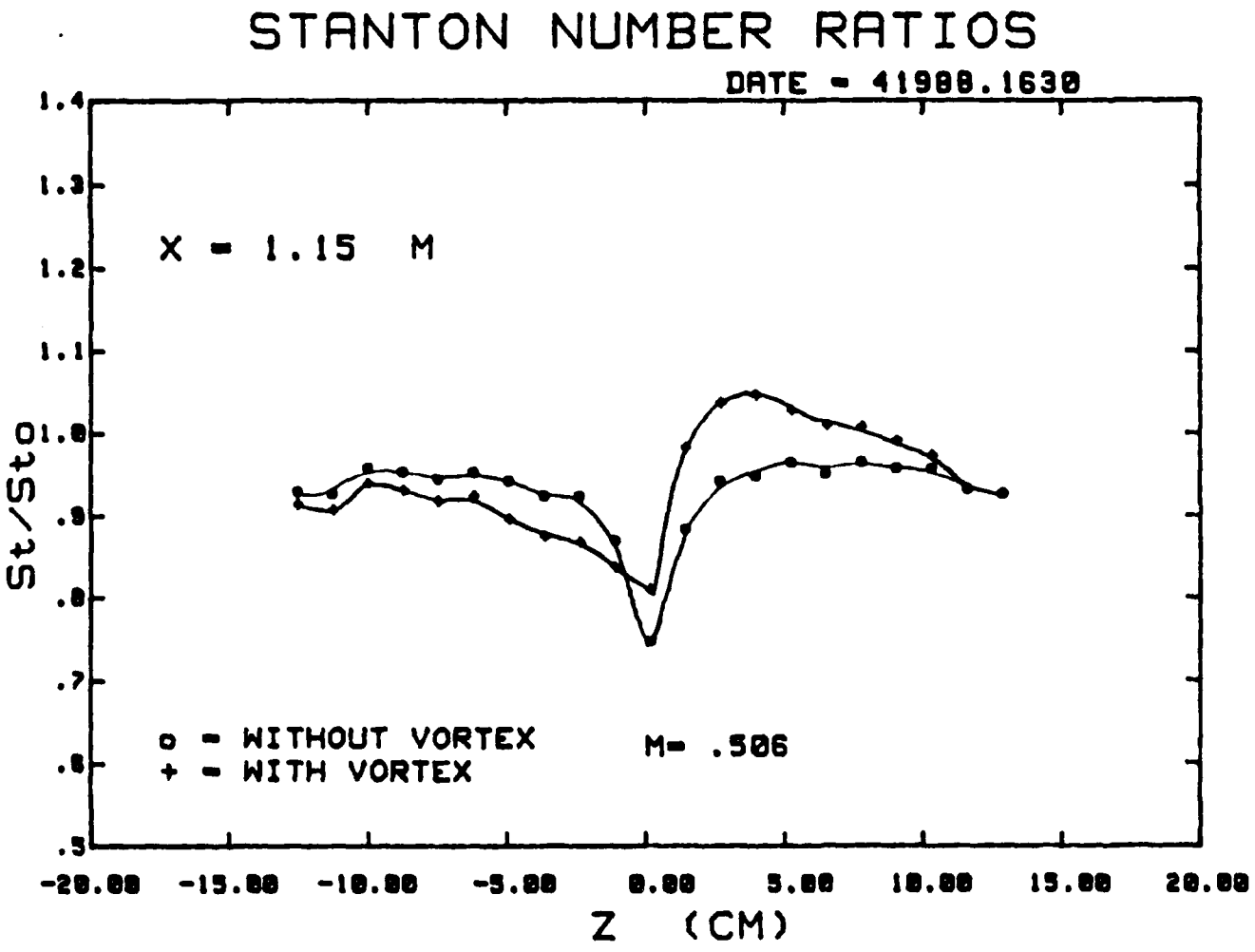

Figure 63. Spanwise Variation of Stanton Number Ratios Vortex #2 Position h

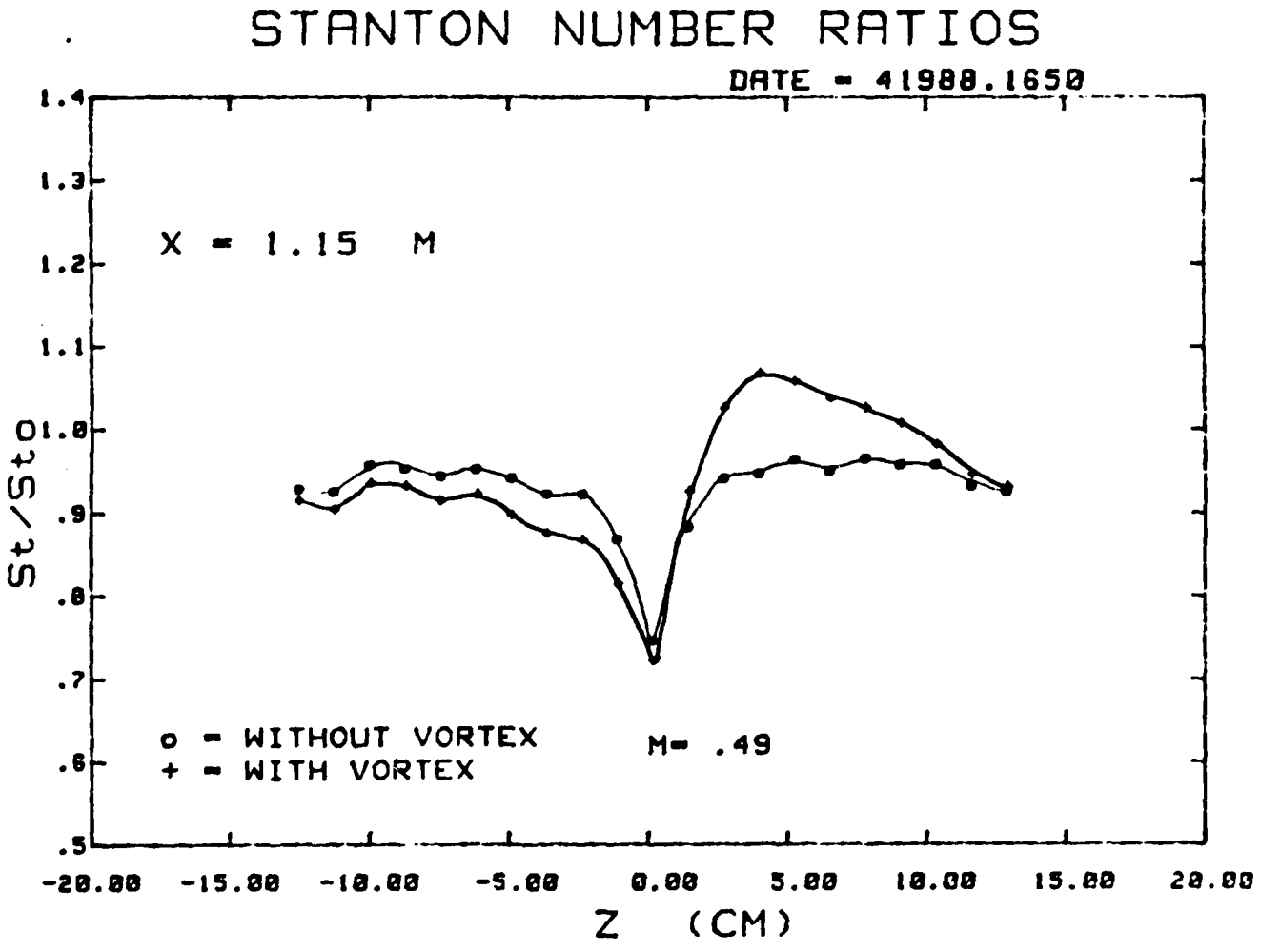

VG 2.0 INCHES FROM C/L, 10 M/S, 3 INJECTION HOLES

Figure 64. Spanwise Variation of Stanton Number Ratios Vortex #2 Position i

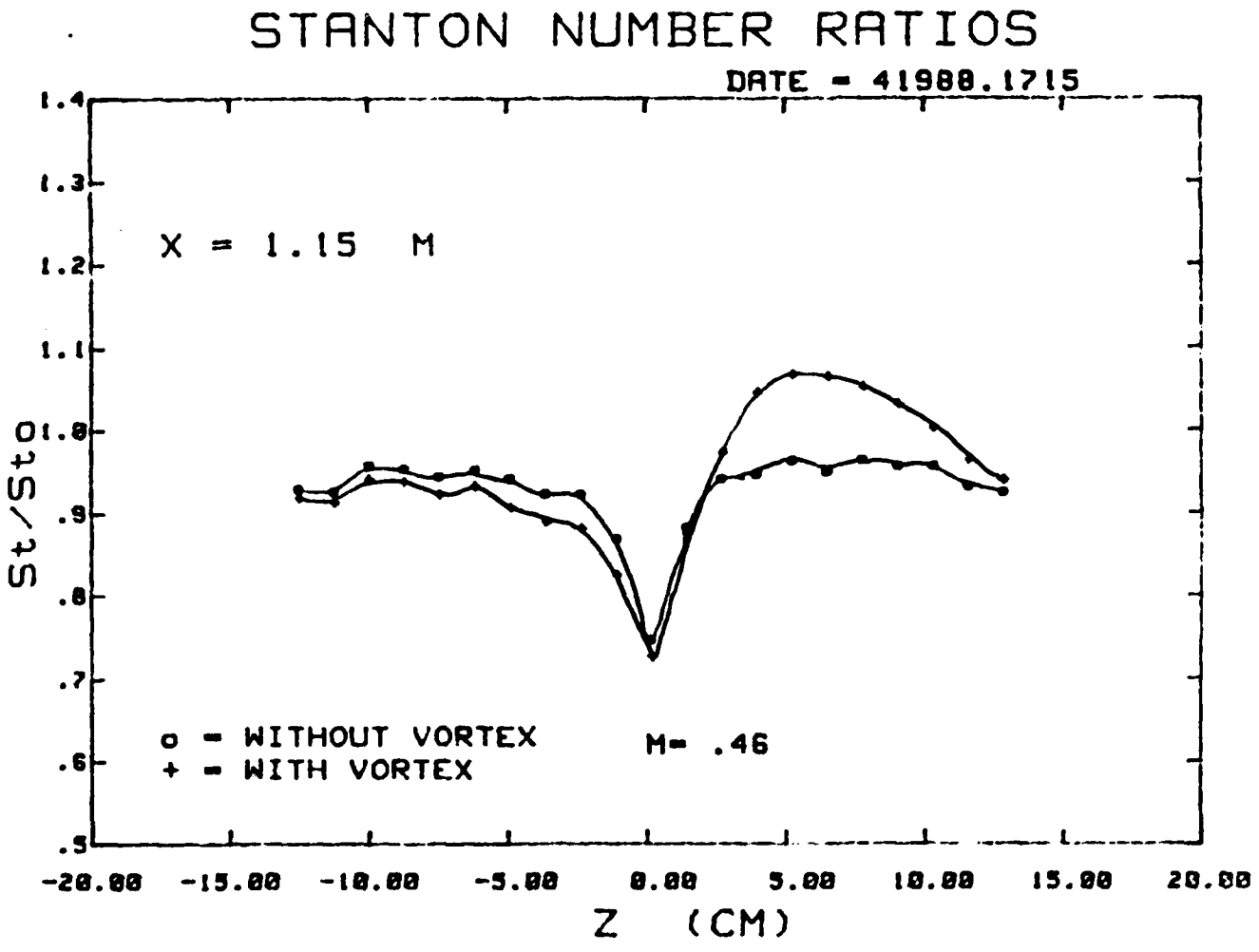

VG 2.5 INCHES FROM C/L, 10 M/S, 3 INJECTION HOLES

Figure 65. Spanwise Variation of Stanton Number Ratios Vortex #2 Position j

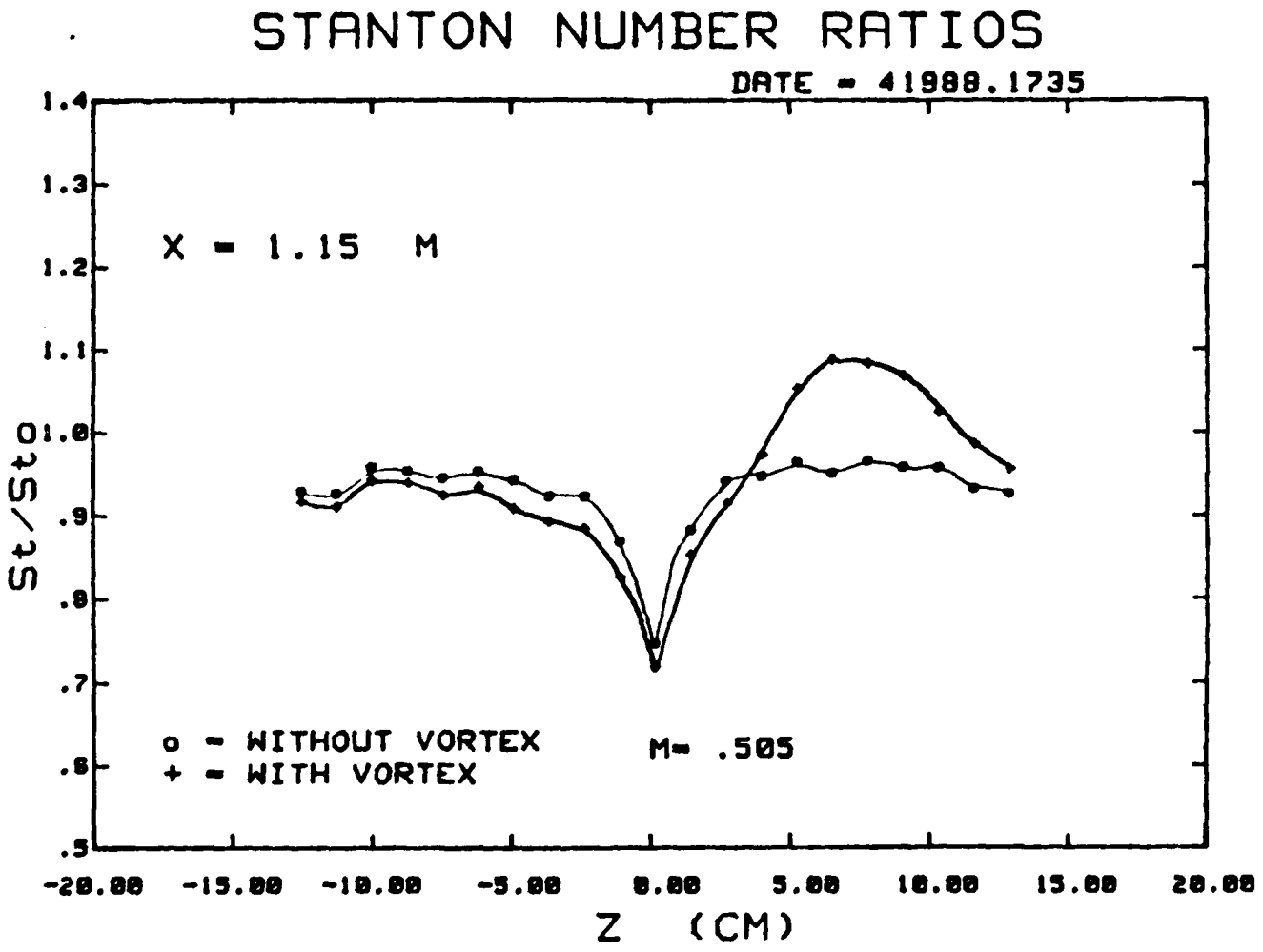

VG 3.0 INCHES FROM C/L, 10 M/S, 3 INJECTION HOLES

Figure 66. Spanwise Variation of Stanton Number Ratios Vortex #2 Position k

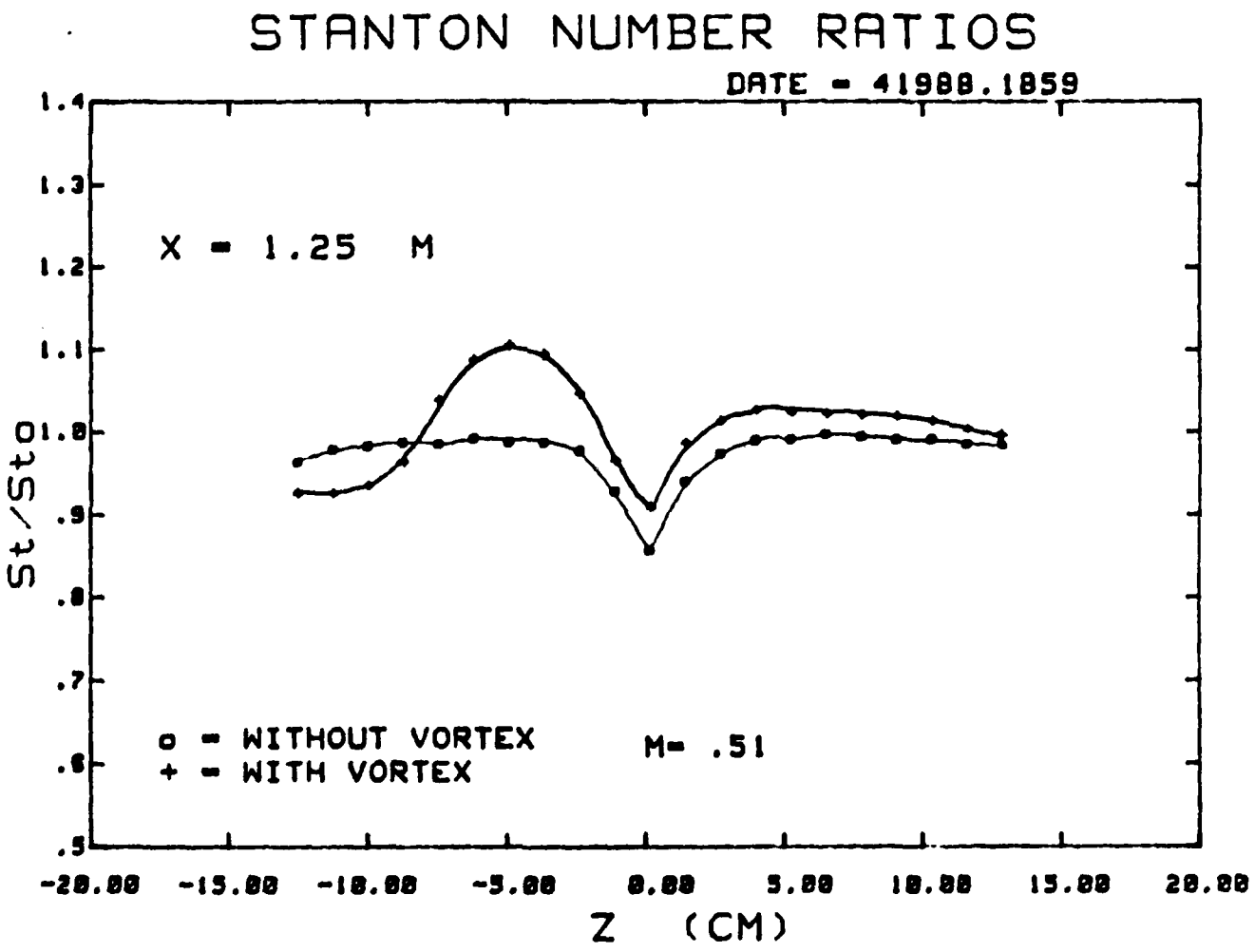

VG -2.0 INCHES FROM C/L, 10 M/S, 3 INJECTION HOLES

Figure 67. Spanwise Variation of Stanton Number Ratios Vortex #2 Position a

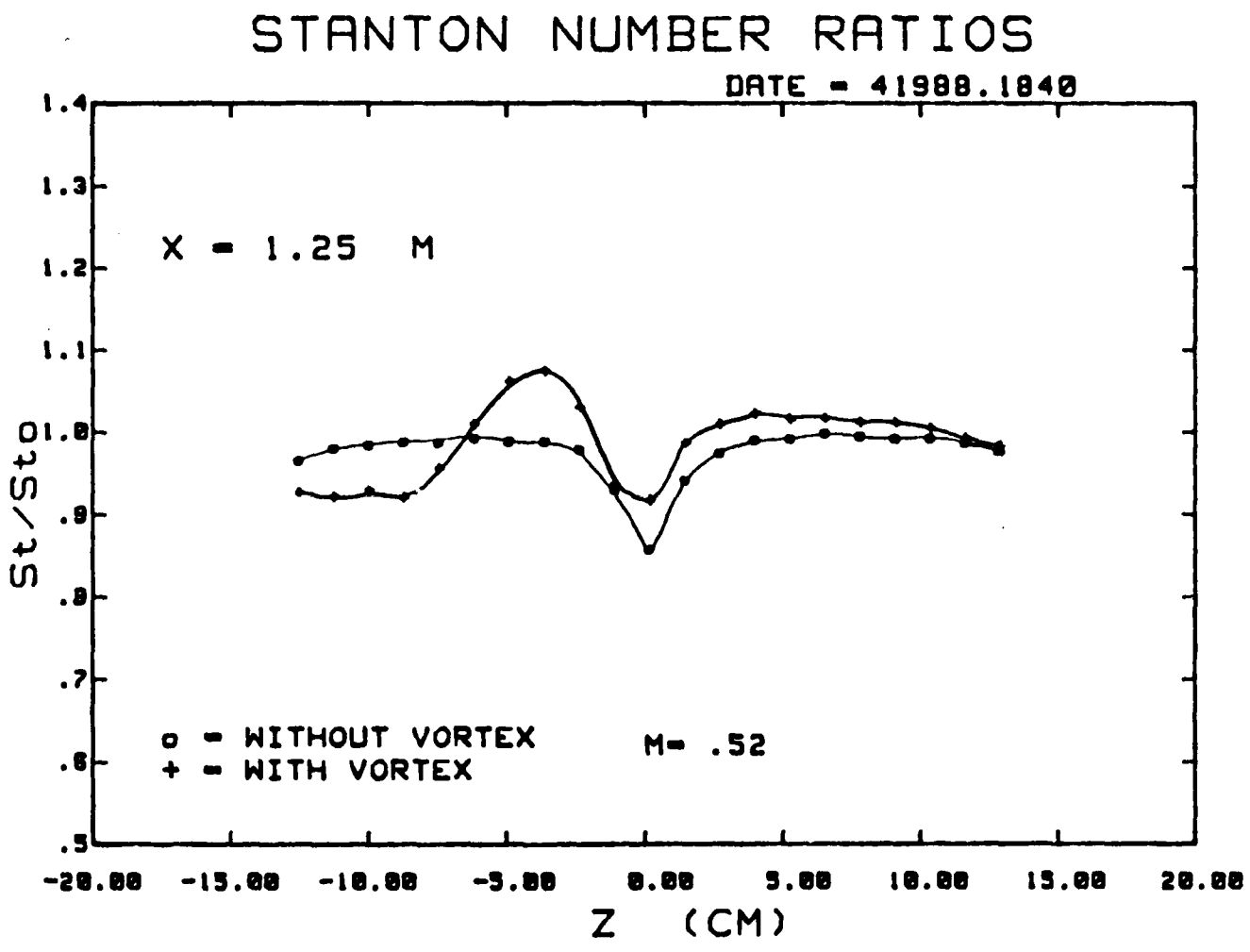

VG -1.5 INCHES FROM C/L, 10 M/S, 3 INJECTION HOLES

Figure 68. Spanwise Variation of Stanton Number Ratios Vortex #2 Position b

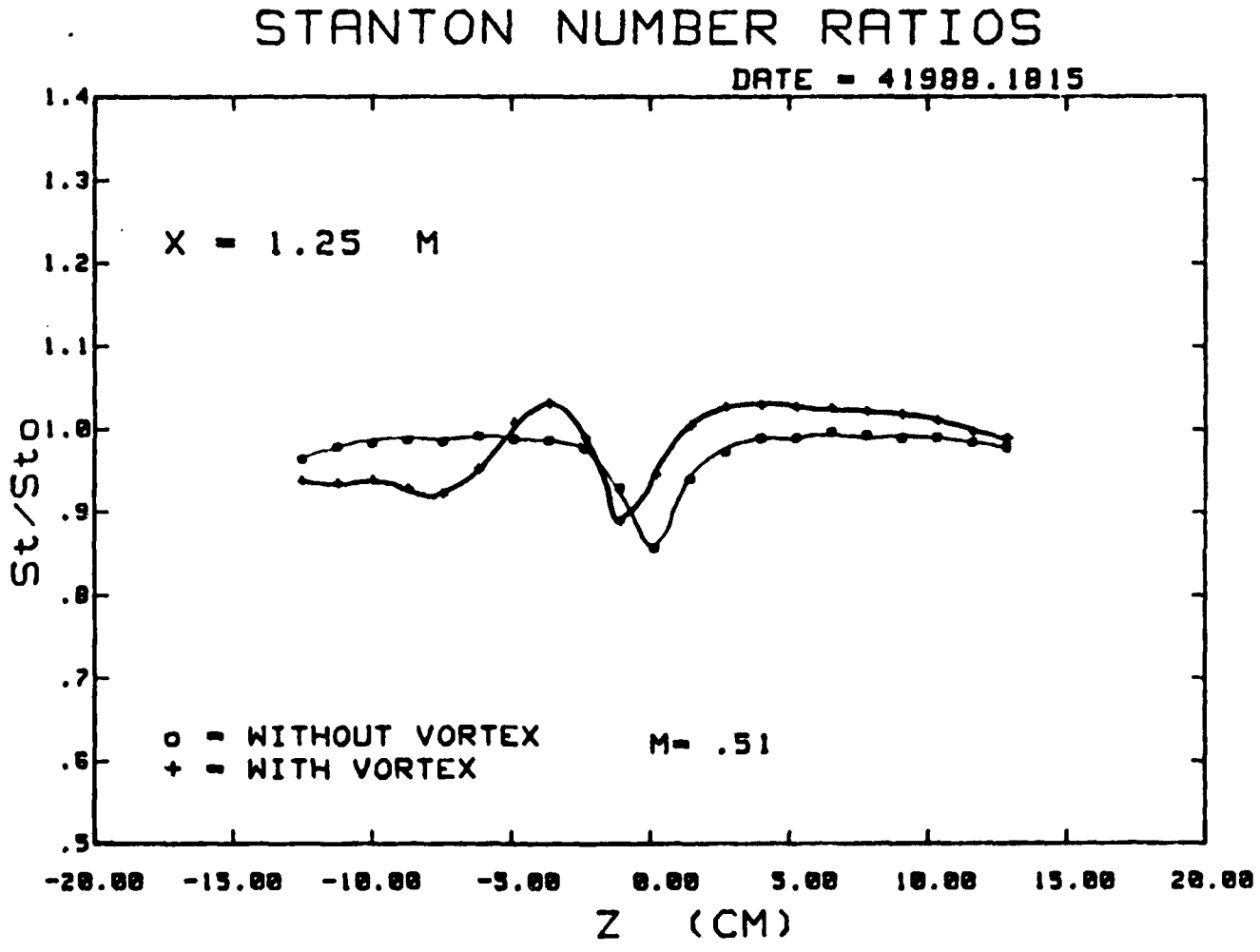

VG -1.0 INCHES FROM C/L, 10 M/S, 3 INJECTION HOLES

Figure 69. Spanwise Variation of Stanton Number Ratios Vortex #2 Position c

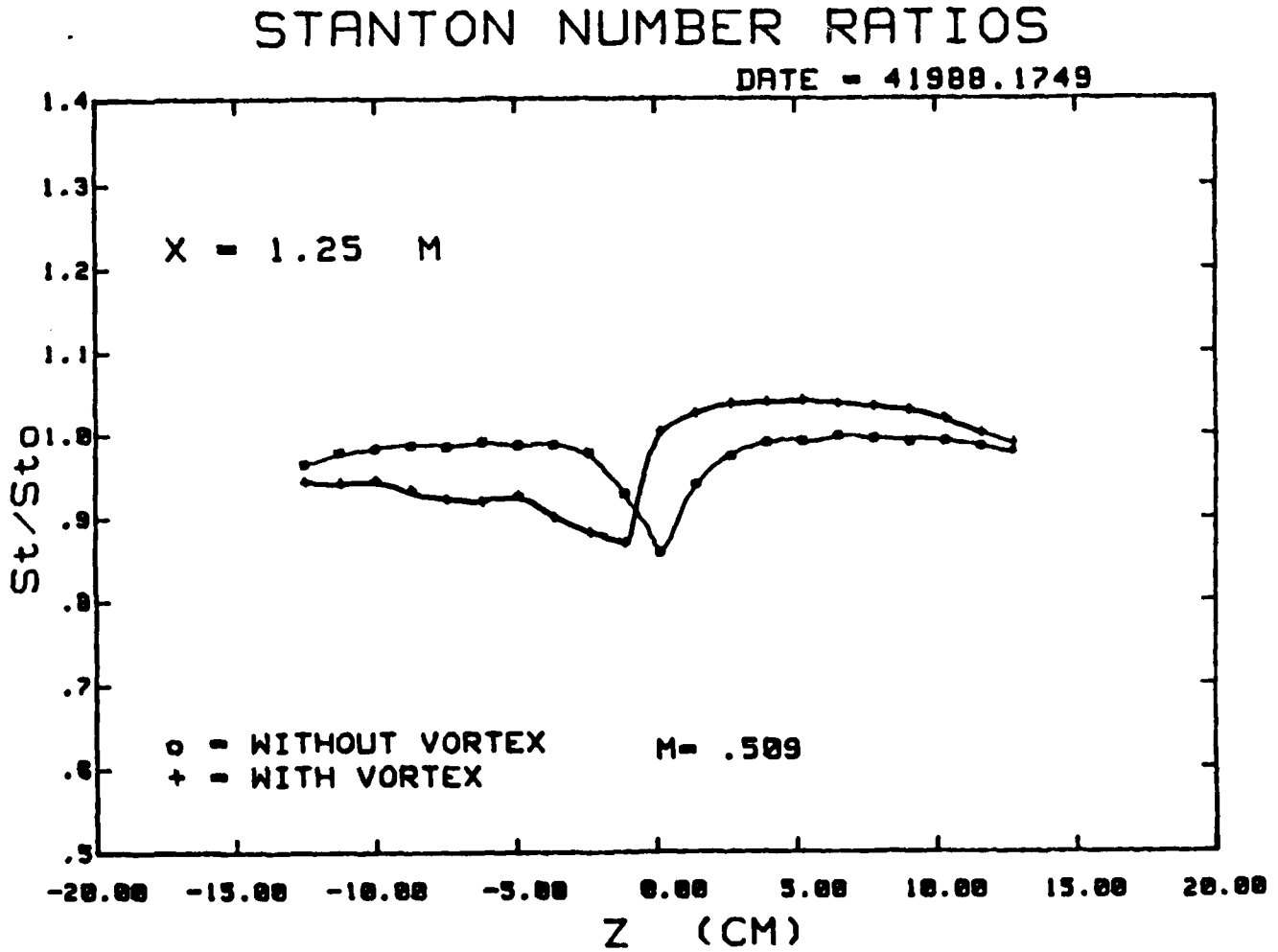

VG -0.5 INCHES FROM C/L, 10 M/S, 3 INJECTION HOLES

Figure 70. Spanwise Variation of Stanton Number Ratios Vortex #2 Position d

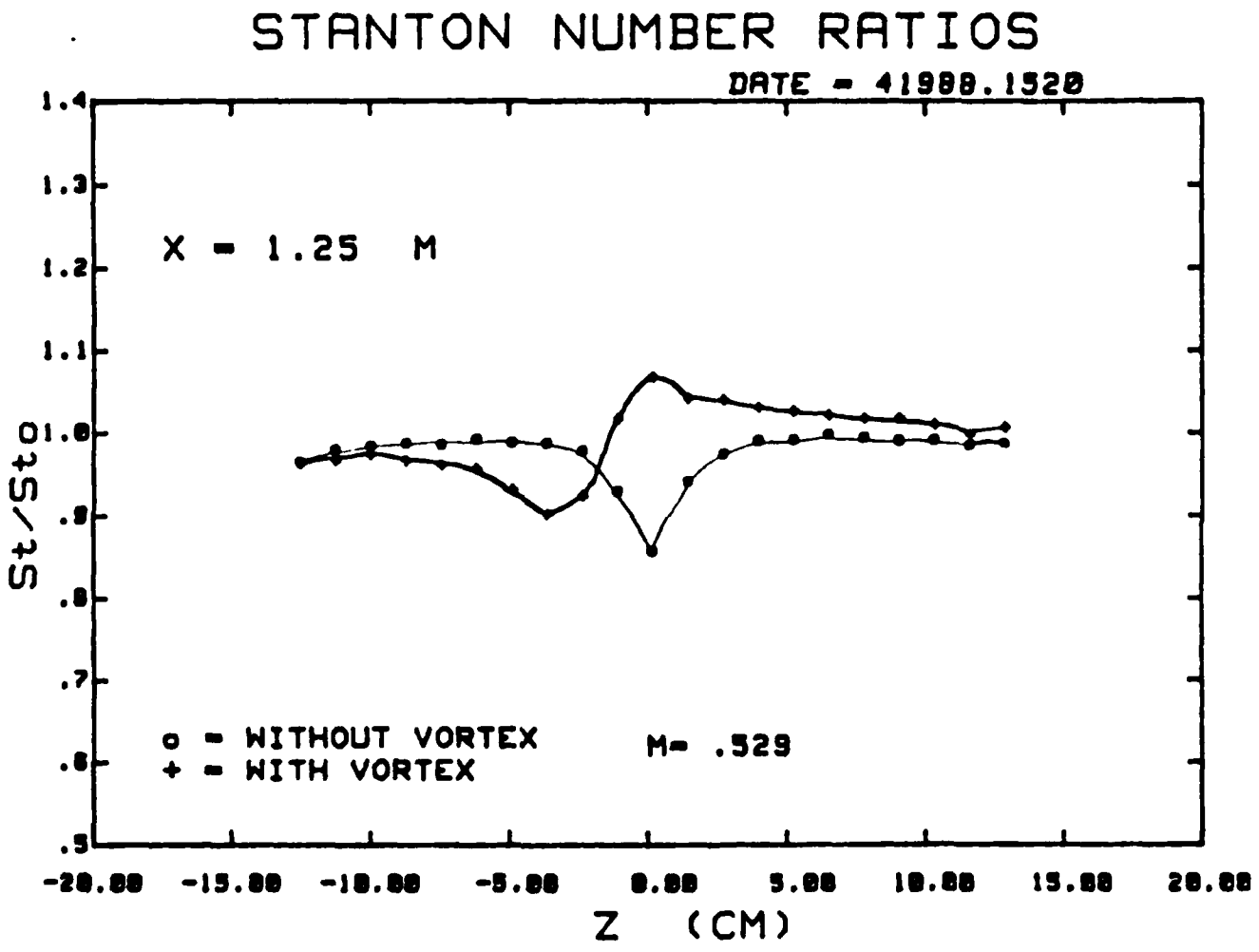

Figure 71. Spanwise Variation of Stanton Number Ratios Vortex #2 Position e

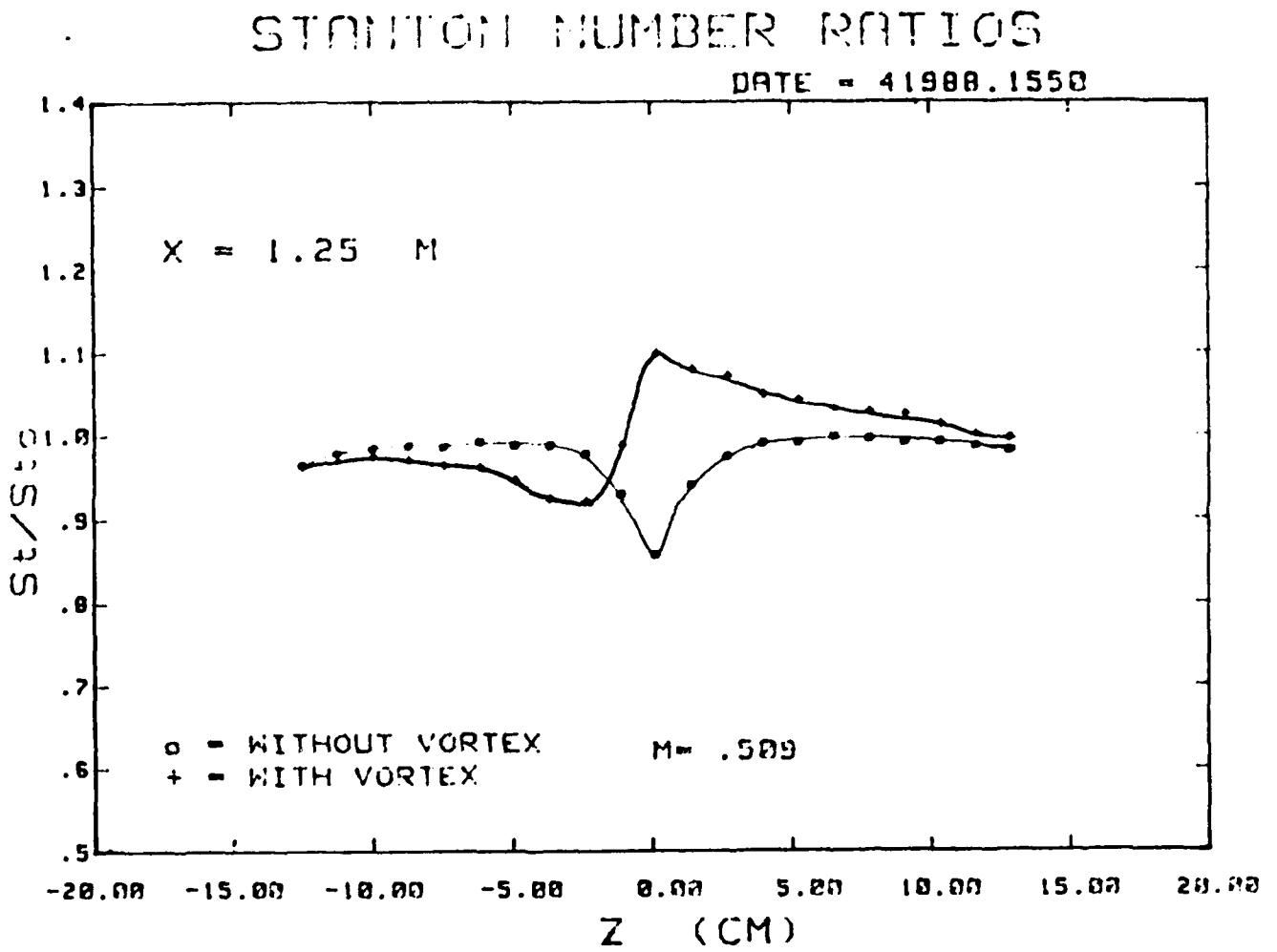

VG .5 INCHES FROM C/L, 10M/S, 3 INJECTION HOLES

Figure 72. Spanwise Variation of Stanton Number Ratios Vortex #2 Position f

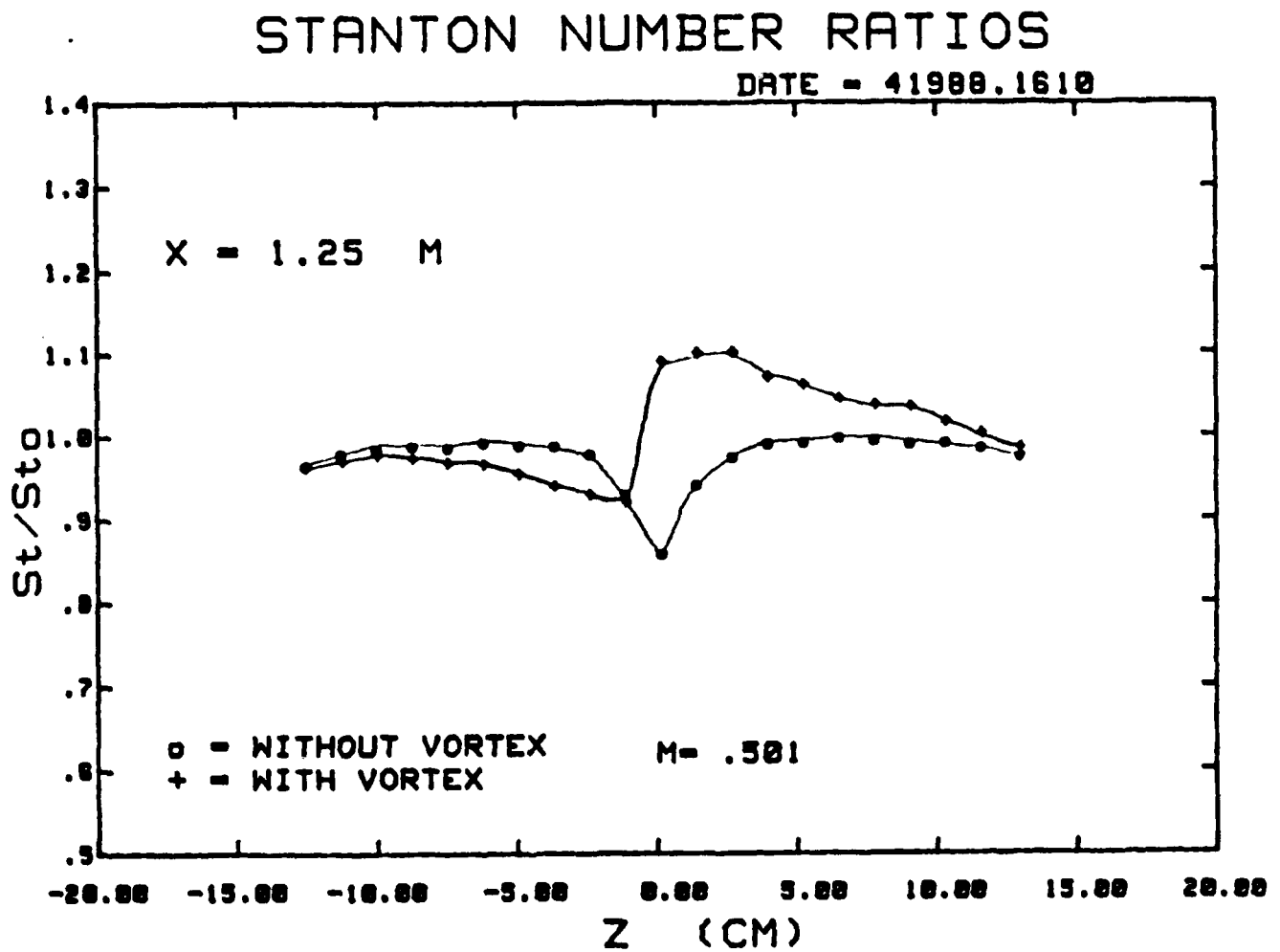

VG 1.0 INCHES FROM C/L, 10 M/S, 3 INJECTION HOLES

Figure 73. Spanwise Variation of Stanton Number Ratios Vortex #2 Position g

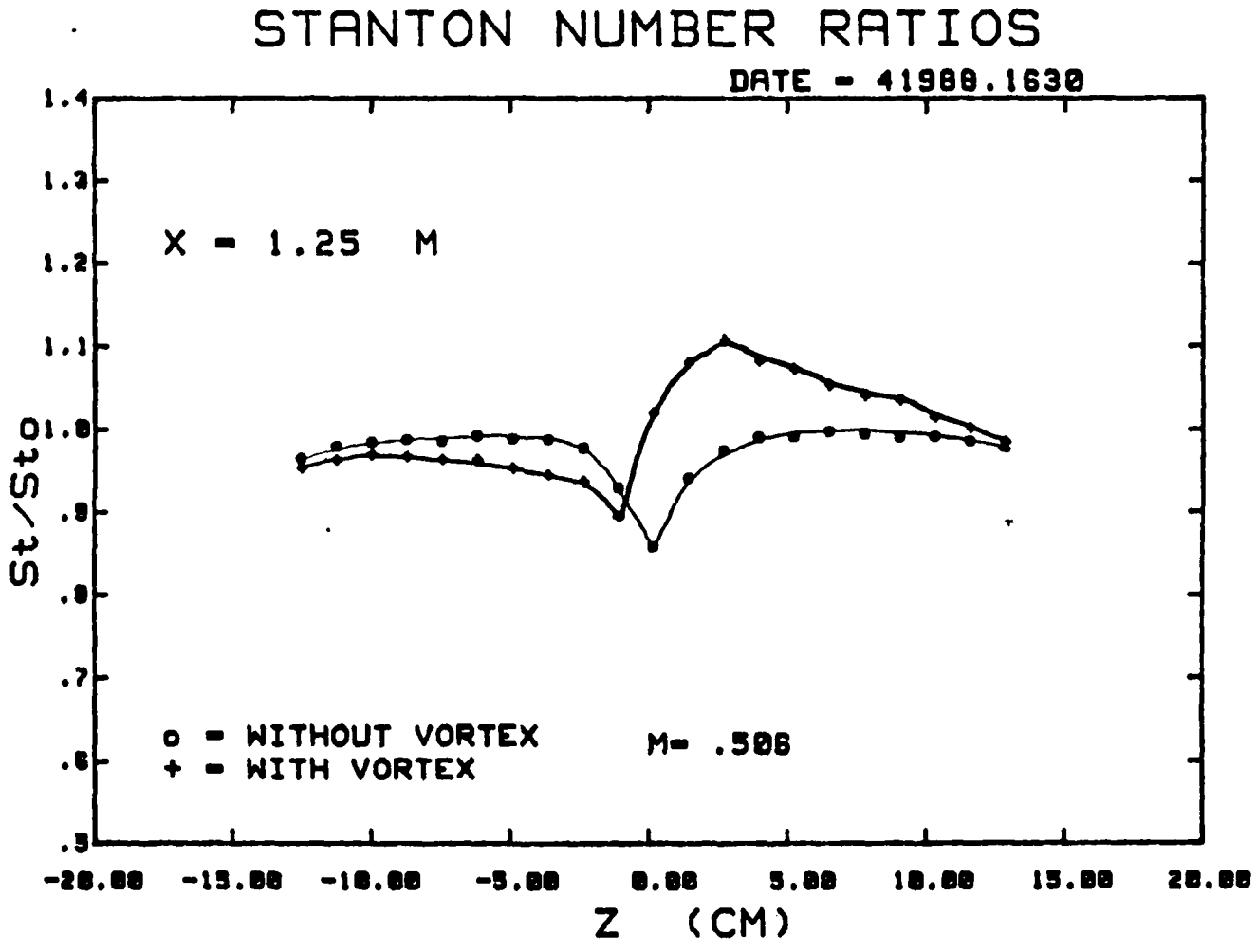

Figure 74. Spanwise Variation of Stanton Number Ratios Vortex #2 Position h

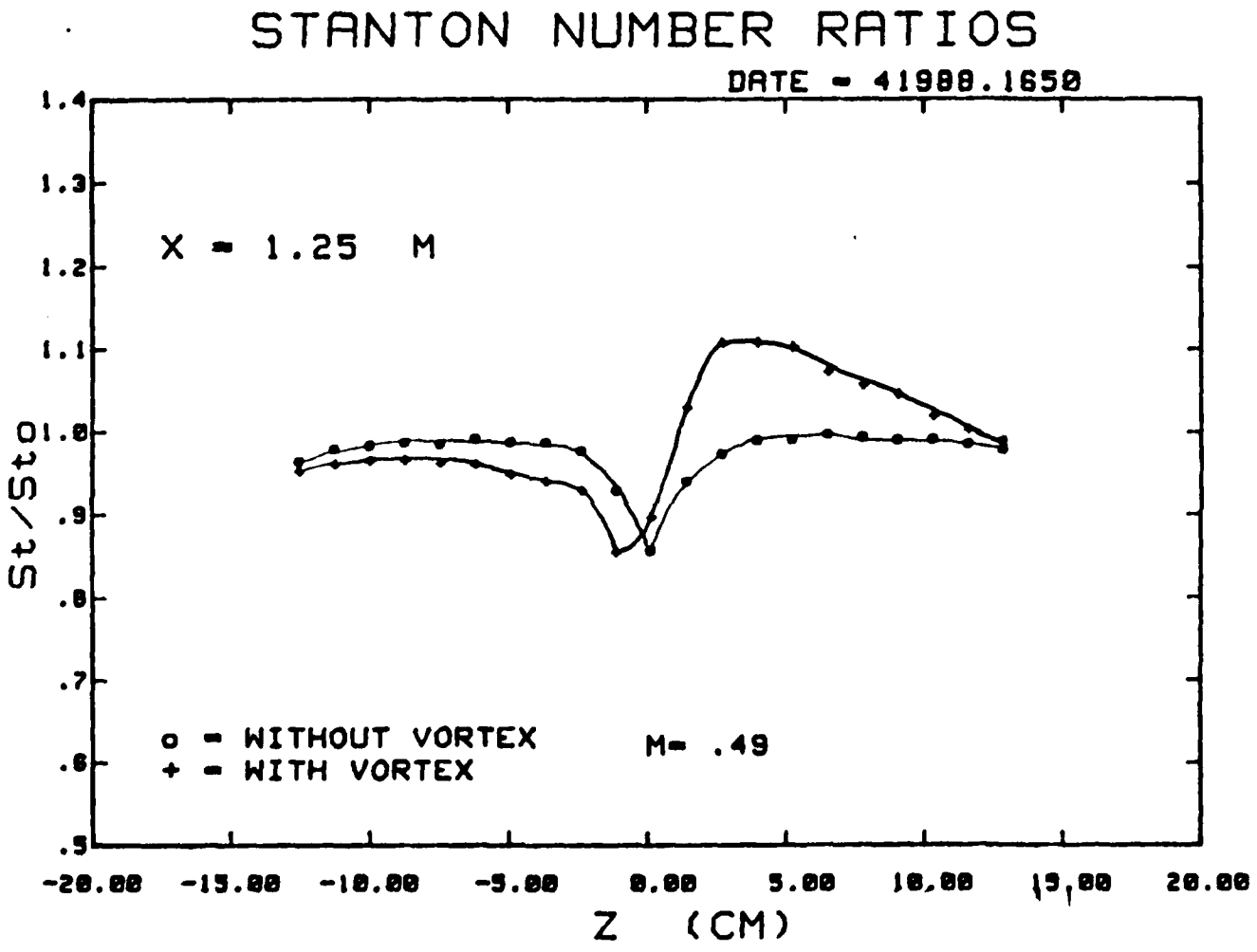

VG 2.0 INCHES FROM C/L, 10 M/S, 3 INJECTION HOLES

Figure 75. Spanwise Variation of Stanton Number Ratios Vortex #2 Position i

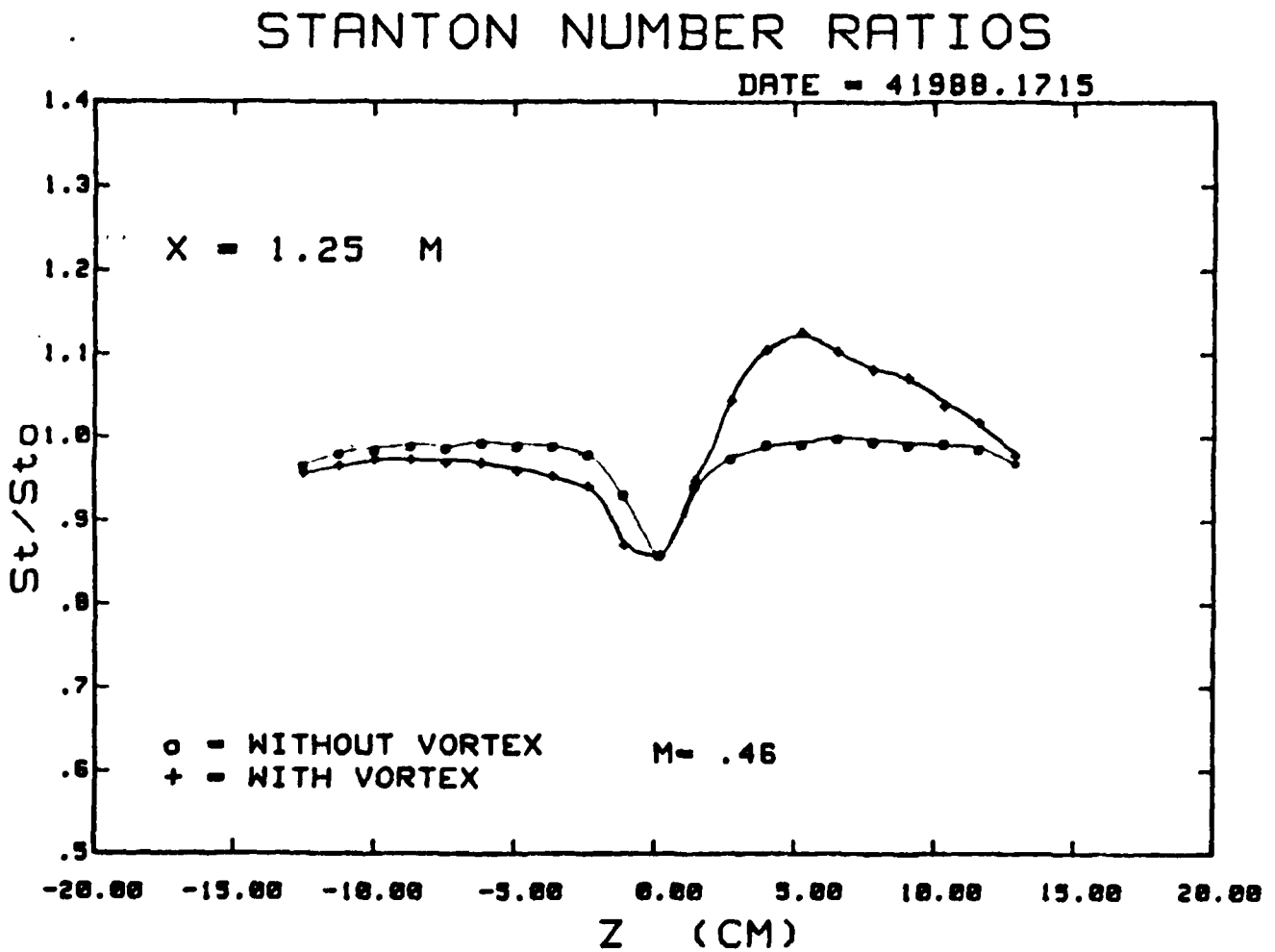

VG 2.5 INCHES FROM C/L, 10 C/L, 3 INJECTION HOLES

Figure 76. Spanwise Variation of Stanton Number Ratios Vortex #2 Position j

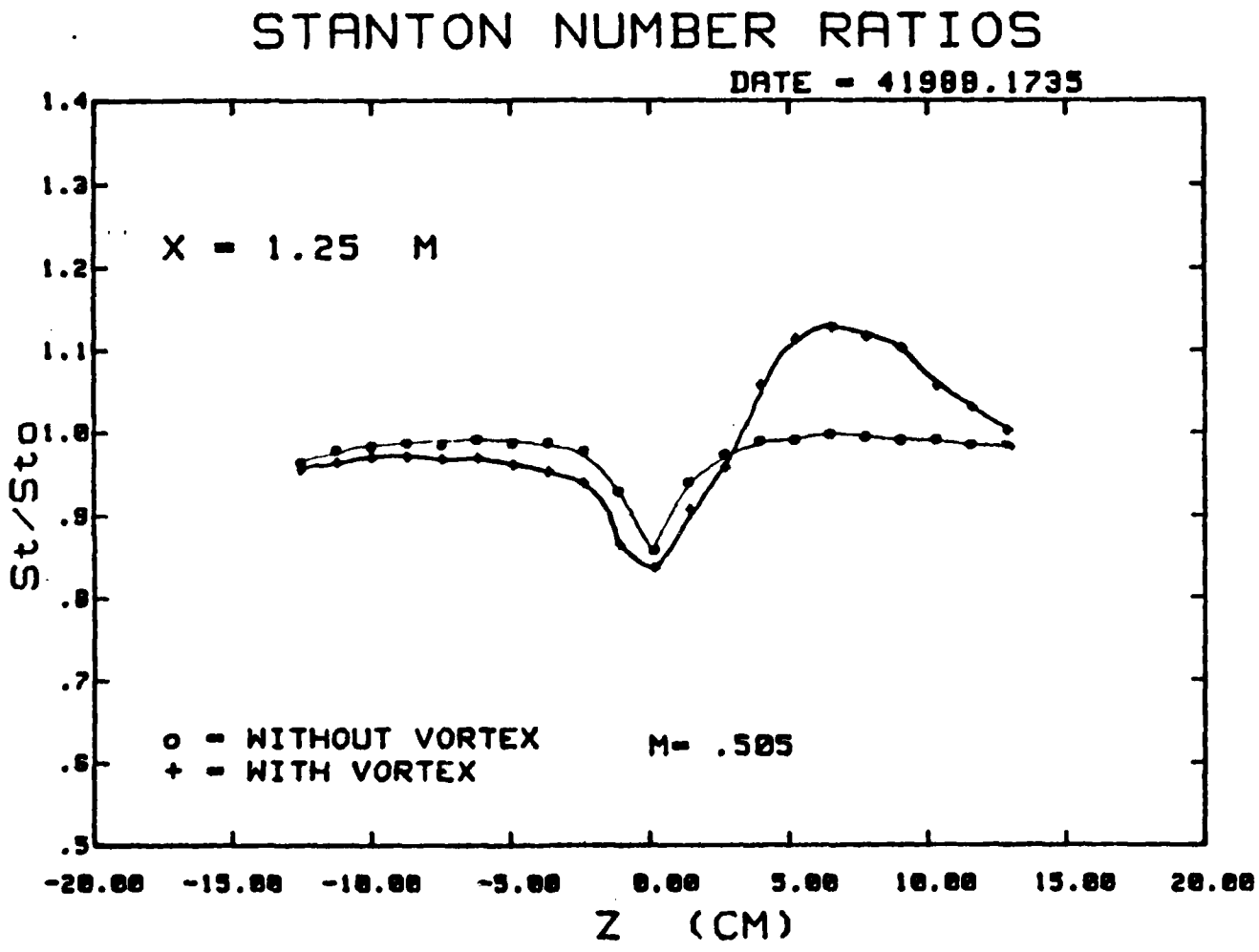

Figure 77. Spanwise Variation of Stanton Number Ratios Vortex #2 Position k

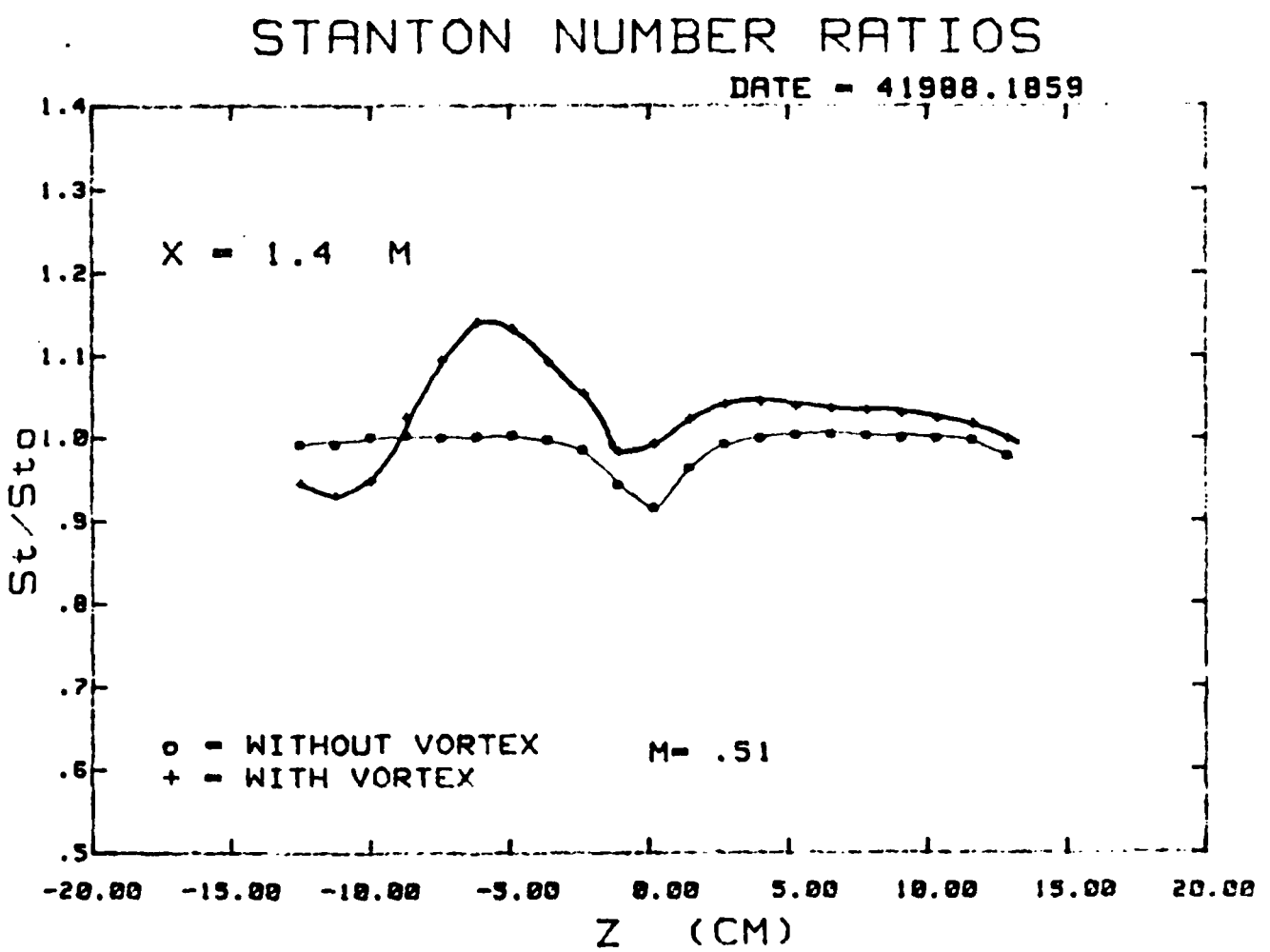

Figure 78. Spanwise Variation of Stanton Number Ratios Vortex #2 Position a

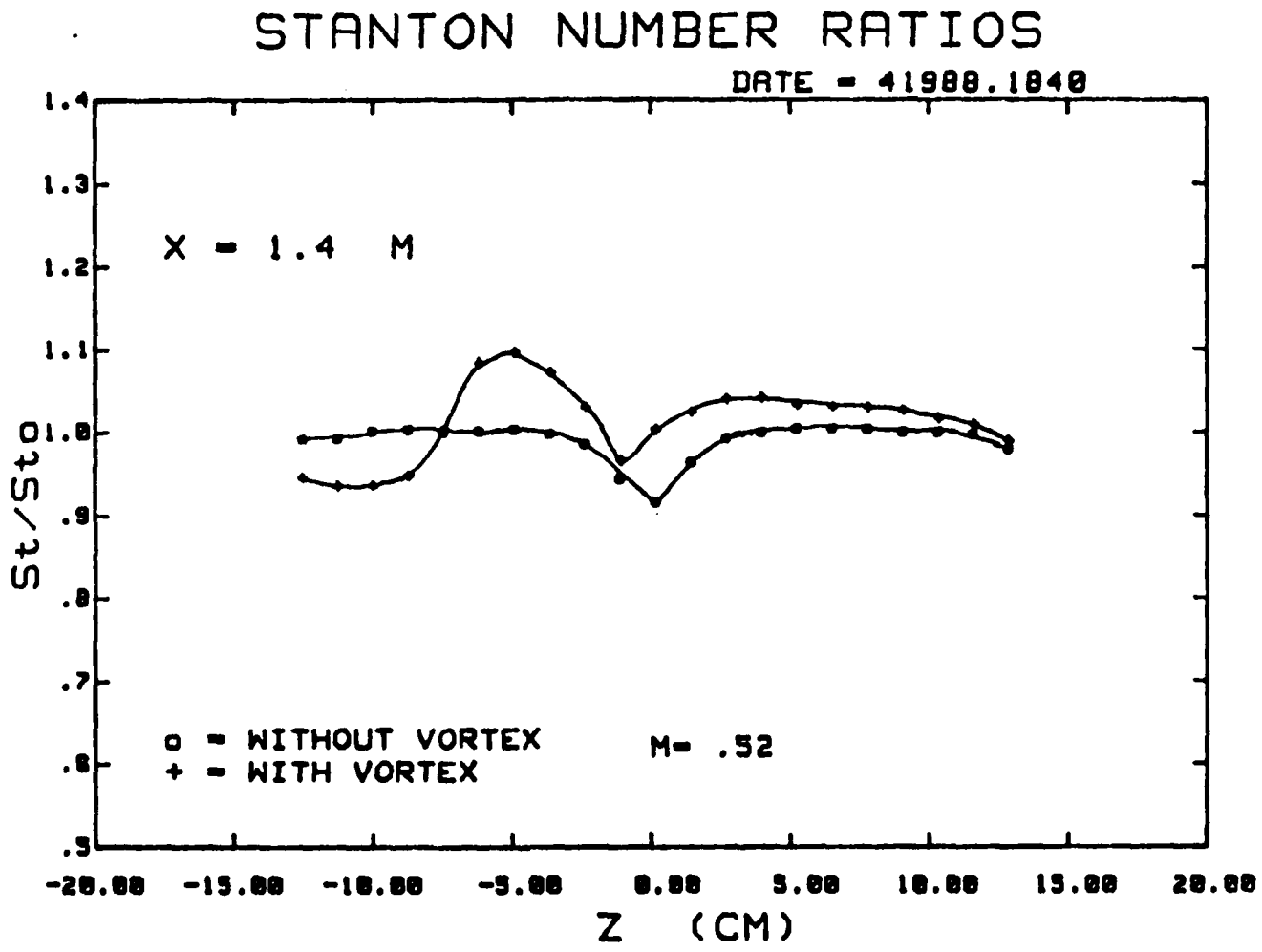

VG -1.5 INCHES FROM C/L, 10 M/S, 3 INJECTION HOLES

Figure 79. Spanwise Variation of Stanton Number Ratios Vortex #2 Position b

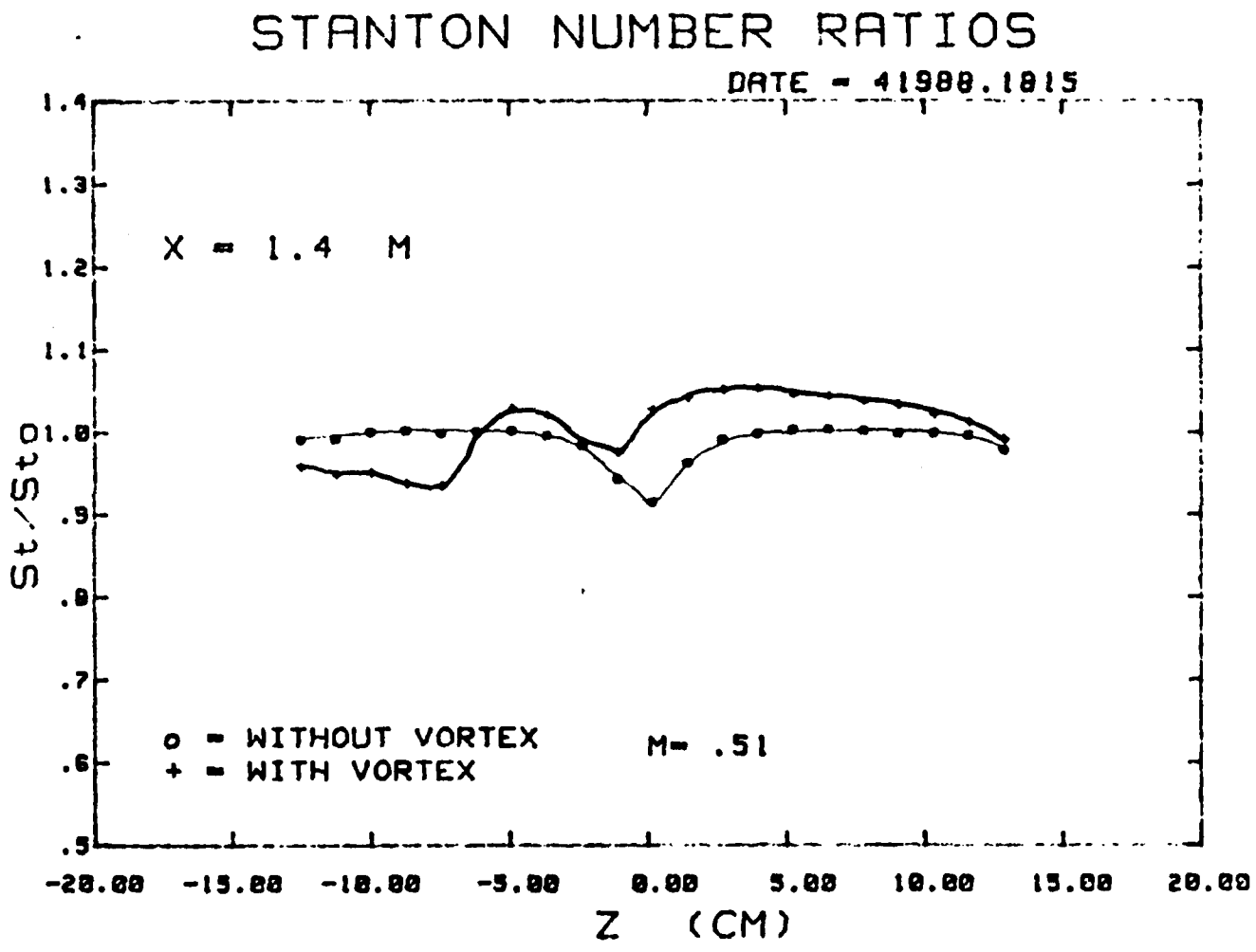

VG -1.0 INCHES FROM C/L, 10 M/S, 3 INJECTION HOLES

Figure 80. Spanwise Variation of Stanton Number Ratios Vortex #2 Position c

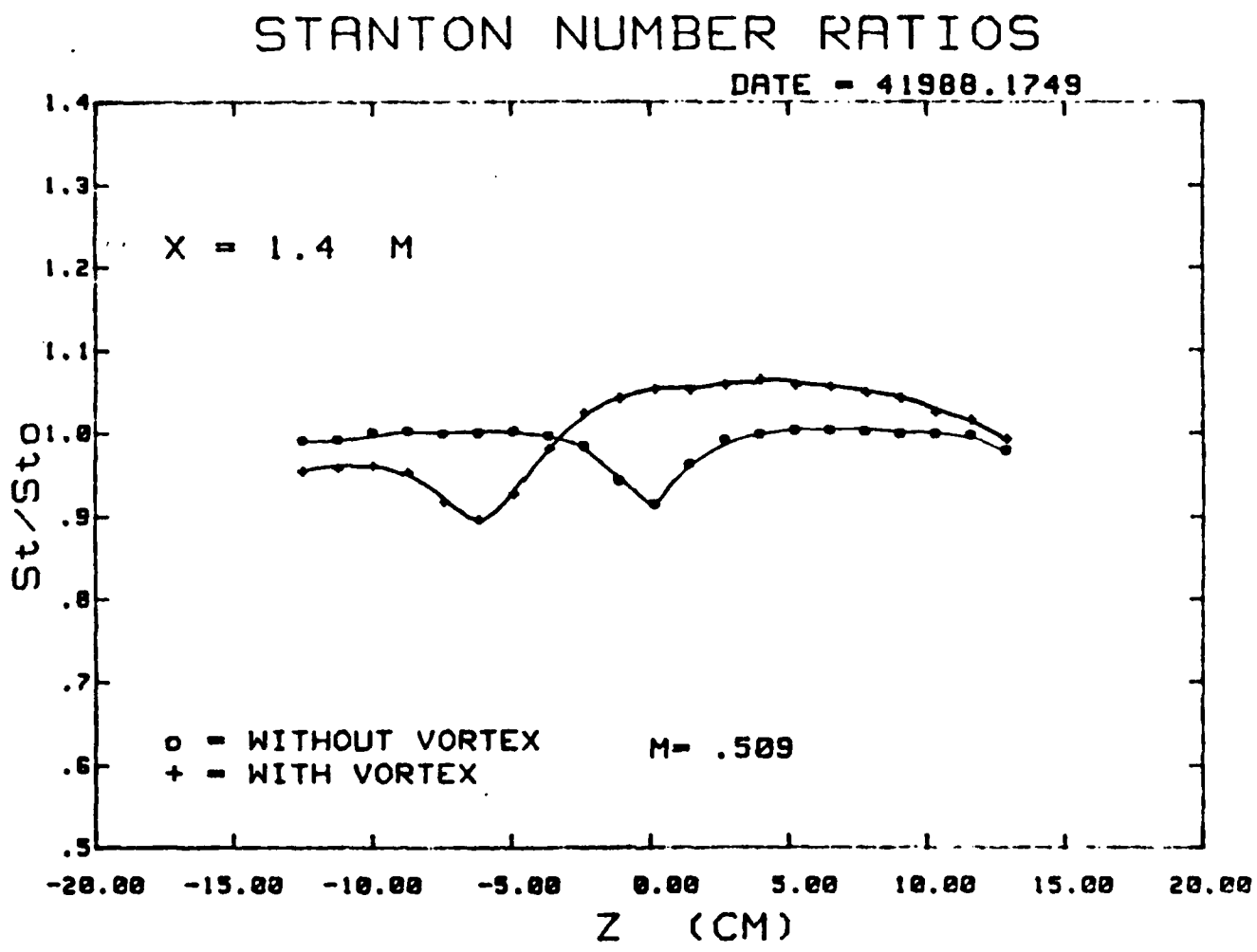

VG -0.5 INCHES FROM C/L, 10 M/S, 3 INJECTION HOLES

Figure 81. Spanwise Variation of Stanton Number Ratios Vortex #2 Position d

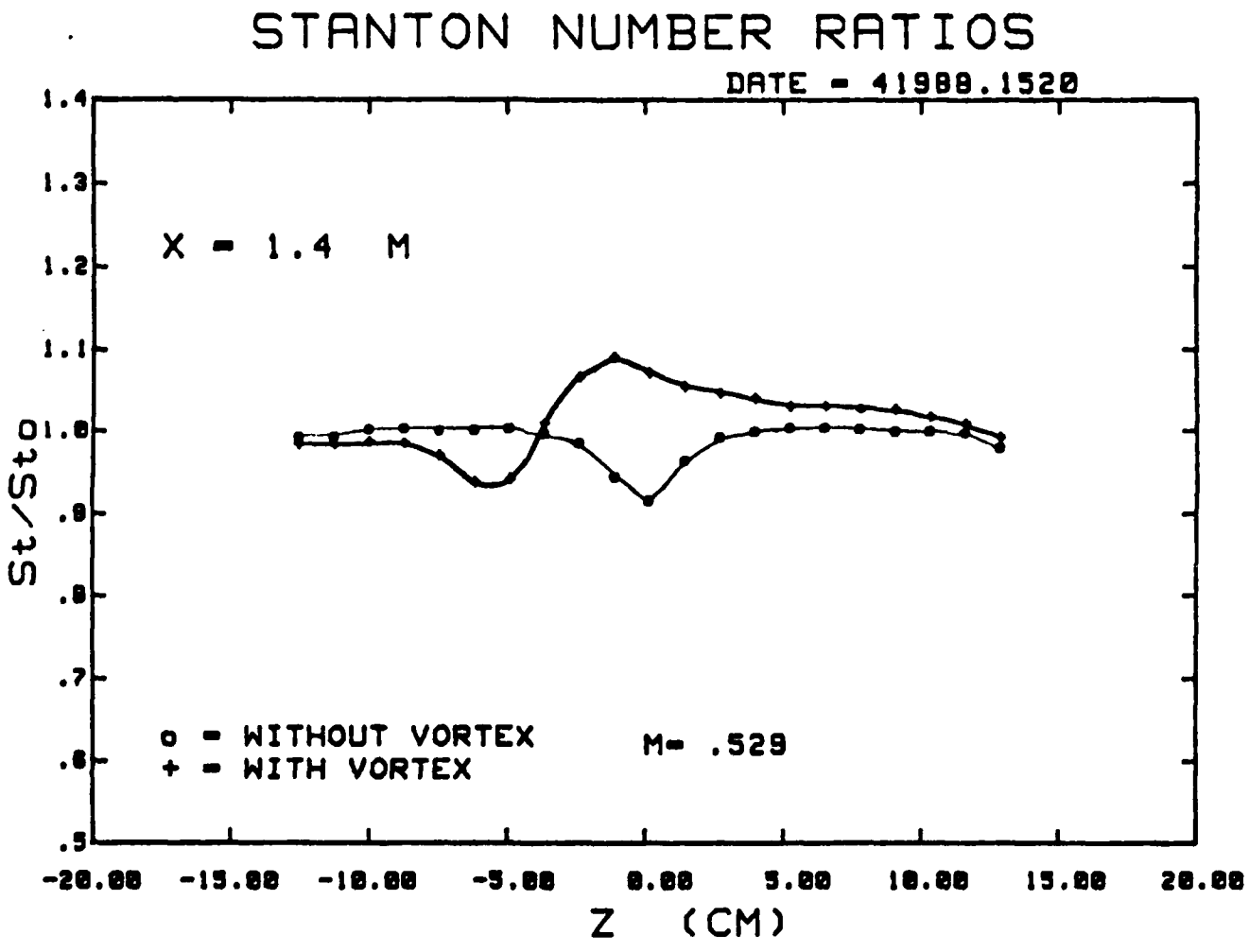

Figure 82. Spanwise Variation of Stanton Number Ratios Vortex #2 Position e

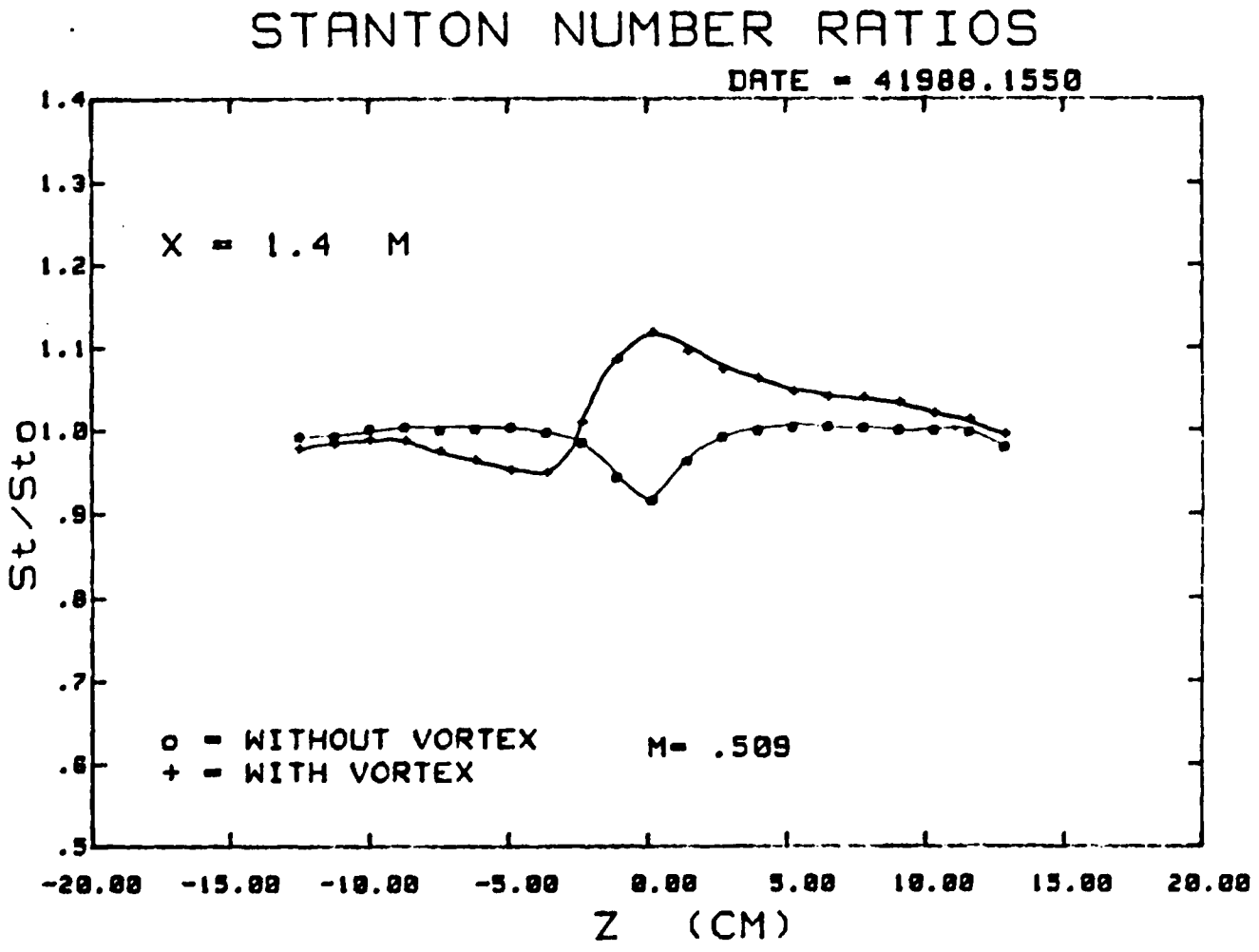

VG 0.5 INCHES FROM C/L, 10 M/S, 3 INJECTION HOLES

Figure 83. Spanwise Variation of Stanton Number Ratios Vortex #2 Position f

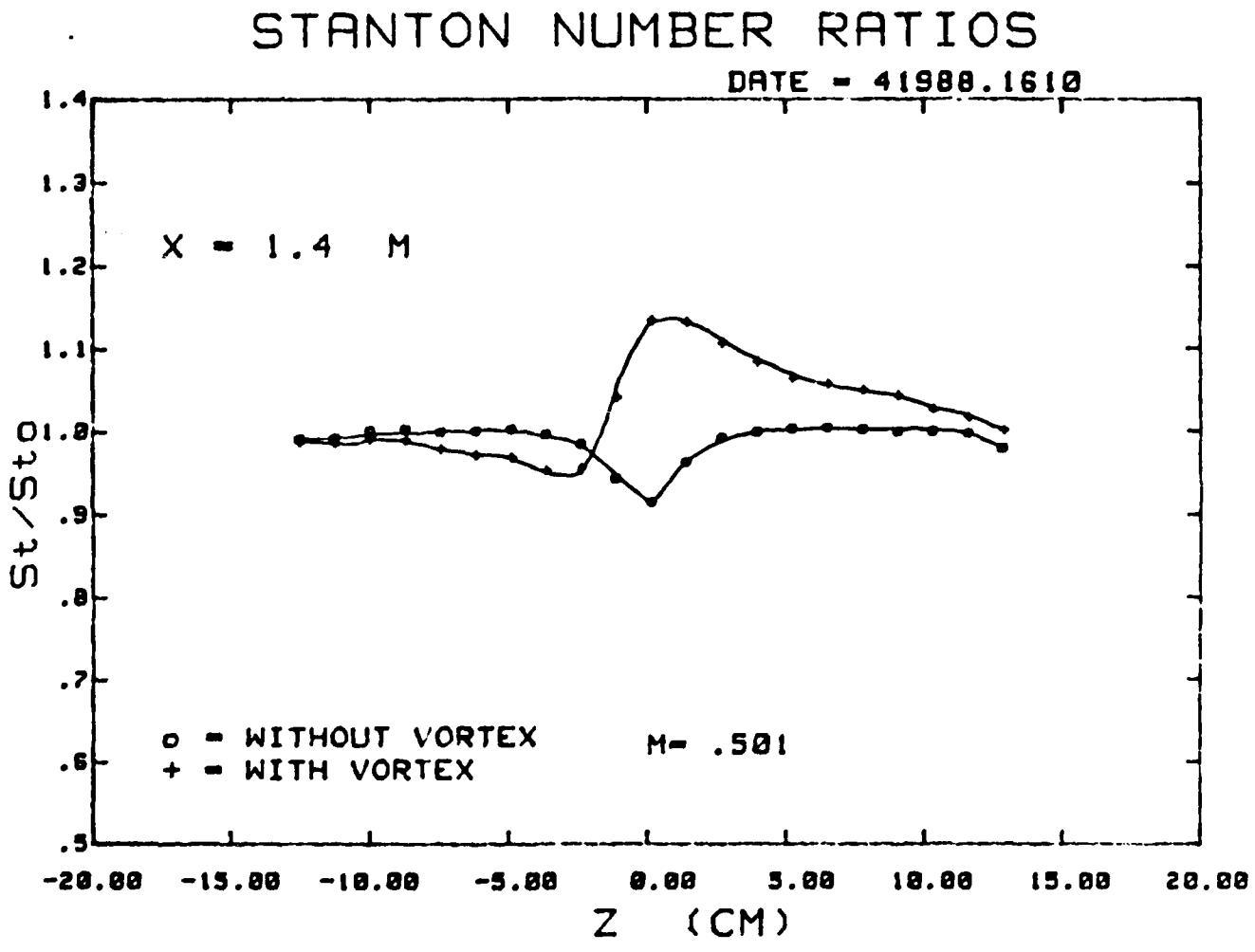

VG 1.0 INCHES FROM C/L, 10 M/S, 3 INJECTION HOLES

Figure 84. Spanwise Variation of Stanton Number Ratios Vortex #2 Position g

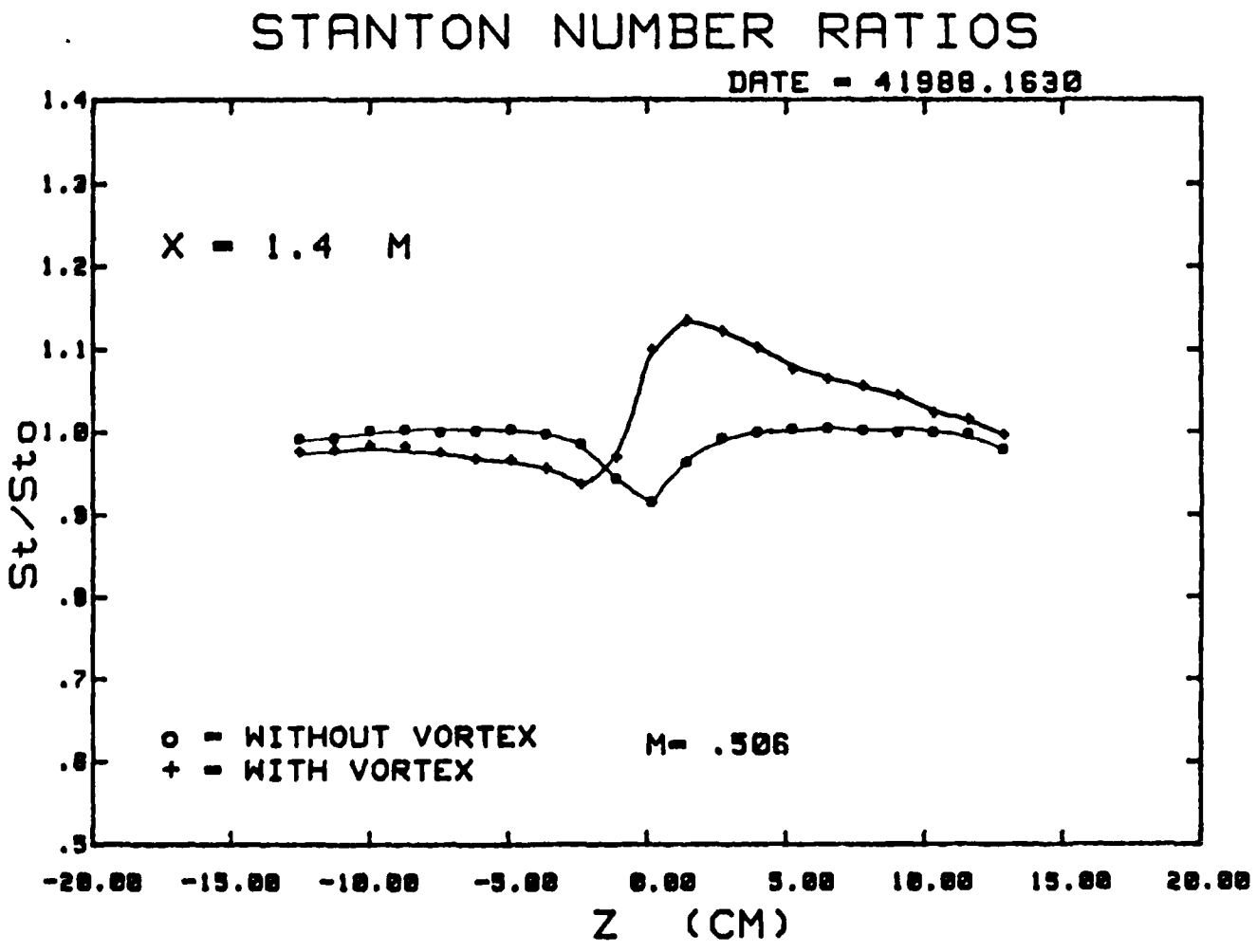

VG 1.5 INCHES FROM C/L, 10 M/S, 3 INJCTION HOLES

Figure 85. Spanwise Variation of Stanton Number Ratios Vortex #2 Position h

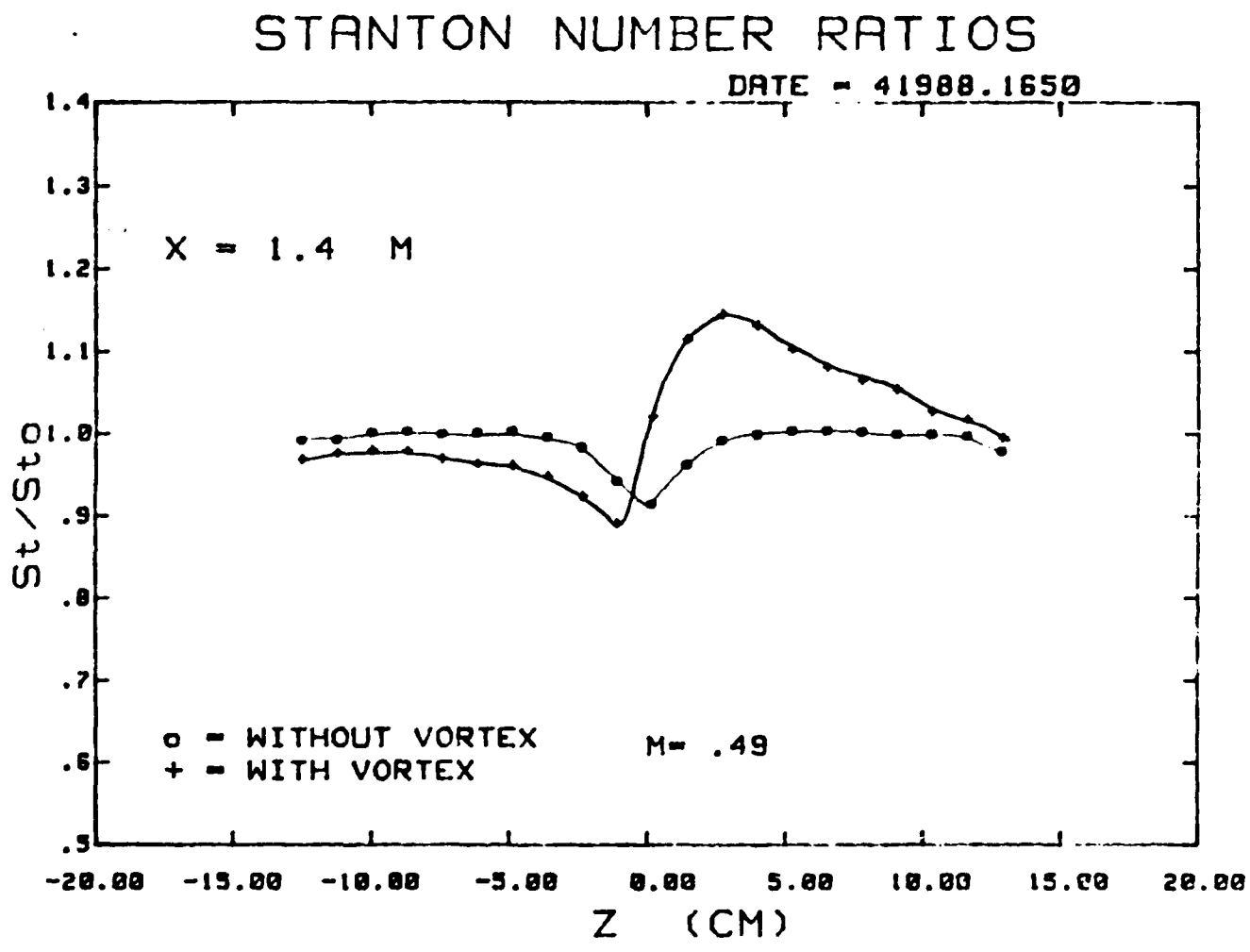

VG 2.0 INCHES FROM C/L, 10 M/S, 3 INJECTION HOLES

Figure 86. Spanwise Variation of Stanton Number Ratios Vortex #2 Position i

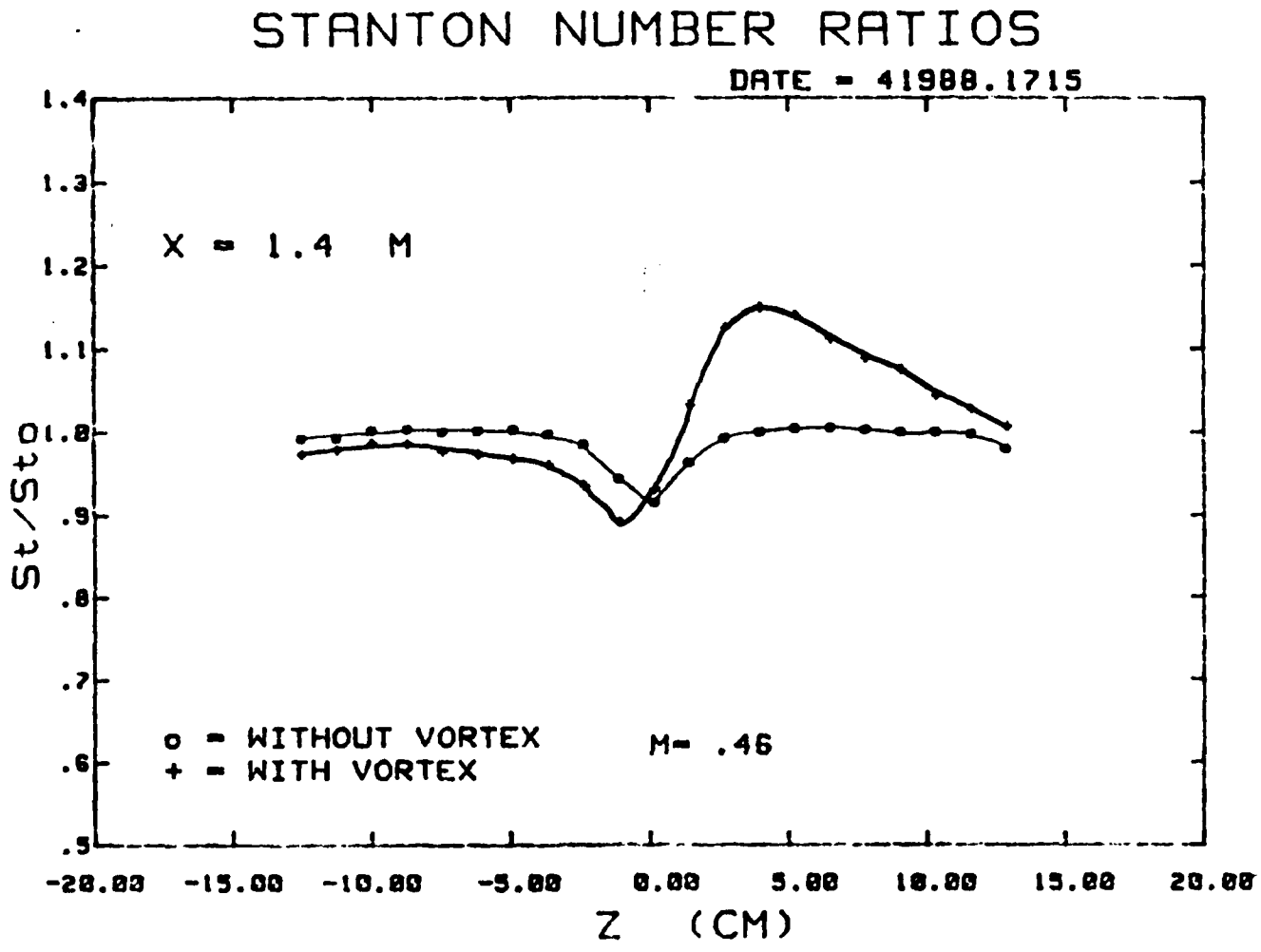

VG 2.5 INCHES FROM C/L, 10 M/S, 3 INJECTION HOLES

Figure 87. Spanwise Variation of Stanton Number Ratios Vortex #2 Position j

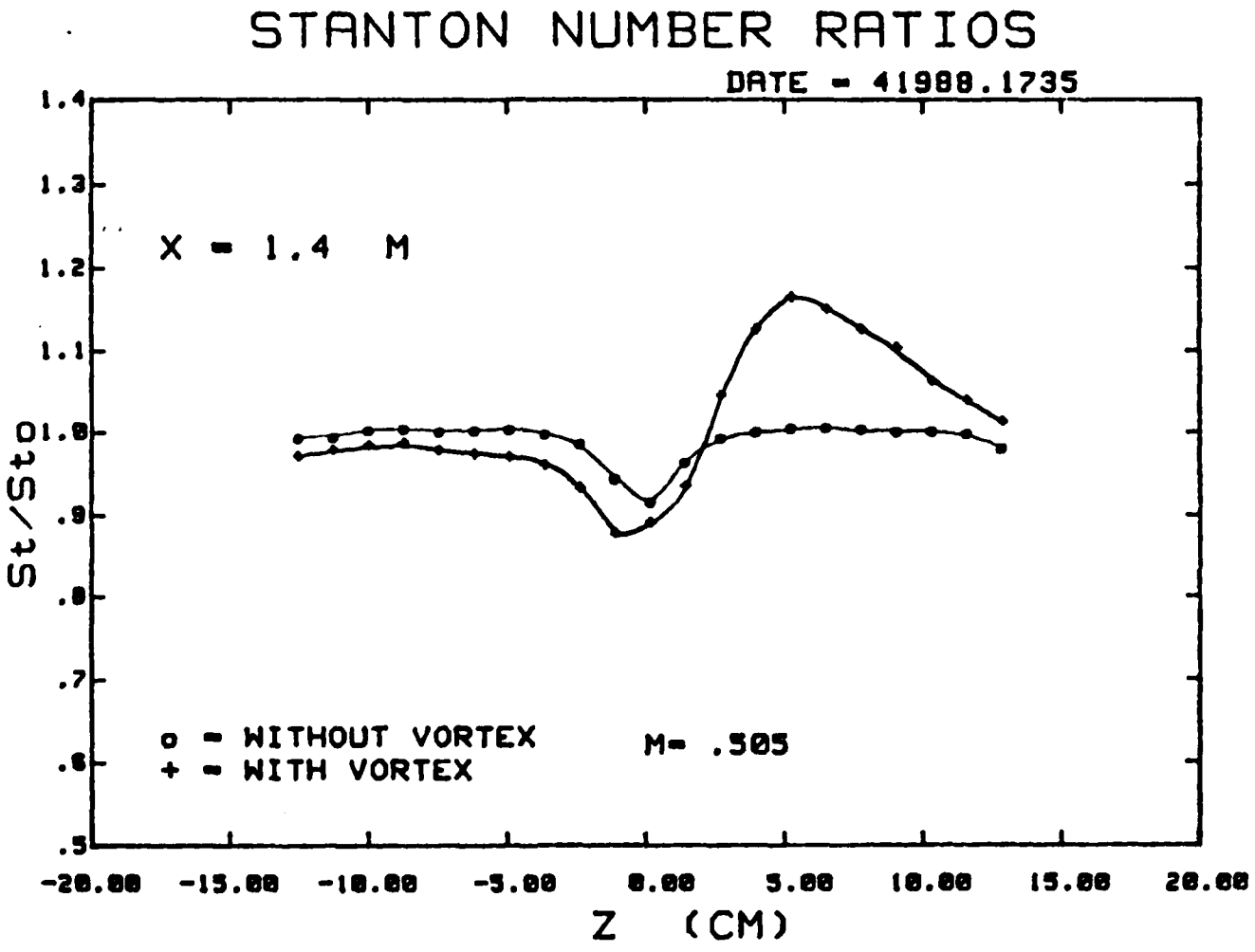

VG 3.0 INCHES FROM C/L, 10 M/S, 3 INJECTION HOLES

Figure 88. Spanwise Variation of Stanton Number Ratios Vortex #2 Position k

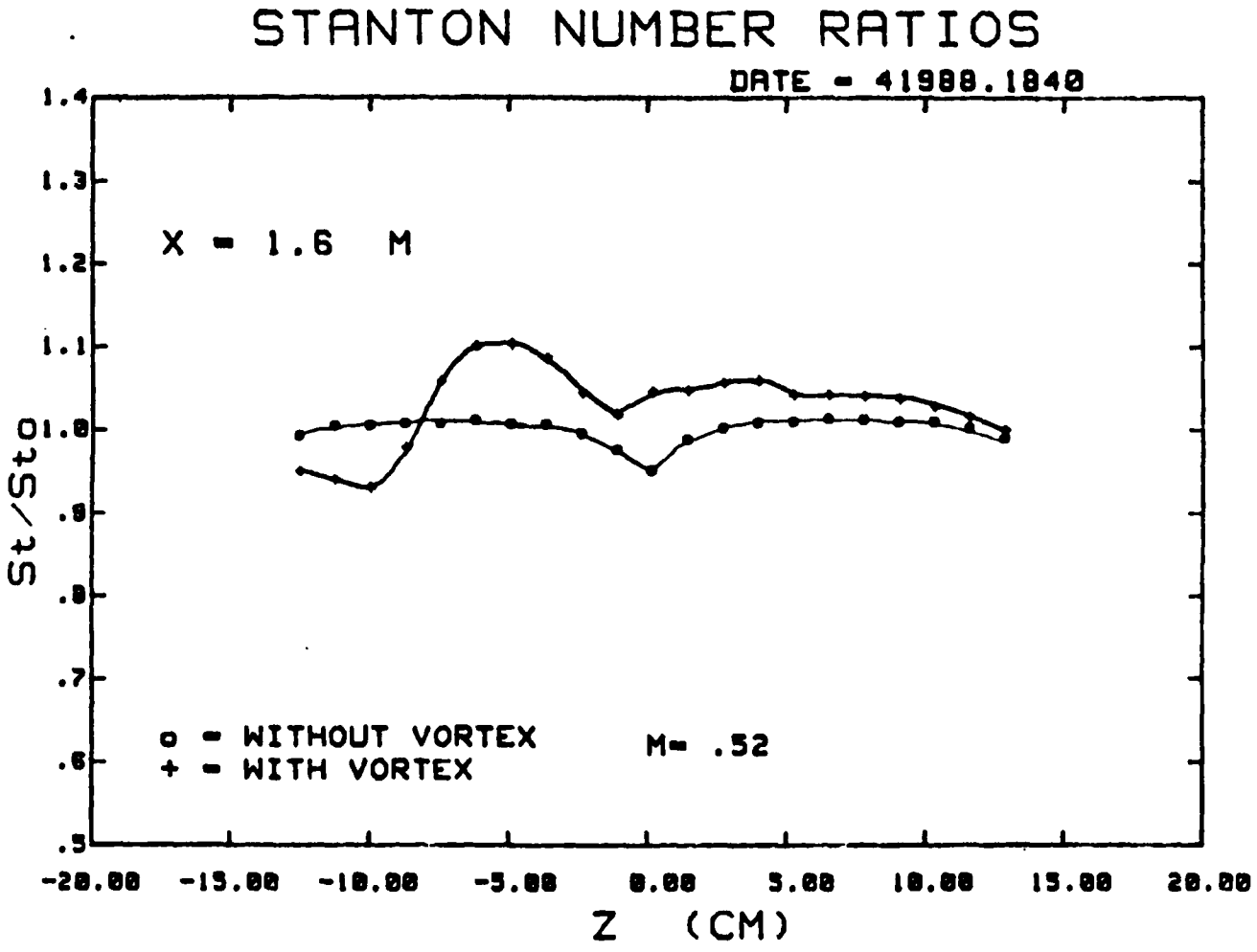

VG -1.5 INCHES FROM C/L, 10 M/S, 3 INJECTION HOLES

Figure 89. Spanwise Variation of Stanton Number Ratios Vortex #2 Position b

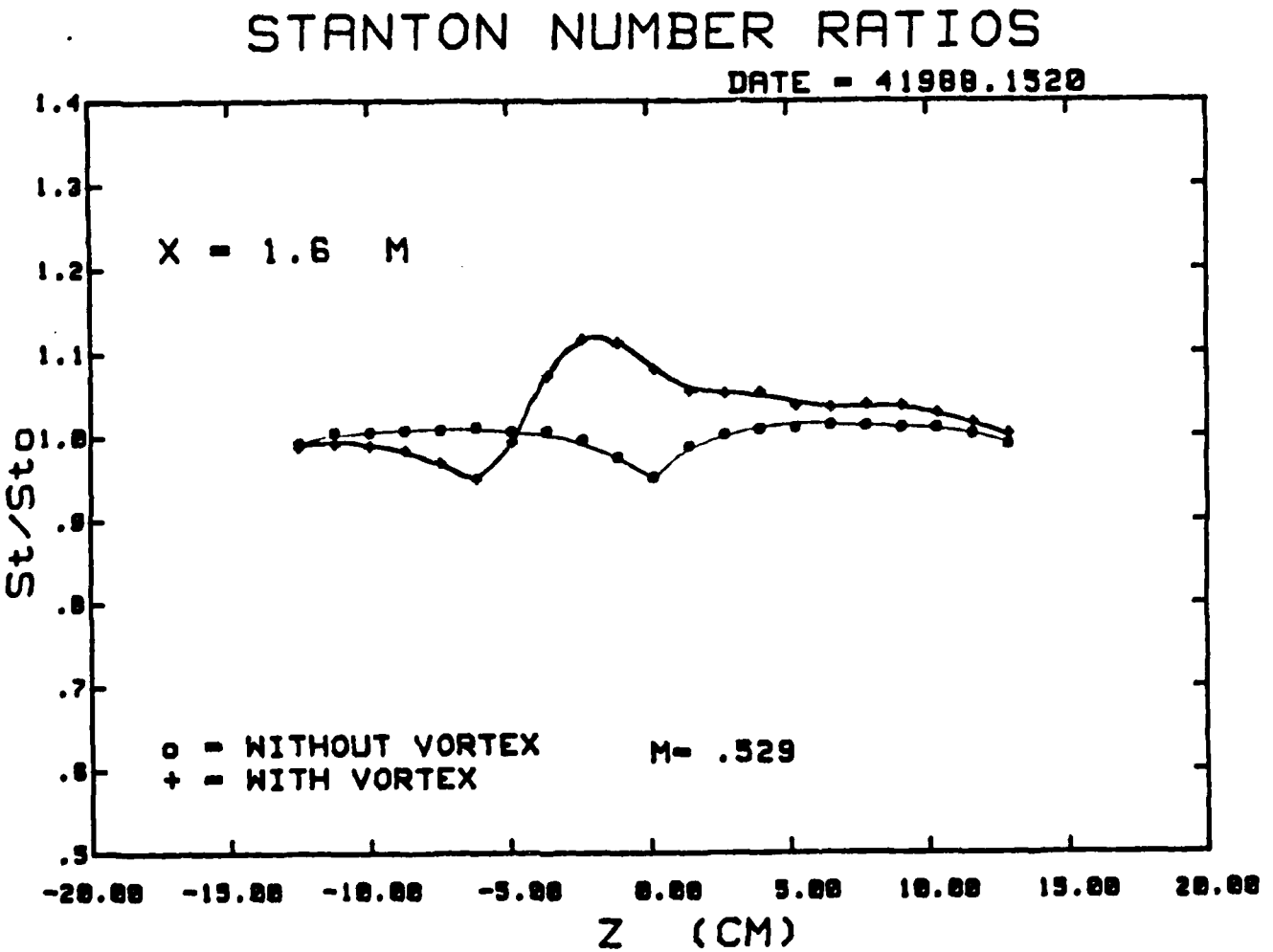

Figure 90. Spanwise Variation of Stanton Number Ratios Vortex #2 Position e

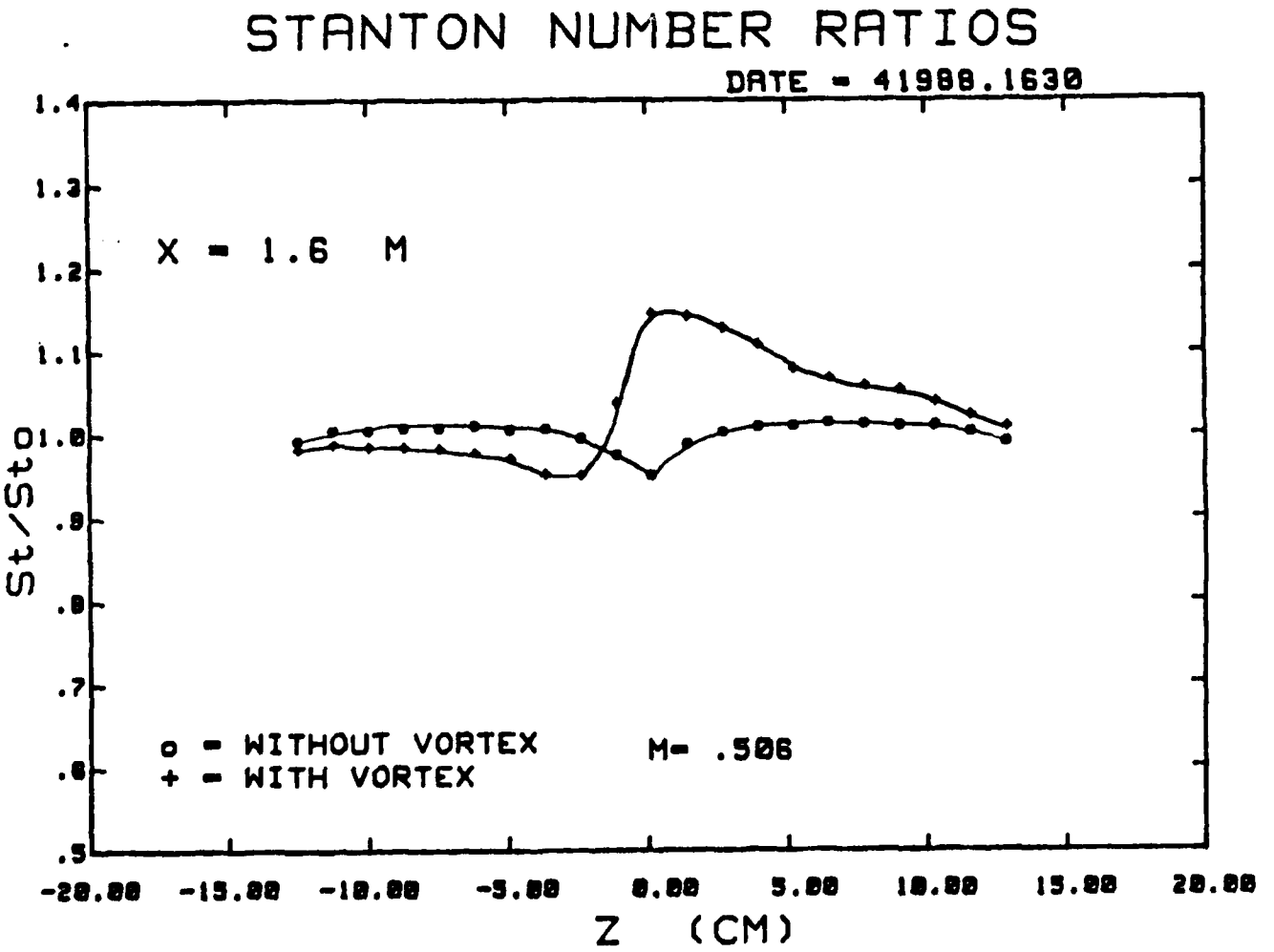

VG 1.5 INCHES FROM C/L, 10 M/S, 3 INJECTION HOLES

Figure 91. Spanwise Variation of Stanton Number Ratios Vortex #2 Position h

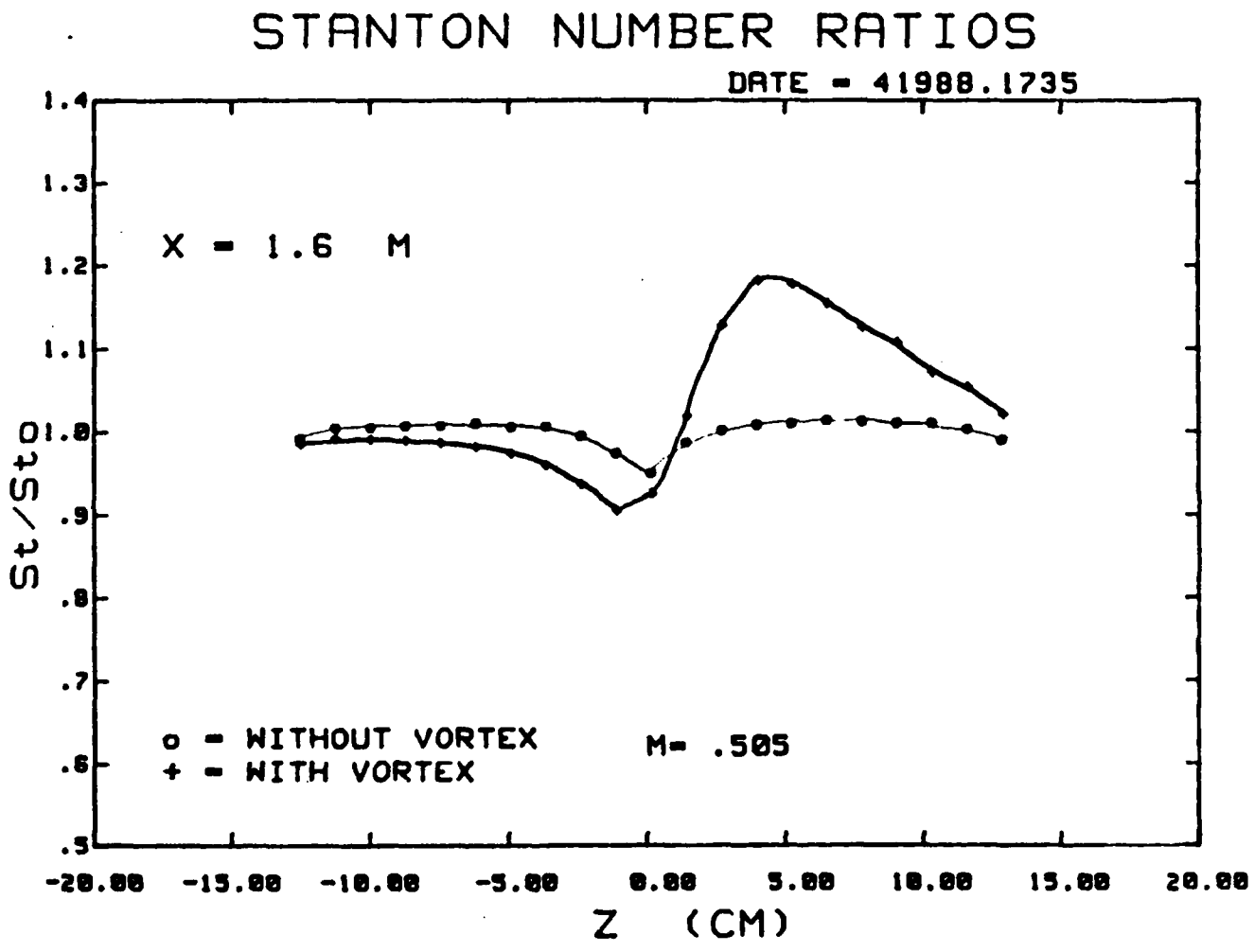

VG 3.0 INCHES FROM C/L, 10 M/S, 3 INJECTION HOLES

Figure 92. Spanwise Variation of Stanton Number Ratios Vortex #2 Position k

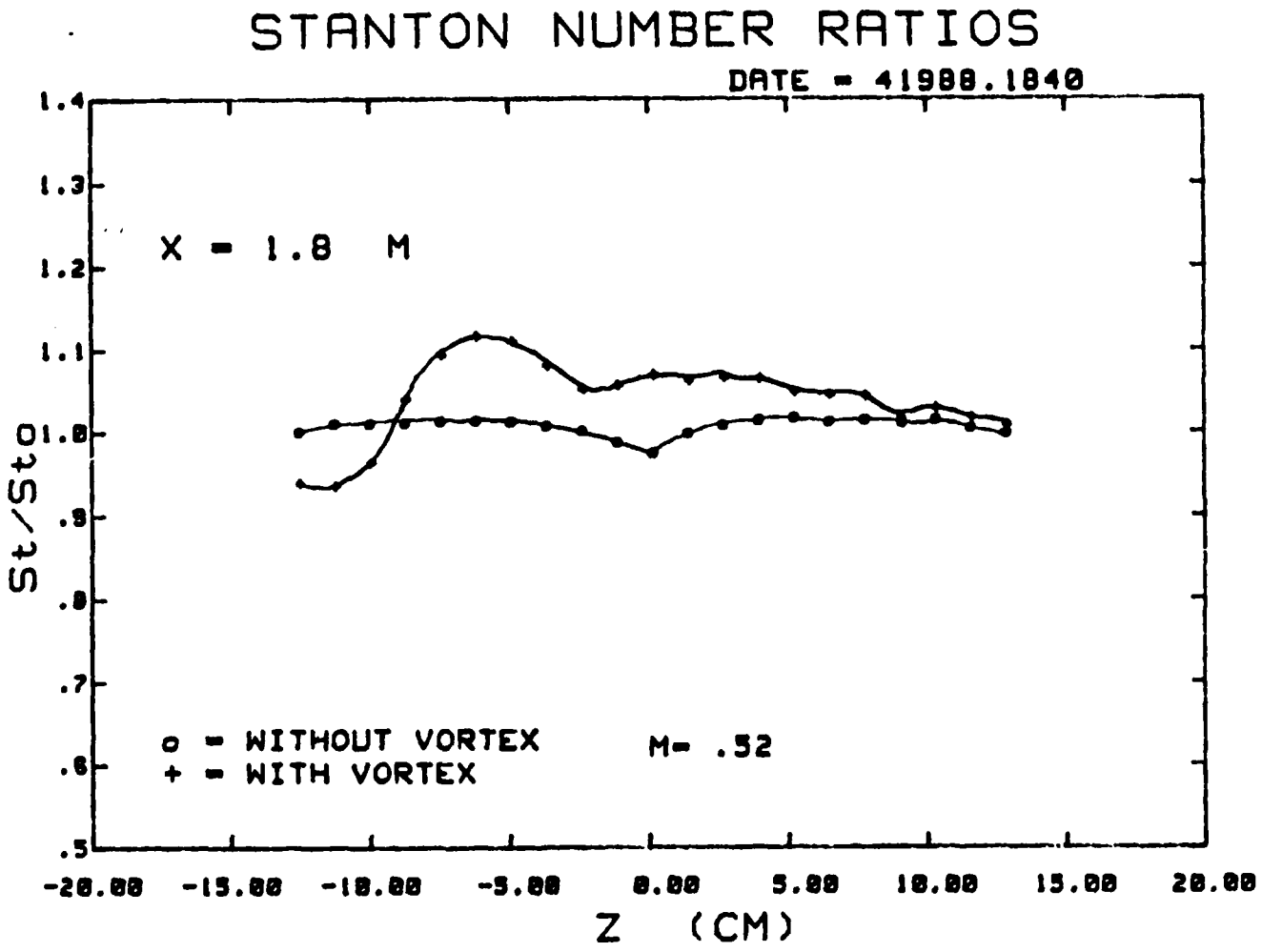

VG -1.5 INCHES FROM C/L, 10 M/S, 3 INJECTION HOLES

Figure 93. Spanwise Variation of Stanton Number Ratios
Vortex #2 Position b

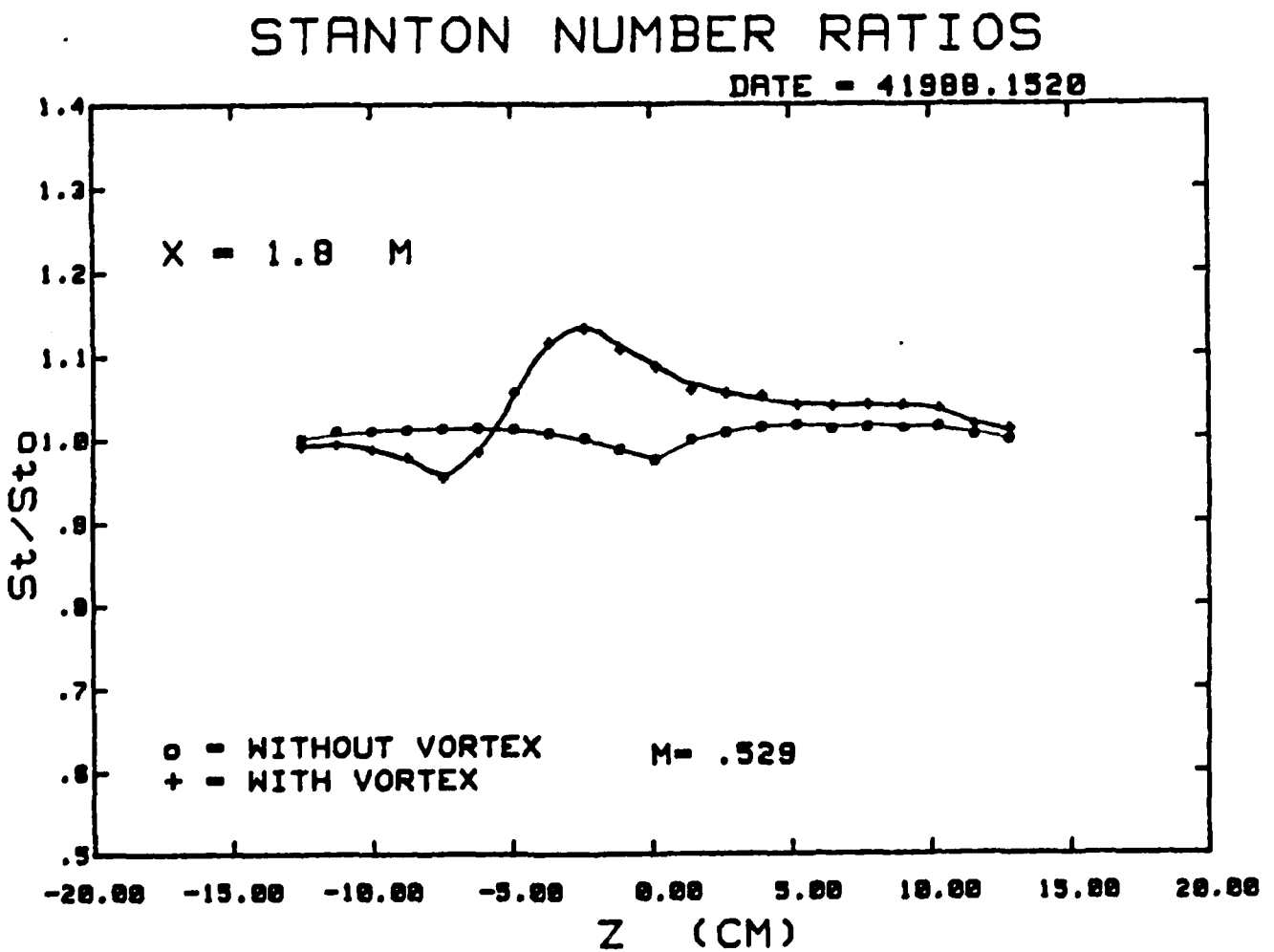

0 IN FROM THE C/L, 10 M/S , 3 INJECTION HOLES

Figure 94. Spanwise Variation of Stanton Number Ratios Vortex #2 Position e

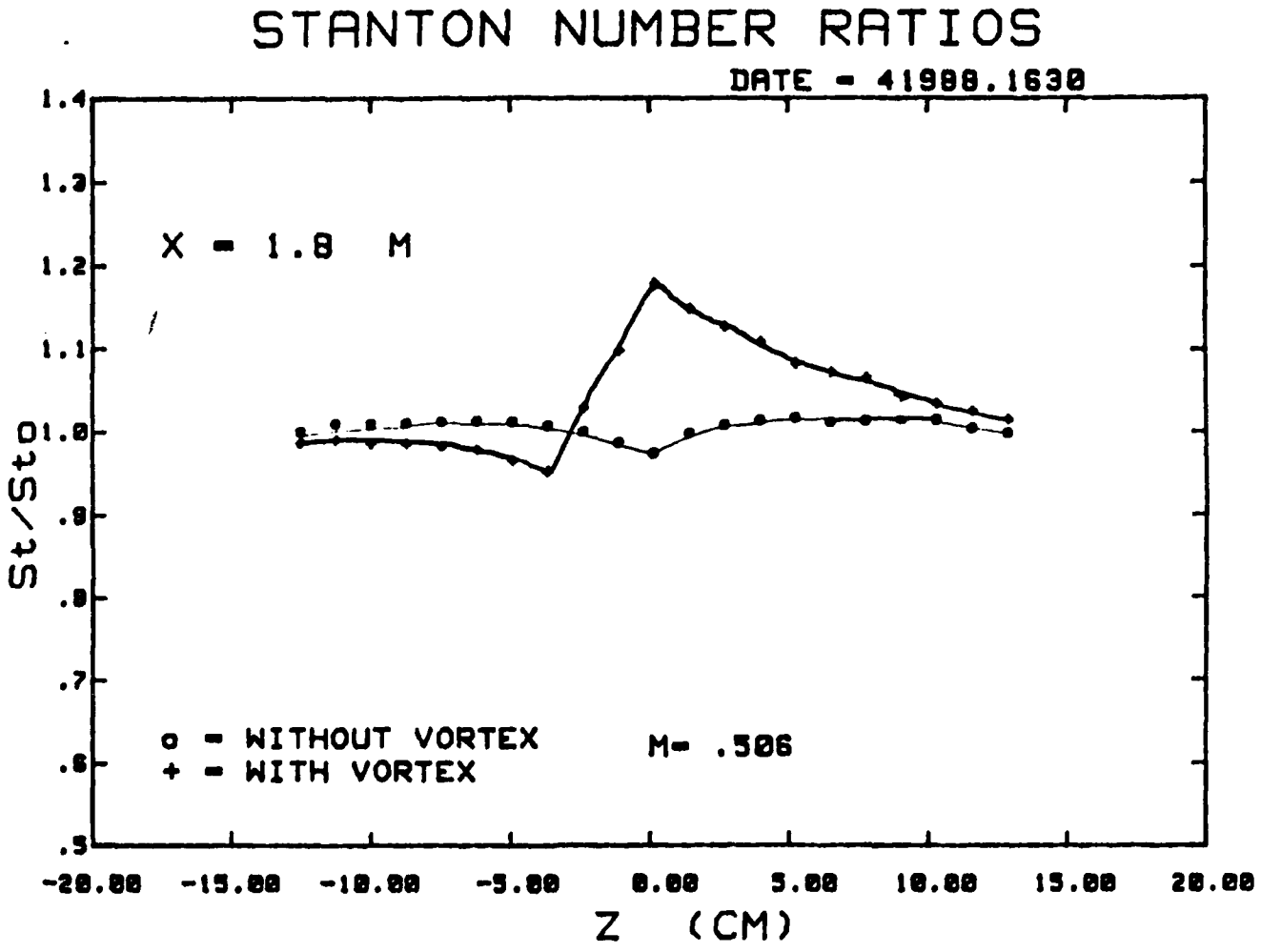

VG 1.5 INCHES FROM C/L, 10 M/S, 3 INJECTION HOLES

Figure 95. Spanwise Variation of Stanton Number Ratios-Vortex #2 Position h

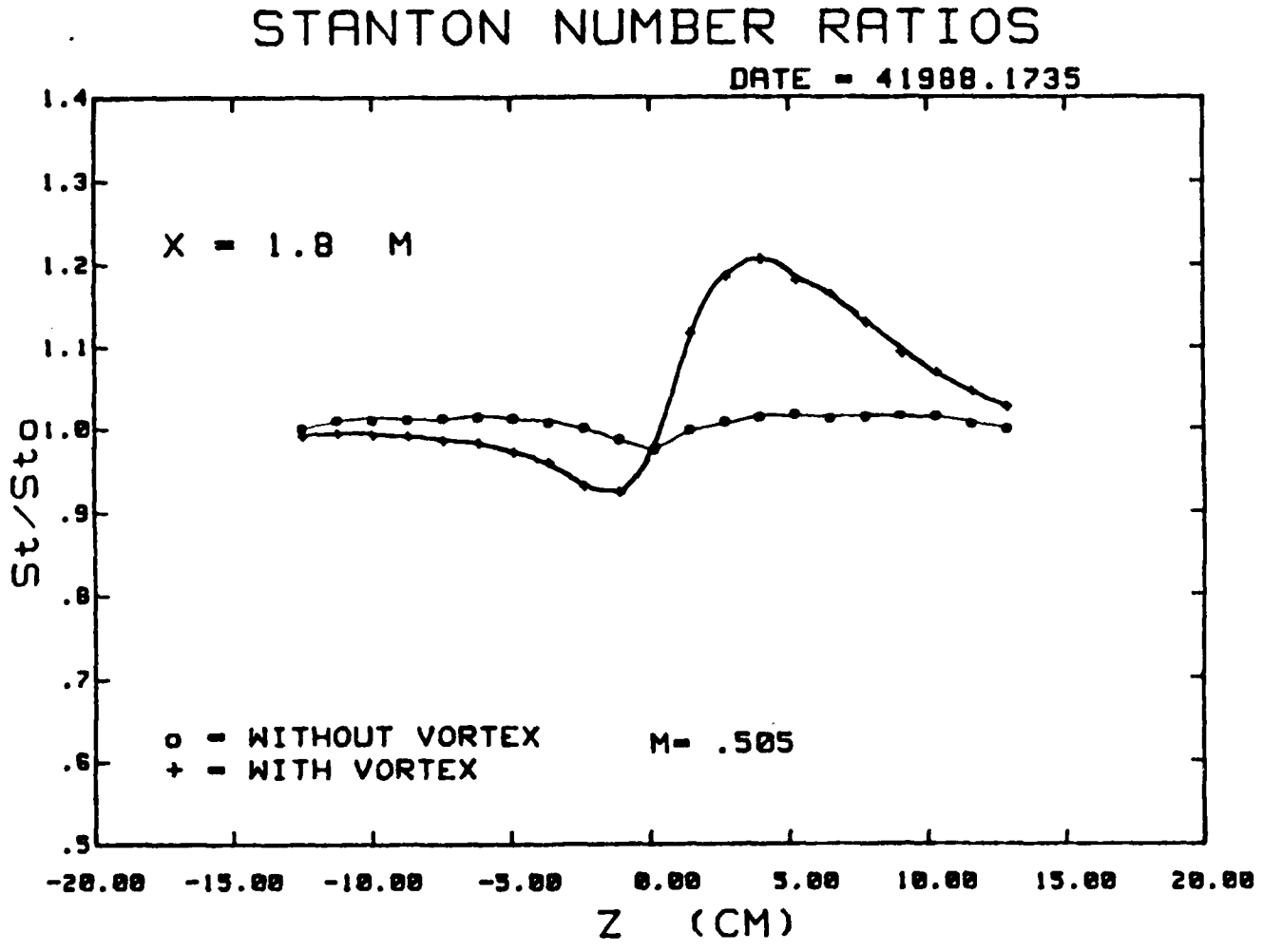

VG 3.0 INCHES FROM C/L, 10 M/S, 3 INJECTION HOLES

Figure 96. Spanwise Variation of Stanton Number Ratios Vortex #2 Position k

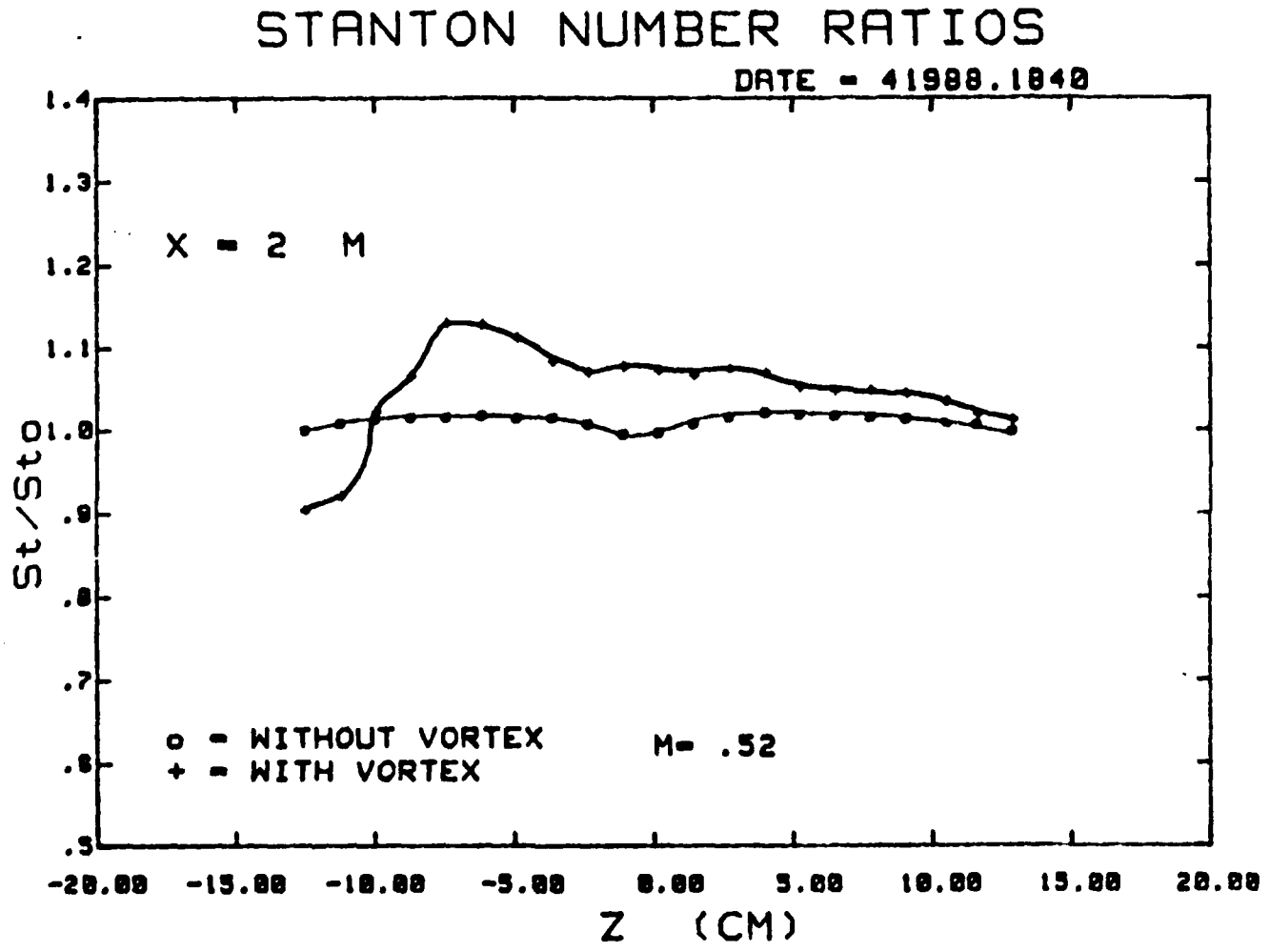

Figure 97. Spanwise Variation of Stanton Number Ratios Vortex #2 Position b

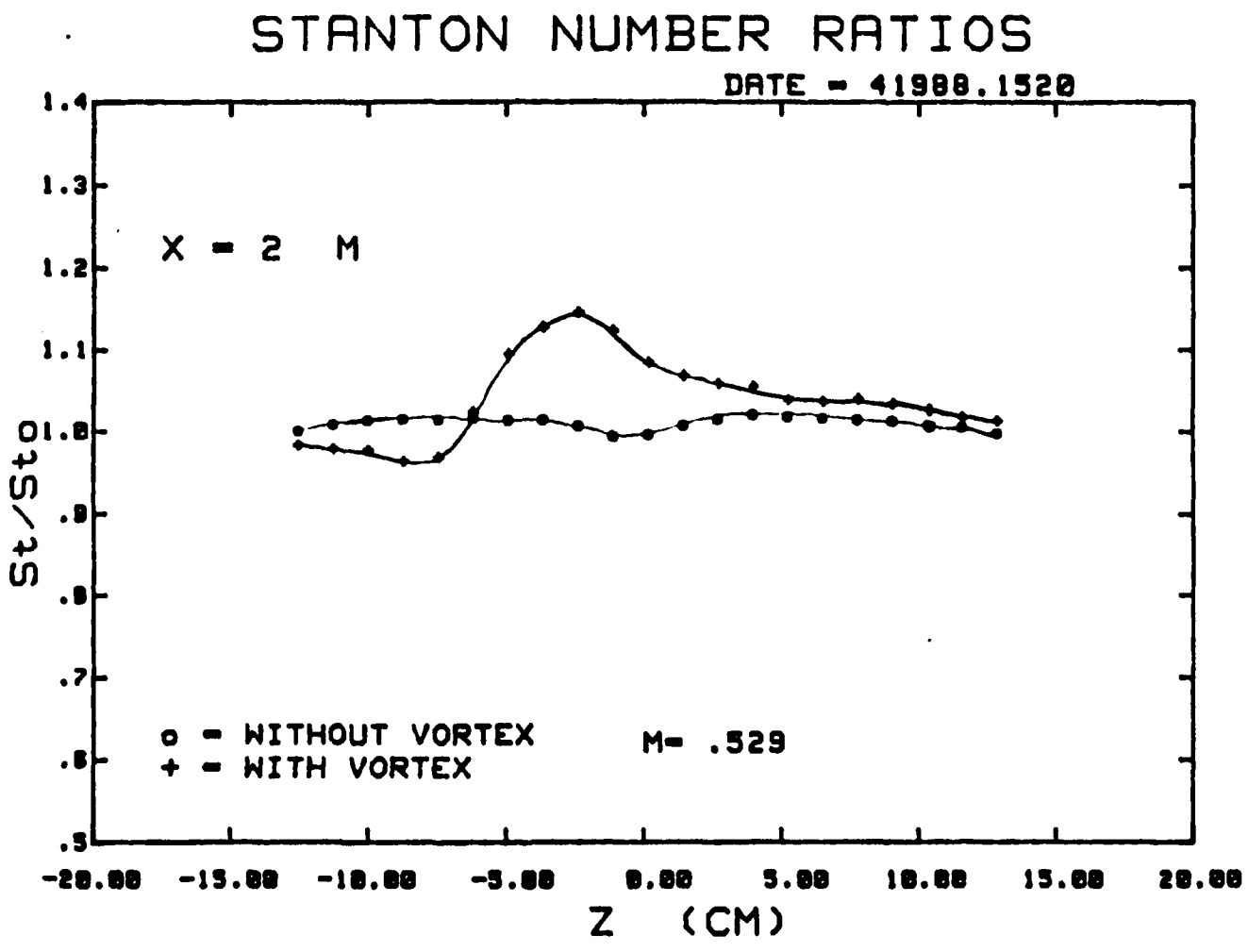

0 IN FROM THE C/L,10M/S,3 INJECTION HOLES

Figure 98. Spanwise Variation of Stanton Number Ratios Vortex #2 Position e

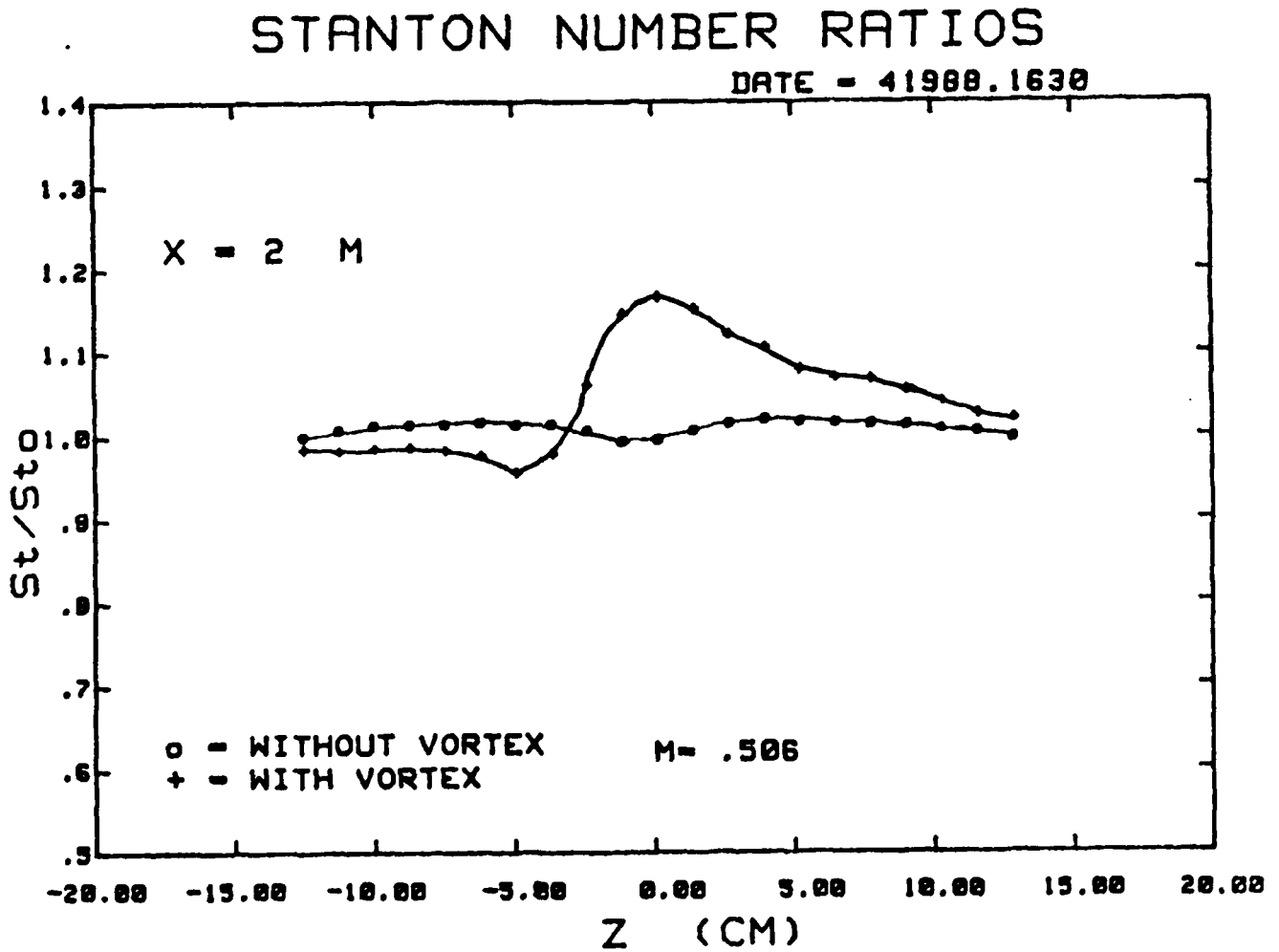

Figure 99. Spanwise Variation of Stanton Number Ratios Vortex #2 Position h

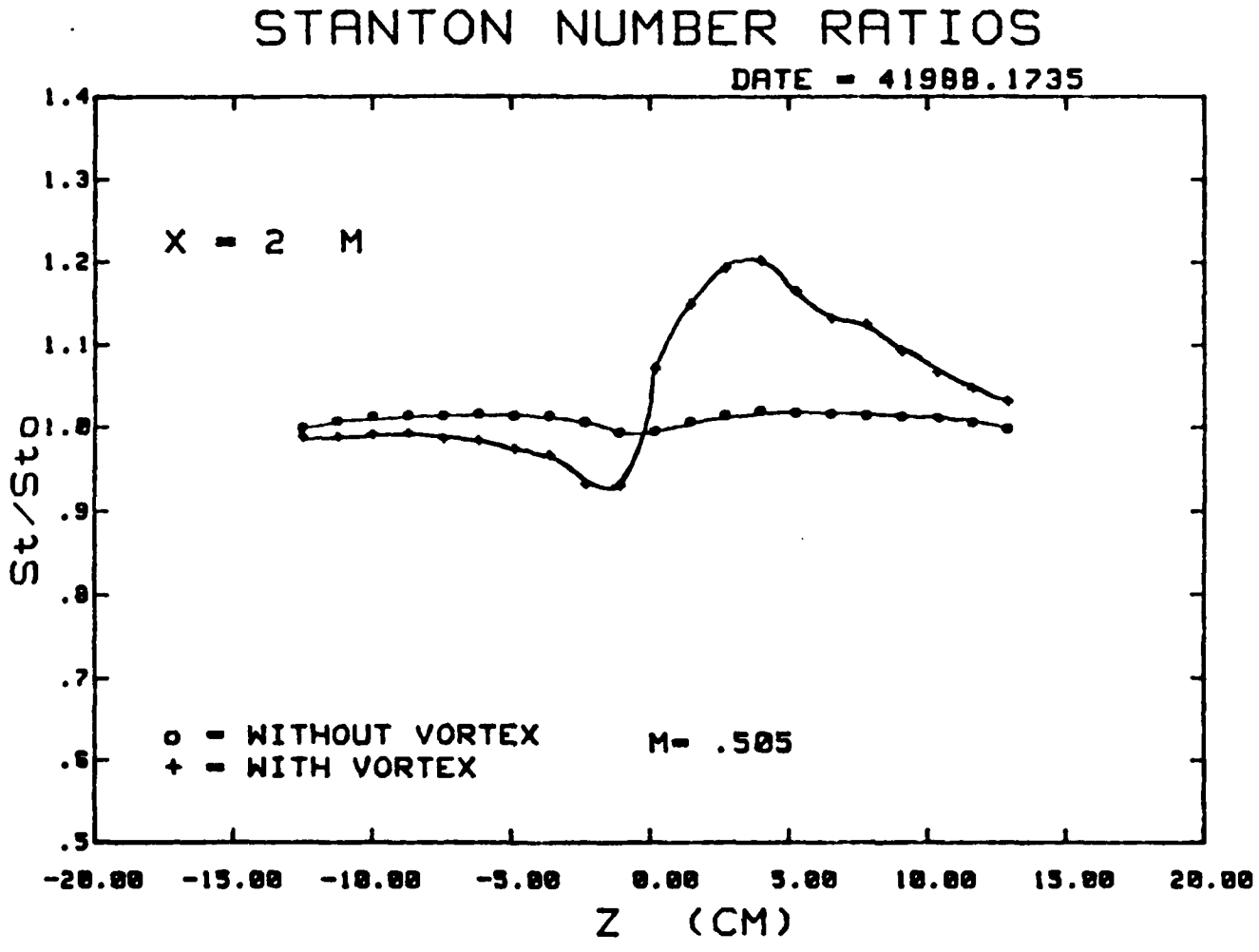

VG 3.0 INCHES FROM C/L, 10 M/S, 3 INJECTION HOLES

Figure 100. Spanwise Variation of Stanton Number Ratios· Vortex #2 Position k

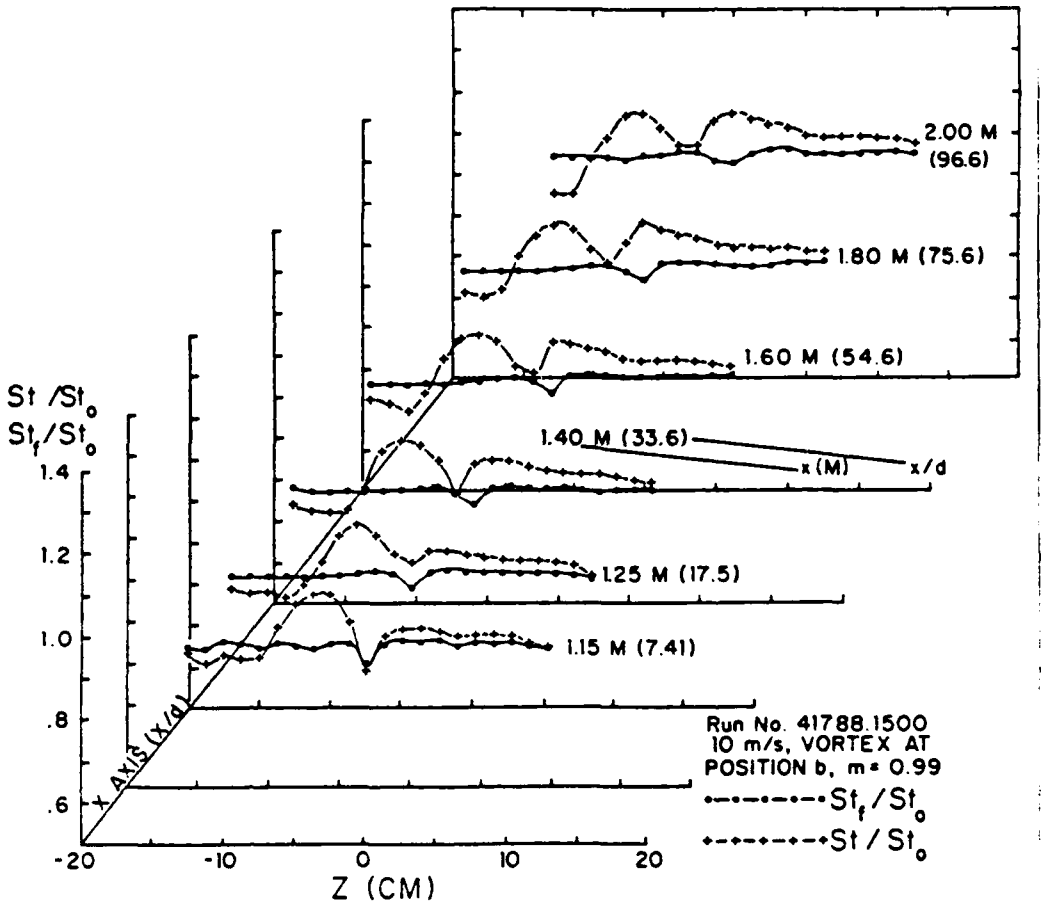

Figure 101. **Local Stanton Number Ratios in Boundary Layers with Film Cooling, with and without an Embedded Vortex**

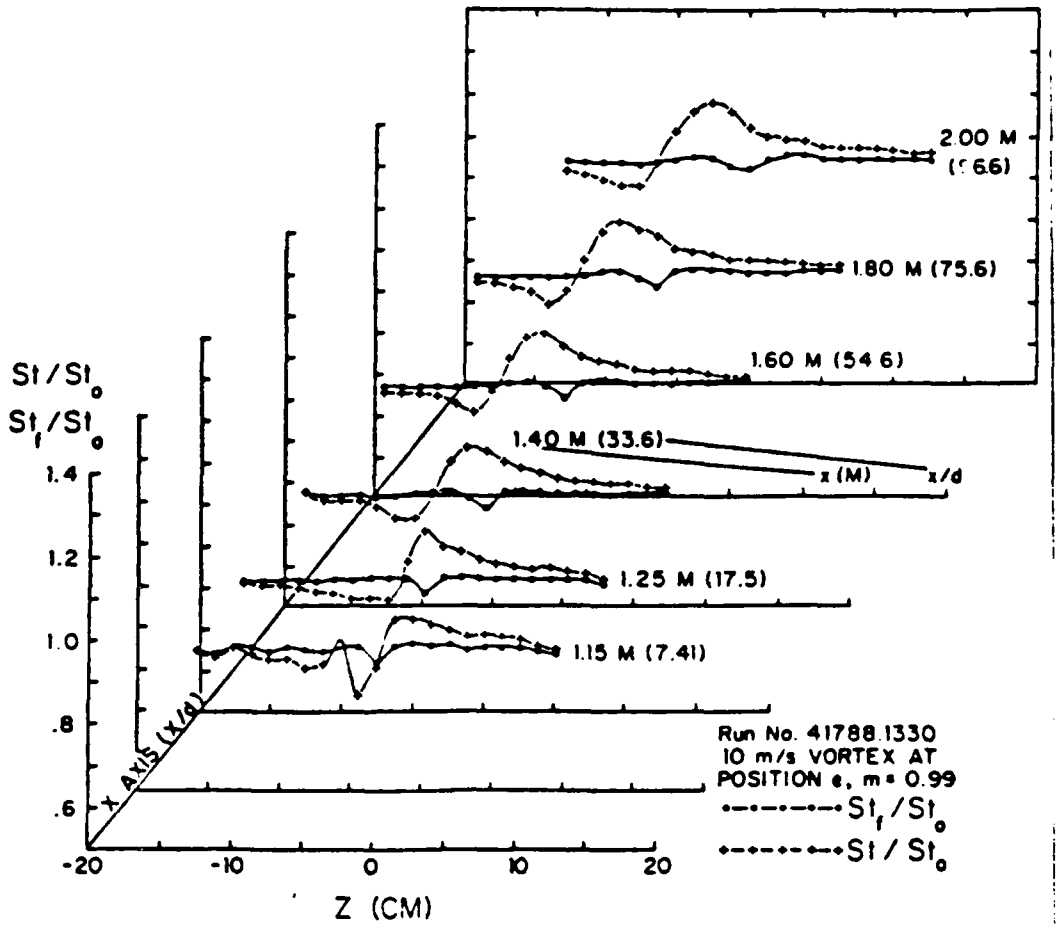

Figure 102. **Local Stanton Number Ratios in Boundary Layers with Film Cooling, with and without an Embedded Vortex**

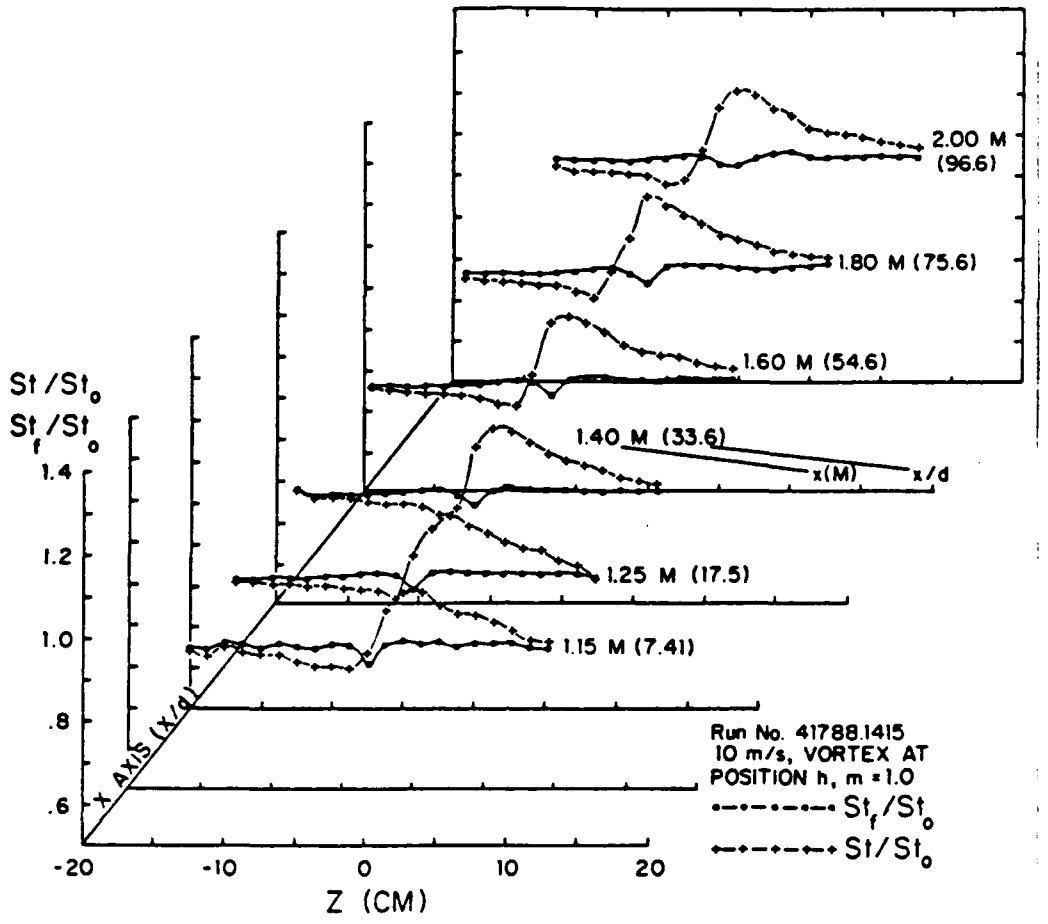

Figure 103. **Local Stanton Number Ratios in Boundary Layers with Film Cooling, with and without an Embedded Vortex**

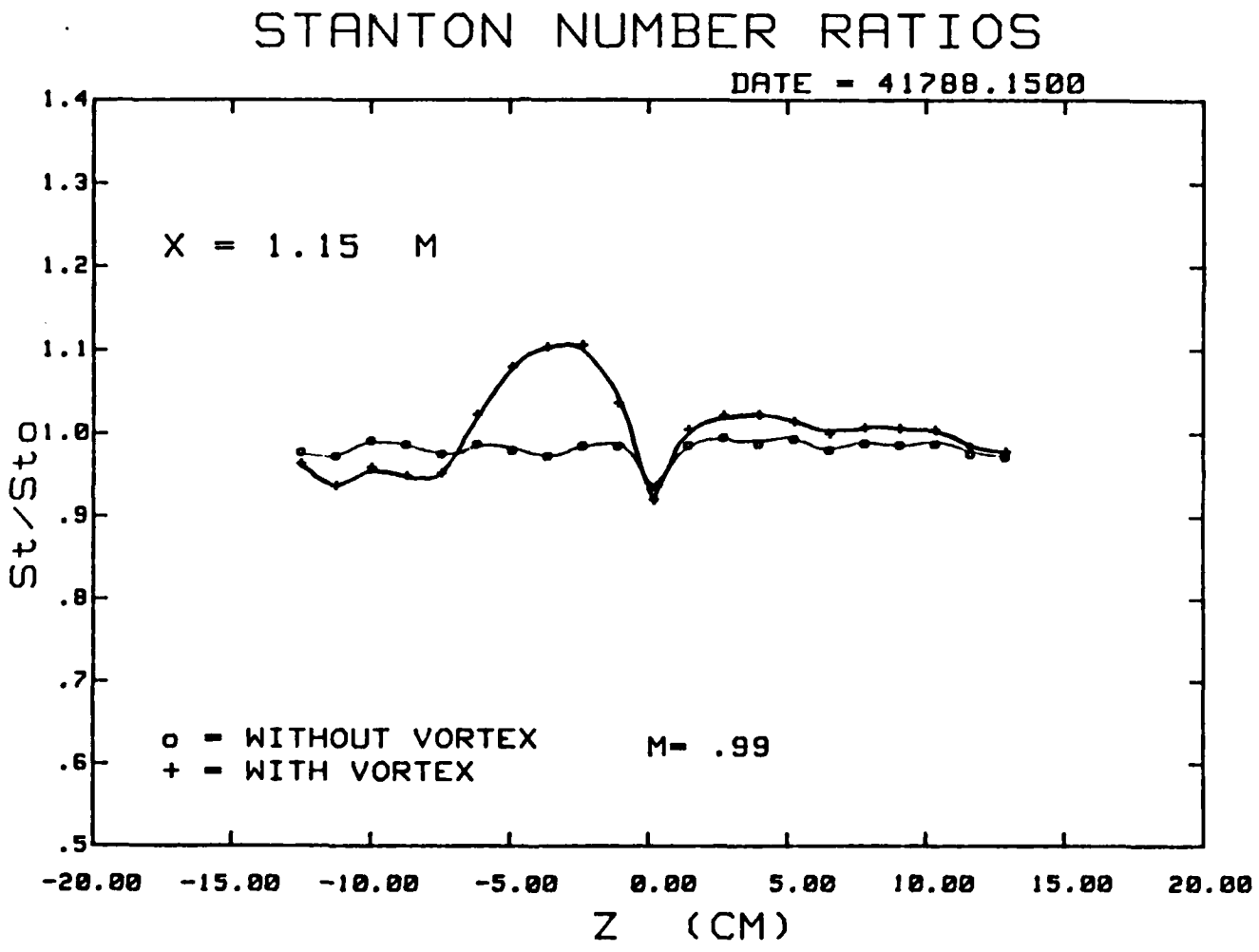

VG -1.5 INCHES FROM C/L, 10 M/S, 3 INJECTION HOLES

Figure 104. Spanwise Variation of Stanton Number Ratios Vortex #2 Position b

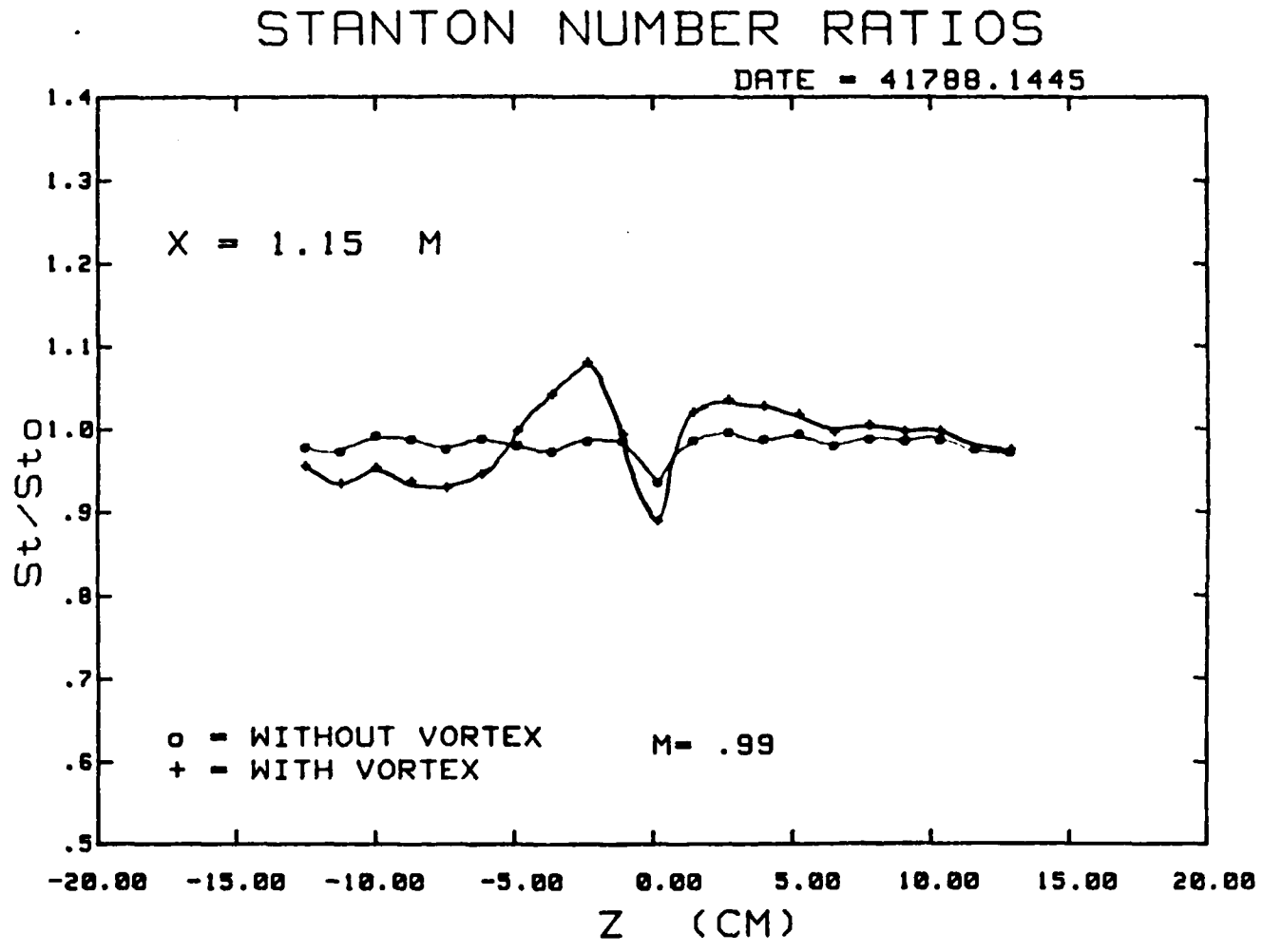

VG -1.0 INCHES FROM C/L, 10 M/S, 3 INJECTION HOLES

Figure 105. Spanwise Variation of Stanton Number Ratios Vortex #2 Position c

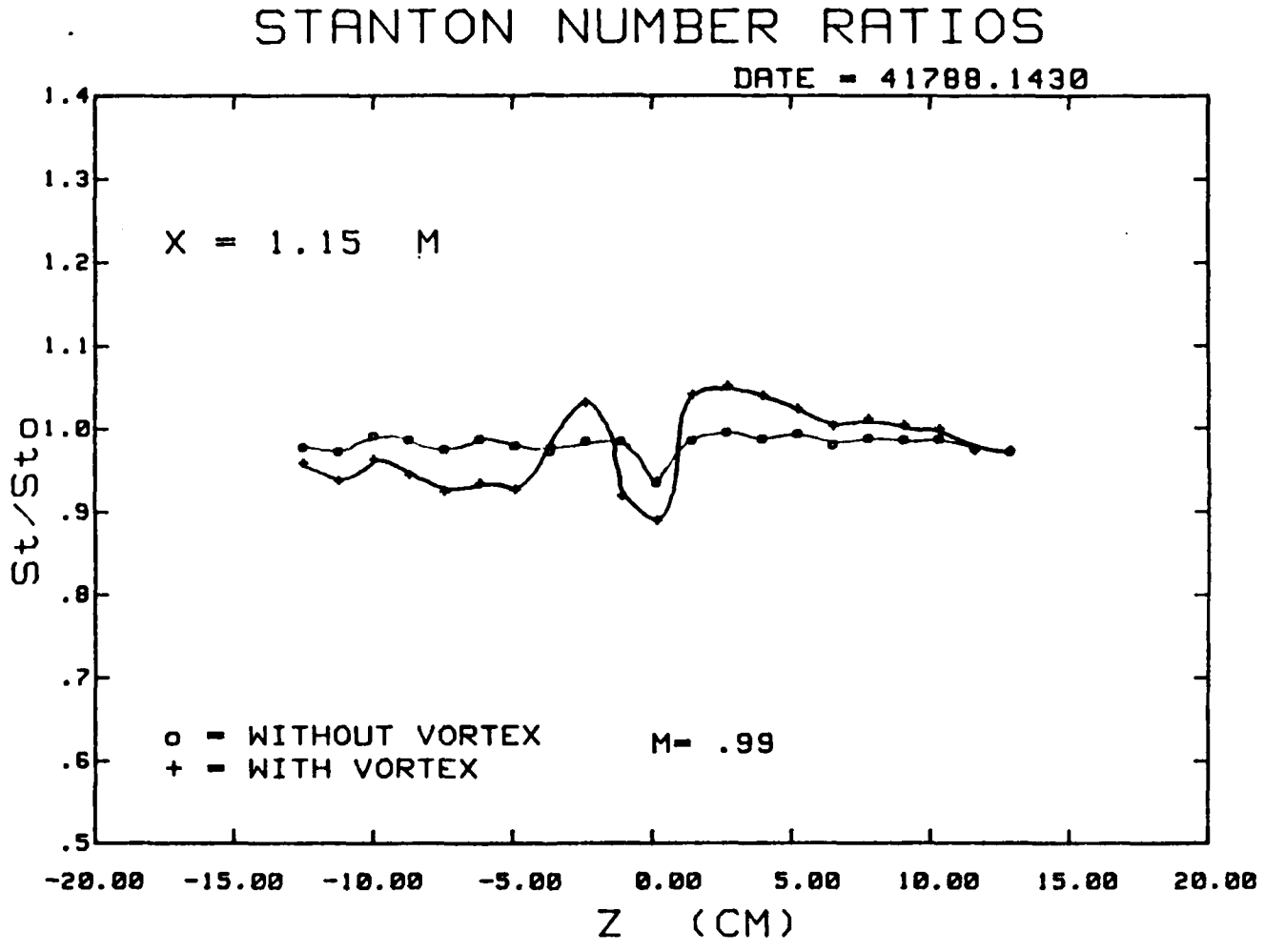

VG -.5 INCHES FROM C/L, 10 M/S, 3 INJECTION HOLES

Figure 106. Spanwise Variation of Stanton Number Ratios Vortex #2 Position d

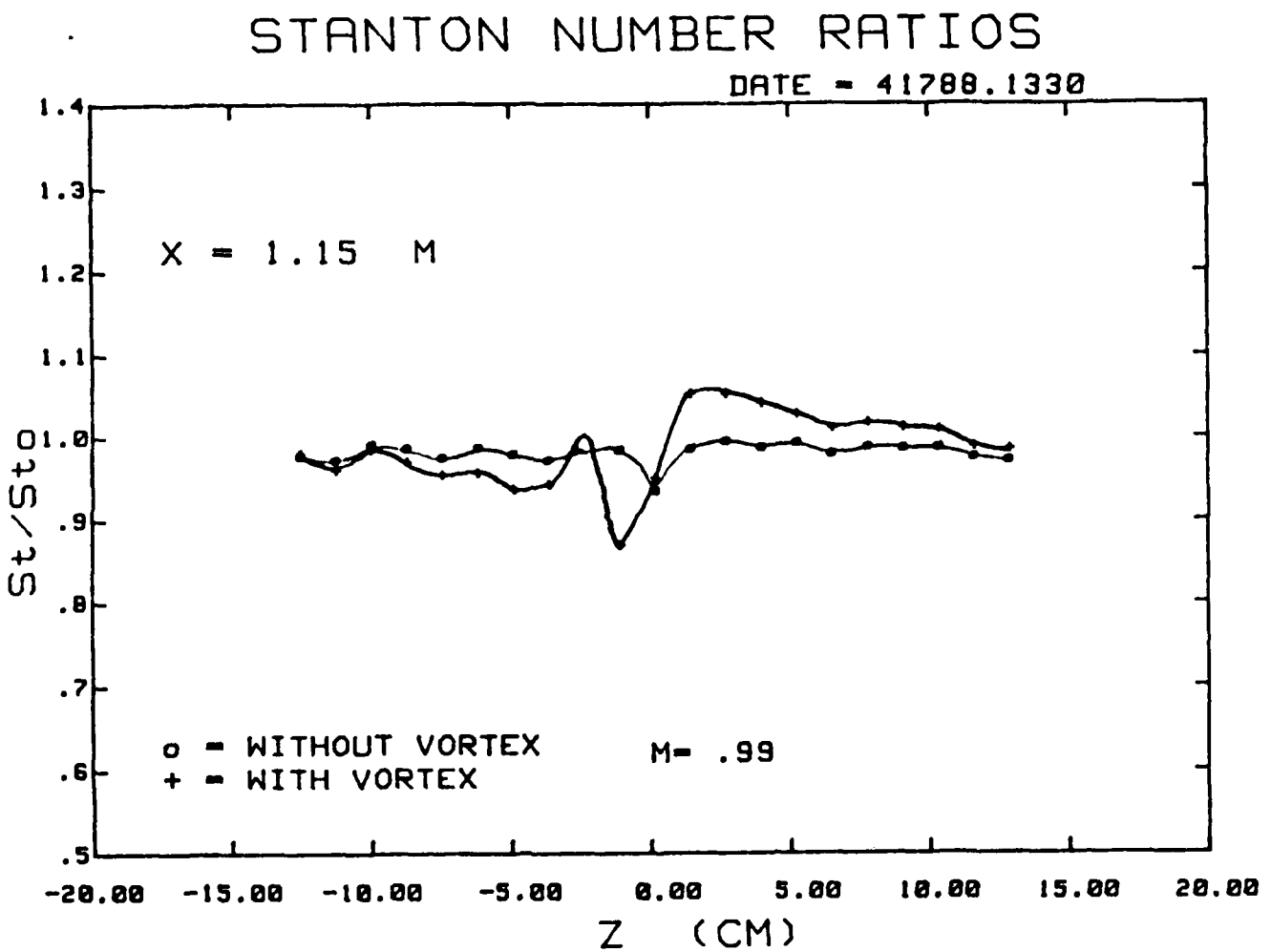

VG 0.0 INCHES FROM C/L, 10 M/S, 3 INJECTION HOLES

Figure 107. Spanwise Variation of Stanton Number Ratios Vortex #2 Position e

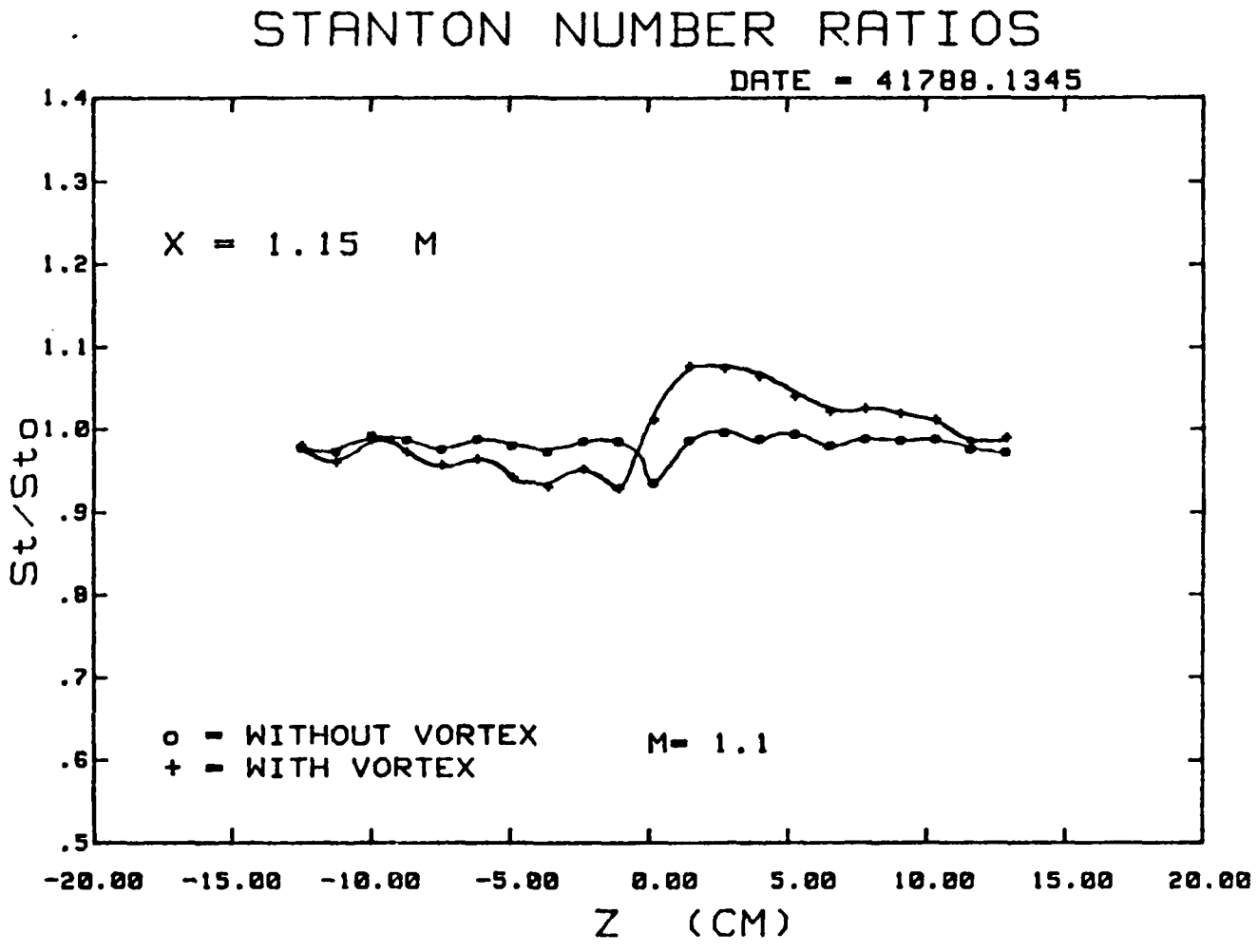

VG 0.5 INCHES FROM C/L, 10 M/S, 3 INJECTION HOLES

Figure 108. Spanwise Variation of Stanton Number Ratios Vortex #2 Position f

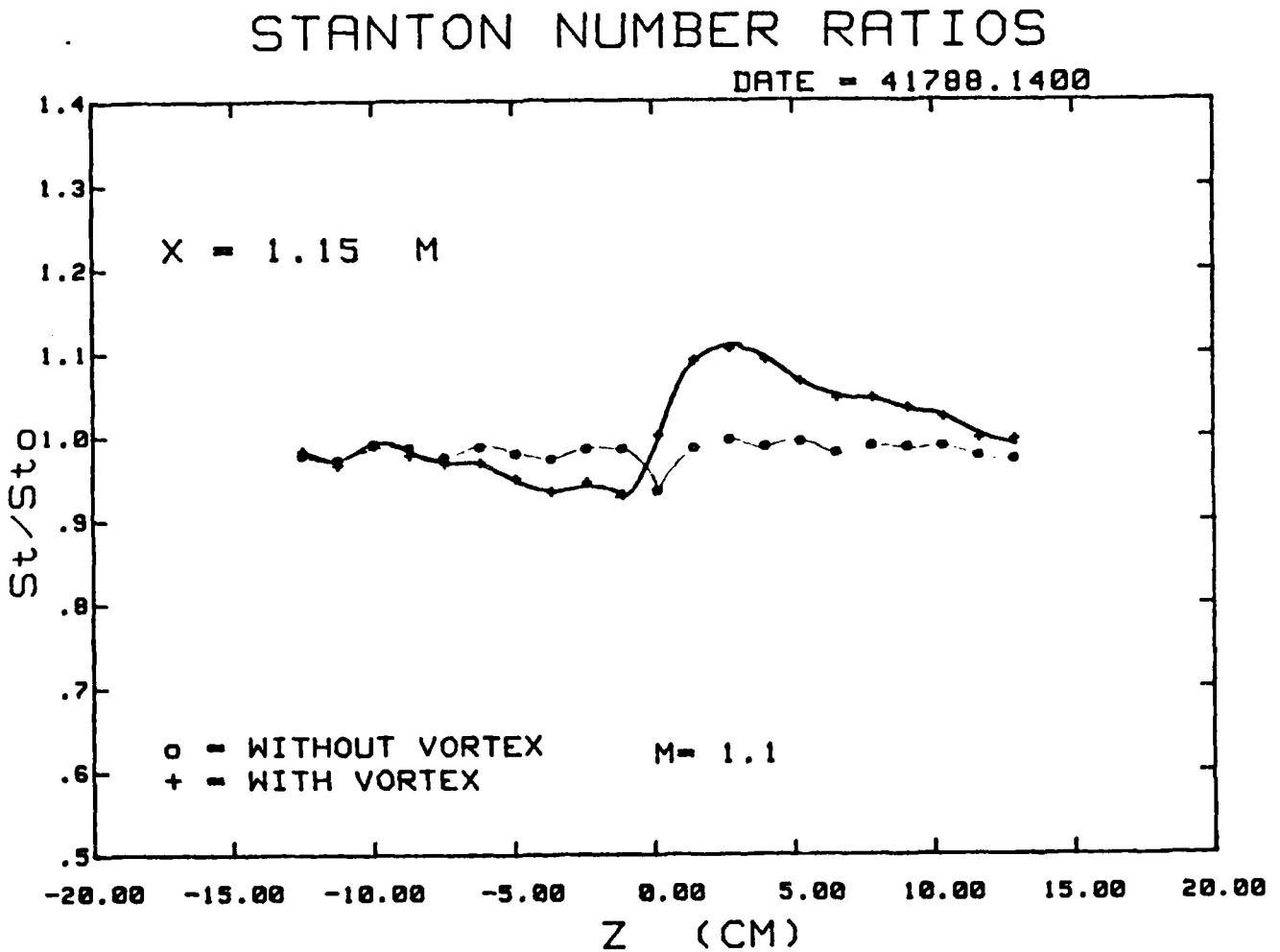

VG 1.0 INCHES FROM C/L, 10 M/S, 3 INJECTION HOLES

Figure 109. Spanwise Variation of Stanton Number Ratios Vortex #2 Position g

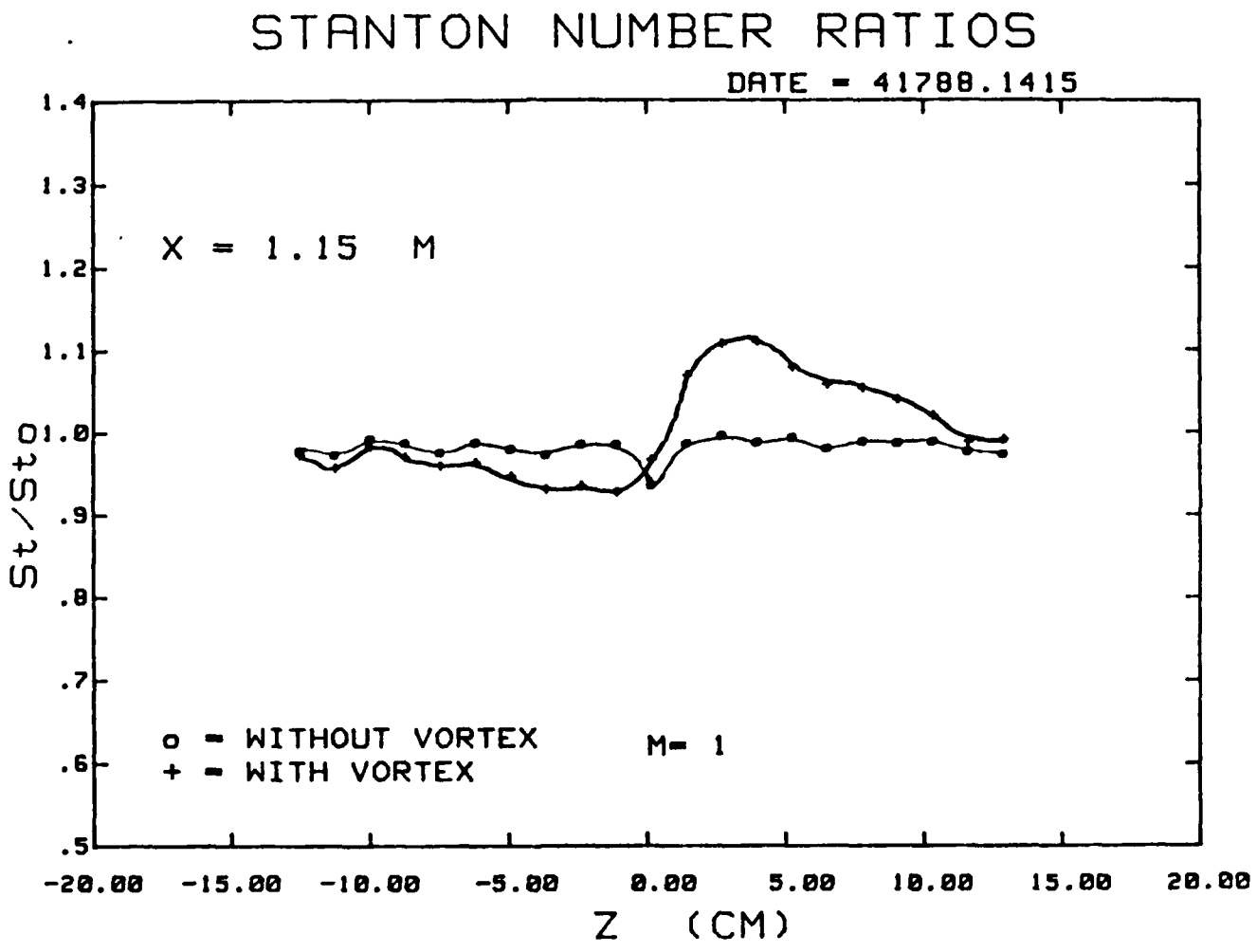

VG 1.5 INCHES FROM C/L, 10 M/S, 3 INJECTION HOLES

Figure 110. Spanwise Variation of Stanton Number Ratios Vortex #2 Position h

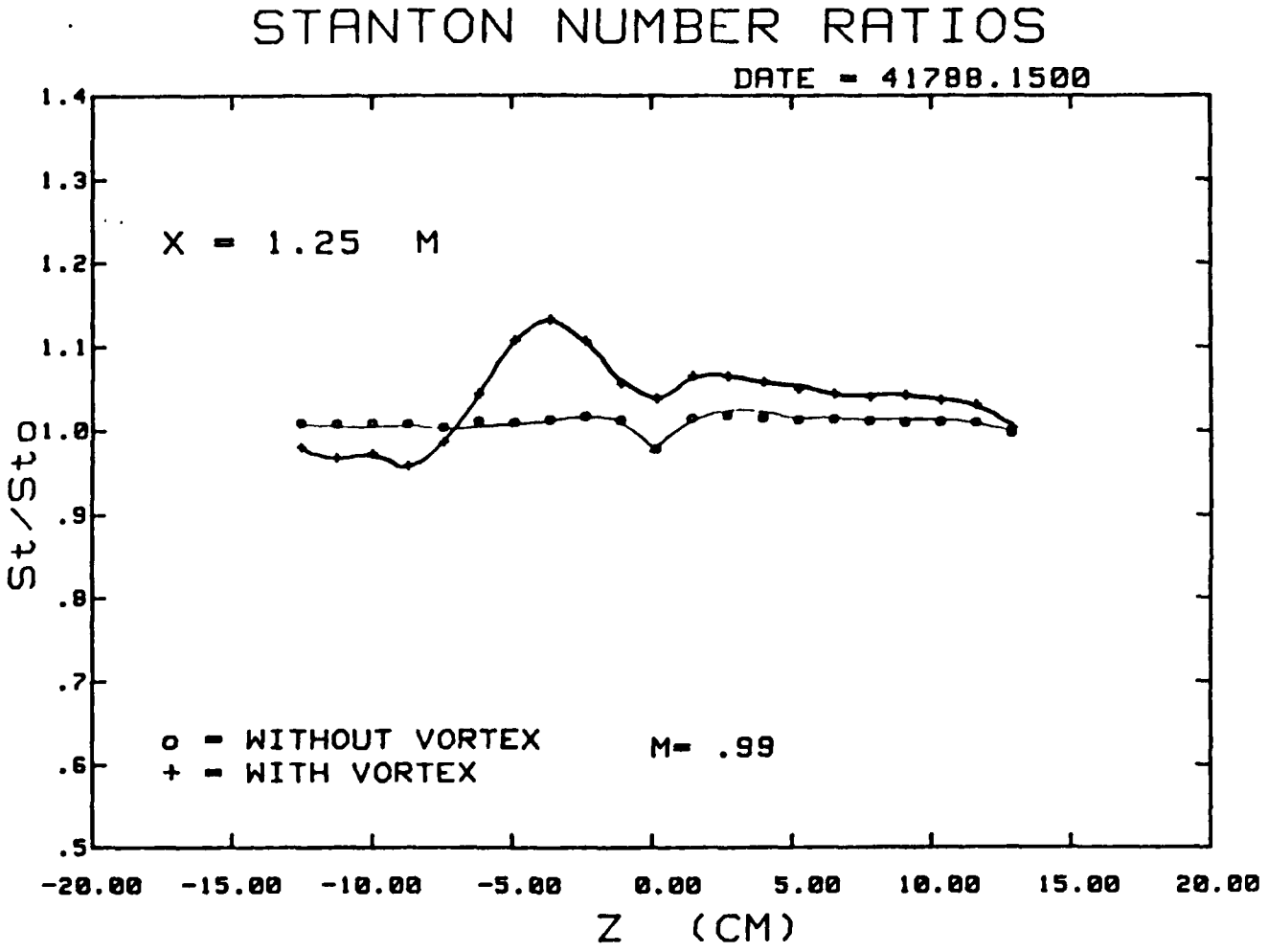

VG -1.5 INCHES FROM C/L, 10 M/S, 3 INJECTION HOLES

Figure 111. Spanwise Variation of Stanton Number Ratios Vortex #2 Position b

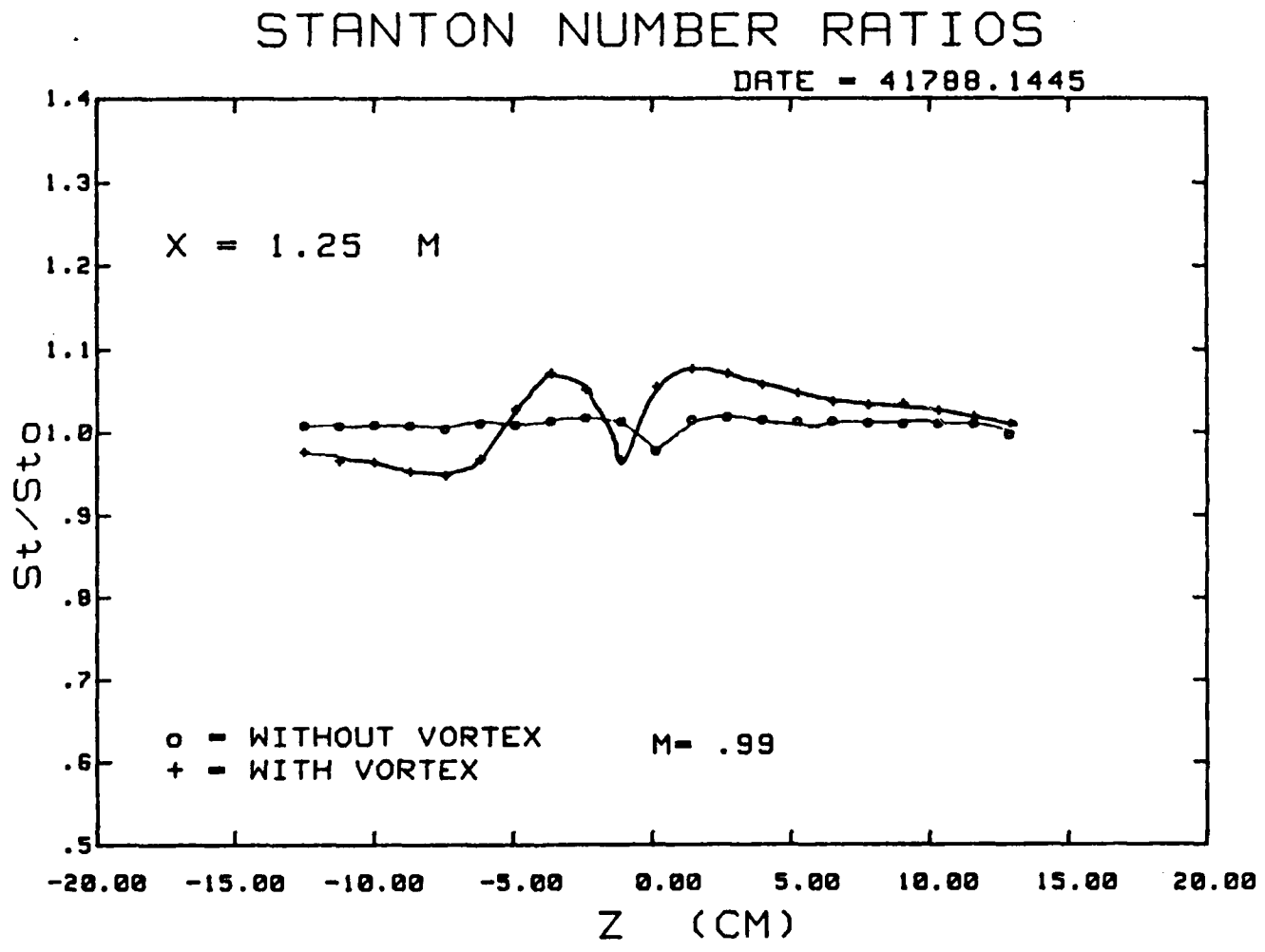

VG -1.0 INCHES FROM C/L, 10 M/S, 3 INJECTION HOLES

Figure 112. Spanwise Variation of Stanton Number Ratios Vortex #2 Position c

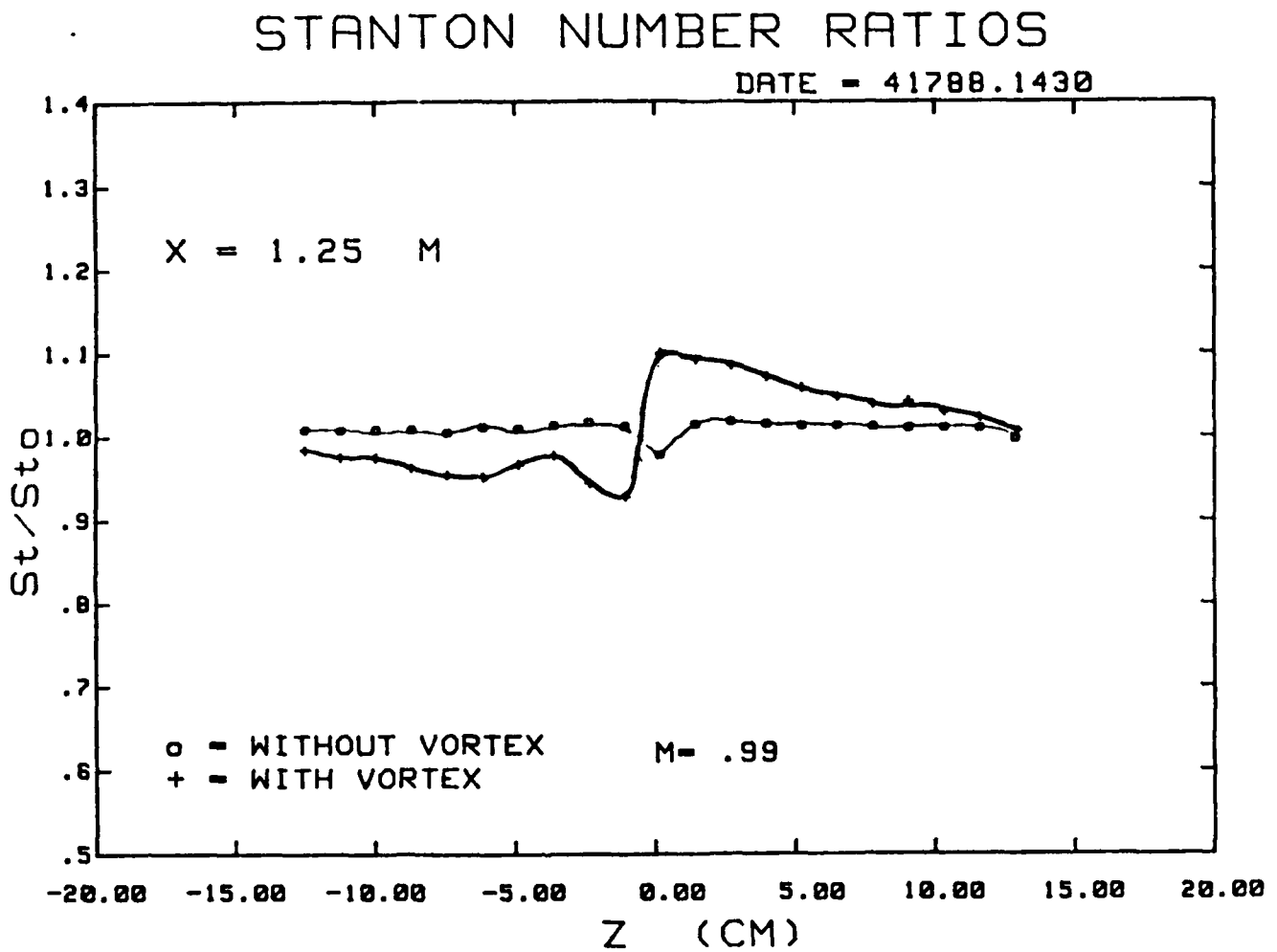

VG -.5 INCHES FROM C/L, 10 M/S, 3 INJECTION HOLES

Figure 113. Spanwise Variation of Stanton Number Ratios Vortex #2 Position d

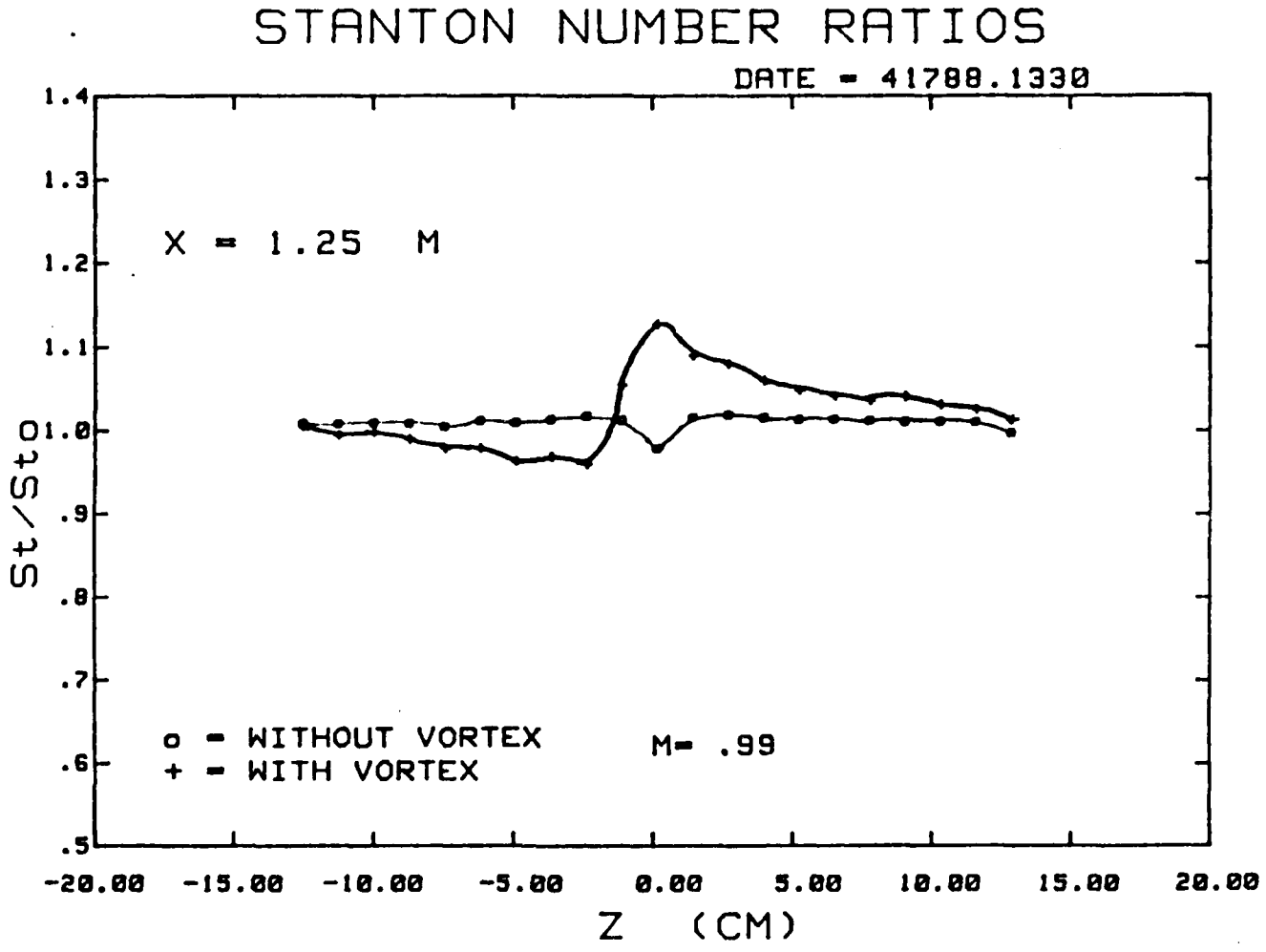

VG 0.0 INCHES FROM C/L, 10 M/S, 3 INJECTION HOLES

Figure 114. Spanwise Variation of Stanton Number Ratios Vortex #2 Position e

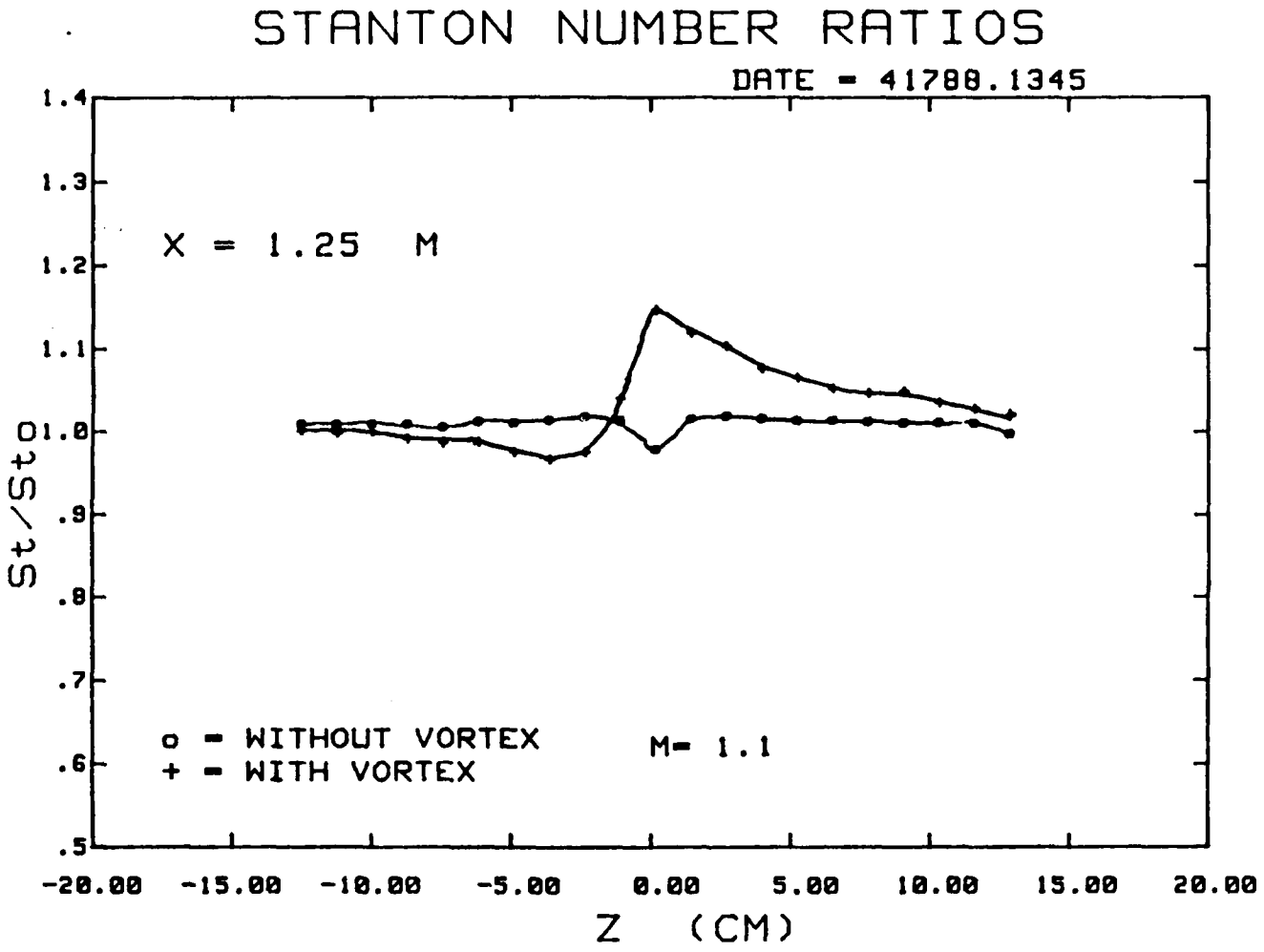

VG 0.5 INCHES FROM C/L, 10 M/S, 3 INJECTION HOLES

Figure 115. Spanwise Variation of Stanton Number Ratios Vortex #2 Position f

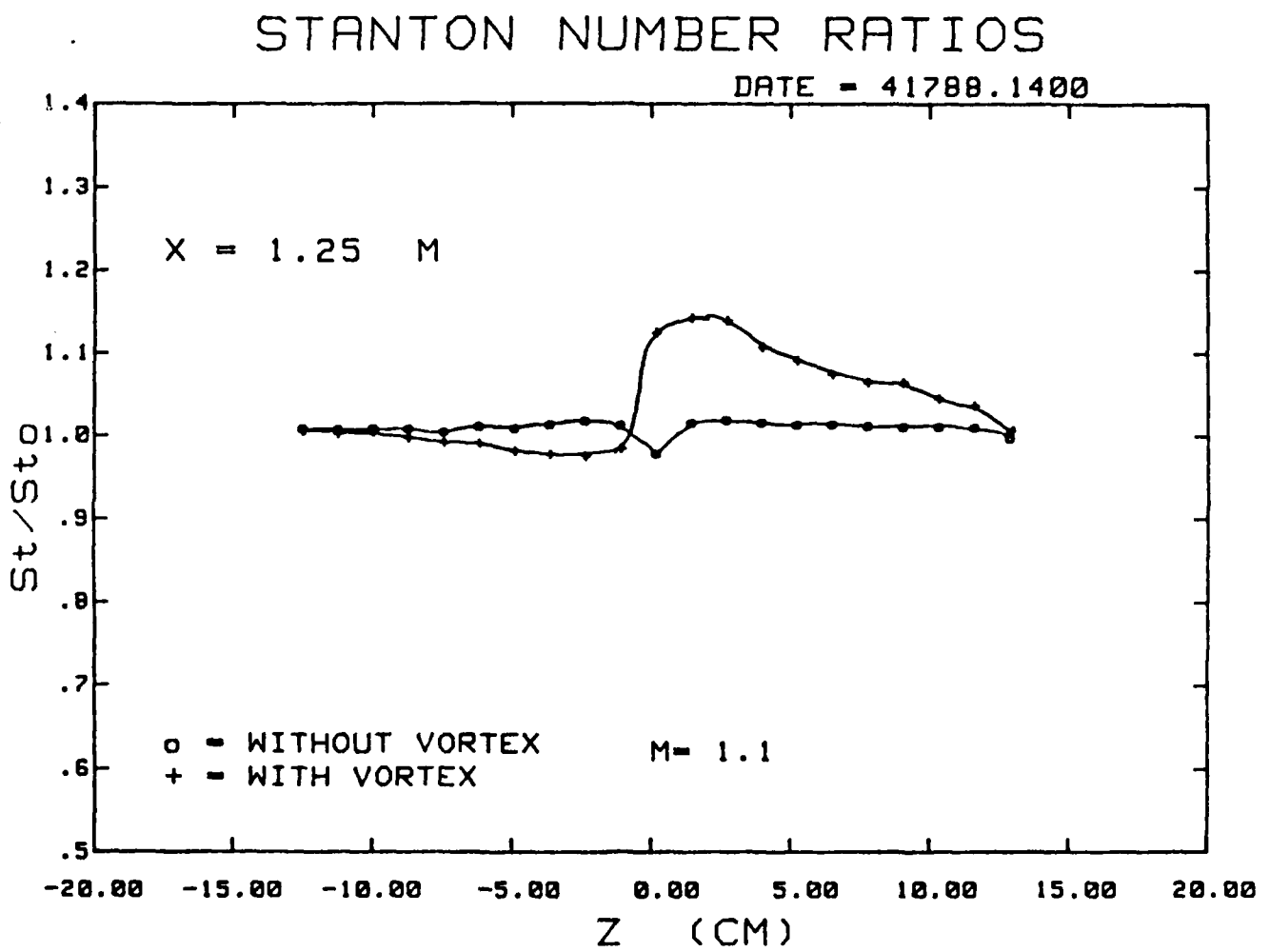

VG 1.0 INCHES FROM C/L, 10 M/S, 3 INJECTION HOLES

Figure 116. Spanwise Variation of Stanton Number Ratios· Vortex #2 Position g

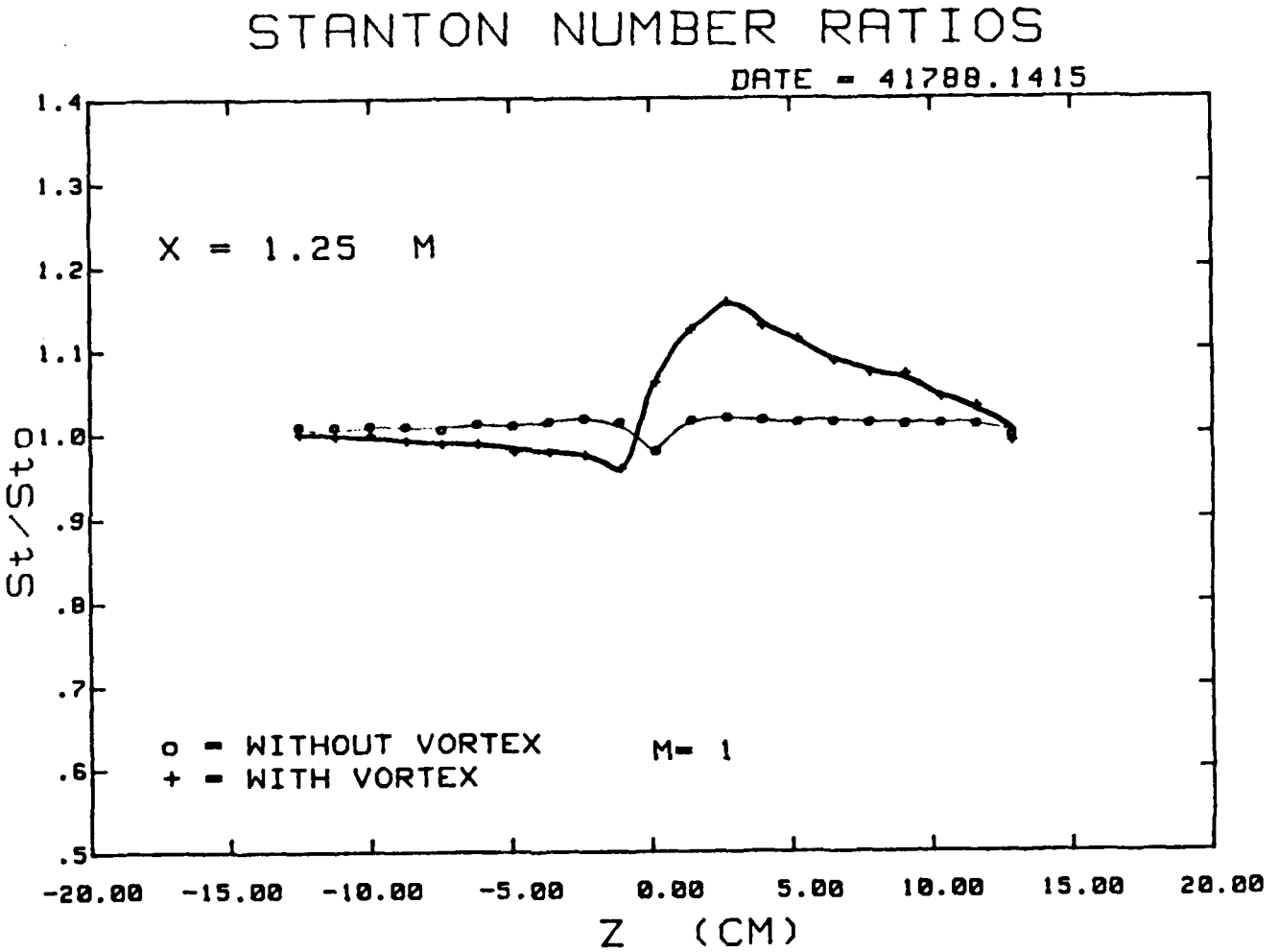

VG 1.5 INCHES FROM C/L, 10 M/S, 3 INJECTION HOLES

Figure 117. Spanwise Variation of Stanton Number Ratios Vortex #2 Position h

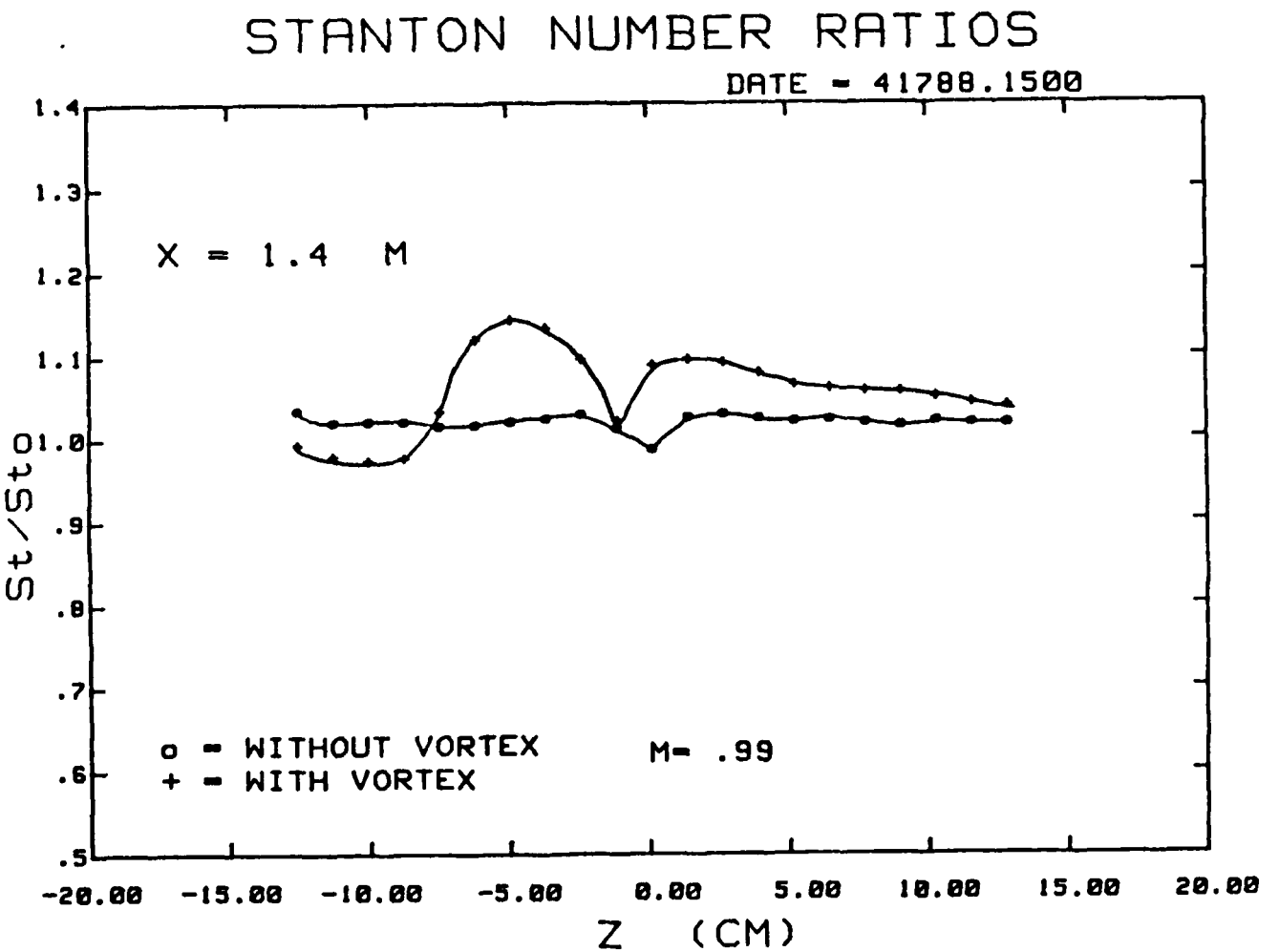

VG -1.5 INCHES FROM C/L, 10 M/S, 3 INJECTION HOLES

Figure 118. Spanwise Variation of Stanton Number Ratios Vortex #2 Position b

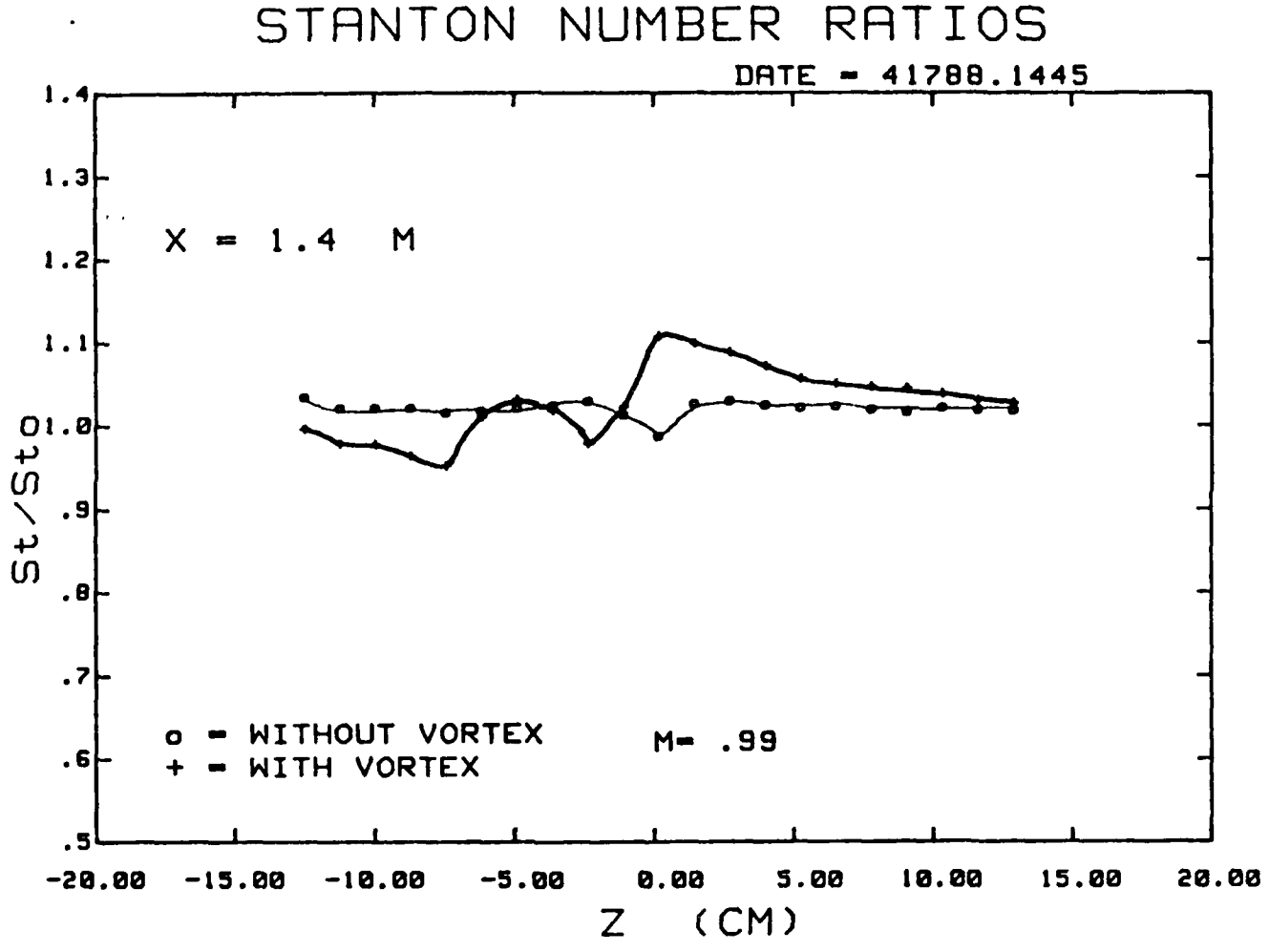

VG -1.0 INCHES FROM C/L, 10 M/S, 3 INJECTION HOLES

Figure 119. Spanwise Variation of Stanton Number Ratios Vortex #2 Position c

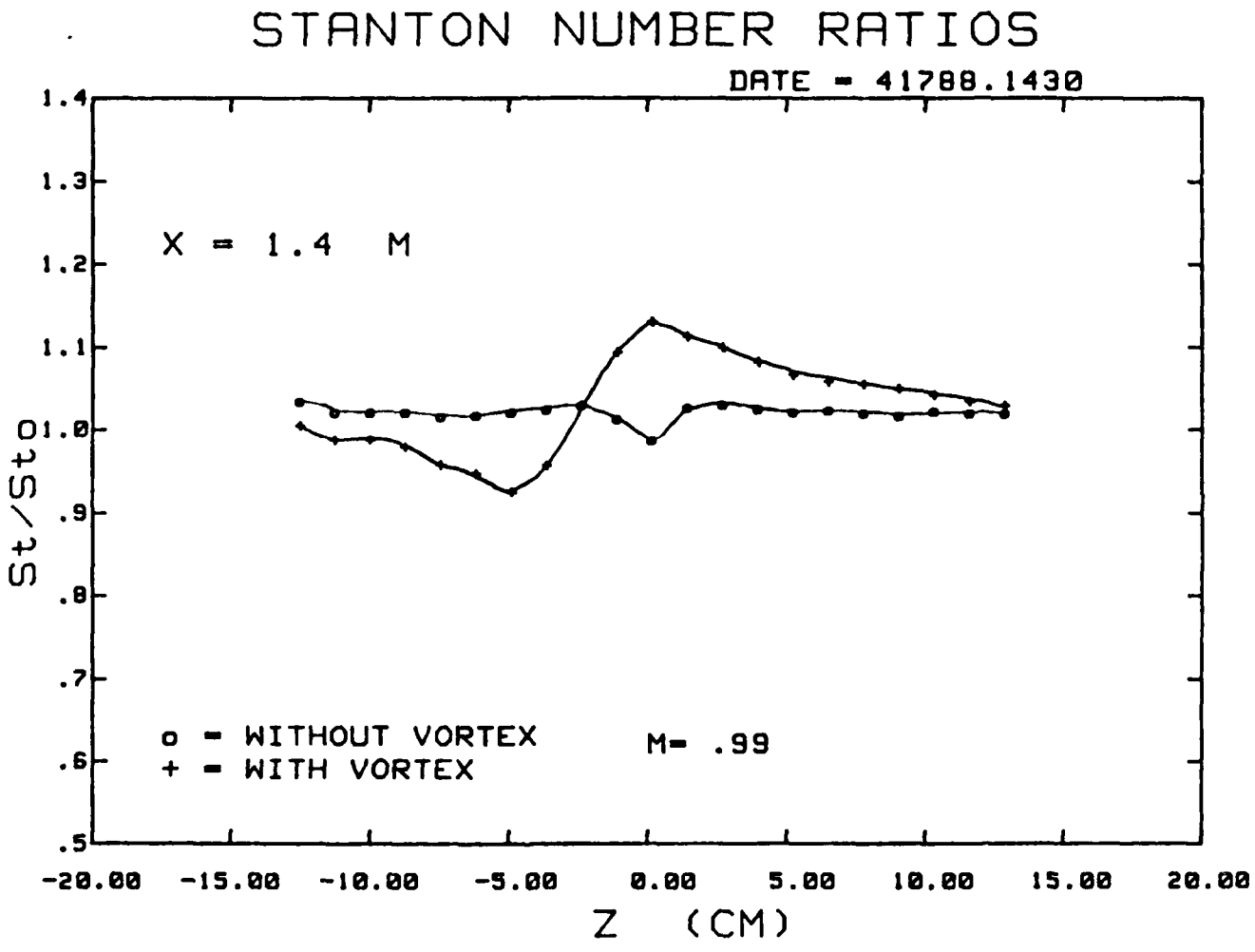

VG -.5 INCHES FROM C/L, 10 M/S, 3 INJECTION HOLES

Figure 120. Spanwise Variation of Stanton Number Ratios Vortex #2 Position d

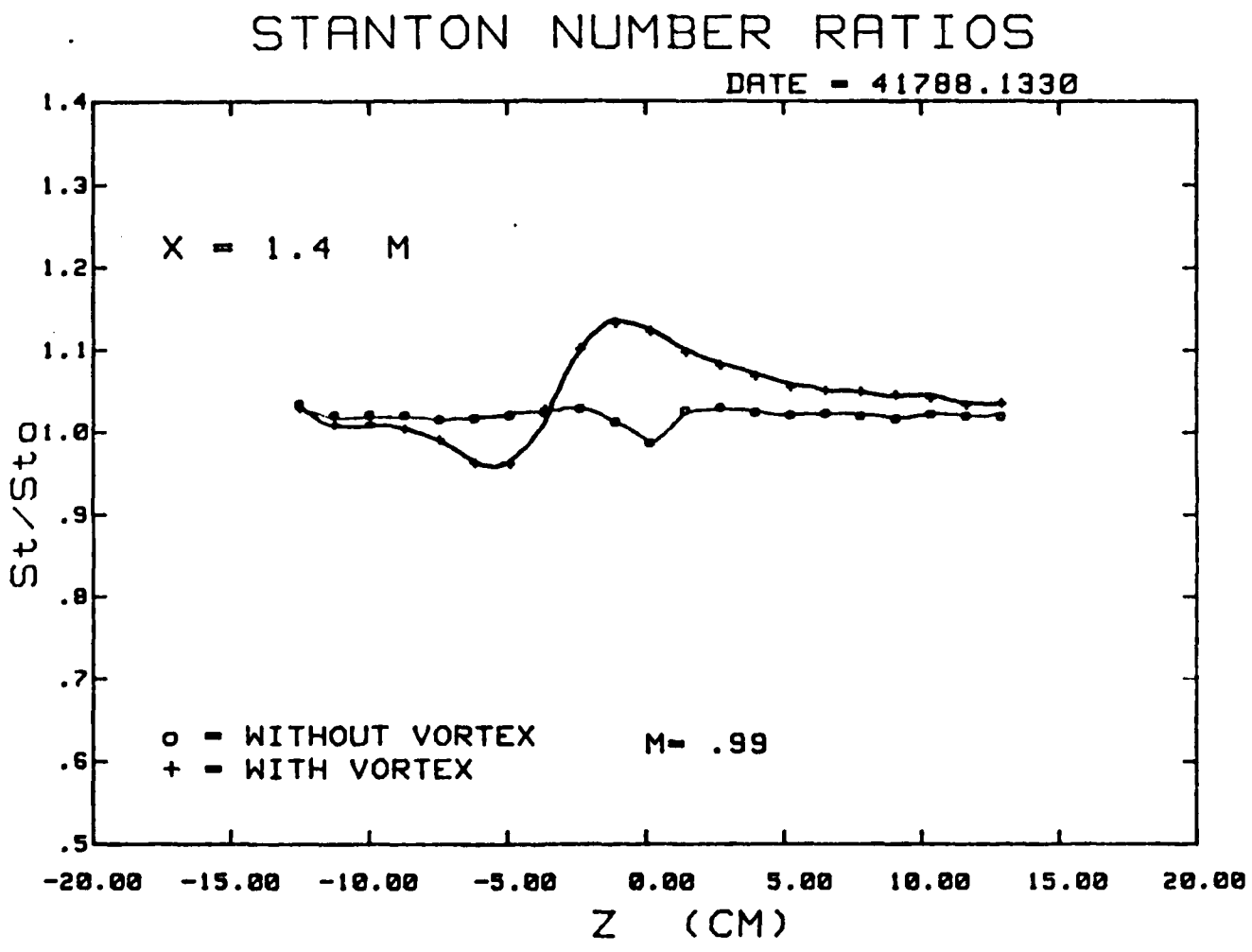

VG 0.0 INCHES FROM C/L, 10 M/S, 3 INJECTION HOLES

Figure 121. Spanwise Variation of Stanton Number Ratios Vortex #2 Position e

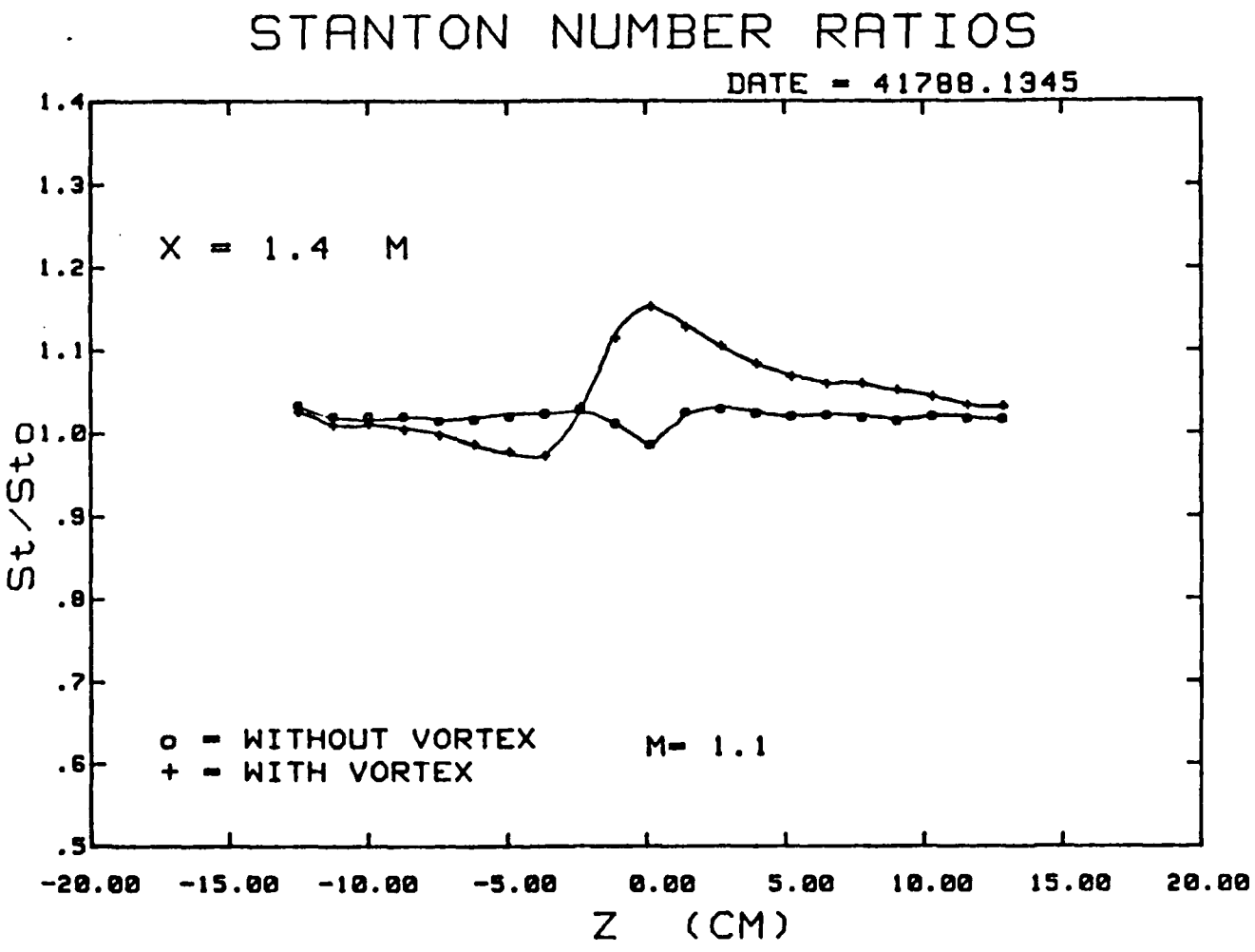

VG 0.5 INCHES FROM C/L, 10 M/S, 3 INJECTION HOLES

Figure 122. Spanwise Variation of Stanton Number Ratios Vortex #2 Position f

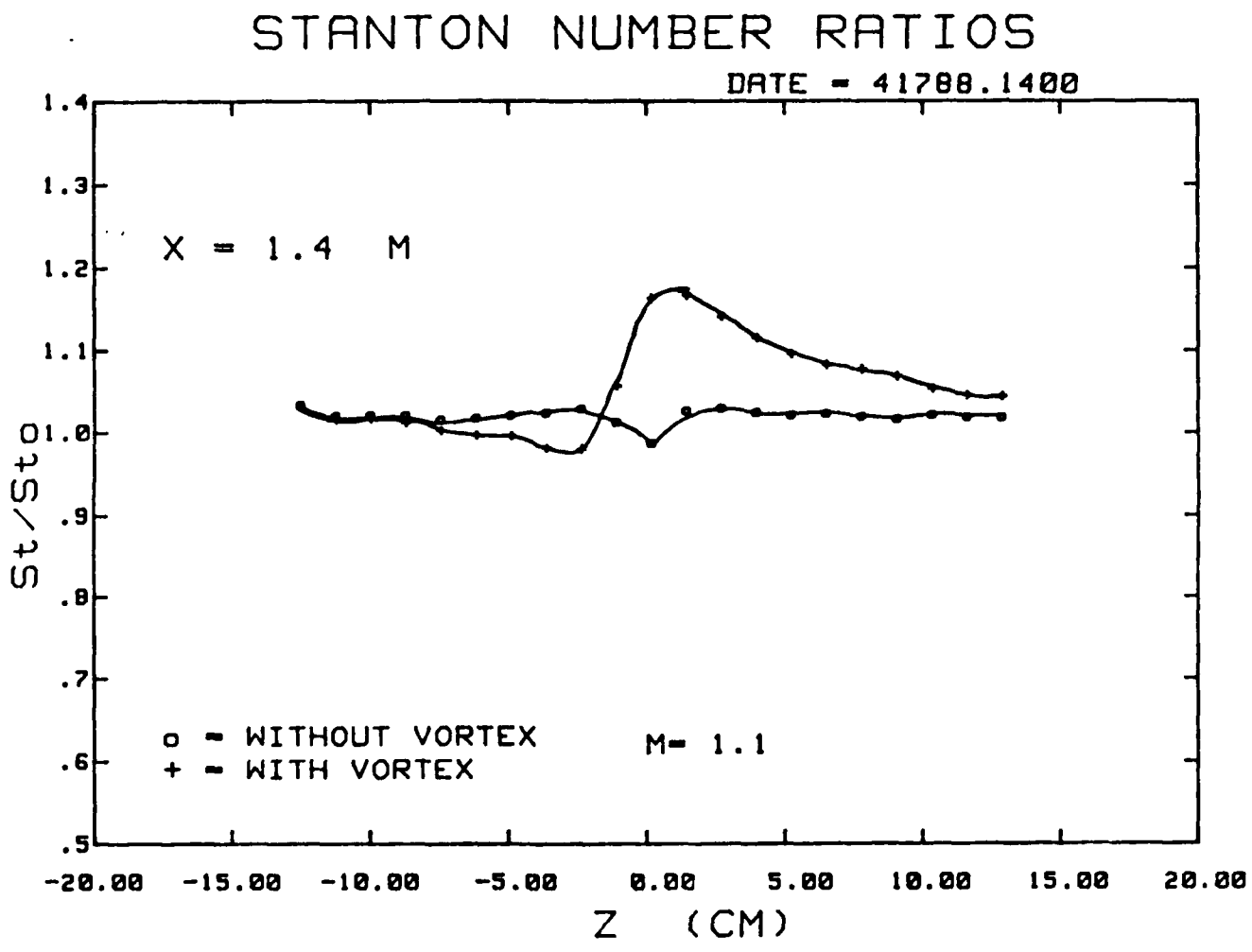

VG 1.0 INCHES FROM C/L, 10 M/S, 3 INJECTION HOLES

Figure 123. Spanwise Variation of Stanton Number Ratios Vortex #2 Position g

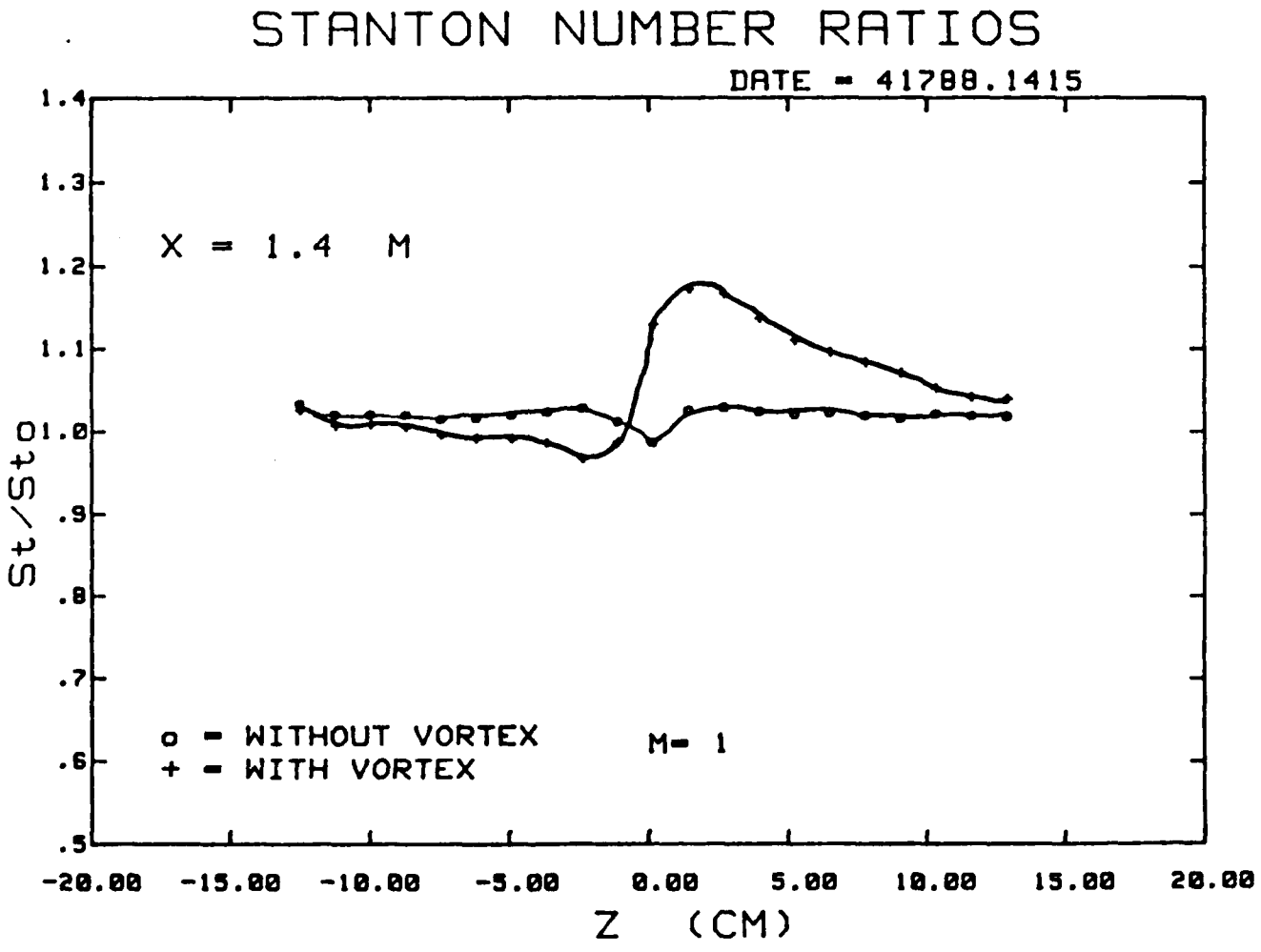

VG 1.5 INCHES FROM C/L, 10 M/S, 3 INJECTION HOLES

Figure 124. Spanwise Variation of Stanton Number Ratios Vortex #2 Position h

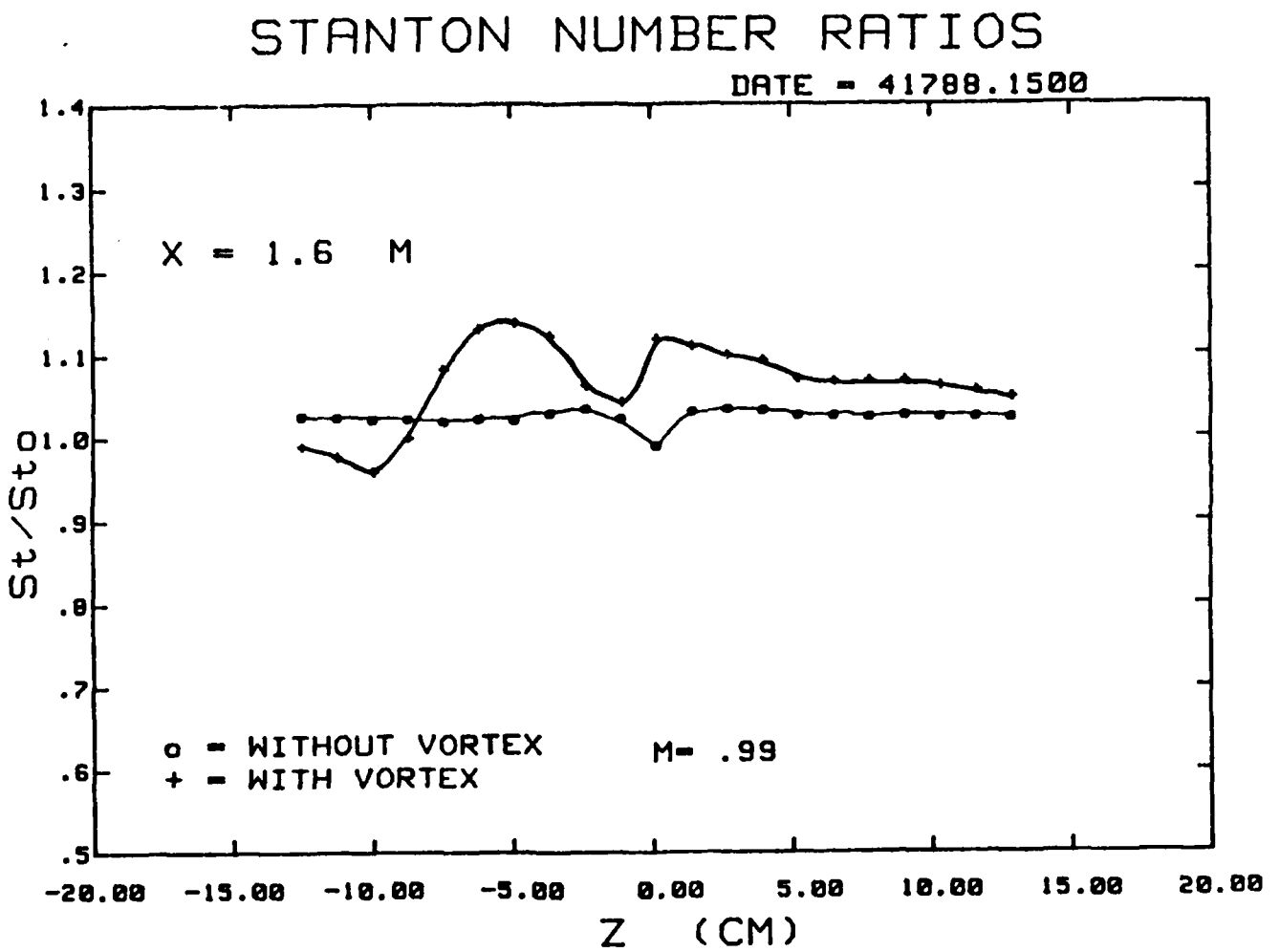

VG -1.5 INCHES FROM C/L, 10 M/S, 3 INJECTION HOLES

Figure 125. Spanwise Variation of Stanton Number Ratios Vortex #2 Position b

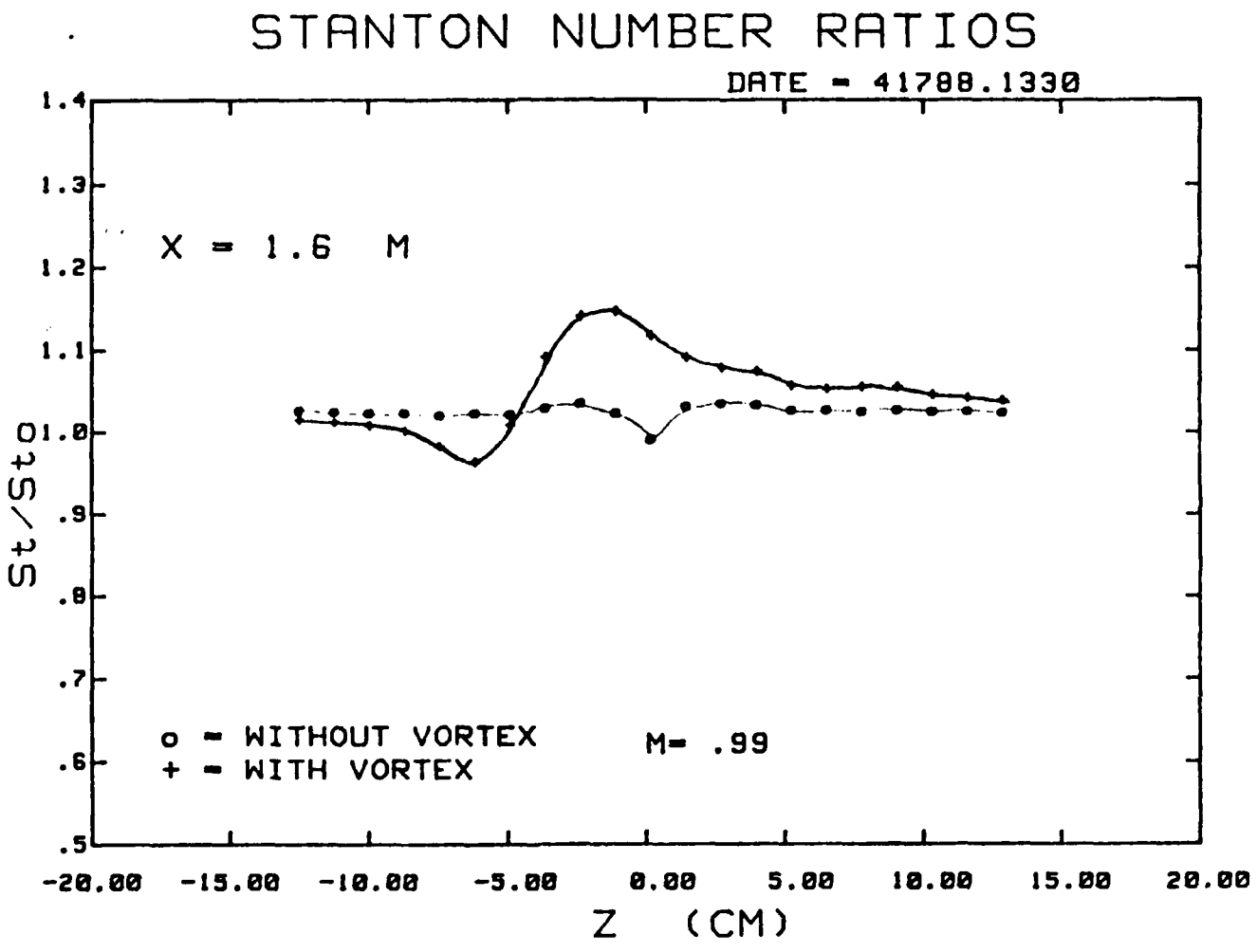

VG 0.0 INCHES FROM C/L, 10 M/S, 3 INJECTION HOLES

Figure 126. Spanwise Variation of Stanton Number Ratios· Vortex #2 Position e

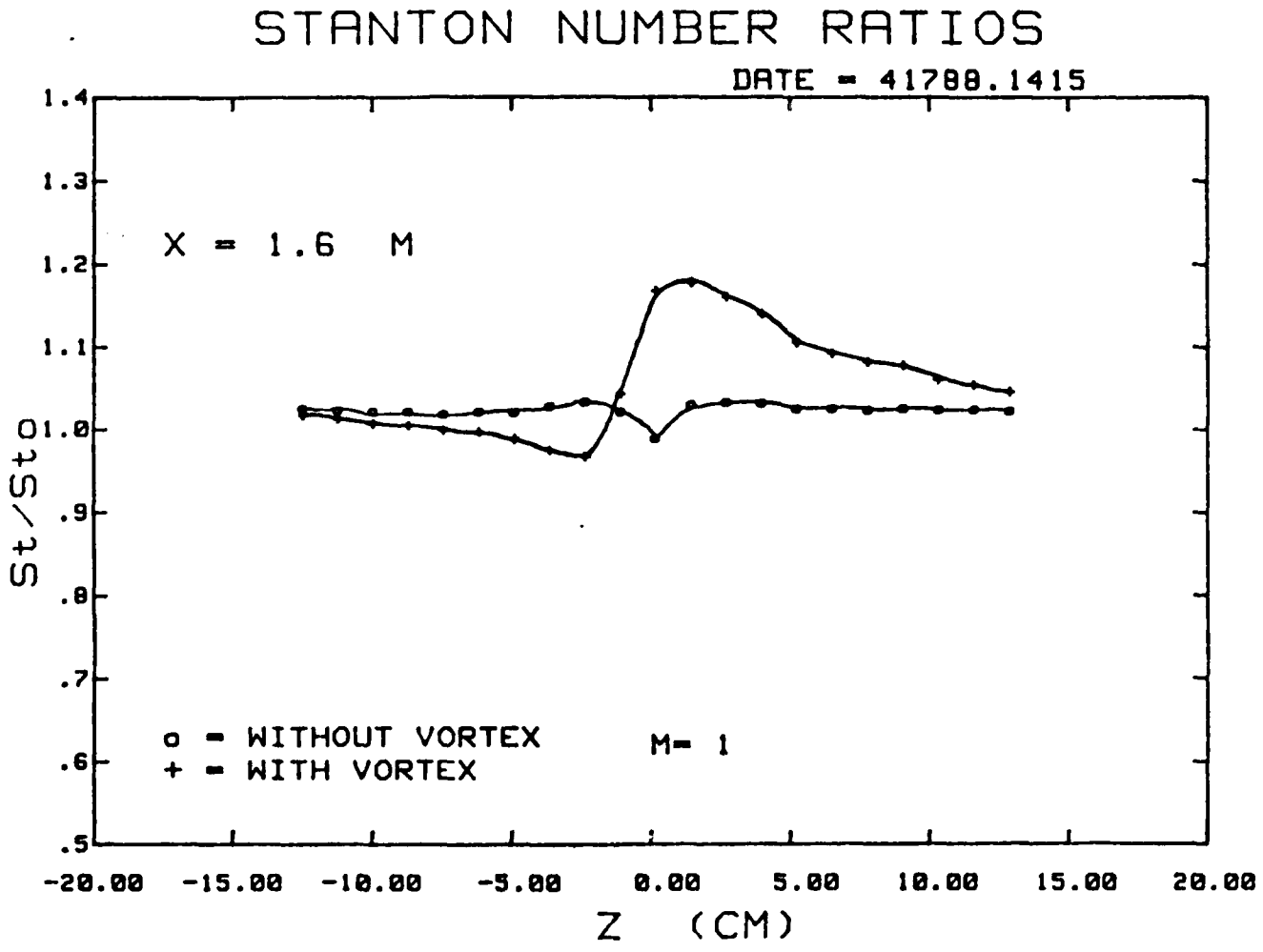

VG 1.5 INCHES FROM C/L, 10 M/S, 3 INJECTION HOLES

Figure 127. Spanwise Variation of Stanton Number Ratios· Vortex #2 Position h

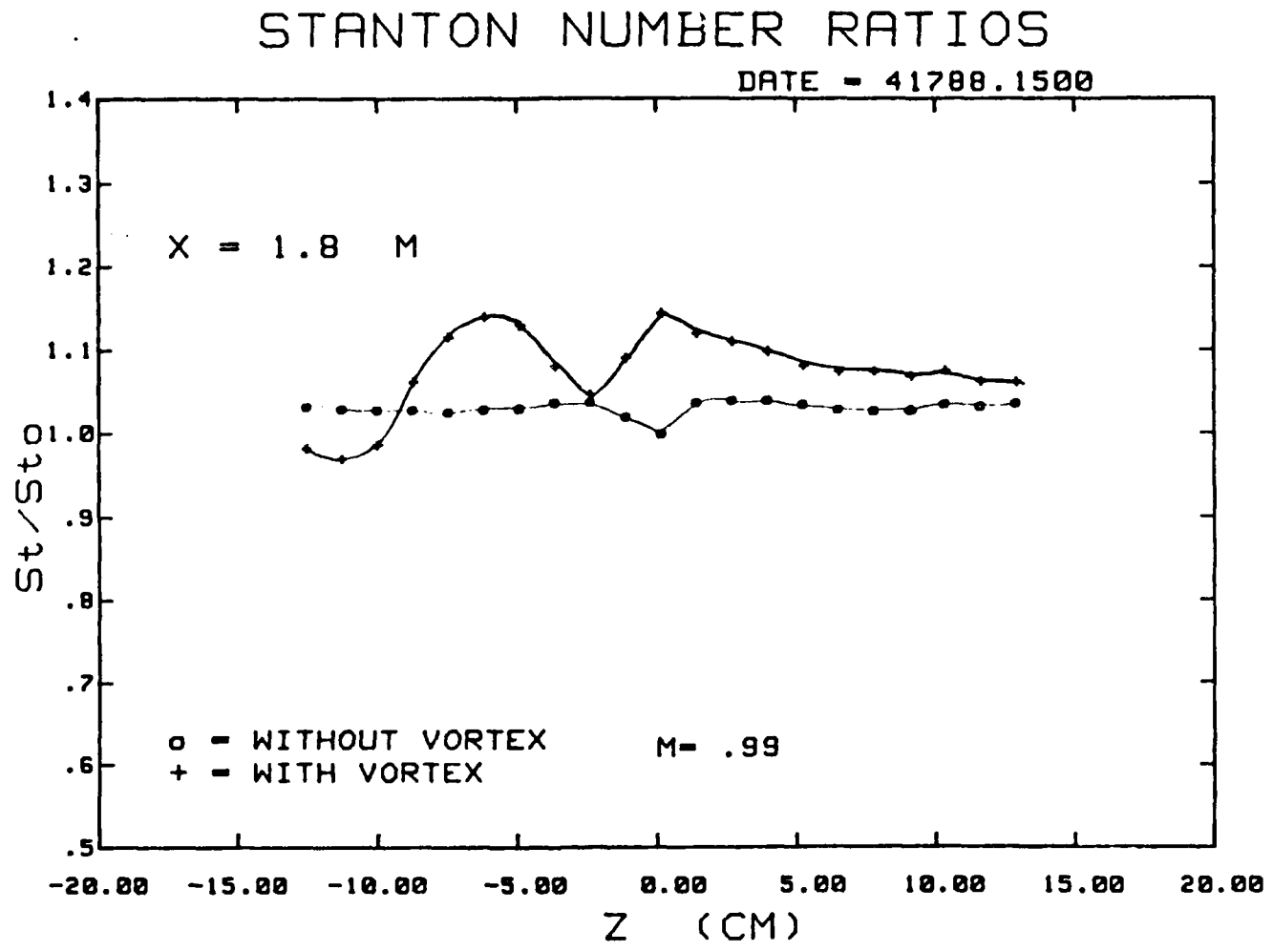

VG -1.5 INCHES FROM C/L, 10 M/S, 3 INJECTION HOLES

Figure 128. Spanwise Variation of Stanton Number Ratios Vortex #2 Position b

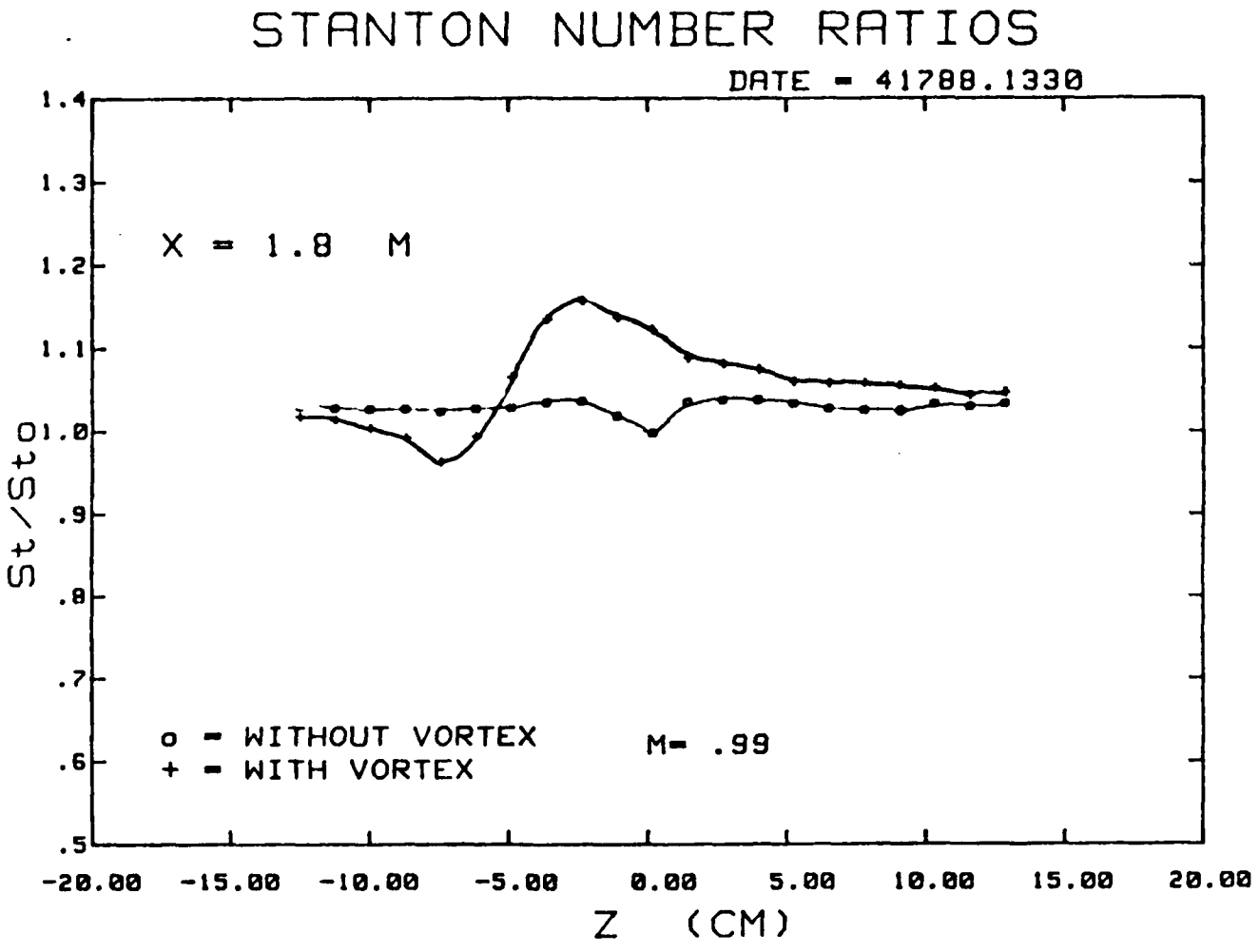

VG 0.0 INCHES FROM C/L, 10 M/S, 3 INJECTION HOLES

Figure 129. Spanwise Variation of Stanton Number Ratios Vortex #2 Position e

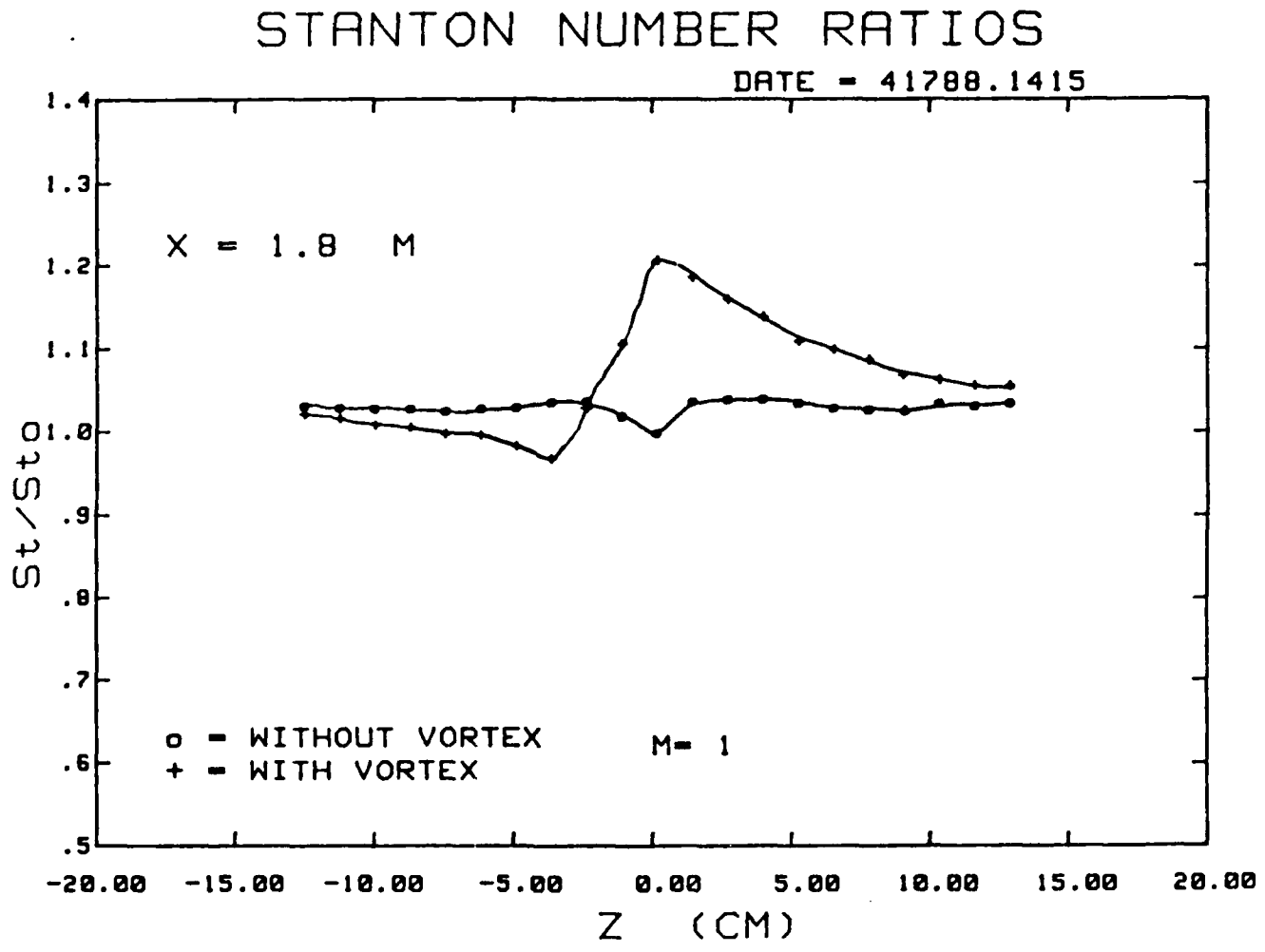

VG 1.5 INCHES FROM C/L, 10 M/S, 3 INJECTION HOLES

Figure 130. Spanwise Variation of Stanton Number Ratios Vortex #2 Position h

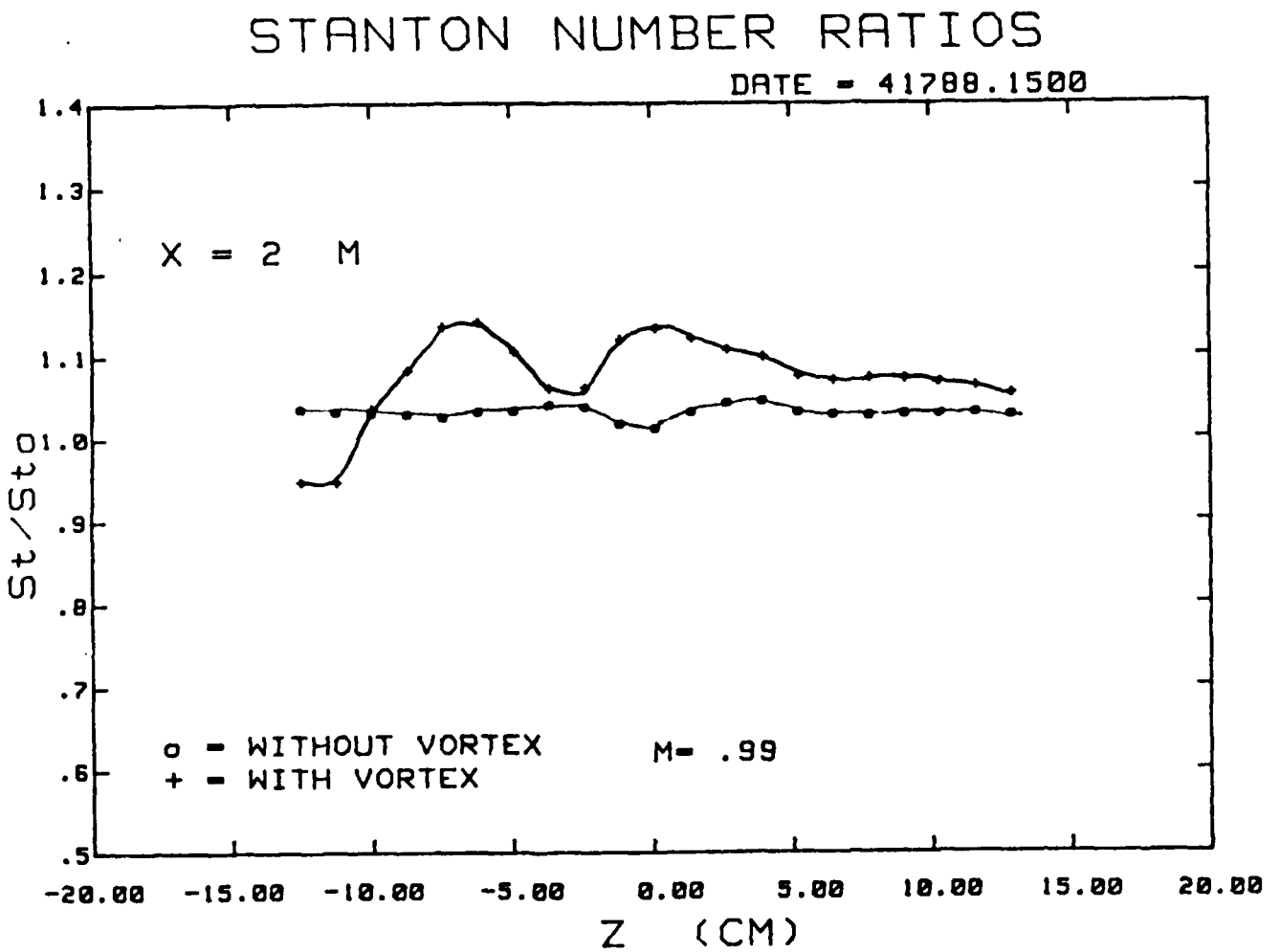

VG -1.5 INCHES FROM C/L, 10 M/S, 3 INJECTION HOLES

Figure 131. Spanwise Variation of Stanton Number Ratios Vortex #2 Position b

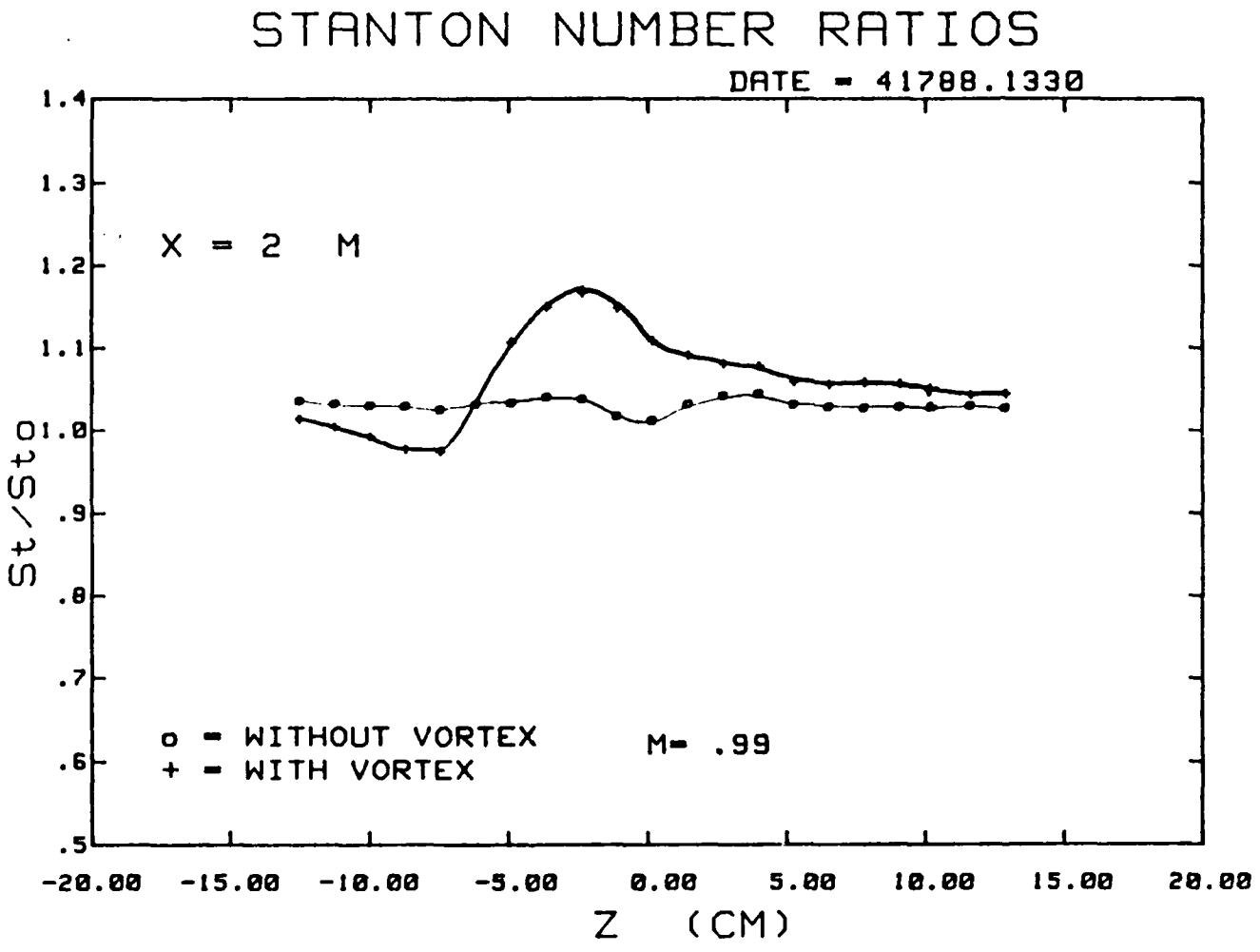

VG 0.0 INCHES FROM C/L, 10 M/S, 3 INJECTION HOLES

Figure 132. Spanwise Variation of Stanton Number Ratios Vortex #2 Position e

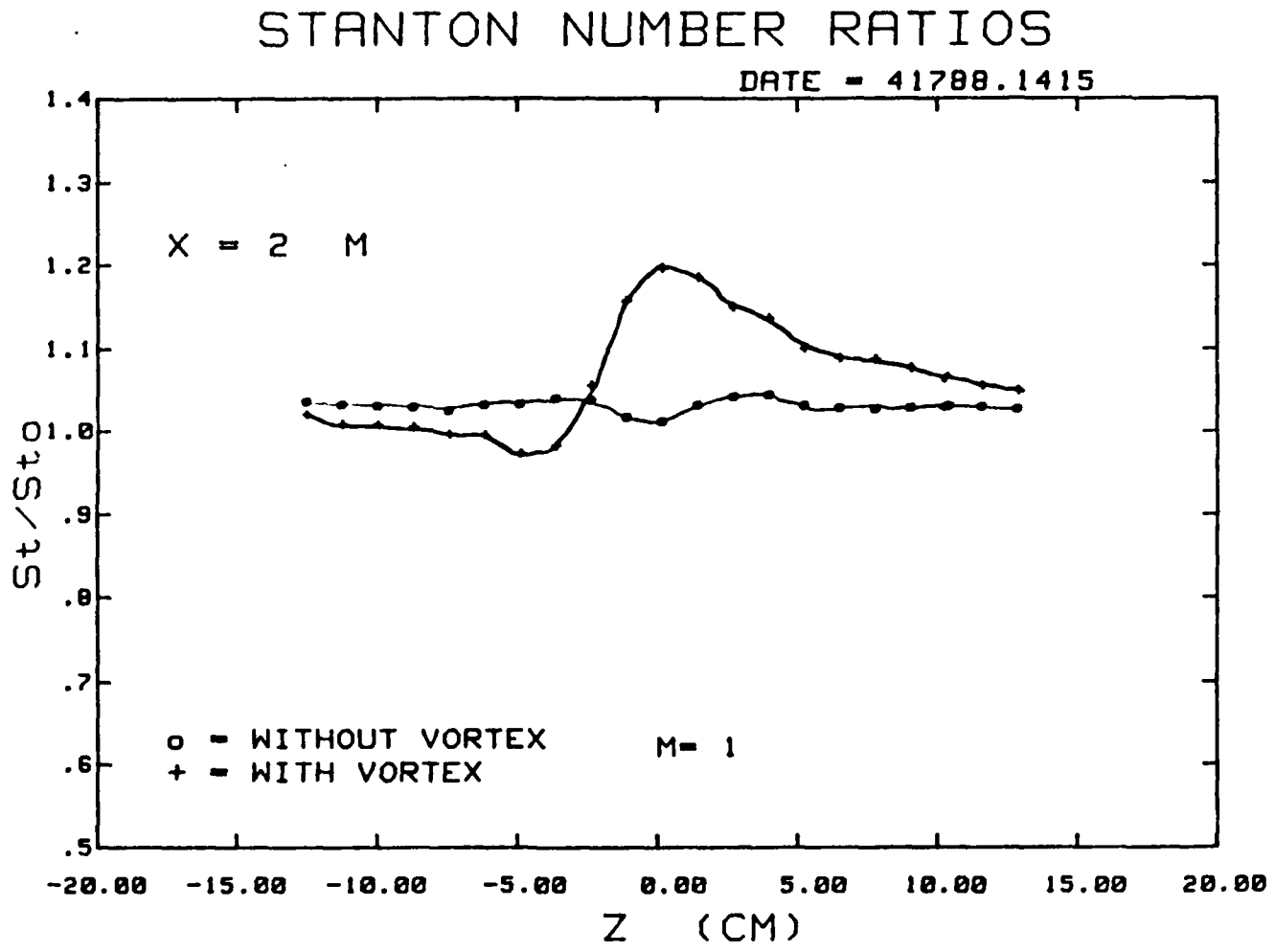

VG 1.5 INCHES FROM C/L, 10 M/S, 3 INJECTION HOLES

Figure 133. Spanwise Variation of Stanton Number Ratios Vortex #2 Position h

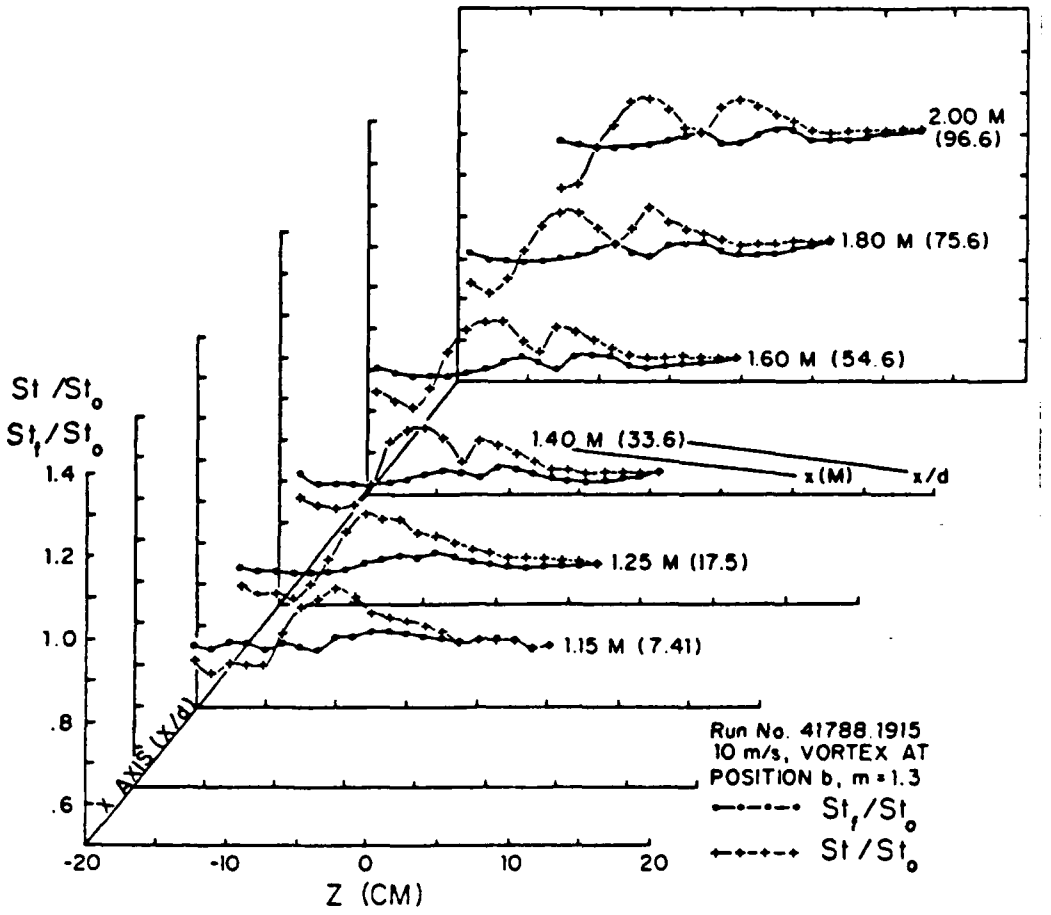

Figure 134. Local Stanton Number Ratios in Boundary Layers with Film Cooling, with and without an Embedded Vortex

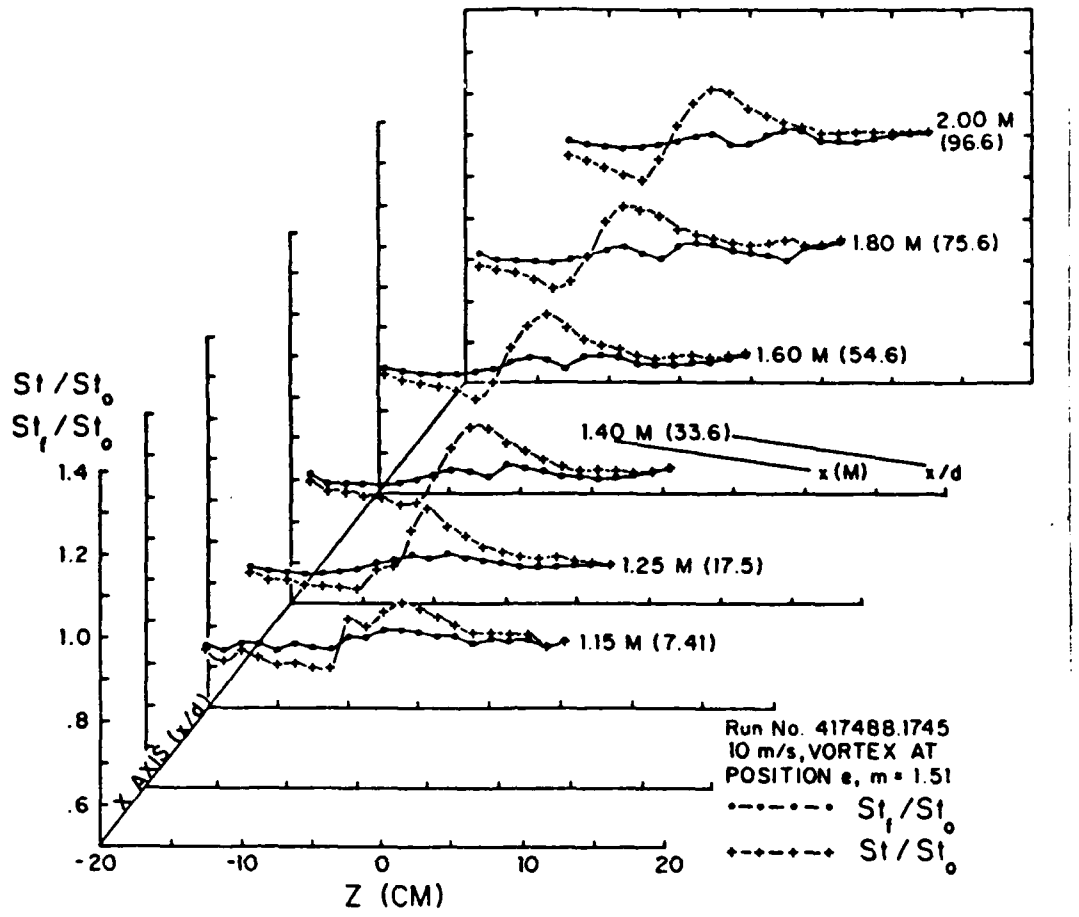

Figure 135. Local Stanton Number Ratios in Boundary Layers with Film Cooling, with and without an Embedded Vortex

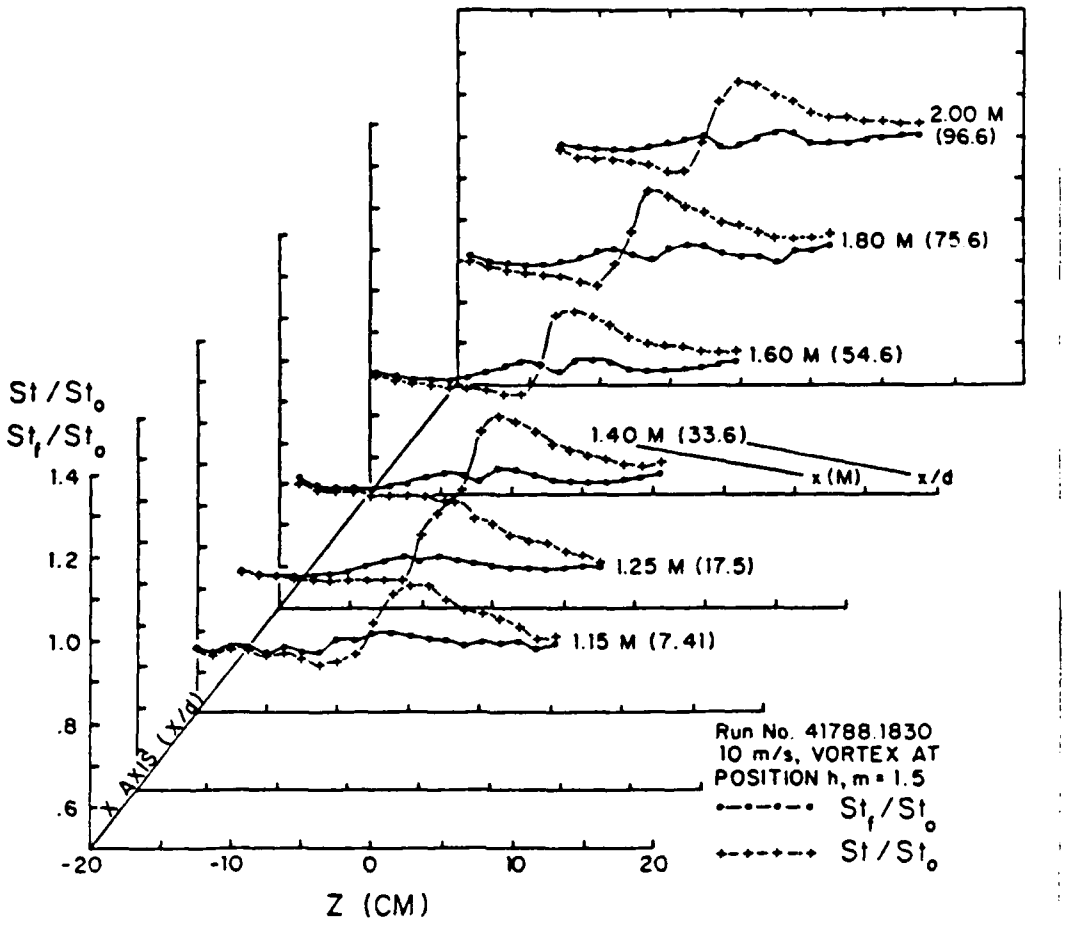

Figure 136. **Local Stanton Number Ratios in Boundary Layers with Film Cooling, with and without an Embedded Vortex**

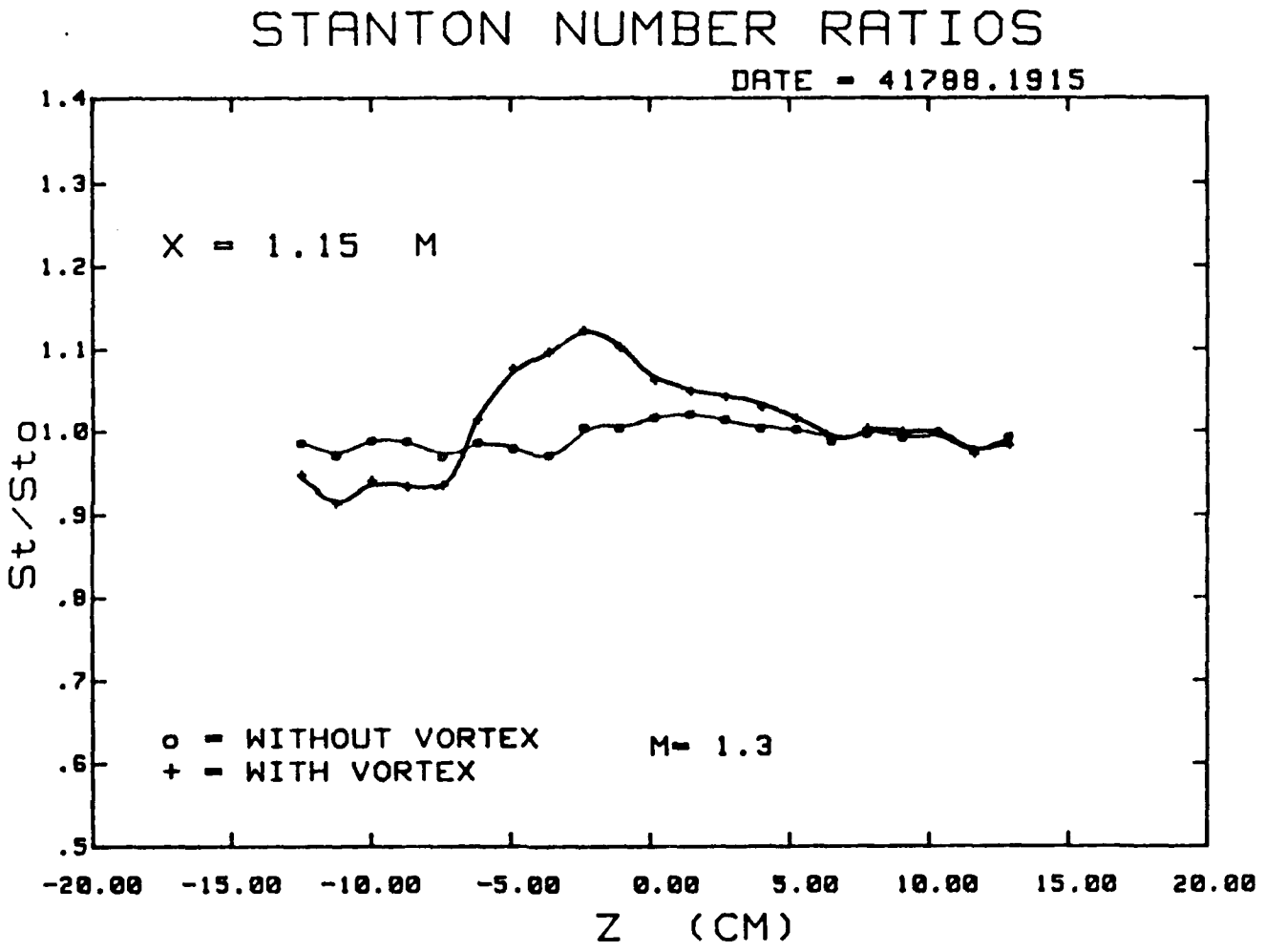

VG -1.5 INCHES FROM C/L, 10 M/S, 3 INJECTION HOLES

Figure 137. Spanwise Variation of Stanton Number Ratios Vortex #2 Position b

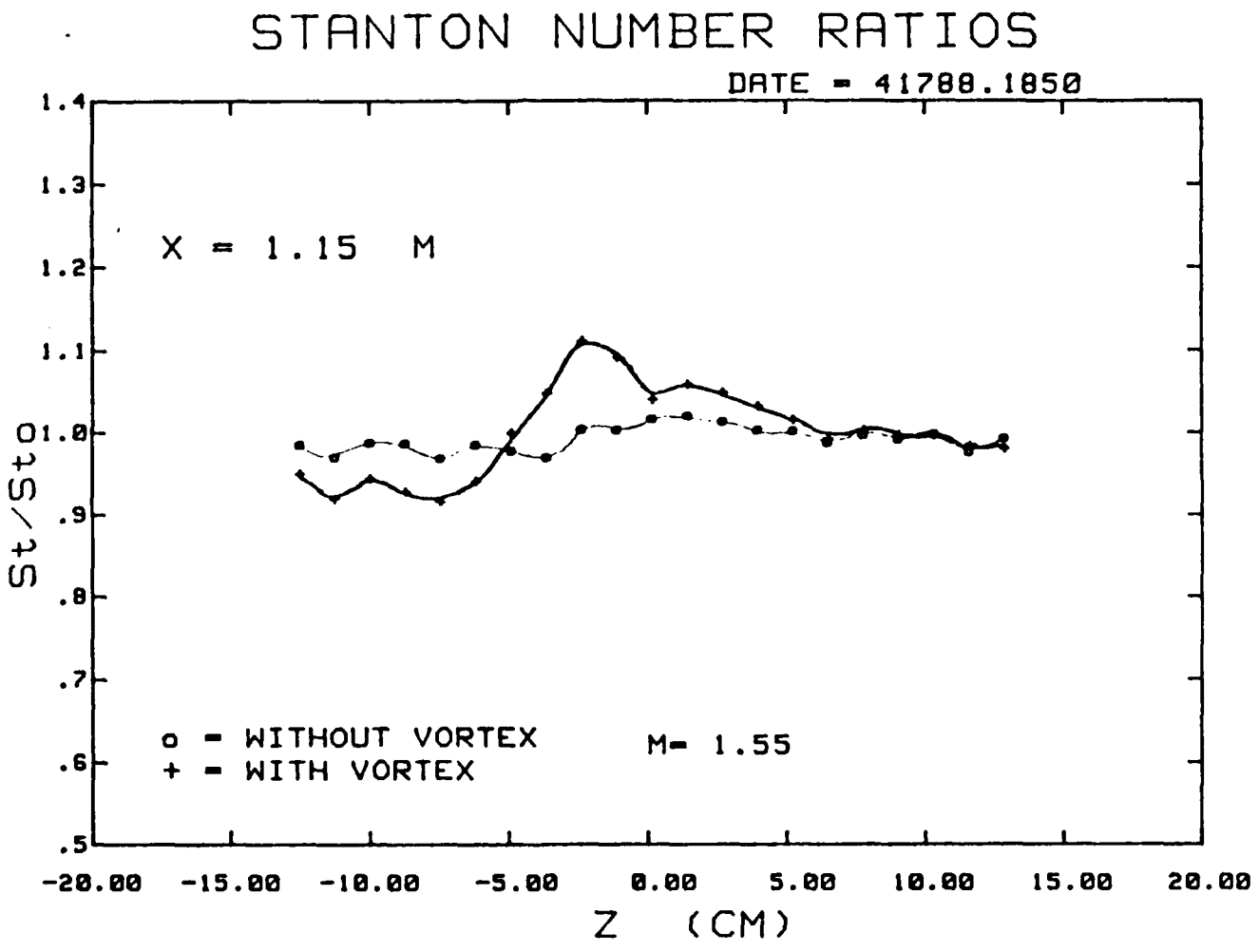

VG -1.0 INCHES FROM C/L, 10 M/S, 3 INJECTION HOLES

Figure 138. Spanwise Variation of Stanton Number Ratios
Vortex #2 Position c

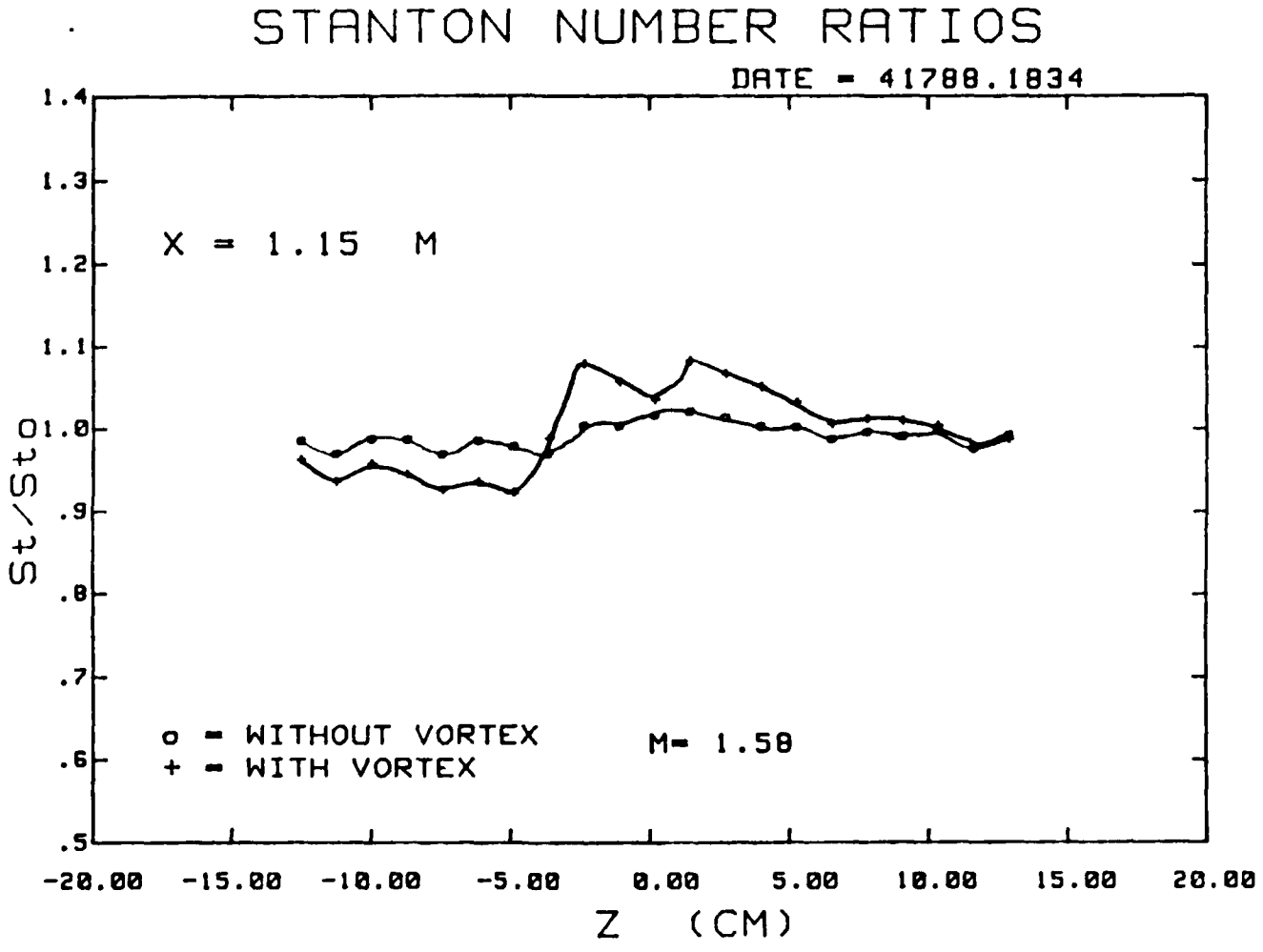

VG -.5 INCHES FROM C/L, 10 M/S, 3 INJECTION HOLES

Figure 139. Spanwise Variation of Stanton Number Ratios Vortex #2 Position d

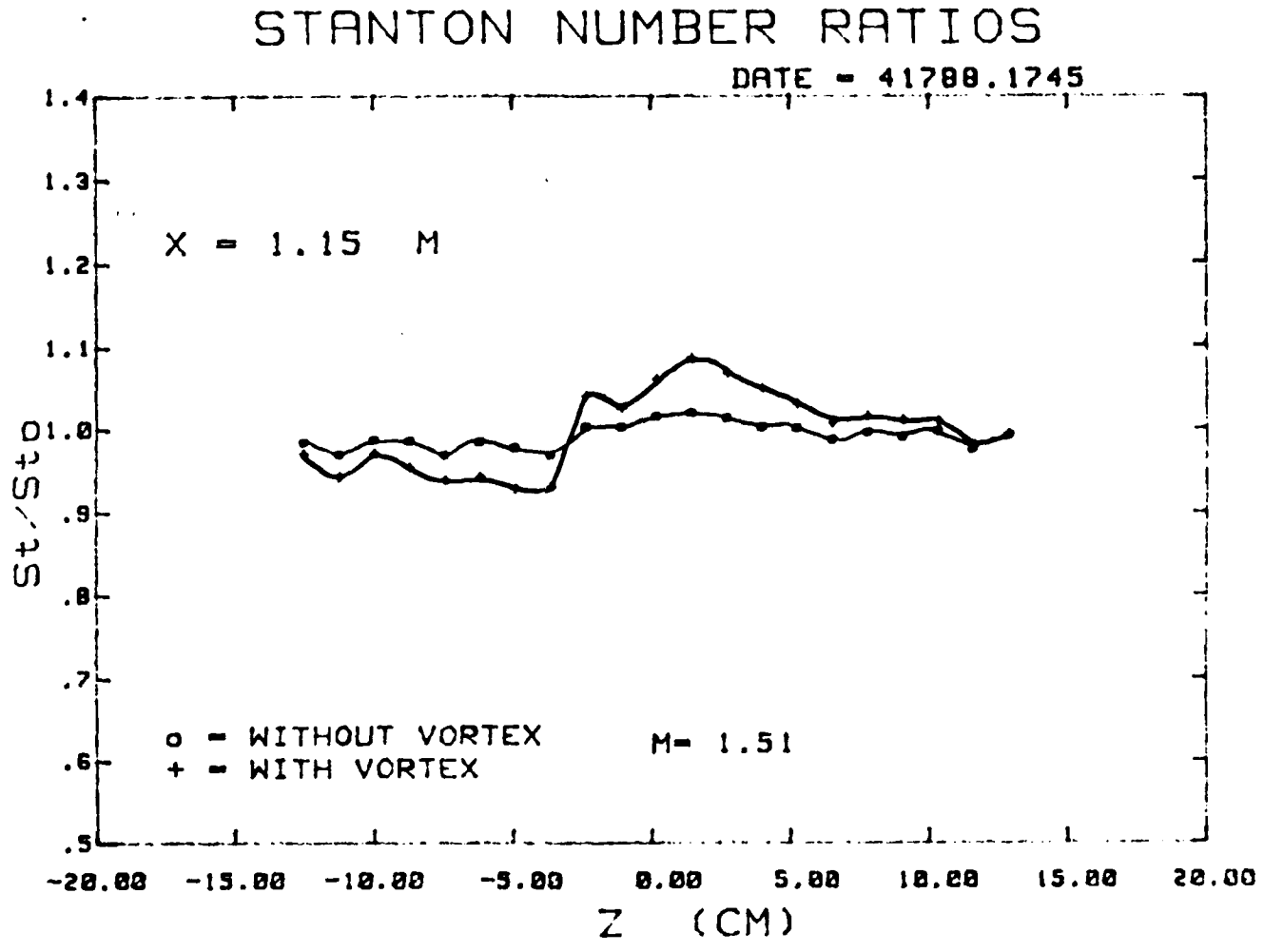

VG 0.0 INCHES FROM C/L, 10 M/S, 3 INJECTION HOLES

Figure 140. Spanwise Variation of Stanton Number Ratios
Vortex #2 Position e

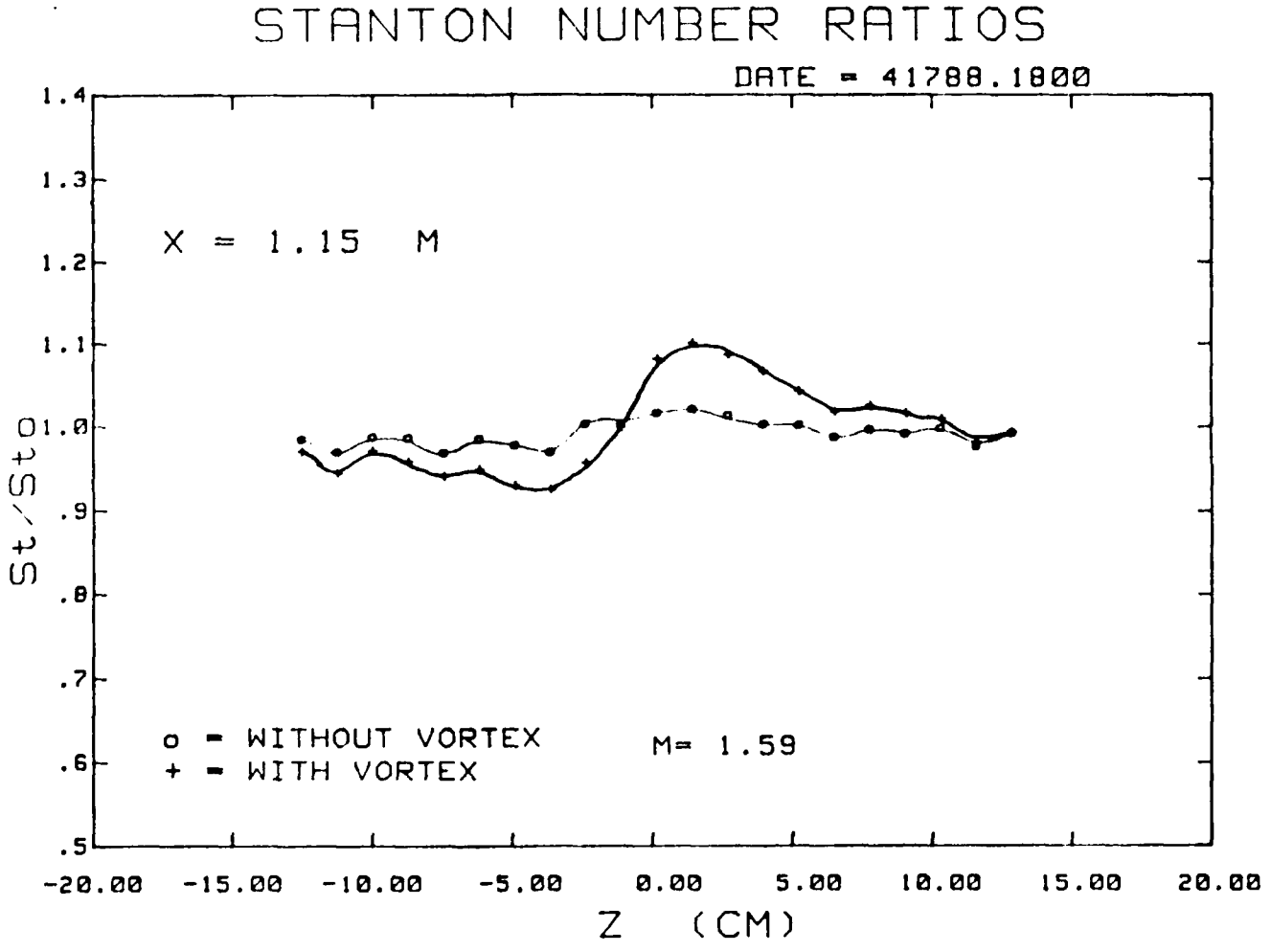

VG 0.5 INCHES FROM C/L, 10 M/S, 3 INJECTION HOLES

Figure 141. Spanwise Variation of Stanton Number Ratios Vortex #2 Position f

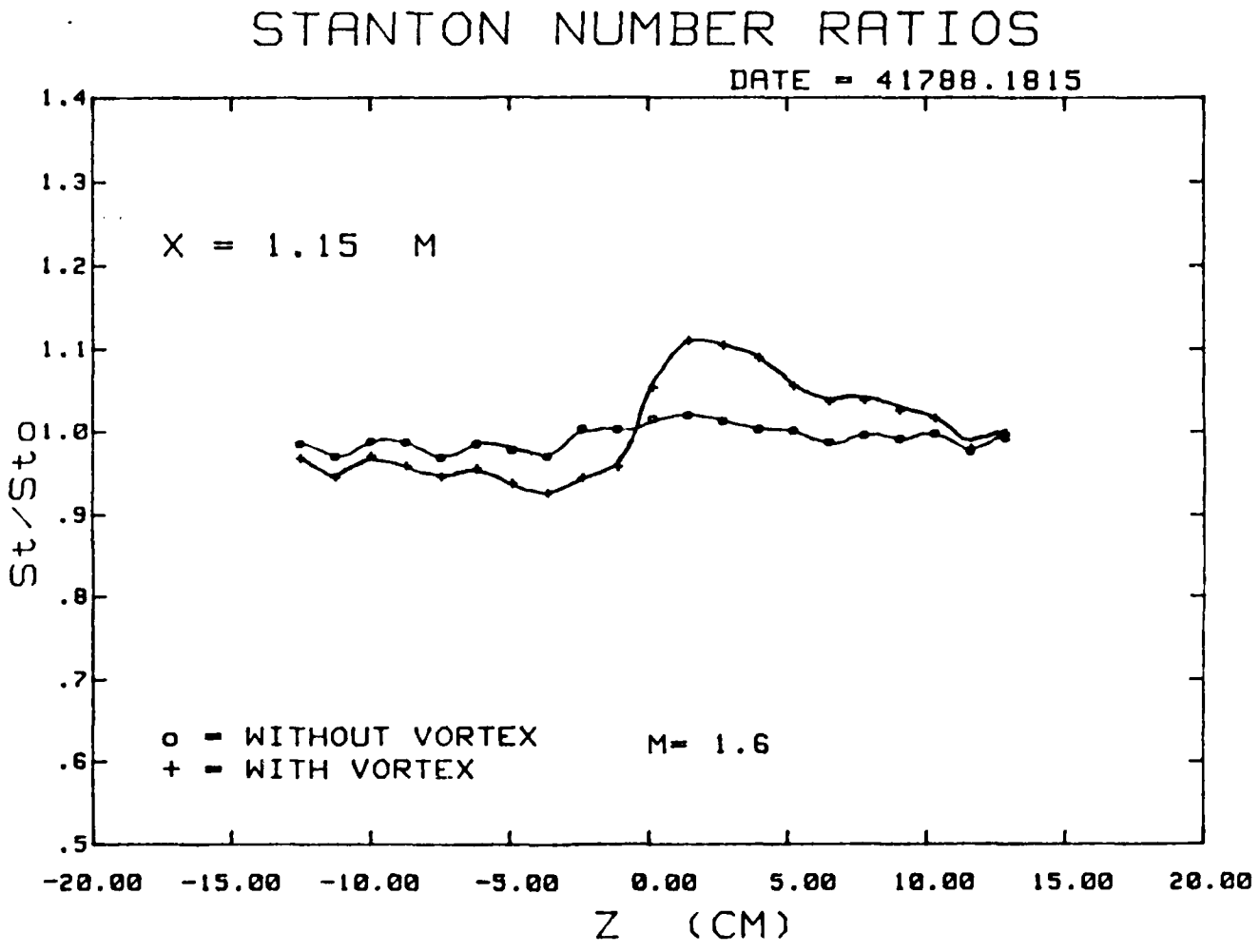

VG 1.0 INCHES FROM C/L, 10 M/S, 3 INJECTION HOLES

Figure 142. Spanwise Variation of Stanton Number Ratios
Vortex #2 Position g

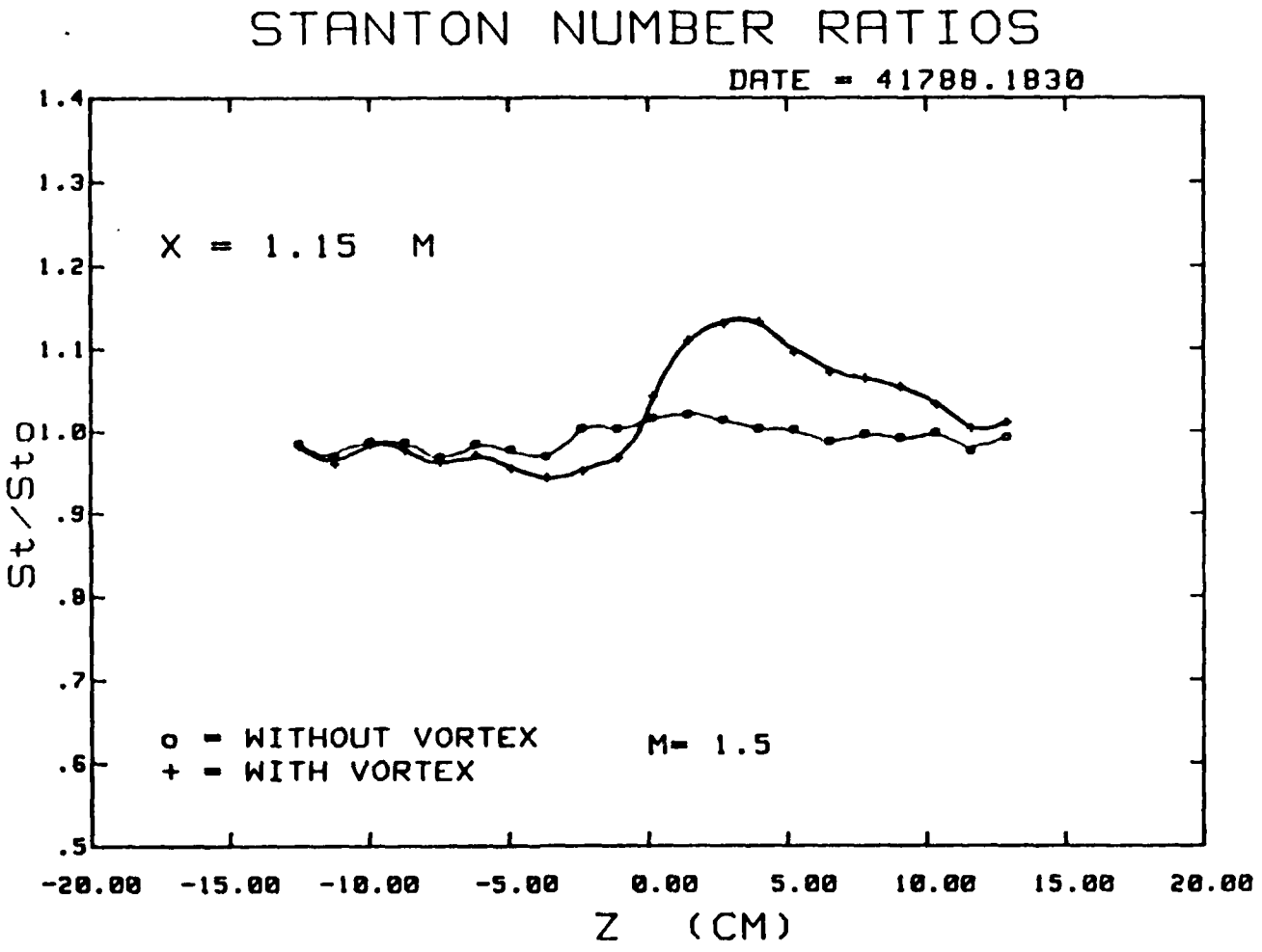

VG 1.5 INCHES FROM C/L, 10 M/S, 3 INJECTION HOLES

Figure 143. Spanwise Variation of Stanton Number Ratios
Vortex #2 Position h

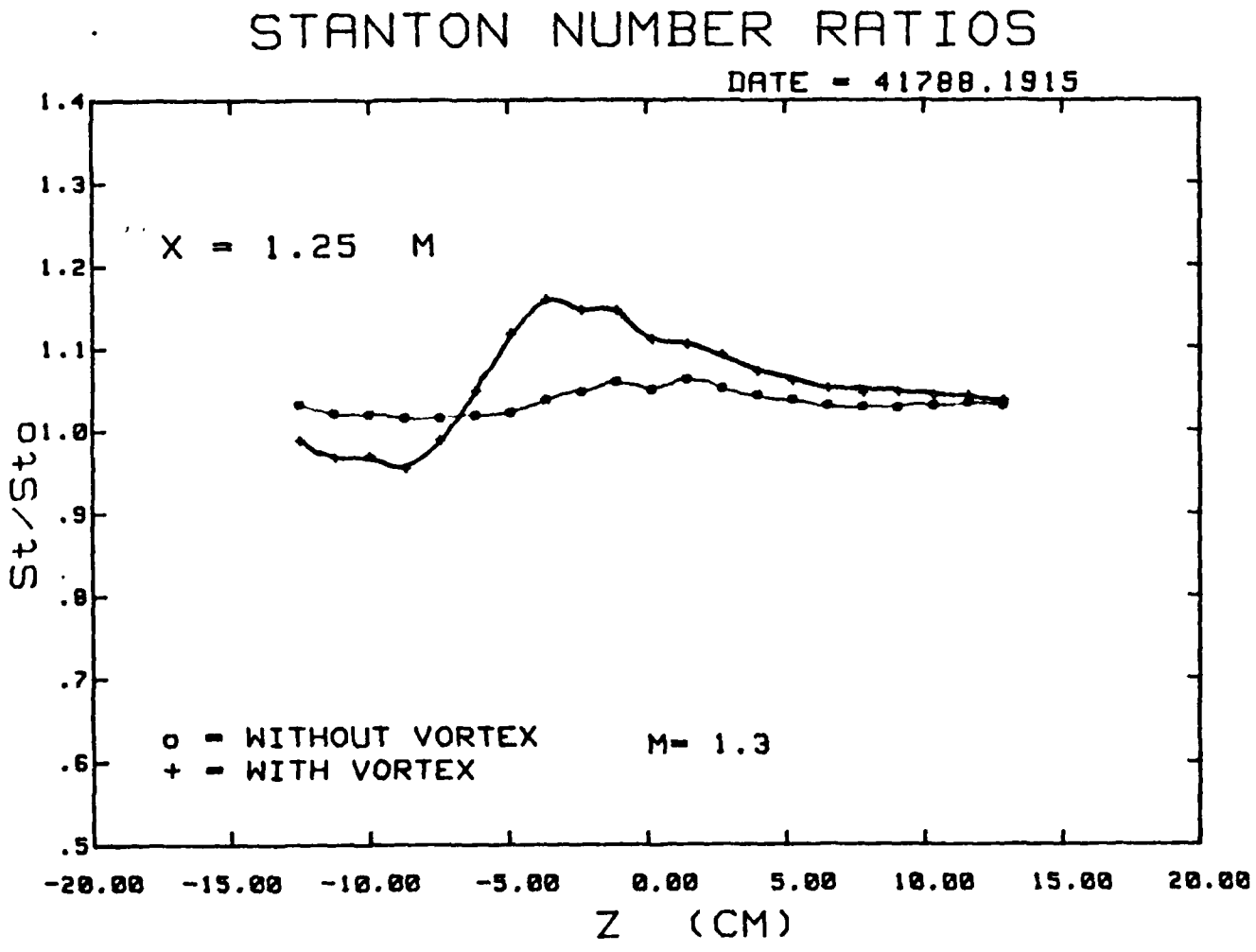

VG -1.5 INCHES FROM C/L, 10 M/S, 3 INJECTION HOLES

Figure 144. Spanwise Variation of Stanton Number Ratios Vortex #2 Position b

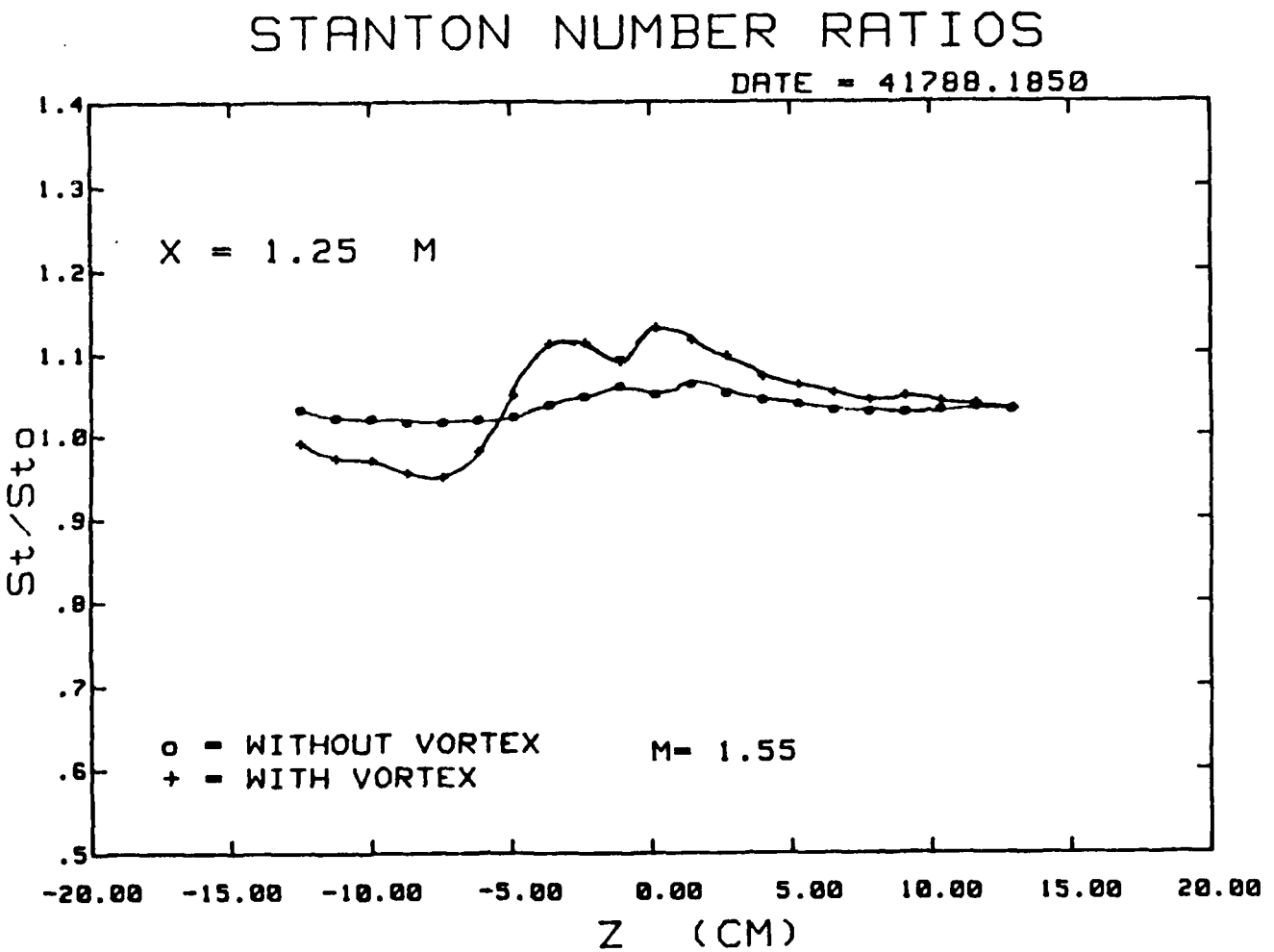

VG -1.0 INCHES FROM C/L, 10 M/S, 3 INJECTION HOLES

Figure 145. Spanwise Variation of Stanton Number Ratios
Vortex #2 Position c

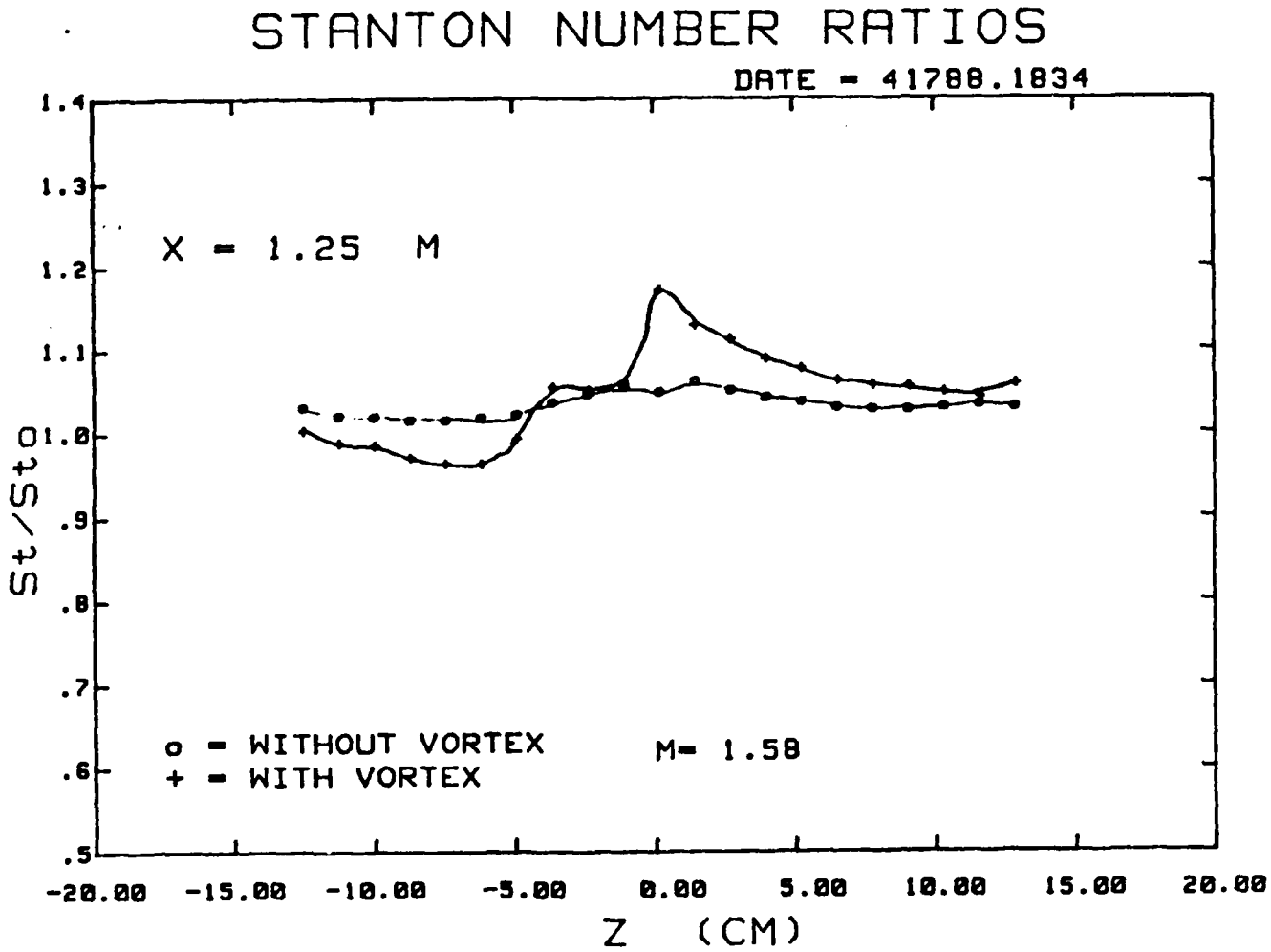

VG -.5 INCHES FROM C/L, 10 M/S, 3 INJECTION HOLES

Figure 146. Spanwise Variation of Stanton Number Ratios Vortex #2 Position d

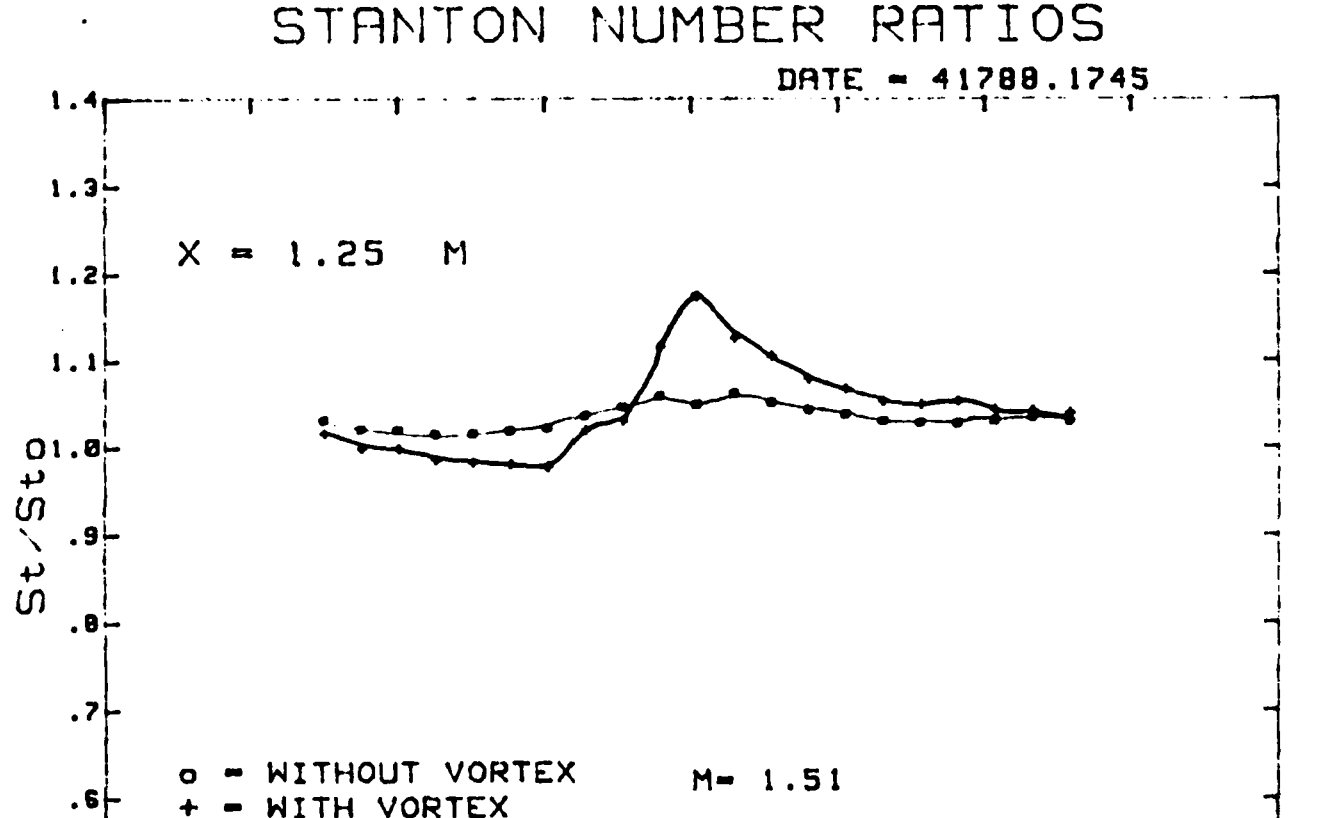

VG 0.0 INCHES FROM C/L, 10 M/S, 3 INJECTION HOLES

Figure 147. Spanwise Variation of Stanton Number Ratios Vortex #2 Position e

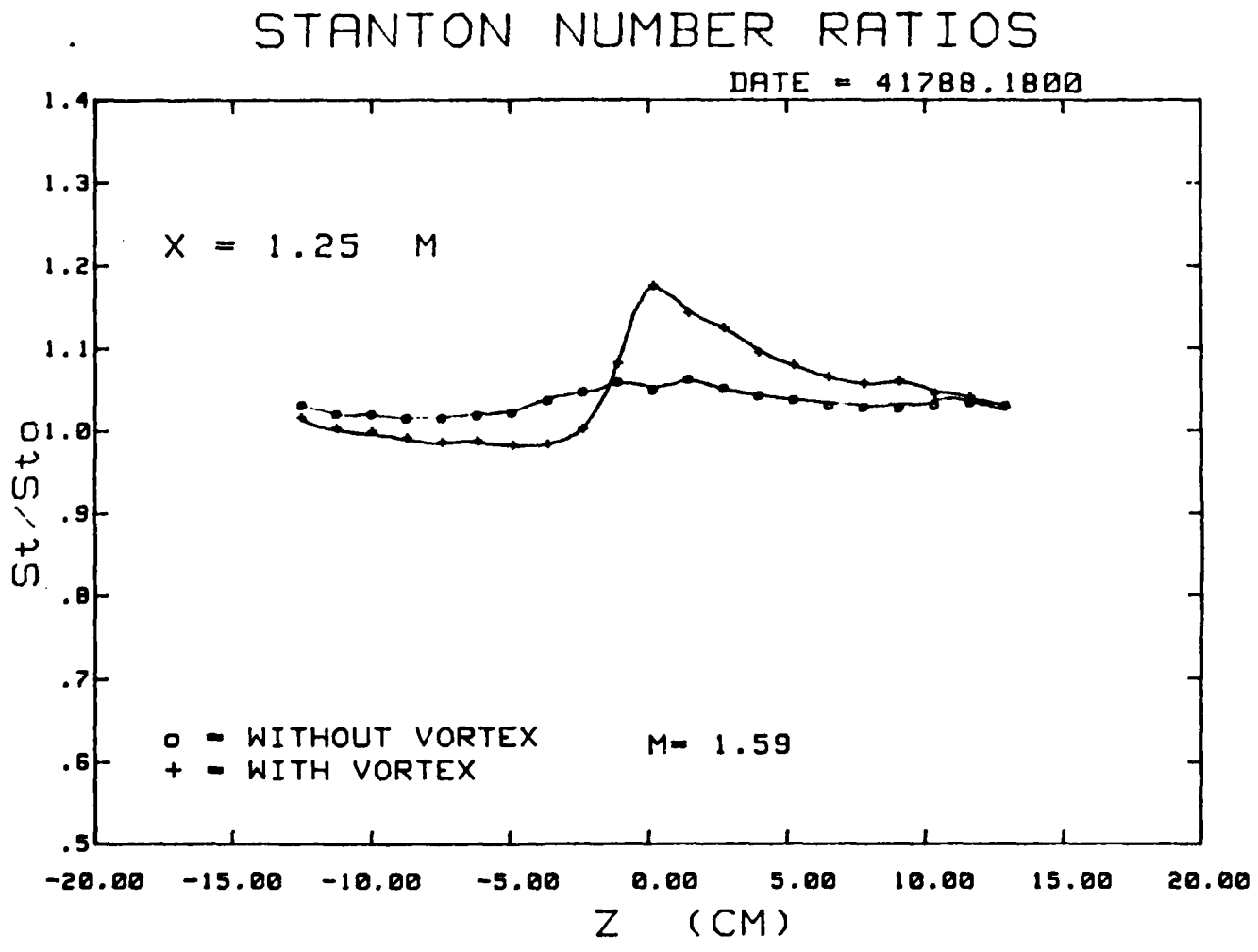

VG 0.5 INCHES FROM C/L, 10 M/S, 3 INJECTION HOLES

Figure 148. Spanwise Variation of Stanton Number Ratios Vortex #2 Position f

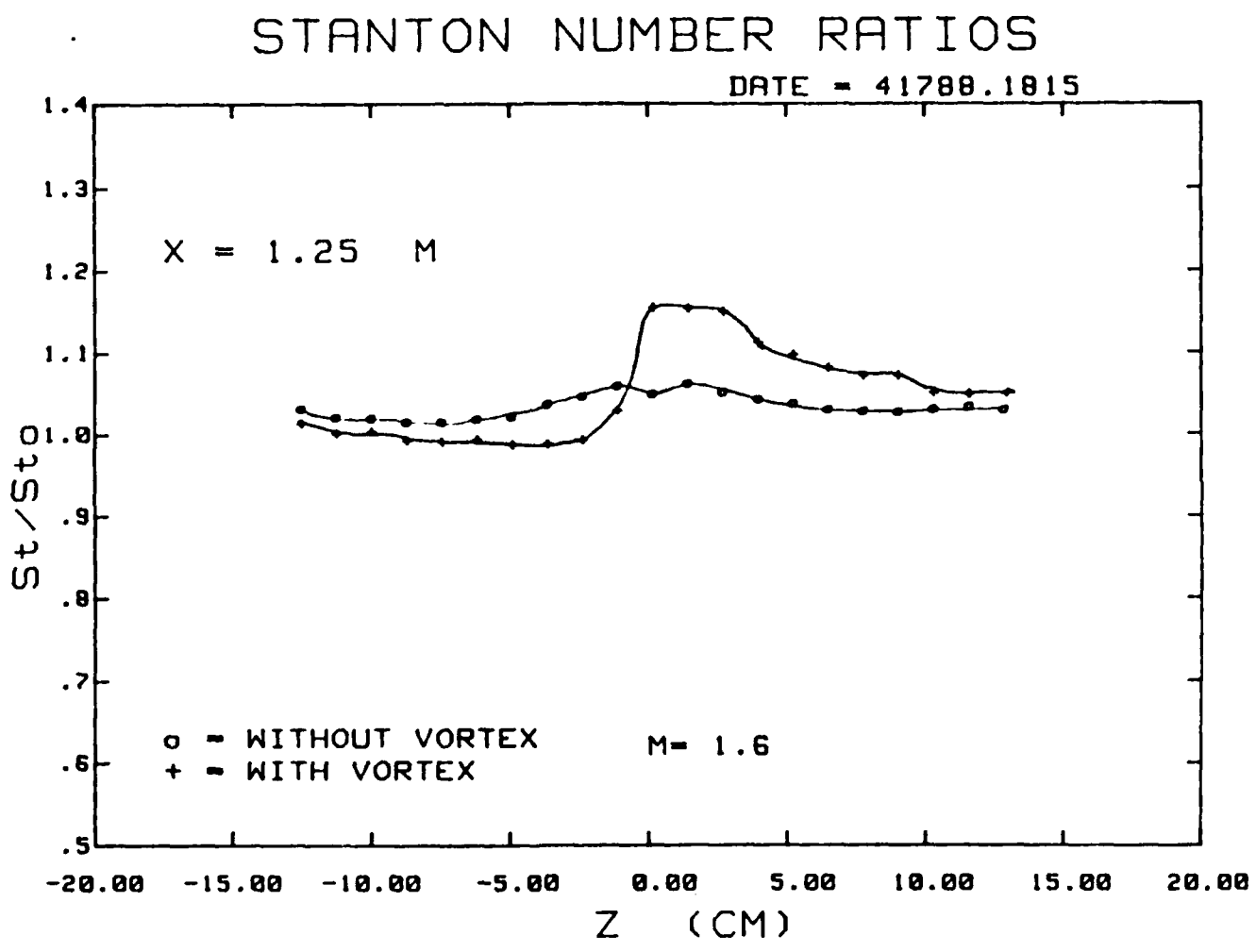

VG 1.0 INCHES FROM C/L, 10 M/S, 3 INJECTION HOLES

Figure 149. Spanwise Variation of Stanton Number Ratios Vortex #2 Position g

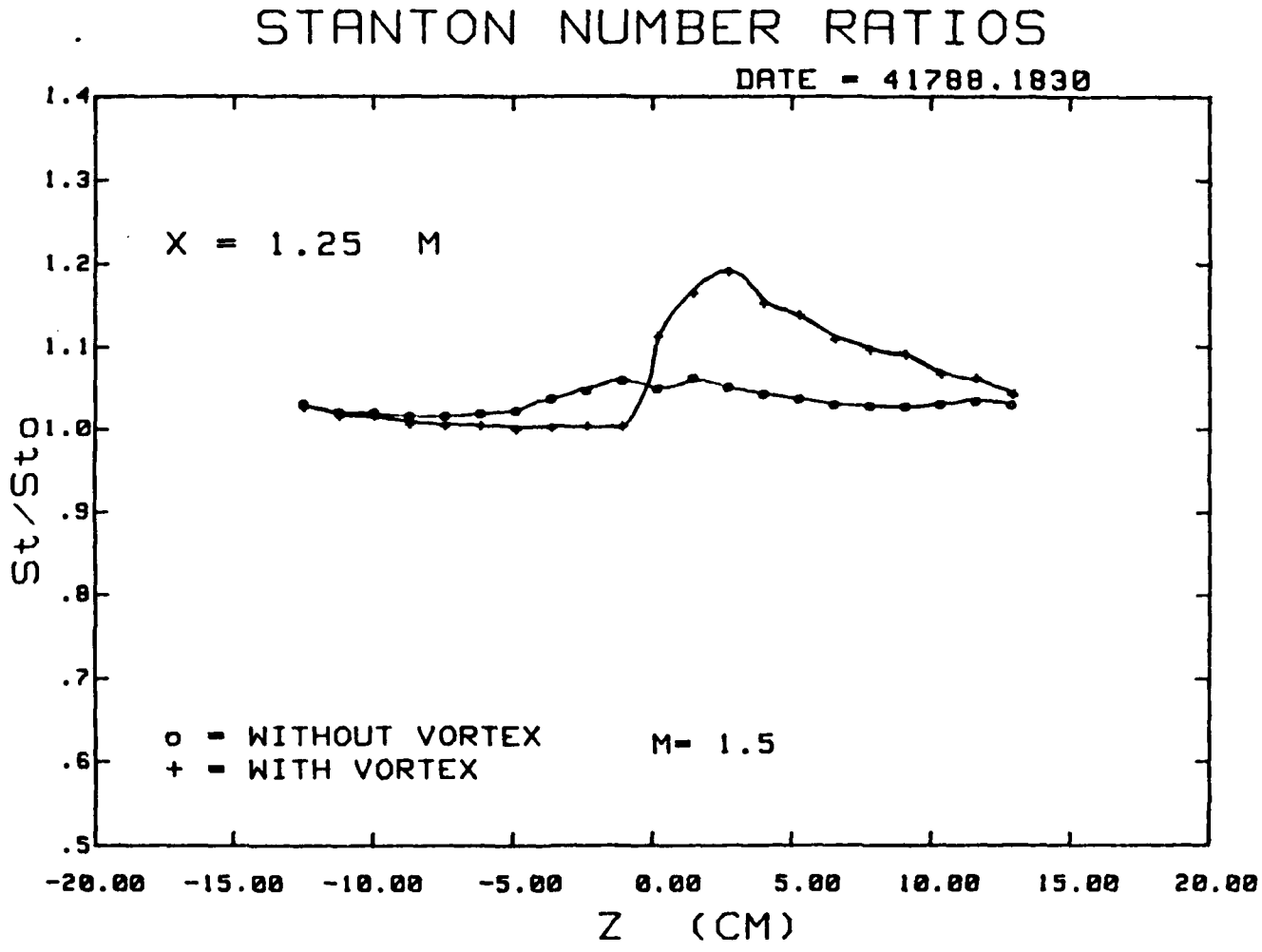

VG 1.5 INCHES FROM C/L, 10 M/S, 3 INJECTION HOLES

Figure 150. Spanwise Variation of Stanton Number Ratios
Vortex #2 Position h

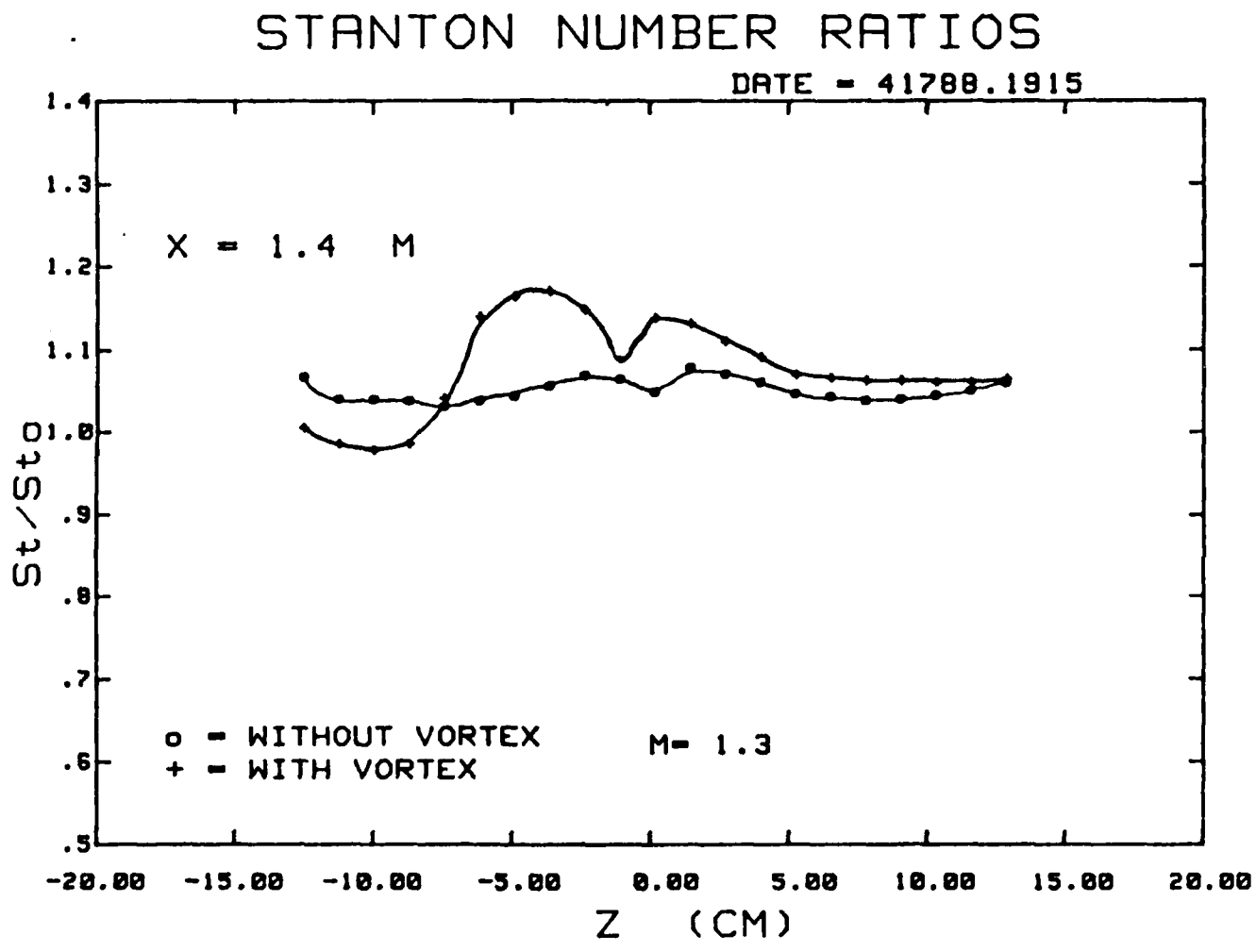

VG -1.5 INCHES FROM C/L, 10 M/S, 3 INJECTION HOLES

Figure 151. Spanwise Variation of Stanton Number Ratios
Vortex #2 Position b

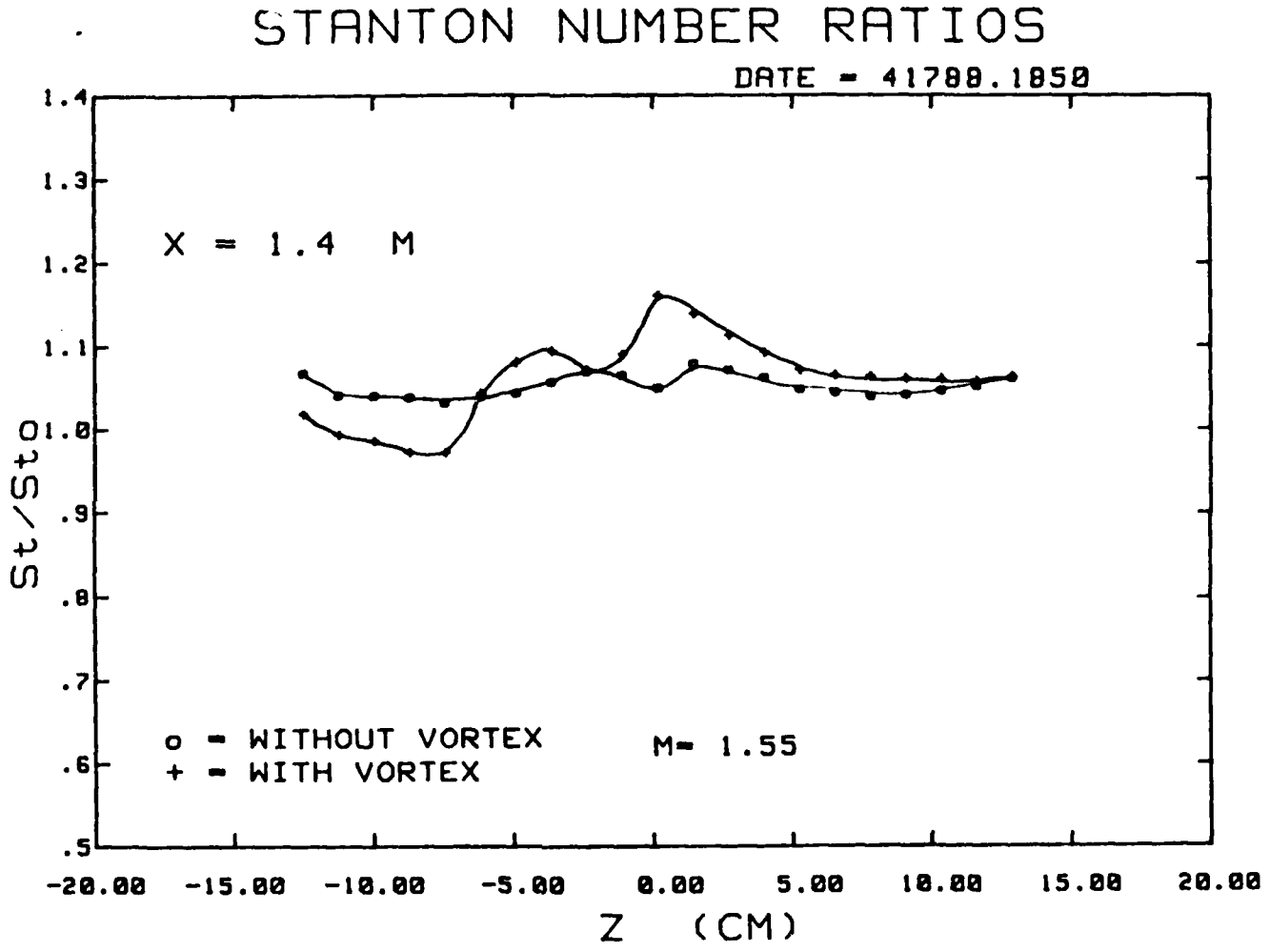

VG -1.0 INCHES FROM C/L, 10 M/S, 3 INJECTION HOLES

Figure 152. Spanwise Variation of Stanton Number Ratios Vortex #2 Position c

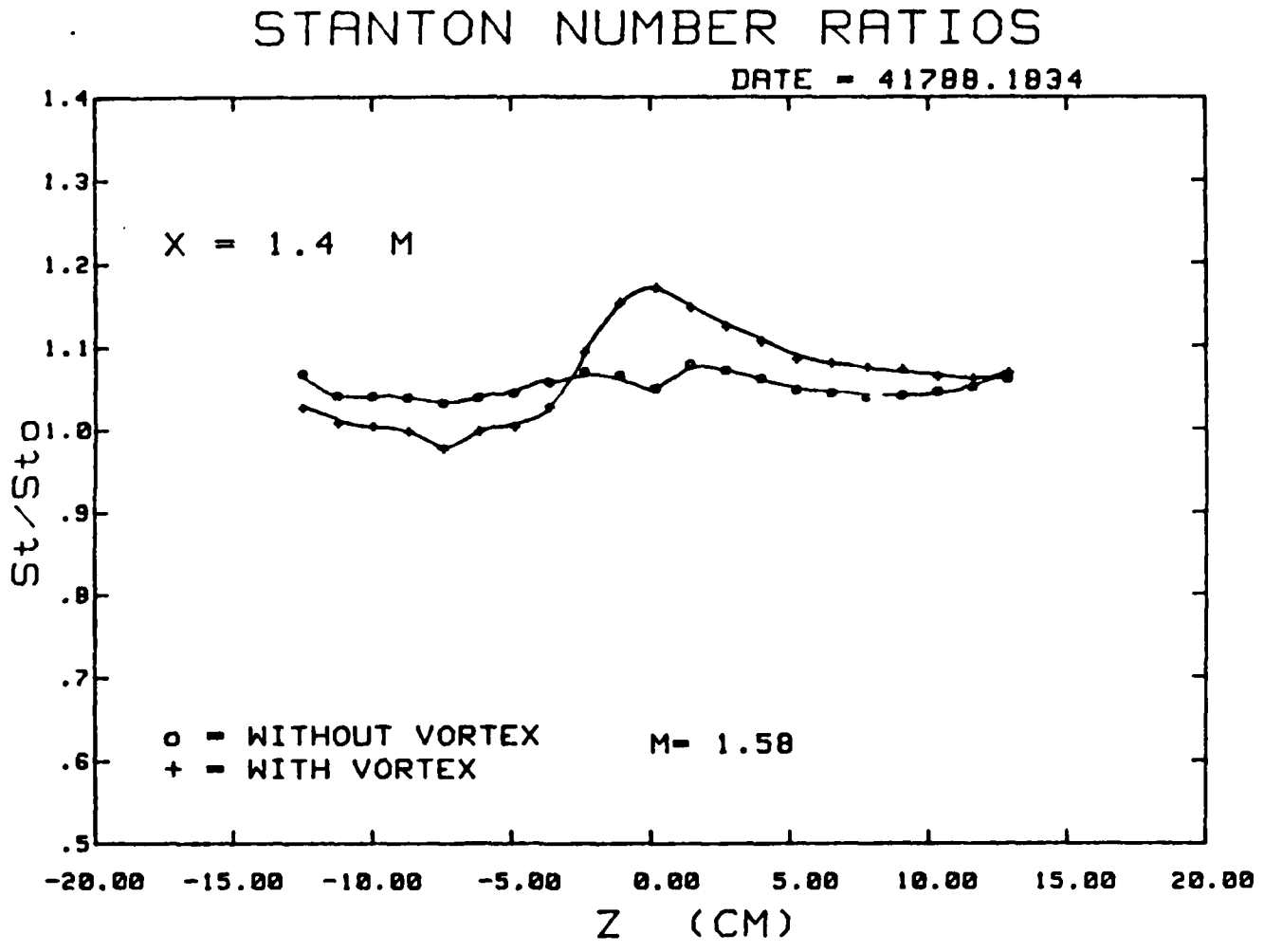

VG -.5 INCHES FROM C/L, 10 M/S, 3 INJECTION HOLES

Figure 153. Spanwise Variation of Stanton Number Ratios Vortex #2 Position d

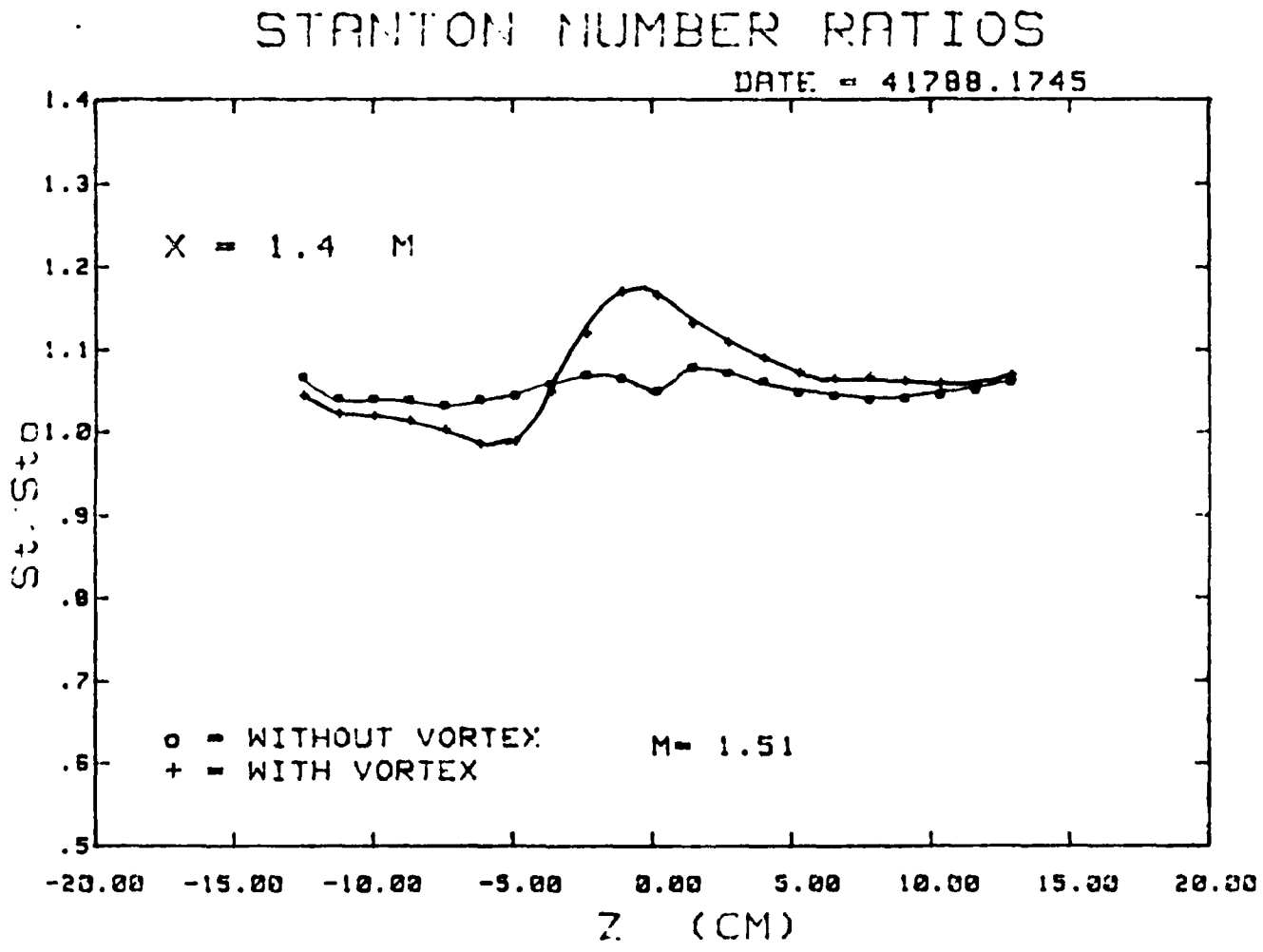

VG 0.0 INCHES FROM C/L, 10 M/S, 3 INJECTION HOLES

Figure 154. Spanwise Variation of Stanton Number Ratios Vortex #2 Position e

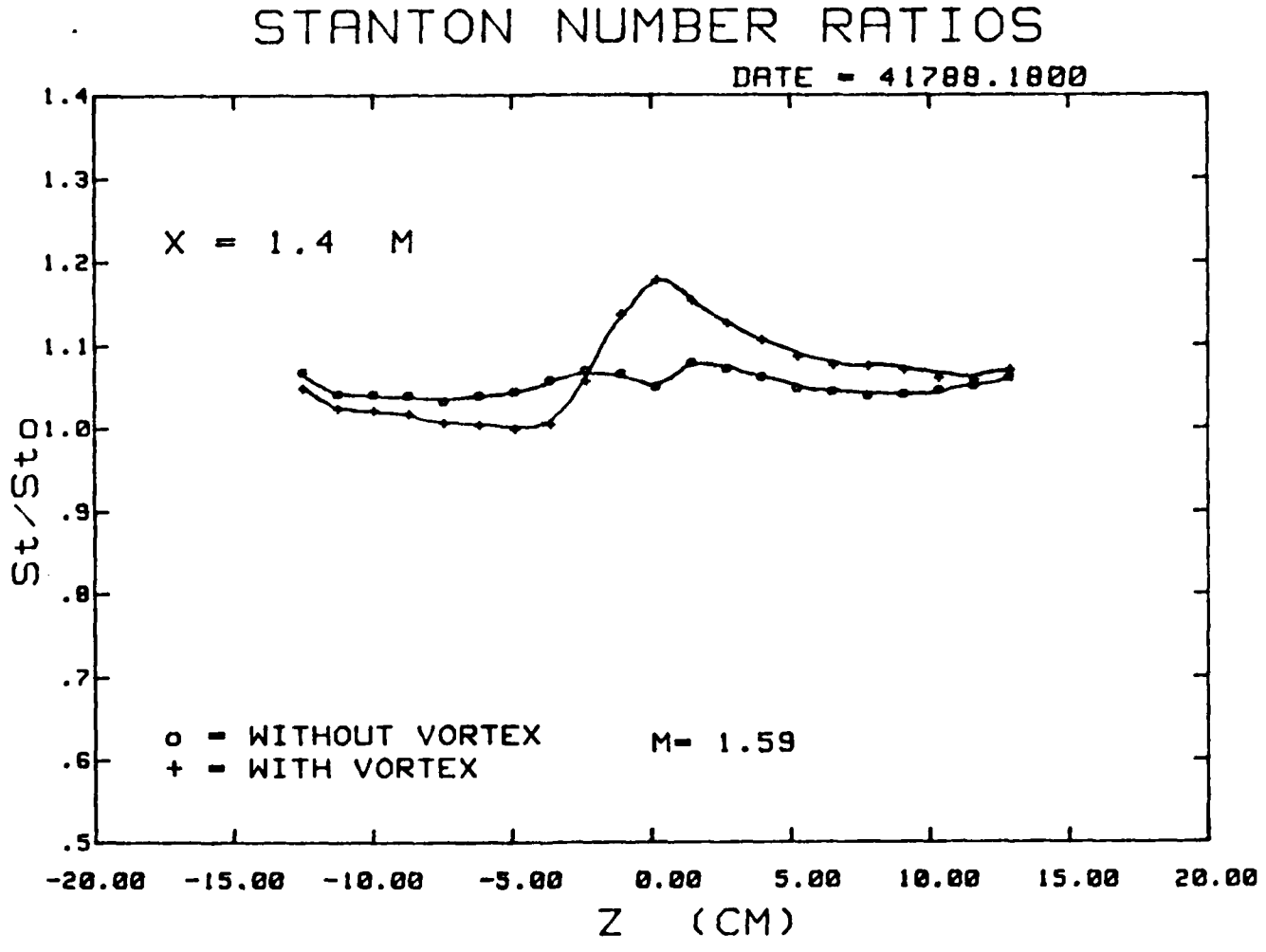

VG 0.5 INCHES FROM C/L, 10 M/S, 3 INJECTION HOLES

Figure 155. Spanwise Variation of Stanton Number Ratios· Vortex #2 Position f

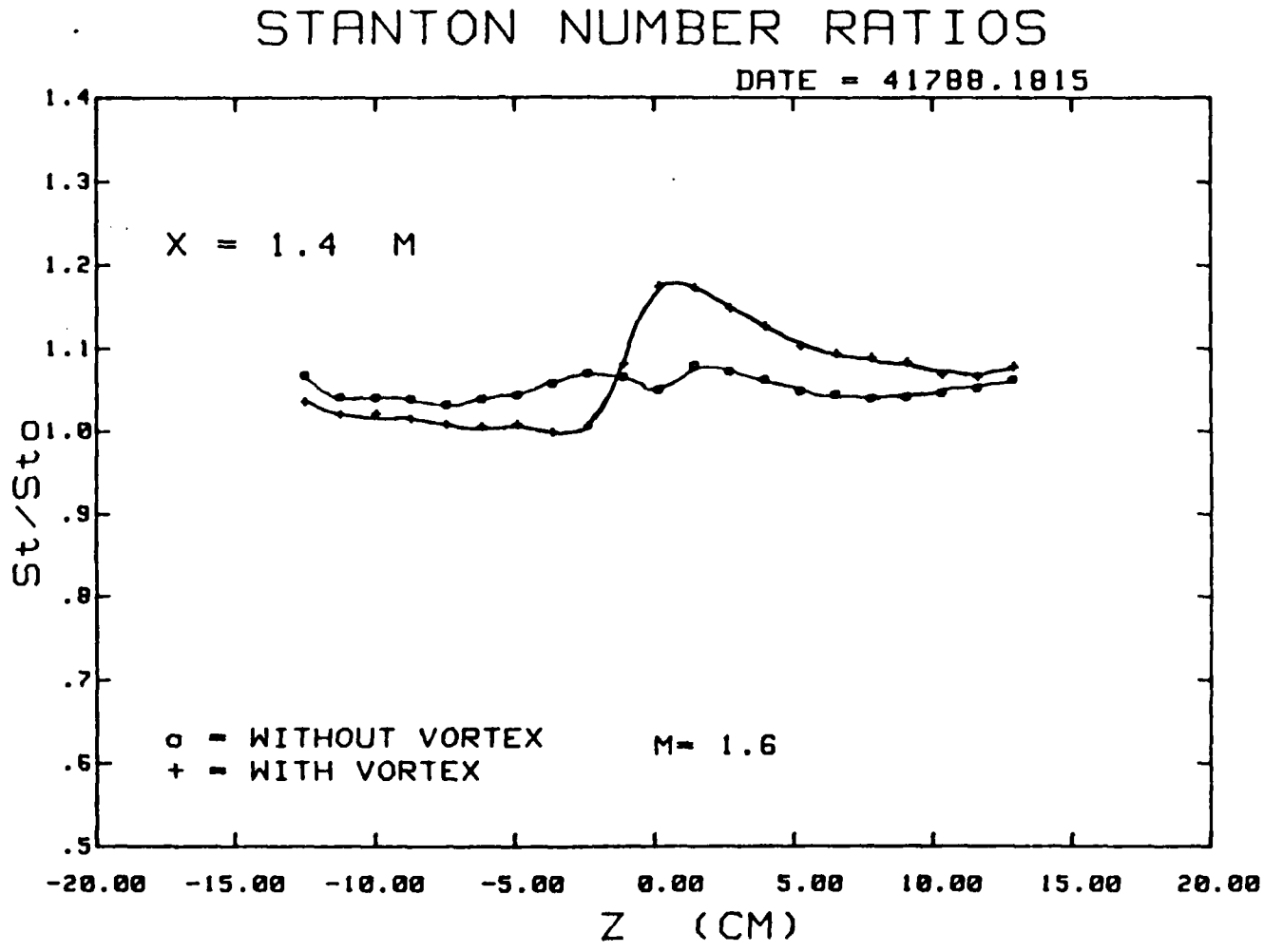

VG 1.0 INCHES FROM C/L, 10 M/S, 3 INJECTION HOLES

Figure 156. Spanwise Variation of Stanton Number Ratios Vortex #2 Position g

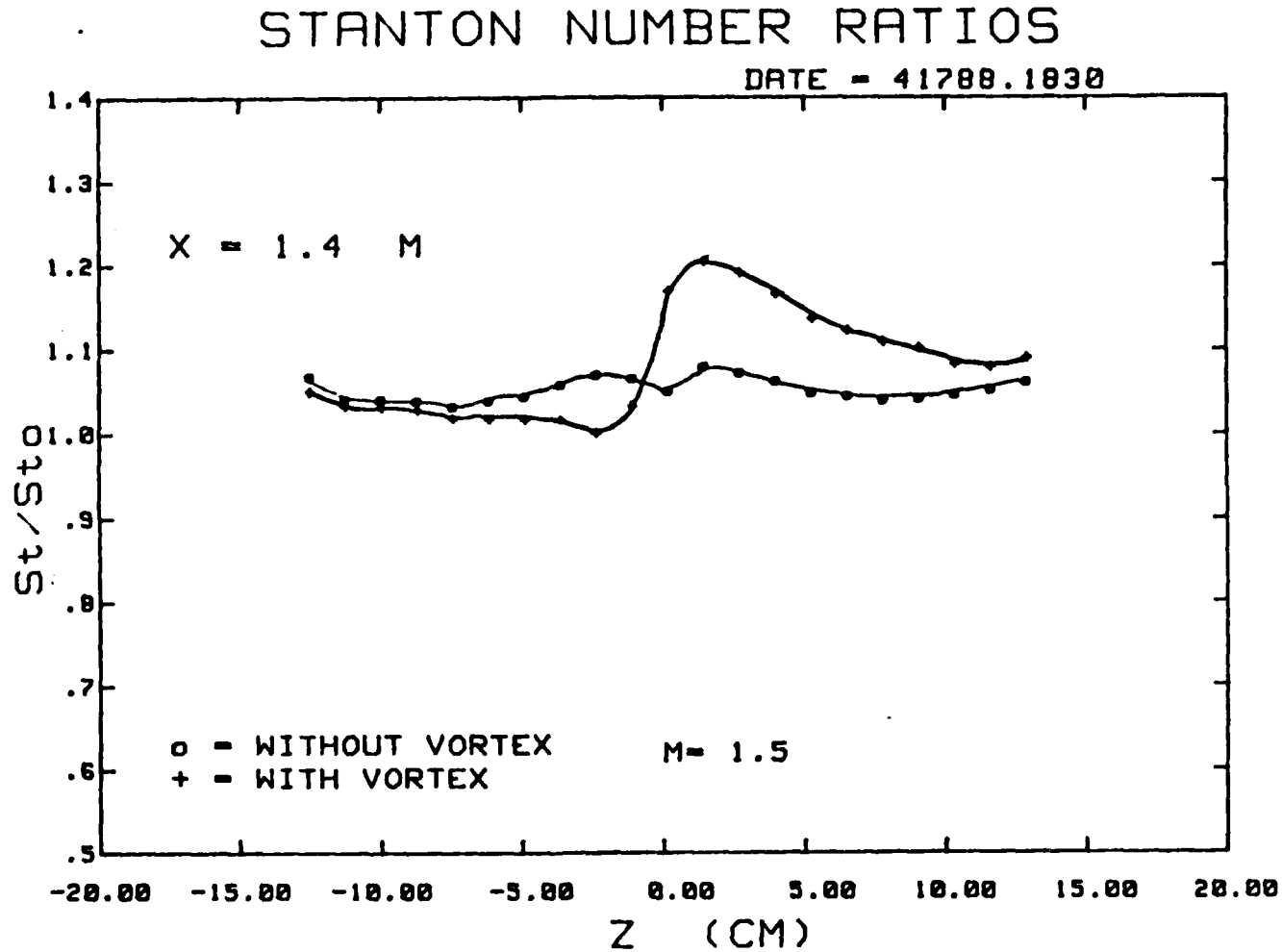

VG 1.5 INCHES FROM C/L, 10 M/S, 3 INJECTION HOLES

Figure 157. Spanwise Variation of Stanton Number Ratios
Vortex #2 Position h

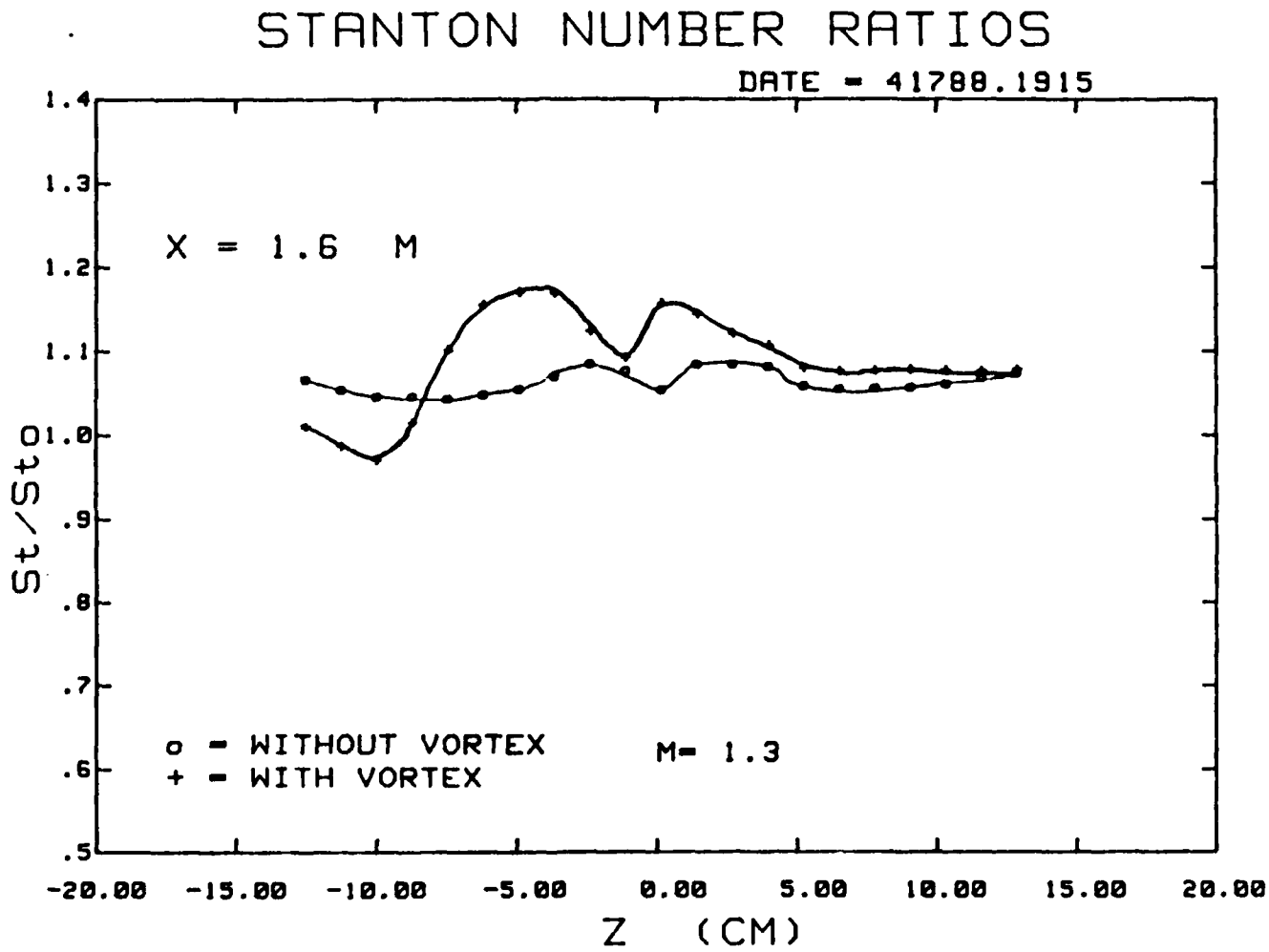

VG -1.5 INCHES FROM C/L, 10 M/S, 3 INJECTION HOLES

Figure 158. Spanwise Variation of Stanton Number Ratios Vortex #2 Position b

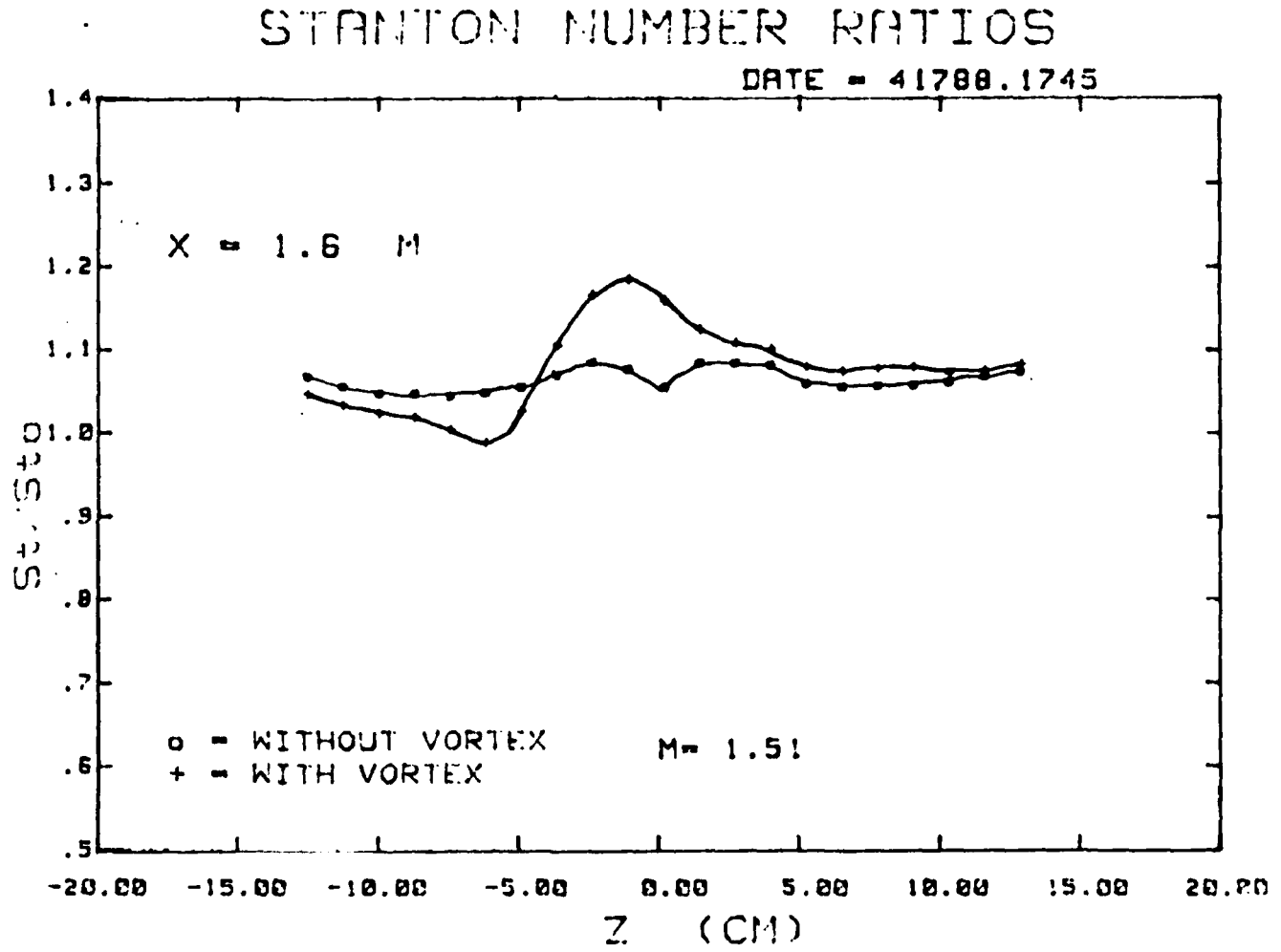

VG 0.0 INCHES FROM C/L, 10 M/S, 3 INJECTION HOLES

Figure 159. Spanwise Variation of Stanton Number Ratios
Vortex #2 Position e

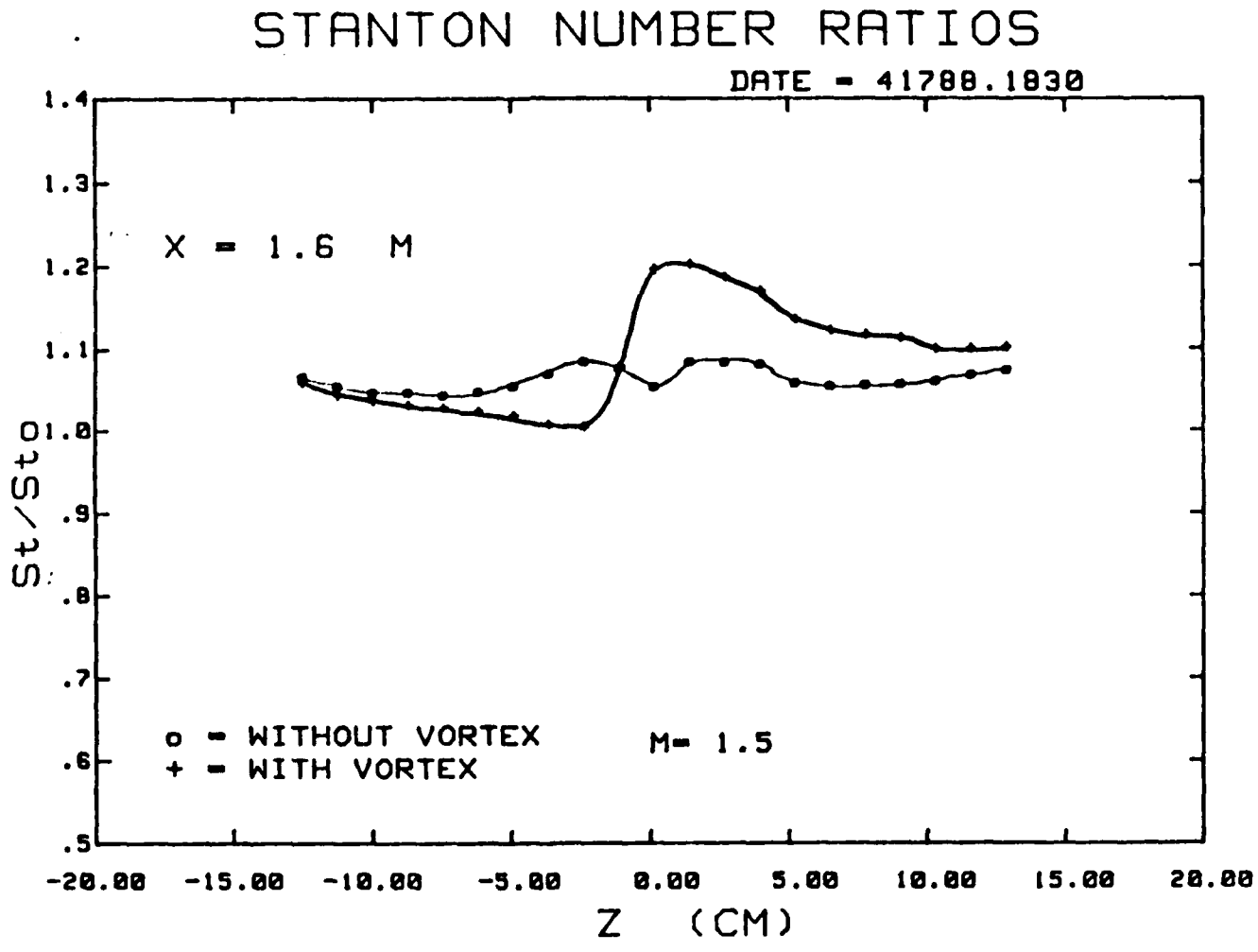

VG 1.5 INCHES FROM C/L, 10 M/S, 3 INJECTION HOLES

Figure 160. Spanwise Variation of Stanton Number Ratios Vortex #2 Position h

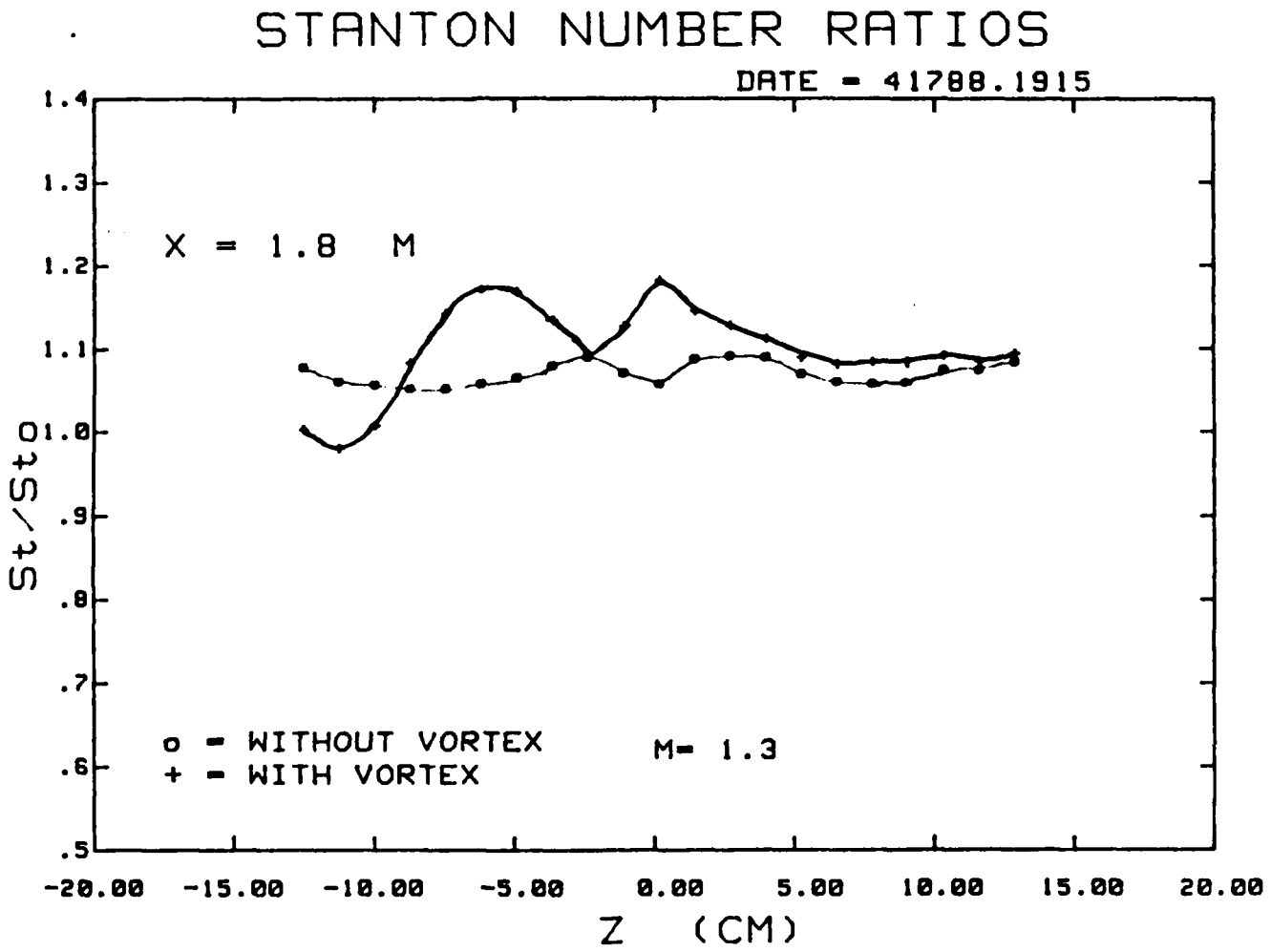

VG -1.5 INCHES FROM C/L, 10 M/S, 3 INJECTION HOLES

Figure 161. Spanwise Variation of Stanton Number Ratios
Vortex #2 Position b

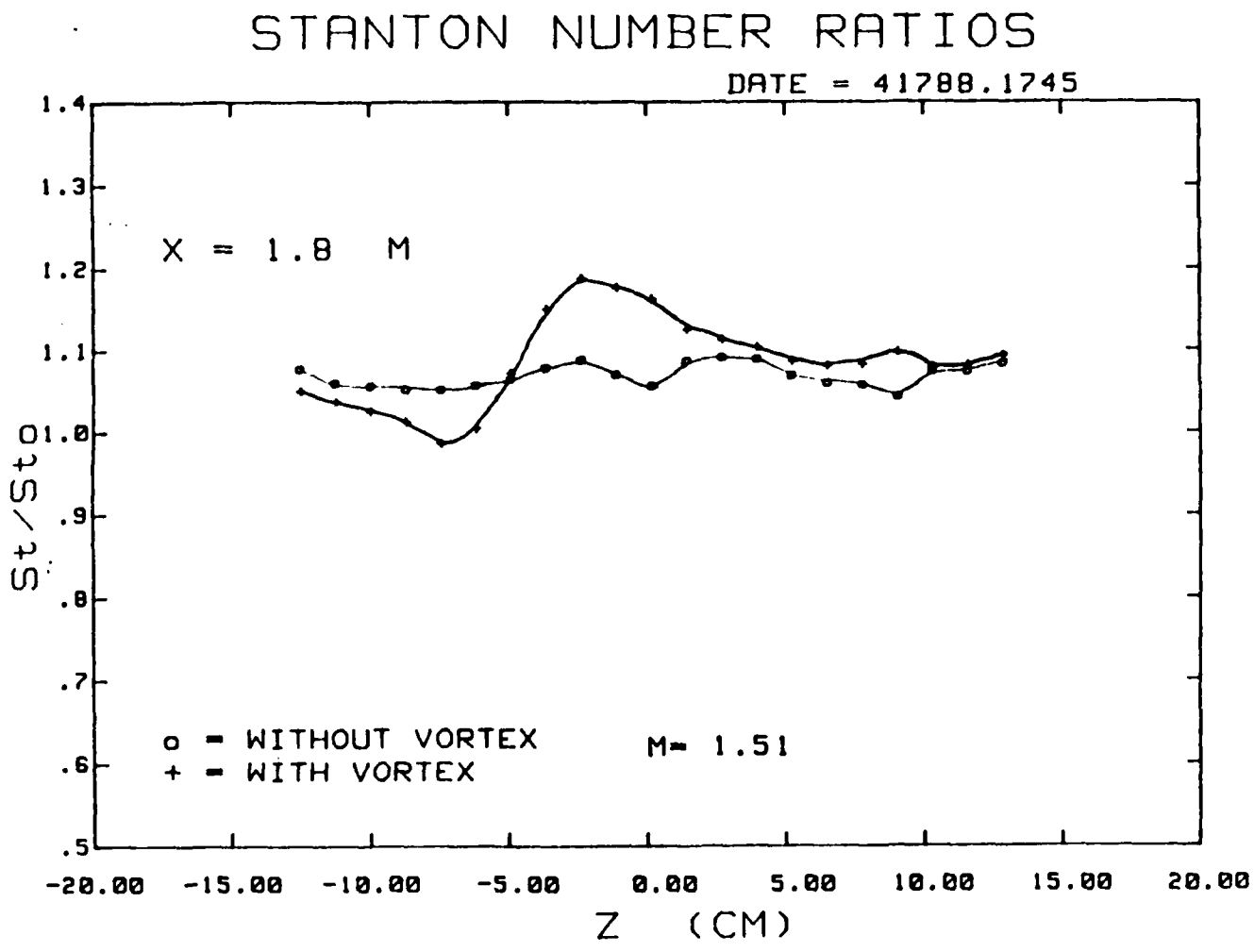

VG 0.0 INCHES FROM C/L, 10 M/S, 3 INJECTION HOLES

Figure 162. Spanwise Variation of Stanton Number Ratios Vortex #2 Position e

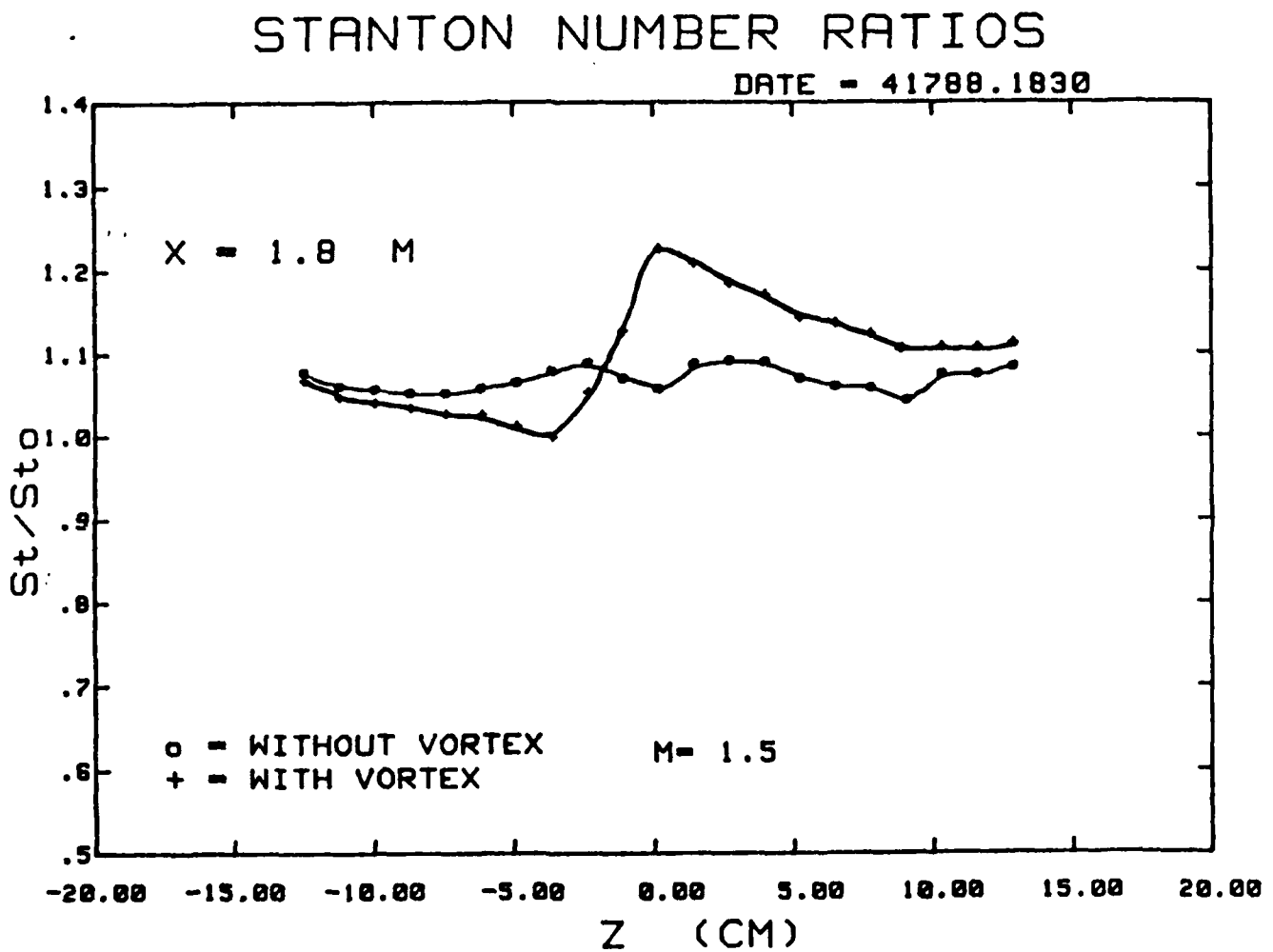

VG 1.5 INCHES FROM C/L, 10 M/S, 3 INJECTION HOLES

Figure 163. Spanwise Variation of Stanton Number Ratios
Vortex #2 Position h

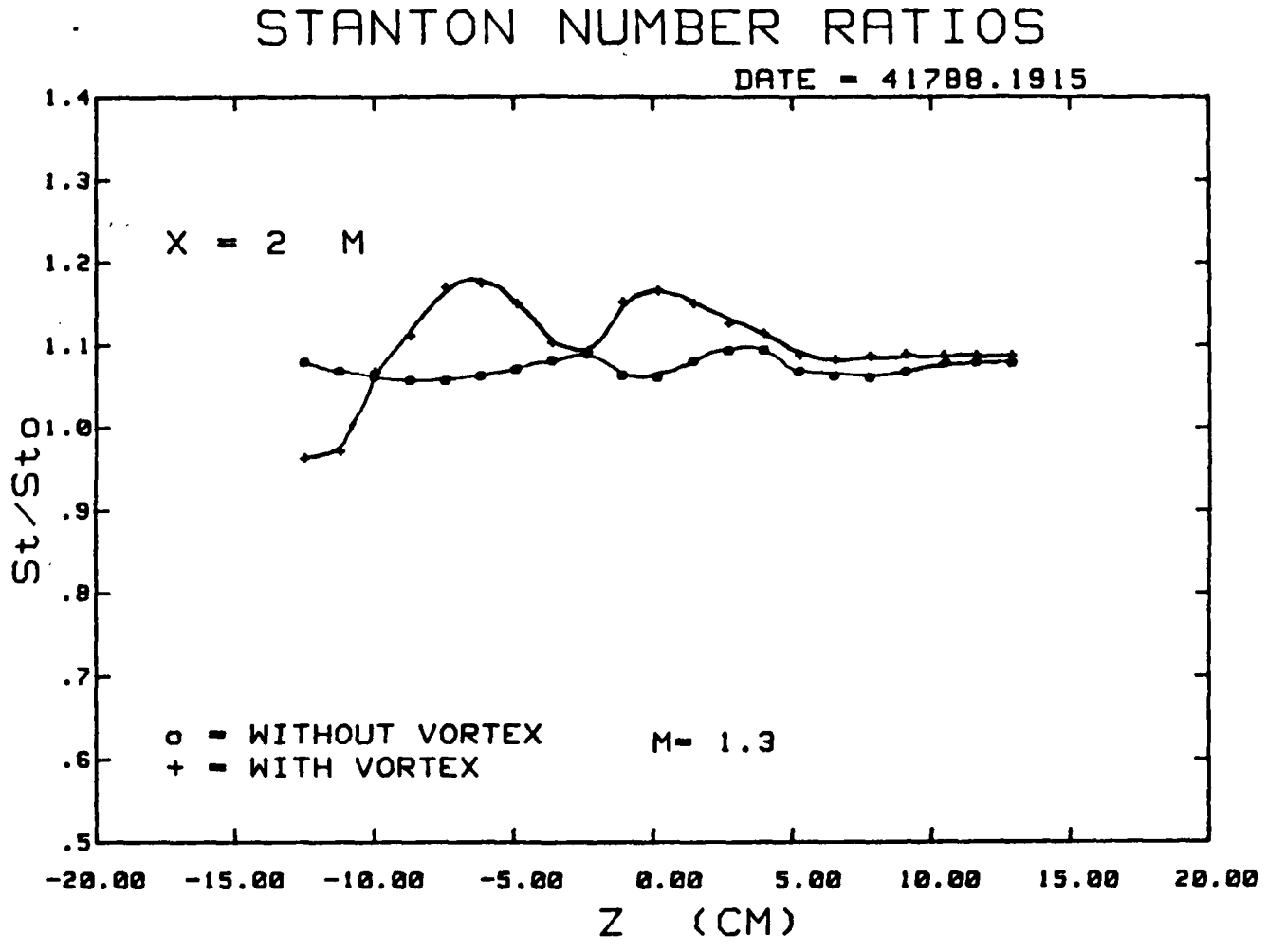

VG -1.5 INCHES FROM C/L, 10 M/S, 3 INJECTION HOLES

Figure 164. Spanwise Variation of Stanton Number Ratios Vortex #2 Position b

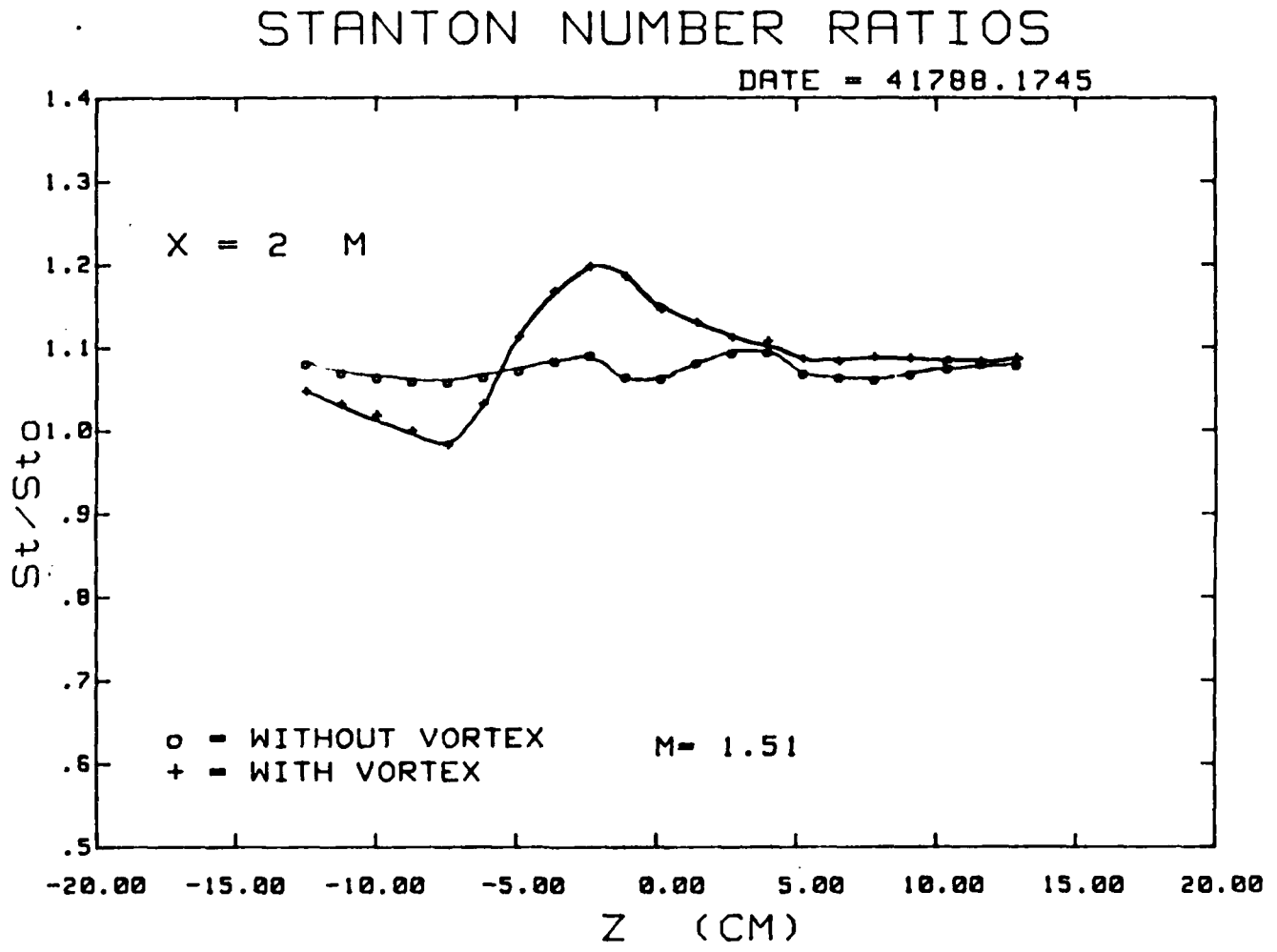

VG 0.0 INCHES FROM C/L, 10 M/S, 3 INJECTION HOLES

Figure 165. Spanwise Variation of Stanton Number Ratios Vortex #2 Position e

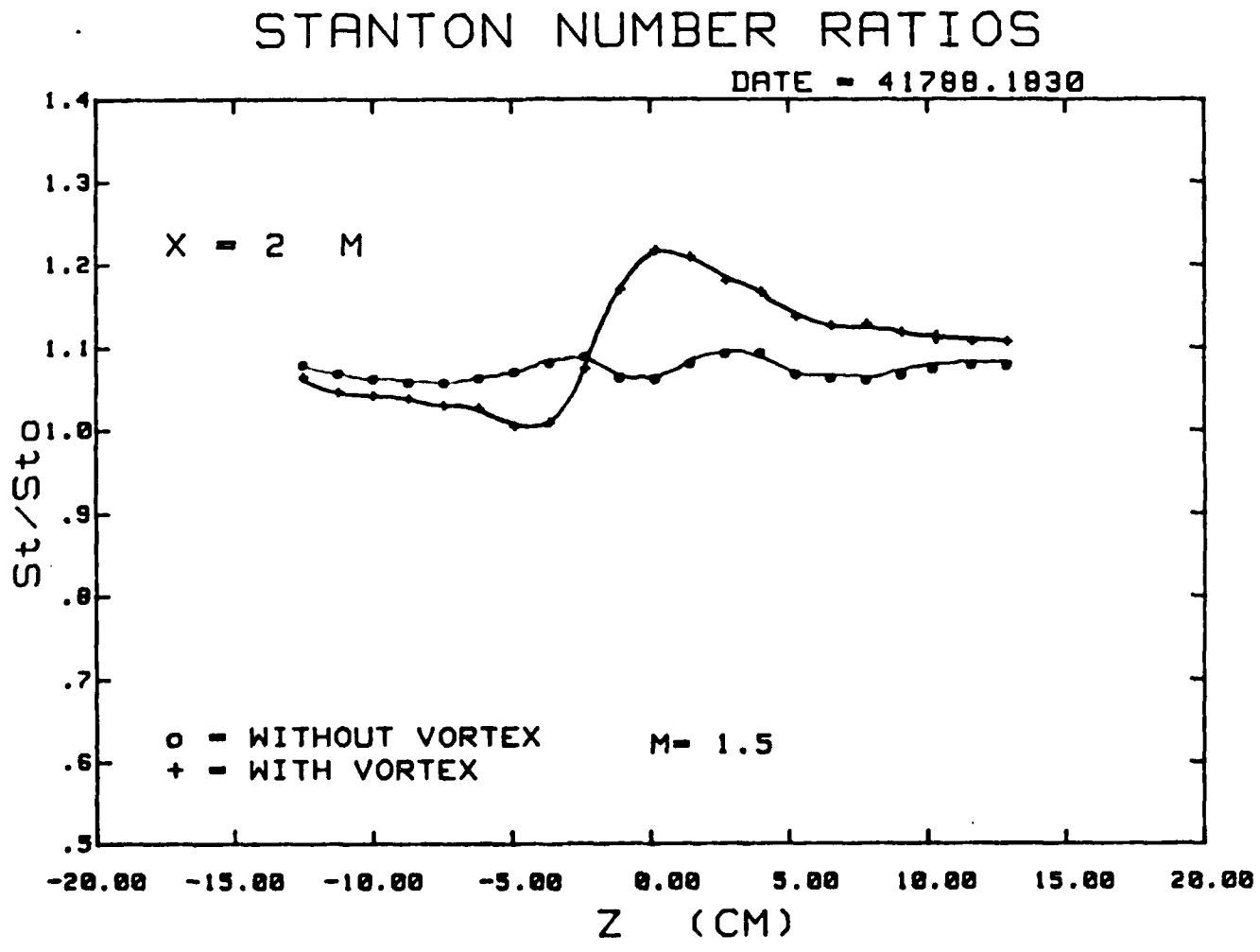

VG 1.5 INCHES FROM C/L, 10 M/S, 3 INJECTION HOLES

Figure 166. Spanwise Variation of Stanton Number Ratios Vortex #2 Position h

APPENDIX B

UNCERTAINITY ANALYSIS

Quantity (Units)	Typical Nominal Valve	Experimental Uncertainty
Tr_∞ (°C)	18.0	.13
Tw (°C)	40.0	.21
Pambient (mm Hg)	760.	.71
P_∞ (mm Hg)	760.	.71
$(Po_\infty - P_\infty)$ (mm water)	6.13	.047
P_∞ (Kg/m^3)	1.23	.009
U_∞ (m/s)	10.0	.06
C_p ($J/kg°k$)	1006.	1.
$q_w A$ (W)	270.	10.5
h ($W/m^2°k$)	24.2	1.03
St	.00196	.000086
St/St_o	1.05	.058
A (m^2)	.558	.0065
m	.98	.05
x/d	54.6	.36

APPENDIX C

SOFTWARE

The following programs are listed:

Temcheq: This program acquires multiple channel thermocouple data and performs energy balance to estimate conduction losses.

Setcond: This program is used to set conditions for data run. It determines injection velocity, Reynolds number, and blowing ratio. It requires terminal input of freestream conditions, % on rotometer, and delta P Plenum. This program gets plenum temperature from thermocouple 148 and gets plate average temperature to calculate Theta.

Stanton3: This program acquires multiple thermocouple data and creates a file to be read by Stanton4.

Stanton4: This program acquires multiple thermocouple data from Stanton3 and calculates heat transfer coefficients and stanton numbers.

Stanfc1: Heat transfer program to acquire thermocouple readings from DAS and Store information files on floppy disk. The files are read by Stanfc2.

Stanfc2: This is a middle program that runs after StanfC1. This program calculates Stanton numbers for all flow conditions from input file data created by StanfC1.

Stanfc3: This program runs after stanfc2. This program processes multiple channel thermocouple data and calculates heat transfer coefficients and Stanton numbers ratios and film-cooling parameters.

ENERB: Energy balance estimation for conduction losses.

ACQTPRO: Heat transfer program to acquire temperatures from automatic traversing device for temperature surveys.

PLOTRUN: Program to read a data file to plot temperature contours.

PTSTAV: Programs read a data file to plot spanwise averaged Stanton numbers vs. Reynolds number.

PTSTLC: Reads a data file to plot spanwise local heat transfer coefficients.

PLSTRTIO: Plots spanwise averaged St/Sto for film cooling only.

PLSTRAVOR: Plots spanwise variations of St/Sto for embedded vortex data only.

PLSTRVV: Plots spanwise variations of St/Sto for film cooling only and St/Sto for film-cooling and embedded vortex by rows.

SURFCONT: Plots surface contours of St_f/St_o.

PLSTRFC: Plots spanwise variations of local St/Sto for film-cooling data only.

Names of variables used are intended to be self-explanatory

LIST OF REFERENCES

1. Blair, M. F.,"An Experimental Study of Heat Transfer and Film-Cooling on Large-Scale Turbine Endwalls,"ASME Transactions--Journal of Heat Transfer, Vol. 96, pp. 524-529, 1974.

2. Goldstein, R. J. and Chen, H. P., "Film-Cooling on a Gas Turbine Blade Near the End Wall,"ASME Transactions--Journal of Engineering for Gas Turbines and Power, Vol.107, pp.117-122, January 1985.

3. Goldstein, R. J. and Chen, H. P., "Film-Cooling of a Turbine Blade with Injection Through Two Rows of Holes in the Near-Endwall Region,"The American Society of Mechanical Engineers, Paper No. 87-GT-196, pp. 1-7, June 1987.

4. Sato, T., Aoki, S., Takeishi, K. and Matsuura, M., "Effect of Three-Dimensional Flow Field on Heat Transfer Problems of a Low Aspect Ratio Turbine Nozzle", Takasago Research and Development Center, Mitsubishi Heavy Industries, Ltd., 1987.

5. Kobayashi, R., "Note on the Stability of a Bounddary Layer on a Concave Wall with Suction,"Journal of Fluid Mechanics, Vol. 52, pp. 269-272, 1972.

6. Kobayashi, R., "Taylor-Gortler Instability of a Boundary Layer with Sucction or Blowing," Report Institute of High Speed Mechanics, Vol. 32, Series B, pp. 129-148, 1975.

7. El-Hady, N. M. and Verma, A. K.,"Instability of Compressible Boundary Layers Along Curved Walls with Suction or Cooling,"AIAA Journal, Vol. 22, No. 2, pp. 206-213, 1984.

8. Joseph, S. L.,"The Effects of an Embedded Vortex on a Film-Cooled Turbulent Boundary Layer,"M. E. Thesis, U. S. Naval Postgraduate School, Monterey, CA., December 1986.

9. Evans, D. L.,"Study of Vortices Embedded in Boundary Layers with Film-Cooling,"M. S. Thesis, U. S. Naval Postgraduate School, Monterey, CA., March 1987.

10. Ortiz, A.,"The Thermal Bahavior of Film Cooled Turbulent Boundary Layers as Affected by Longitudinal Vortices", M. E. Thesis, U. S. Naval Postgraduate School, Monterey, CA., September 1987.

11. Westphal R. V., Pauley W. R. and Eaton J. K.,"Interaction Between a Vortex and a Turbulent Boundary Layer, Part I: Mean Flow Evolution and Turbulence Properties,"NASA Technical Memorandum 88361, January 1987.

12. Westphal, R. R., Eaton, J. K., and Pauley, W. R., "Interaction Between a Vortex and a Turbulent Boundary layer in a Streamwise Pressure Gradient", Fifth Symposium on Turbulent Shear Flows, Cornell University, Ithaca, NY 1985.

13. Eibeck, P. A. and Eaton, J. K.,"Heat Transfer Effects of a Longitudinal Vortex Embedded in Turbulent Boundary Layer,"ASME Transactions-Journal of Heat Transfer, Vol. 109, pp. 16-23, February 1987.

14. Ligrani, P. M. and Camci, C.,"Adiabatic Film Cooling Effectiveness From Heat Transfer Measurements in Compressible Variable-Property Flow," Journal of Heat Transfer, Vol. 107, pp. 313-320, May 1985.

15. Schwartz, G. E.,"Studies of thee Interactions Between Vortices and Shear Layers", M. S. Thesis, Naval Postgraduate School, September 1988.

INITIAL DISTRIBUTION LIST

		No. of Copies
1.	Defense Technical Information Center Cameron Station Alexandria, Virginia 22304-6145	2
2.	Library, Code 0142 Naval Postgraduate School Monterey, California, 93943-5002	2
3.	Department Chairman, Code 69 Department of Mechanical Engineering Naval Postgraduate School Monterey, California, 93943-5000	1
4.	Professor Phillip M. Ligrani, Code 69Li Department of Mechanical Engineering Naval Postgraduate School Monterey, California, 93943-5000	10
5.	Dr. Dick Rivir Components Branch Turbine Engine Division Aero Propulsion Laboratory Department of the Air Force Air Force Wright Aeronautical Laboratories Wright-Patterson Air Force Base, Ohio, 45433	10
6.	LCDR Warren W. Williams RT 1 Box 8 Dryden, Virginia 24243	4

		No of Copies
7.	Naval Sea Systems Command PMS 350 Washington, D. C. 20362	1
8.	Commanding Officer David Taylor R & D Center Carderrock Laboratory Bethesda, Maryland 20084	1